Liquid/solid interfacial rheology : from numerical simulations to experiments

Suzanne Lafon

université
PARIS-SACLAY

Liquid/solid interfacial rheology: from numerical simulations to experiments

Rhéologie à l'interface liquide/solide : des simulations numériques aux expériences

Thèse de doctorat de l'université Paris-Saclay

École doctorale n°564 Physique en Île-de-France (PIF)
Spécialité de doctorat : Physique
Graduate School : Physique. Référent : Faculté des sciences d'Orsay

Thèse préparée dans les unités de recherche **Laboratoire de Physique des Solides (Université Paris-Saclay, CNRS)** et **Laboratoire Léon Brillouin (Université Paris-Saclay, CEA, CNRS)**,
sous la direction de **Frédéric RESTAGNO**, directeur de recherche,
et la co-direction de **Alexis CHENNEVIERE**, chargé de recherche CEA.

Thèse soutenue à Paris-Saclay, le 10 novembre 2023, par

Suzanne LAFON

Composition du jury

Membres du jury avec voix délibérative

Lydéric BOCQUET Directeur de recherche, Université PSL	Président
Jean-Louis BARRAT Professeur, Université Grenoble-Alpes	Rapporteur et examinateur
Karin JACOBS Professeure, Université de Saarland, Allemagne	Rapportrice et examinatrice
Thomas SALEZ Chargé de recherche, Université de Bordeaux	Examinateur

THESE DE DOCTORAT
NNT : 2023UPASP144

université PARIS-SACLAY

ÉCOLE DOCTORALE
Physique en Île-de-France (PIF)

Titre: Rhéologie à l'interface liquide/solide : des simulations numériques aux expériences **Mots clés:** Glissement, Frottement liquide/solide, Polymères

Résumé: L'objectif de cette thèse est d'étudier la rhéologie des liquides au voisinage d'une paroi rigide. En particulier, nous nous intéressons aux mécanismes moléculaires qui sous-tendent le glissement et le frottement liquide/solide. Pour cela, nous étudions l'effet de la température sur la dynamique des liquides près de la surface.

Dans un premier temps, nous utilisons des simulations de dynamique moléculaire d'un liquide modèle pour étudier la dépendance en température du frottement. Nous montrons qu'à haute température, le frottement et le glissement sont des processus activés, avec une barrière d'énergie contrôlée par l'énergie d'interaction liquide/solide. Au contraire, le liquide surfondu présente deux comportements différents : pour de fortes interactions avec la paroi, le frottement, comme la viscosité, diverge de manière super-Arrhenienne. Au contraire, pour des interactions plus faibles, le frottement est fortement réduit, car les premières couches de liquide en contact avec la surface cristallisent.

Dans un second temps, nous nous concentrons sur le frottement entre une solution semi-diluée de polystyrène et une surface solide. Tout d'abord, nous utilisons la réflectivité de neutrons pour déterminer le profil de concentration du liquide près de la paroi. En particulier, nous montrons qu'une déplétion en polymère à l'interface n'empêche pas l'adsorption de chaînes sur le substrat. Ensuite, nous avons développé une nouvelle méthode pour mesurer le frottement à l'aide d'un rhéomètre. De manière surprenante, nous observons une forte dépendance du coefficient de frottement avec le taux de cisaillement, ce qui suggère que le liquide interfacial est rhéo-fluidifiant, avec un temps de relaxation typique qui est différent de celui du liquide en volume. Enfin, nous avons étudié la cinétique d'adsorption des polymères fondus. Nous montrons que le PDMS présente un taux d'adsorption étonnamment élevé par rapport aux autres polymères, ce qui est attribué à l'interaction particulièrement forte entre le PDMS et la surface.

Title: Liquid/solid interfacial rheology: from numerical simulations to experiments **Keywords:** Slip, Liquid/solid friction, Polymers

Abstract: The purpose of this thesis is to study the near-wall rheology of liquids. In particular, we are interested in the molecular mechanisms underlying slip and liquid/solid friction. To this end, we probe the temperature effect on the dynamics of liquids near the solid.

In a first part, we use molecular dynamics simulations of a glass-forming model liquid to study the temperature-dependence of friction. We show that, at high temperatures, both friction and slippage are activated processes, with an energy barrier that is controlled by the liquid/solid interaction energy. On the contrary, the supercooled liquid exhibits two different behaviours: for strong liquid/solid interactions, the friction, as the viscosity, diverges in a super-Arrhenian fashion. For weaker interactions, friction is strongly reduced as the first liquid layers in contact with the wall crystallise.

In a second part, we focus on friction between polystyrene semi-dilute solutions and a solid wall. First, we use neutrons reflectivity to determine the near-surface concentration profile. In particular, we show that a polymer depletion at the interface does not prevent chain adsorption onto the substrate. Then, we develop a new method to measure liquid/solid friction using a rheometer. Surprisingly, we have observed a strong shear-rate dependency of the friction coefficient, which suggests that the interfacial liquid is shear-thinning, with a typical relaxation time that is different from the bulk one. Finally, we study the adsorption kinetics of polymer melts. We show that PDMS exhibits a particularly large adsorption rate compared to other polymers, and this is attributed to the strong interaction between PDMS and the surface.

Acknowledgments

Ce travail a bénéficié de l'aide et de l'investissement d'un très grand nombre de personnes, et j'aimerais en remercier les principaux protagonistes.

Je remercie tout d'abord le jury d'avoir accepté d'évaluer ce travail. Merci à Jean-Louis Barrat et Karin Jacobs d'avoir pris le temps de rapporter cette longue thèse. Merci à Thomas Salez d'avoir relu avec autant d'attention mon manuscrit, en plus d'avoir évalué ma soutenance. Merci enfin à Lydéric Bocquet d'avoir accepté de présider ce jury. Ce fut un honneur de vous avoir tous les quatre dans mon jury.

Marie Curie décrivait les "*conversations devant le tableau noir*" comme des souvenirs qui lui étaient chers, car elles agissent "*comme un stimulant de l'intérêt scientifique et de l'ardeur au travail, sans interrompre le cours des réflexions et sans troubler cette atmosphère de paix et de recueillement qui est la véritable atmosphère d'un laboratoire*"[a]. Je voudrais remercier les deux personnes qui, non seulement sont à l'origine de ce projet de thèse, mais grâce à qui cette image a pris du sens pour moi : mes directeurs de thèse, Frédéric et Alexis. Fred, tu m'as proposé un sujet sur mesure, qui s'adaptait à ce que je voulais faire, et tu as fait en sorte que, au fil de ces trois années, nous puissions cocher tous les critères que j'avais listés. C'est une chance rare que j'ai eue et je te remercie de me l'avoir fournie. Merci d'avoir répondu aussi vite, aussi bien et avec autant de pédagogie à toutes mes questions, des plus idiotes aux plus complexes, ou à défaut, d'avoir trouvé des interlocuteurs avec qui nous avons pu échanger. Alexis, ces trois années en tant que directeur de thèse officiel ont mis en avant à quel point tu es un encadrant génial, drôle et attentif au bien-être des gens avec qui tu travailles. Merci d'avoir activement fait en sorte qu'on se sente bien au LLB, merci pour tous tes conseils en informatique (du traitement de réflectivité neutrons au hacking de radios), merci d'avoir toujours été disponible pour Tiago et moi. Merci à tous les deux pour votre encadrement toujours bienveillant et positif, pour les réunions qui nous boostent et pour votre énergie au quotidien. Merci enfin d'avoir fait attention à notre santé pendant la thèse et à nos perspectives de carrière après la thèse.

Je souhaite également remercier les personnes qui ont collaboré, de près ou de loin, à ce travail. Tout d'abord, je remercie Laurent Joly et Samy Merabia, qui ont eu la gentillesse de m'accueillir à Lyon pendant deux semaines. Merci Laurent de m'avoir appris aussi efficacement les bases de la dynamique moléculaire en un temps record. Merci à tous les deux pour les nombreuses réunions que l'on a eues, vos conseils et votre réactivité. C'était un plaisir de travailler avec vous. Je remercie aussi Etienne Fayen et Patrick Judeinstein pour leur aide dans mes débuts de dynamique moléculaire, et la gestion du cluster. Un grand merci à Philipp Gutfreund, notre local contact à l'ILL à Grenoble, qui nous a accueillis et accompagnés durant nos deux (difficiles) sessions de réflectivité neutrons sur D17. Merci aussi à Simone Napolitano et Erik Toms, qui nous ont accueillis à Bruxelles pour les manips de diélectrique. Je remercie enfin les membres de mon CST,

[a] Madame Curie, Eve Curie, Gallimard (1981)

Giuseppe Foffi et Elie Raphaël, pour votre bienveillance et votre investissement lors des réunions annuelles. Merci en particulier à Giuseppe pour tous tes conseils pour la suite. Je remercie également Amélie, ma mentore durant ma première année, pour son écoute et ses conseils réguliers.

Durant ces trois années, j'ai eu la chance d'encadrer deux stagiaires, Oriane Merlaud et Lilian Dahan. Merci Oriane d'avoir été aussi assidue et volontaire malgré les très longs trajets que tu devais faire pour venir quotidiennement. Merci Lilian d'avoir pris en main aussi rapidement les manips de rhéo. Je vous souhaite à tous les deux le meilleur pour la suite.

Enfin, je voudrais remercier tous les gens qui ont participé à rendre mon quotidien de thésarde agréable. D'une part, je remercie tous les gens de l'équipe MMB, au CEA, pour leur accueil, leur bienveillance et leur curiosité. Daniel, merci pour ton aide avec les mesures de rhéo, de m'avoir sauvé la mise quand j'ai fait des bêtises avec et de n'avoir pas (trop) râlé quand tu devais étaler des solutions viscoélastiques qui ne veulent pas sortir de leur flacon. Merci pour tes sarcasmes, même si ton humour est très mauvais, j'ai tout de même (un peu) rigolé. Merci Marion pour ton aide précieuse, tes tutos vidéos pour la FRAP, ta présence et ton soutien depuis que tu es revenue en région parisienne. Merci Annie pour tes cours à Cargèse, les glaces en bord de mer, et tes récits de voyage. Merci Arnaud pour ton aide précieuse dans le design de la cellule neutrons, même dans les rushs juste avant les manips. Merci aussi à tous les autres formidables permanents de l'équipe que j'ai eu la chance de côtoyer : Christiane, Clémence, Fabrice, François, Lay-Theng, Marianne, Marie-Claire, Patrick, Sophie et Stéphane. Merci enfin aux doctorant.e.s et postdoctorant.e.s de l'équipe que j'ai croisés, de près ou de loin : Cécile, Christelle, Hugo, Maeva, Maja, Manon, Oriana, Qjang, Simeon et beaucoup d'autres encore.

D'autre part, je remercie les membres du LPS, en particulier l'administration du labo, qui fait de son mieux pour nous faciliter la vie malgré la lourdeur démentielle de l'administratif français. Merci à Véronique, Sophie et Mélanie en particulier. Merci également à la directrice du laboratoire, Pascale Foury, qui nous a soutenus dans notre tâche de représentants des non-permanent.e.s, et qui a toujours été de bonne volonté pour organiser les sensibilisations aux Violences Sexistes et Sexuelles qui me tenaient à cœur. Je remercie aussi tous les gens d'Elinstru et du service info, pour leur aide précieuse. Je remercie également les doctorant.e.s avec qui j'ai eu le plaisir d'échanger au cours de ces trois années, Mateo, Marina, Baptiste, Antoine, Etienne, Jean-Baptiste, Andréa, Léo, Noémie, Hélène, Malar, Gauthier, Aurélien, Jules, Malo, et bien d'autres.

Je remercie enfin tous les gens de l'équipe MMOI, pour votre accueil et le climat sympathique et agréable dans lequel vous nous permettez de travailler au quotidien. François, merci d'avoir partagé ton bureau avec moi pendant plus d'un an et demi, et merci pour tes conseils avisés en matière de code et de postdoc. Merci Liliane pour ton aide tout au long de ma thèse, tu es une incroyable source de connaissances et une pédagogue infiniment douée, et je suis heureuse d'avoir pu travailler avec toi. Merci à tous les permanent.e.s de l'équipe qui apportent soutien, bonne volonté et curiosité au quotidien. En particulier, merci à Manue et Anniina de nous fournir des modèles inspirants de chercheuses. Merci à Sandrine pour les cafés gossip, les concours de Tuc et pour l'énergie que tu nous apportes.

Viens ensuite le tour des non-permanent.e.s. Merci tout d'abord à mon super co-thésard, Tiago. Tu as subi avec moi ces deux manips neutrons de l'enfer, toujours plein de bonne volonté et d'énergie, qui m'ont permis de tenir bon. Merci pour ta présence calme et positive, et merci d'avoir été à l'écoute quand ça allait moins. Merci pour Cargèse, pour Biarritz, pour Athènes (on se retrouve toujours au bord de la mer avec toi, étonnamment), et pour toutes les discussions, scientifiques ou non, que l'on a eues. Merci ensuite à mon deuxième co-bureau, Alexis. Merci d'être quelqu'un sur qui on peut compter autant, que ce soit quand on veut faire une pause parce qu'on n'en peut plus de rédiger, ou bien quand on a coincé une voiture dans la pampa et qu'il faut trouver comment la tracter sur la route 50 mètres plus haut. Merci aussi d'avoir partagé avec moi cette (lourde) tâche de représenter les non-permanent.e.s du labo. Merci Julian de m'avoir fourni de (très) nombreuses occasions de faire des pauses pour papoter (et gossiper, je rappelle que tu es un pro de la pêche aux informations), et d'avoir fait attention à ce que tout le monde suive un rythme de travail sain. Merci aussi de m'avoir accompagnée à l'autre bout de l'Europe, pour une semaine de vacances dans des conditions affreusement sympathiques le long du Péloponnèse. Merci à Elina de m'avoir accompagnée dans nos diverses visites de musées grecs, et merci d'avoir pris l'initiative de nous maintenir en forme grâce à tous les gâteaux que tu as amenés. Merci aussi aux irréductibles membres du "Lunch inside", j'ai nommé Manon, Marina, Marie (notre déléguée des jeunes MMOI, merci d'avoir joué ce rôle indispensable), et le trio des cool kids Alice R. (toujours prête à aider tout le monde), Marion (grande maîtresse des remarques subtiles, rigolotes et malaisantes placées toujours comme il faut) et Théophile (que je remercie non seulement pour ses anecdotes rigolotes du quotidien, mais aussi pour avoir accepté de prendre notre relève de représentant des non-permanent.e.s). Merci à Aymeric d'avoir animé mon début de thèse de soirées à Orsay, ainsi qu'à Alice E., Baptiste, Shailesh, Tatiana, Laura, Christophe et aux deux nouveaux loustics, Victor et Salomé, qui vont prendre la relève.

Enfin, je tiens à remercier ma famille, pour son soutien et son enthousiasme tout au long de ce cursus éprouvant. Je remercie également mes amis, dont beaucoup ont fait le déplacement pour ma soutenance. Merci à Juju, Marine, Maïka, Marina, Zoubi, Zuki, Pauline, Maud, Ludi, Anto, Apo, Gabriel, Caro, Victor... Merci à Zoubi, Yugi et Martin de m'avoir fourni l'occasion de m'aérer brièvement l'esprit à la montagne au milieu de ma rédaction. Merci à Aurel d'avoir fêté avec moi la fin de ma rédaction en bivouaquant (sous l'orage) au milieu des Pyrénées. Merci à Gro d'avoir saupoudré ces trois années de sessions de chill et de fun facts animaliers. Merci à Clémence, qui a dû me supporter tout du long, et répondre à mes questions de science à n'importe quelle heure (du jour et de la nuit) et sur n'importe quel sujet, et qui s'est assurée que la piètre cuisinière flemmarde que je suis mange correctement. Merci à vous trois pour votre incroyable (au bas mot) inspiration en matière de blagues scientifiques. Merci à mon indétrônable partenaire de grimpe, Gaétan, qui a trouvé que la clé pour me faire grimper du dévers était de m'acheter avec des pains au chocolat, et qui m'a fourni moult occasions ludiques de m'aérer l'esprit (hihi). Merci enfin à Emma de m'avoir permis de m'enfuir à l'autre bout du monde méditer dans des temples bouddhistes ou gravir l'Atlas en jean. J'ai hâte de voir à quoi va ressembler la suite.

Merci à toutes et à tous !

Contents

General Introduction

This thesis has a common thread: the behaviour of liquids near a solid, which guided me throughout the last three years. This is not a single scientific question, but rather a direction I have tried to steer, in my own way and with the great help and advices of my supervisors and coworkers. Thus, this is not a 180-page answer to a single fixed question, but rather a composition in two acts and multiple scenes, revolving around a common theme and − hopefully − raising some nice scientific questions along the way.

That being said, I can now introduce the subject of this work. The title of this thesis is "Liquid/solid interfacial rheology". The word **rheology** comes for ancient greek $\rho\epsilon\omega$ (*to flow*) and $\lambda o\gamma o\varsigma$ (*the study*) and means *the study of flows*. Thus, we are interested in the way liquids flow in the vicinity of solid surfaces, and more generally, the dynamics of liquids near walls. In particular, we want to provide microscopic models to describe the liquid/solid friction. For non-specialist readers, the notion of liquid friction might be surprising. Unfortunately, this is not a very visual concept, and it is difficult to imagine. Therefore, I propose a more visual analogy. Imagine that you are in the middle of a crowd, moving along a corridor. Everyone is moving in the same direction. Necessarily, you are pulled along by your immediate neighbours, and you find yourself moving in the same direction as everyone else. Now, you are in the same crowd, but you are at the edge, close to the wall. The whole crowd is moving in the same direction, and again, you are being pulled forward. Yes, but this time, on the other side, there is the wall. If you move forward, you are bound to rub against that wall, and that is going to be painful. So you resist as much as you can, so as not to move forward, so as not to rub against that wall. This wall would be covered in silk, the rubbing would be less painful for you, and you might agree to let yourself be carried along by the flow. But under these conditions, you resist, and you stay put. As a result, your immediate neighbours are slowed down. And so do their neighbours. And so on. Eventually, the average speed of the whole crowd is reduced. By refusing to move against the wall, you have changed the whole flow.

This image, which I admit is somewhat anxiety-provoking, is an illustration of what a liquid molecule can experience in a flow. Let us take the case of a pipe through which water is flowing. The water molecules at the centre of the pipe will move fast, dragging along their neighbours. The more strongly they interact with each other, the more likely they are to pull each other along. This is called **viscosity**. Conversely, just as you do not want to rub against the corridor wall, water molecules near the wall are reluctant to move forward. This resistance to flow near a wall is called **friction**. Now, if the wall is made more "pleasant" for water molecules (for a water molecule, it is not a matter of covering it with silk, but with specific chemical molecules), then they will agree to move forward along the pipe wall. This is called **slippage**. If the water molecules close to the wall slip, then they no longer hold back their immediate neighbours, and the flow as a whole is accelerated.

This metaphor introduces a key concept that we will be discussing a lot in this work:

the competition between viscous drag and flow resistance near the wall due to friction. The consequence of these two antagonistic effects is slippage: high slippage if the viscous entrainment is strong, low slippage if the liquid/solid friction dominates. The aim of this work is to provide a better understanding of the molecular processes at play in a liquid flowing near a solid surface. In particular, we would like to understand how temperature (and therefore molecular agitation) plays a role in this problem. As all this happens on very small scales, there are many questions about how to properly measure the behaviour of molecules on such small lengths, which will discussed along this thesis.

A question I have been hearing a lot during the last three years is: "What is the point of studying this? What are the applications?" Actually, the question of liquid/solid friction is useful in a broad variety of domains. In geoscience, to describe the flow of such viscous liquids as magmas, it is necessary to be able to quantify their slip. Similarly, reducing friction is an important goal for oil extraction, because the energy applied to extract oil from the ground is directly linked to the friction of the liquid on the solid walls. In sports, liquid/solid friction often plays a major role. It is a central question for surfing or skiing, for instance. At a much smaller scale, in biology, there are a lot of flows for which liquid/solid friction matters. We can think of blood flows in arteries and veins: the fat covering the inside of the vessels lubricates the flow. We can also mention water filtration through the kidneys, as well as water permeation through cell membranes. These processes need to be efficient and to minimize the energy loss due to liquid/solid friction. The wonderful machine that is our body does this incredibly well. Furthermore, in microfluidics, we often use chemical coatings such as silanisation to make some surfaces hydrophobic and, thus, slippery. Besides, the recent field of nanofluidics requires looking at flows on tiny length scales, so tiny that the near-surface behaviour of liquid molecules becomes a central question, and it is necessary to provide microscopic models to describe them.

The first chapter of this thesis is a state-of-the-art about the concepts that will be used throughout this work. We will introduce the mathematical definition of slip and friction, the temperature dependencies of the liquid dynamics (both in bulk and at the vicinity of a solid wall) and we will give some basic results about polymer physics, which will be required to understand the experimental part about liquid polymers. Then, the first part of this thesis deals with Molecular Dynamics simulations. We will use a model liquid, called a Lennard-Jones liquid, to try and understand the effect of temperature on slip and friction for a very simple system. In a first chapter, we present the numerical methods used to simulate such liquid. In a second chapter, we discuss the friction of a bi-disperse Lennard-Jones liquid, which is able to reach a supercooled state. In the third and last chapter of this first part, we briefly mention what happens for a purely monodisperse Lennard-Jones fluid, which cannot reach supercooled conditions and crystallizes. Afterwards, in the second and largest part of this work, we will focus on the behaviour of liquid polymers near a solid rigid wall. The first chapter of this part is a summary of the various experimental methods used. The second chapter presents some neutrons reflectivity measurements to probe the near-surface concentration profile in a polymer solution facing a solid substrate. In a third chapter, we focus on the near-surface rheology of polymer solutions, using two different techniques. In the fourth and last chapter, we switch to polymer melts, and we discuss their adsorption kinetics in comparison with relaxation

processes obtained by dielectric measurements. Finally, we draw a general conclusion to this work, summarizing what we have seen in the various chapters, and the questions raised by our results.

Chapter 1

State-of-the-art

Contents

The present work aims at describing the molecular mechanisms underlying these two ways of dissipating energy: the viscous dissipation inside the liquid and the friction dissipation at the liquid-solid interface. There is a fundamental difference between these two dissipations: the first one is a *bulk* dissipation, while the other one is a *surface* dissipation. These two behaviours are related to the ability of the liquid molecules to relax the stress, both in the bulk and at the interface. Therefore, their dynamics is strongly related to the thermal agitation of the liquid molecules, and thus, temperature is a key parameter in order to understand the corresponding microscopic mechanisms.

The purpose of this chapter is to provide the key physical ingredients that will be used throughout this manuscript. In Section 1.1, we start by presenting Navier's formalism of the slip boundary condition, introducing the liquid/solid friction coefficient λ. We discuss existing models describing the role of temperature on the dynamics of bulk and interfacial liquids in Section 1.2. In Section 1.3, we then take a brief detour into polymer physics, since liquid polymers are good candidates to exhibit strong slip on solid surfaces. We conclude this introduction by a discussion on the specificity of slip and friction of polymers compared to other liquids.

1.1 Friction at the liquid-solid interface

To describe the movement of a liquid, we need to assume the behaviours of the liquid near the boundaries of the flow. The question of the boundary condition near a solid wall has been addressed many years ago, during the derivation of the famous Navier-Stokes equations. In the present section, we summarize the historical description – still in use – of the liquid-solid slip and friction.

1.1.1 Definition of the liquid-solid friction coefficient

Viscosity. The constitutive equation of the sheared fluid relates the bulk stress σ_{bulk} to the shear-rate $\dot{\gamma}$ through:

$$\sigma_{\text{bulk}} = \eta\dot{\gamma} \tag{1.1}$$

This defines the **shear viscosity**, η, of the fluid. For a planar Couette flow (see Fig. 1.1), if we write z the normal to the wall and $v(z)$ the velocity of the liquid, the shear-rate is $\dot{\gamma} = \mathrm{d}v/\mathrm{d}z$ and thus:

$$\sigma_{\text{bulk}} = \eta\frac{\mathrm{d}v}{\mathrm{d}z} \tag{1.2}$$

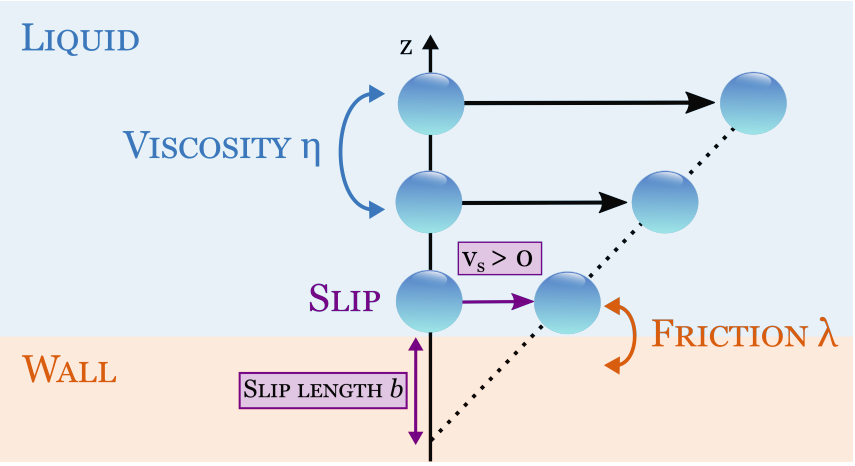

Figure 1.1: Cartoon of slip at the liquid-solid interface.

Friction. Liquid-solid friction was first described by Navier himself [1] in 1823. He made the hypothesis that the stress at the wall $\sigma_{\text{L/S}}$ is proportional to the relative velocity of the liquid at the wall v_s:

Definition of the liquid/solid friction coefficient λ

$$\sigma_{\text{L/S}} = \lambda v_s \tag{1.3}$$

with λ a coefficient, which is called the **friction coefficient** (in $\text{kg.m}^{-2}\text{.s}^{-1}$). v_s is the **slip velocity**: this is the velocity of the liquid at the wall in the referential where the wall is immobile. λ is the key parameter of the present work, and thus we will discuss its

dependencies in subsection 1.1.3. Its value is usually very large ($10^6 - 10^8$ kg.m^{-2}.s^{-1} for liquid polymers on silicon wafers, see [2,3] for PDMS on bare and grafted wafers, $10^4 - 10^5$ kg.m^{-2}.s^{-1} for hexadecane on sapphire and OTS surfaces [4]).

Slip length. We can define a **slip length** b as:

$$\eta \frac{\mathrm{d}v}{\mathrm{d}z}(z_{\text{wall}}) \equiv \eta \frac{v_{\text{s}}}{b} \tag{1.4}$$

The slip length b corresponds to the distance from the interface at which the velocity profile linearly extrapolates to 0. Using the stress continuity $\sigma_{\text{bulk}} = \sigma_{\text{L/S}}$, we can thus express b in terms of λ and η using Eqs. 1.2 and 1.3:

Slip length

$$b = \frac{\eta}{\lambda} \tag{1.5}$$

For a finite λ, we can see that there is always slip. In practice, the effect of slip on the overall flow is negligible if the typical size ℓ of the flow is much larger than the slip length: $\ell \gg b$, which corresponds to a friction coefficient $\lambda \gg \eta/\ell$. Its value can vary between a few nanometres for water on various smooth surfaces [5,6], a few hundred nanometres for hexadecane on sapphire and OTS [4], and even a few millimetres for some polystyrene semi-dilute solutions [7].

Eq. 1.5 deserves a physical discussion. η is a pure bulk quantity describing the liquid-liquid friction, while λ describes a local liquid-solid friction which depends on the liquid/wall interaction. Thus, b is the result of the competition between liquid-liquid friction, which tends to make the liquid slip, and the liquid-solid friction, which tends to slow down the liquid in contact with the wall. It is a quantity that is often used by the slip community because it is usually the quantity experimentally accessible with velocimetry techniques (contrary to λ). Throughout this manuscript, we will discuss the relevance of using λ instead of b, the slip length being somehow the measurable consequence of the competition between viscous flow and liquid-solid friction. Fig. 1.2 recapitulates various boundary conditions (no-slip, finite slip and infinite slip).

A consequence of the slip boundary condition is that in many experiments, the usual Navier-Stokes equation can actually be applied with a no-slip boundary condition by shifting the wall by a distance $-b$. For instance, for the planar Couette geometry, with slip on the bottom surface only, the shear-rate is:

$$\dot{\gamma} = \frac{\mathrm{d}v}{\mathrm{d}z} = \frac{U}{h+b} \tag{1.6}$$

as if the thickness of the cell was shifted by a distance b.

Similarly, for a Hagen-Poiseuille flow in a slippery cylindrical pipe, the velocity profile $v(r)$ is given by:

$$v(r) = -\frac{(R+b)^2}{4\eta L} \Delta P (r^2 - (R+b)^2) \tag{1.7}$$

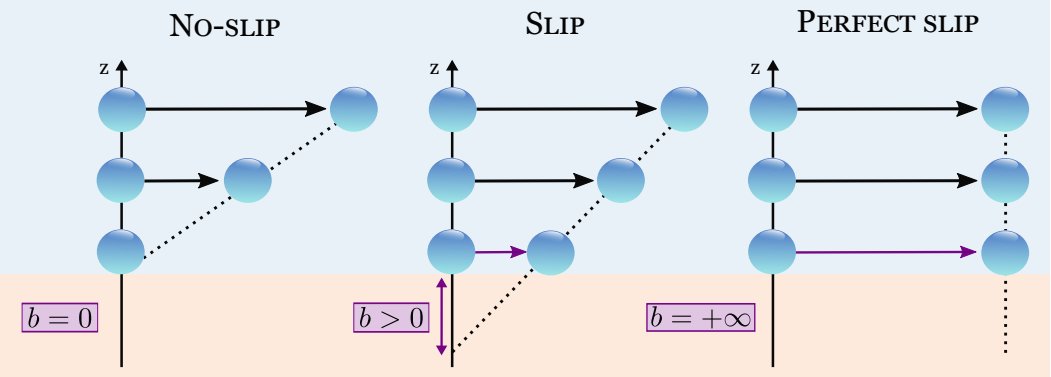

Figure 1.2: Left: no-slip boundary condition. Middle: finite slip boundary condition. Right: infinite slip boundary condition. Adapted from Lauga *et al.* [8].

with L the length of the pipe, R its radius and ΔP the pressure difference between the extremities of the pipe. This is formally equivalent to a no-slip Hagen-Poiseuille flow in a pipe of effective radius $R+b$. This is how – historically – the existence of slip was inferred (see [9, 10]), as mentioned in Section 1.1.5. A practical consequence is the increased pore permeability due to slip. The permeability of a pore K is defined as the ratio of the flow rate to the pressure drop (Darcy's law). The pore permeability in case of slip is given by:

$$K = K_{\text{no-slip}} \left(1 + 8\frac{b}{R}\right) \tag{1.8}$$

with $K_{\text{no-slip}}$ the permeability without slip, b the slip length on the edges of the pore and R the pore radius. Thus, if the slip length is of the same order of magnitude than the pore radius, the permeability is increased by a factor 10. This is very useful for example for desalination of water and osmotic energy conversion (now called *blue energy*) [11–13] for which the challenge is to create membranes that are both highly **selective** (permeable to water molecules only) but also highly **permeable** (inside which the flow of water is as high as possible). This is also useful to reduce the energy cost of enhanced oil recovery, for which you want a very low solid/liquid friction of oil and water inside porous media.

1.1.2 Fluctuation-dissipation theorem

All these quantities can also be defined for a liquid at equilibrium, using the fluctuation-dissipation theorem. Indeed, the Green-Kubo formula relates the correlations of the stress fluctuations to the local dissipation. In the bulk, this corresponds to the viscosity, which can thus be calculated through [14]:

$$\eta = \frac{V}{k_B T} \int_{-\infty}^{+\infty} \langle \sigma_{\text{bulk}}(0) \sigma_{\text{bulk}}(\tau) \rangle_{\text{eq}} d\tau \tag{1.9}$$

with V the volume of the liquid, and where $\langle . \rangle_{\text{eq}}$ denotes the average over all configurations.

Similarly, the correlations of the stress fluctuations at the wall are related to the friction coefficient λ through [14, 15]:

$$\lambda = \frac{S}{k_{\text{B}} T} \int_{-\infty}^{+\infty} \langle \sigma_{\text{wall}}(t) \sigma_{\text{wall}}(0) \rangle_{\text{eq}} dt \tag{1.10}$$

with S the surface of the wall. In practice, it is impossible to have access experimentally to the correlations of the L/S stress, and this expression is mainly used to measure an equilibrium value of λ in numerical simulations[a]. This will be discussed in Section 2.3.1.

1.1.3 The dependencies of slip and friction

Effect of the contact angle. Liquid-solid (L-S) friction strongly depends on the liquid-solid interaction energy ε_{LS}. A rough estimate using Kubo's formula (Eq. 1.10) yields:

$$\lambda = \frac{1}{k_{\text{B}}TS}\int_{-\infty}^{+\infty}\langle F_{\text{wall}}(t)F_{\text{wall}}(0)\rangle_{\text{eq}}dt \simeq \frac{1}{k_{\text{B}}TS}\langle F_{\text{wall}}^2\rangle\tau \tag{1.11}$$

with F the force exerted by the molecules of the liquid on the wall and τ the typical relaxation time of those. Now, the ensemble average of the force $\langle F_{\text{wall}}^2\rangle$ can be expressed as:

$$\langle F_{\text{wall}}^2\rangle = \langle\left(\sum_i f_i\right)^2\rangle \simeq N_{\text{inteface}}\langle f_1^2\rangle \simeq N_{\text{inteface}}\left(\frac{\varepsilon_{\text{LS}}}{a}\right)^2 \tag{1.12}$$

with $N_{\text{interface}} = aS\rho_{\text{f}}$ the number of molecules which interact with the wall, a their typical size and ρ_{f} the density of the fluid. We thus end up with:

$$\lambda \propto \varepsilon_{\text{LS}}^2 \tag{1.13}$$

This quantity can be related to the contact angle θ combining the Young-Dupré equation: $\gamma_{\text{LV}}\cos\theta = \gamma_{\text{SV}} - \gamma_{\text{LS}}$ and the Laplace equation: $\gamma_{\alpha\beta} = -\rho_\alpha\rho_\beta\epsilon_{\alpha\beta}$ with α and β being either the liquid L, the vapour V or the solid S. $\epsilon_{\alpha\beta}$ can be calculated using $\epsilon_{\alpha\beta} = \int_{-\infty}^{+\infty} rV_{\alpha\beta}(r)dr$ with $V_{\alpha\beta}(r)$ the interaction potential between α and β molecules/atoms separated by a distance r from each other. We end up with $\varepsilon_{\text{LS}} \propto 1+\cos\theta$ where γ is the surface tension and ρ the density. Using the Green-Kubo's relations, we can show that [5]:

$$\lambda \propto \varepsilon_{\text{LS}}^2 \propto (1+\cos\theta)^2 \tag{1.14}$$

Therefore, $\lambda \xrightarrow{\theta\to\pi} 0$, meaning that the slip length diverges when the contact angle approaches π. Indeed, this corresponds to the ideal situation where there is no interaction between the liquid and the wall, and thus no dissipation at the wall. $b(\theta)$ is plotted in Fig. 1.3, taken from Bocquet and Charlaix [6]. The left figure corresponds to Molecular Dynamics simulations. The dotted line corresponds to a regression using Eq. (1.14). Experimental measurements are shown in the right figure. We see that, in practice, it is very difficult to reach very high contact angles and thus the divergence of b at $\theta = \pi$ is less visible experimentally.

Effect of the structure of the wall. Liquid molecules flowing on a solid surface are very sensitive to the structure of the wall, and in particular its potential landscape. This will be discussed in depth in Chapter 3.

[a] To my knowledge, the only experimental attempt has been carried out by Joly *et al.* [16] in 2006: they measured the near-surface diffusion coefficient of water on silica surfaces using Fluorescence Correlation Microscopy.

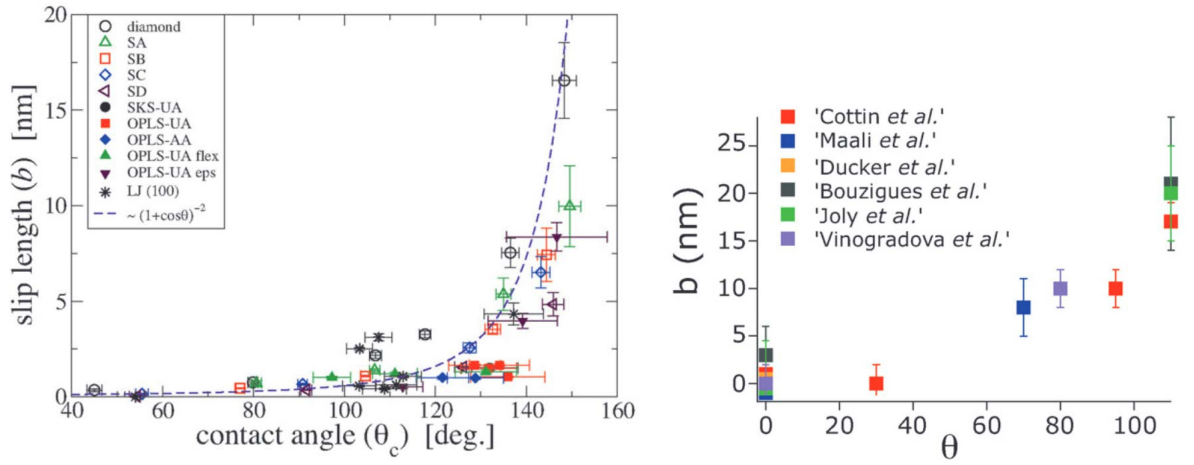

Figure 1.3: Slip length b as a function of the contact angle θ from numerical simulations (left) and experimental measurements (right). Taken from [6] (fig. 4).

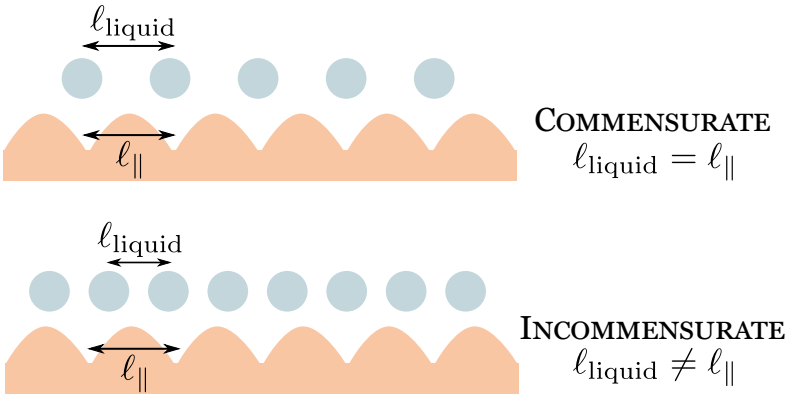

Figure 1.4: Schematic illustrating the concept of commensurability. The orange periodic profile is the wall potential. The blue disks are the liquid molecules.

For example, for a crystalline wall, if we write $q_{\parallel} = 2\pi/\ell_{\parallel}$ (see Fig.1.4) its main reciprocal lattice vector and $S_{\text{liq}}(q)$ the 2-dimensional structure factor of the liquid at the interface, we can show that [15,17–20]:

$$\lambda \propto S_{\text{liq}}(q_{\parallel}) \tag{1.15}$$

$S_{\text{liq}}(q_{\parallel})$ describes the **commensurability** between the solid structure and the liquid layer at the interface [21]. The complete derivation of Eq. 1.15 is given by Barrat and Bocquet in [17]. A liquid is commensurate with the wall if its structure matches with that of the wall, or, in other words, if both structures "see" each other A schematic illustration is shown in Fig. 1.4. For this simplistic case, if the average distance between the liquid molecules is different from the period of the crystalline wall, the liquid is not able to follow the wall profile, and thus the friction is reduced. This is reminiscent of solid-solid friction, which is nicely illustrated by Dienwiebel *et al.* in [22], where they measure friction between two graphite layers as a function of the rotational angle between the two. They observe that the friction force displays peaks at two specific angles, illustrating the commensurability of the substrates at these two specific values (see Fig. 1.5).

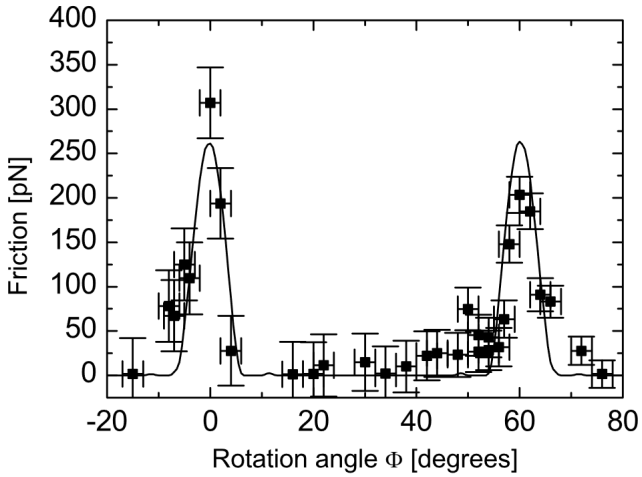

Figure 1.5: Friction between two solid graphite sheets. Taken from Dienwiebel *et al.* [22].

In addition, for flow inside curved nanochannels, the friction coefficient can also depend on the curvature of the tube, as described in [20, 23, 24]. This is the so-called "mango effect".

Furthermore, there have been some experimental evidences that the structure of the wall plays a key role in liquid-solid friction. McGraw *et al.* [25] measured the slip length of various polymer melts on alkylsilane Self-Assembled Monolyers (SAMs). In particular, they compared the slip length on pure octadecyltrichlorosilane (OTS), pure dodecyltrichlorosilane (DTS) and mixed OTS-DTS silanes SAMs. They observed that the maximum slip length is reached when the density of exposed alkyl chains is minimised, that is for the mixed OTS-DTS SAMs. Besides, the structure of the wall can cause a partial structuration of the liquid at its vicinity. For example, it has been evoked [26] that polystyrene is able to stack near SAMs thanks to $\pi - \pi$ interactions. This stacking

might be influenced by the structure of the underlying SAM. All this illustrates the fact that structure of the substrate has a key role in liquid-solid friction.

Quantum effects. It has been shown recently that there is a quantum coupling between electrons in the wall and the charge carriers inside the liquid. The friction coefficient can be decomposed as the sum of a classical friction λ_c and a quantum friction λ_q [27]. In general, $\lambda_q \ll \lambda_c$ so that the quantum term is hidden by the classical friction, but if one uses an extremely smooth wall, the quantum contribution becomes non-negligible. This is well described in [27]. In our case, we will focus only on the **classical friction**, and we will not describe any quantum effects herein.

Effects of the flow. There are several ways through which the friction and the slip length can depend on the flow properties. Firstly, if the fluid is viscoelastic, there is a transient regime at the beginning of the flow during which the slip length increases, and then reaches a constant value b_∞. This has been pointed out by Grzelka *et al.* [7], who have shown that the permanent regime is reached after a few reptation times. This is illustrated in Fig. 1.6 where their model is superimposed to all their slip measurements on two different surfaces and five different concentrations of PS/DEP solutions.

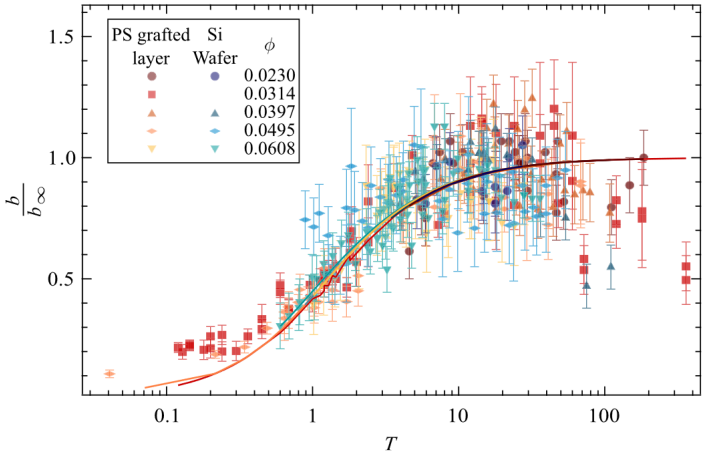

Figure 1.6: Normalised slippage as a function of the normalised shearing time T for PS/DEP 10.2 Mg/mol and of various volume fractions ϕ. Orange data correspond to slip on a polymer brush (5 kg/mol PS, grafting density $\Sigma = 0.12$) while blue data correspond to slip on a bare wafer. The measurements are conducted with Tracking of Photobleached Patterns technique, described in Chapter 7. The figure is taken from [7].

They have proposed a model to describe the time-dependent slip length $b(t)$ of viscoelastic polymer solutions:

$$b(T) = h\left(\frac{T(1+X)}{T - \frac{X}{1+X}e^{-T(1+X)} + \frac{X}{1+X}} - 1\right) \tag{1.16}$$

with $T = t/\tau_{\text{rept}}$ and $X = b_\infty/h$, h being the thickness of the liquid. This model appropriately describes their data, measured using the "Tracking of Photobleached Pattern" (TPP, see Chapter 7) technique on PS/DEP semi-dilute entangled solutions. In their

model, they assume a constant friction coefficient λ with respect to time and shear-rate.

However, λ can also depend on the shear-rate $\dot{\gamma}$. The first example of this is the case where some polymer chains are attached to the wall. The coupling between the flowing polymers and the attached chains results in the so-called **slip transition**: at low $\dot{\gamma}$, entanglements between bulk and adsorbed chains significantly reduce slippage, whereas above a threshold shear-rate $\dot{\gamma}_c$, they disentangle and thus the slippage increases (and the friction decreases) [28–31] (see Fig. 1.7). This is illustrated in Fig. 1.7, taken from Migler *et al.* [29], where the authors have measured the slip velocity v_s as a function of the applied shear-rate $\dot{\gamma}$ (left graph) and the slip length b as a function of the slip velocity (right graph). This is not the only way through which λ can depend on the shear-rate: Ilton *et al.* [32] have attributed the shear-rate dependency to the partial desorption of adsorbed chains, and in addition, using numerical simulations of a pure Lennard-Jones liquid [33], Thompson and Troian have observed a shear-rate dependent λ. This will be discussed in depth in Chapter 4.

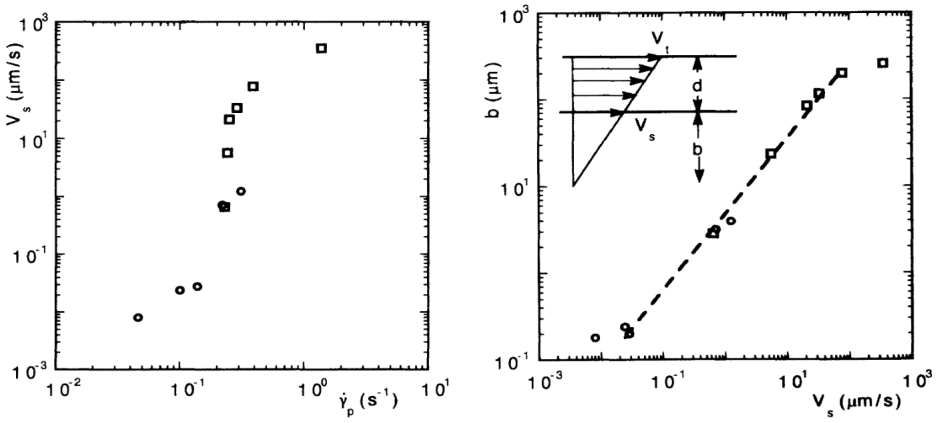

Figure 1.7: Slip transition of PDMS melt on OTS (left: slip velocity v_s as a function of the shear-rate $\dot{\gamma}$, right: slip length b as a function of v_s). Taken from [29].

1.1.4 Difference with solid-solid friction

We make a brief comment on the difference with solid-solid friction. When a rigid solid slides onto another rigid substrate, the friction force F – which is the force opposite to the direction of the solid and resisting its displacement – is related to the normal force N by the phenomenological Amontons-Coulomb's law:

$$F = \mu_d N \tag{1.17}$$

where μ_d is the dimensionless dynamic (or kinetic) friction coefficient. The proportionality between N and F stems from the fact that the real and the apparent contact areas ($\mathcal{A}_{real}$ and $\mathcal{A}_{app}$) are different since, microscopically, surfaces have asperities; as illustrated in Fig. 1.8. The friction force is proportional to the real contact area $\mathcal{A}_{real}$ which linearly increases with the normal force N because of plastic [34] or elastic [35] deformation of the asperities. Thus, we have $F \propto N$.

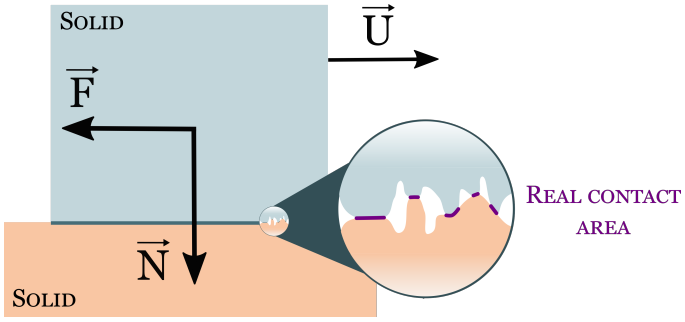

Figure 1.8: Cartoon of the solid-solid friction. $U = \|\overrightarrow{U}\|$ is the sliding velocity, $F = \|\overrightarrow{F}\|$ and $N = \|\overrightarrow{N}\|$ are the friction and normal forces, respectively.

The third Amontons' law states that μ_d is independent of U, the velocity of one of the solids with respect to the other (see Fig. 1.8). In reality, it has been observed that it actually has a logarithmic dependence on U (for small U):

$$\mu_d = \mu_{d0} - \beta_d \ln \frac{U}{U_0} \tag{1.18}$$

with β_d a constant, often around 10^{-2} [36].

The dependence of μ_d with U is attributed to the rejunevation of contacts [37]: the higher the sliding velocity, the smaller the contact time between two asperities. If the contact time increases, the friction increases. This can be attributed to either the creep of asperities in contact [38], or the water condensation between asperities, yielding to small capillary bridges [39, 40][b].

In contrast with solid-solid friction, for a liquid on a solid, the real contact area is the same as the measured contact area. In addition, the liquid at the interface is entrained by the bulk liquid, which creates a link between the boundary condition and the bulk flow. This is, of course, not the case for a rigid solid, which moves as a whole. For elastomers, as for liquids, the real contact area is the same as the apparent one, and at the molecular scale, monomers are fluid-like. Thus, the friction of elastomers on solid surfaces is very similar to liquid/solid friction [2, 41].

1.1.5 Experimental measurement of slip lengths and friction coefficients

There is a wide variety of techniques to measure slip, which have been reviewed in [8, 42]. If the system size is on the same order of magnitude as the slip length, slip affects usual macroscopic quantities, and thus, slip can be inferred from the measurement of those quantities. This is called **indirect measurements**. On the contrary, some techniques are able to directly visualise the slip boundary condition and give direct access to the slip length. This is called **direct measurement**. In this section, we list the various direct

[b] In [40], J. Crassous *et al.* measured the static solid-solid friction coefficient μ_s as a function of the logarithm of the contact time $\ln t_w$. They observed a linear trend, with a humidity-dependent slope. In particular, the slope is almost 0 at very low humidity, suggesting that capillary bridges are good candidates for the dependence of friction with contact time.

and indirect techniques used to probe the slip boundary condition.

- **Capillary technique:** the relation between the flow rate Q inside a thin capillary and the pressure difference ΔP is measured [43, 44]. The slip velocity and the slip length are deduced using the Stokes' equation. This is the technique used for one of the first experimental measurements of the slip length done by Churaev, Sobolev and Somov [10] in the 1980*s*. They measured a slip length around 10 nm ($\lambda \simeq 0.4 \pm 0.1\ 10^5$ kg.m^{-2}.s^{-1}) for water and 70 nm ($\lambda \simeq 0.3 \pm 0.2\ 10^5$ kg.m^{-2}.s^{-1}) for mercury, both in silanized glass capillaries.

- **Shear rheology:** thanks to the great sensitivity of rheometers, it is possible to extract slip lengths using a shear rheology measurement. The usual procedure is to look at the torque Γ as a function of the apparent shear rate $\dot{\gamma}_{\text{app}}$ [44, 45, 45, 46] for different liquid thicknesses. The slip length and the slip velocity can be deduced by comparing $\Gamma(\dot{\gamma}_{\text{app}})$ at two different thicknesses. This is discussed in depth in Chapter 7.

- **Surface Force Apparatus (SFA) and Atomic Force Microscope (AFM):** a sphere mounted on a cantilever oscillates inside the liquid. The force as a function of the distance between the tip and the surface is measured, from which the slip length is extracted. Cottin-Bizonne *et al.* [47] measured the slip length of water and dodecane on various smooth surfaces. They were able to measure slip lengths as small as 10 nm.

- **Particle Image Velocimetry (PIV):** the velocity profile is measured through the tracking of fluorescent particles in the fluid. The slip length is deduced by fitting the velocity profile. Joseph *et al.* [48] measured a slip length of water on superhydrophobic surfaces ("forests" of carbon nanotubes) around 1 µm. The disadvantage of this technique is that large particles can alter the flow, and small particles are subject to strong Brownian diffusion, which is not easy to account for. One has to choose the right interval to measure slip properly.

- **Evanescent waves microscopy:** there are two types of configuration. In both cases, fluorescent probes are inserted in the liquid and the near-surface dynamics is probed by exciting the fluorescence of the near-wall molecules only, using evanescent waves. The first configuration is called **Fluorescence Recovery After Photobleaching (FRAP)** and is the signature of L. Légers's group's work [49]. Fluorescent molecules are dissolved in the liquid and the near-surface fluorescence is bleached. The slip length is measured by looking at the dynamics of fluorescence recovery near the wall. The second configuration is called **Total Internal Reflection Fluorescence Microscopy (TIRF)**. Fluorescent particles are injected inside the liquid. The near-surface velocity profile is measured by observing the flow of the near-wall fluorescent particles, from which we can deduce the slip velocity and the slip length [50, 51]. The limitations of this technique are similar to the PIV.

- **Tracking of photobleached patterns (TPP):** this is the child of the FRAP technique. As in FRAP, a small amount of fluorescent polymers are dissolved inside the liquid polymer. The fluorescence is bleached along a line, which is then sheared by the flow. The slip length and the true shear-rate are measured by tracking the displacement of the bleached pattern throughout the shear.

- **Dynamics of dewetting and capillary levelling:** the kinetics of dewetting of thin polymer films heated above their glass transition temperature is observed. Thin film profiles are measured with a microscopy technique (either optical microscopy or with an Atomic Force Microscopy (AFM)). The velocity of the hole growth is related to the slip length. Baümchen *et al.* [32] measured slip lengths of dewetting polystyrene films around 0.1 µm on PTFE surfaces and $1-10$ µm on silanised surfaces. In the levelling technique, the slip length is measured by looking at the dynamics of flattening of an initially stepped polymer film.

- **Fluorescence correlation spectroscopy (FCS):** this is one of the rare experimental techniques able to measure the **zero-flow** near-wall dynamics of a liquid. It relies on the measurement of fluorescence intensity autocorrelation function of fluorescent beads inside the confined liquid. By studying the average residence time of the beads as a function of the confinement thickness, it is possible to calculate the **"zero shear-rate" slip length** of the liquid on the surface. Joly *et al.* [16] have developped this technique to measure the slip length of water on wetting and non-wetting surfaces. They report slip lengths around 18 nm for water on a nonwetting surface. This technique is also used to probe the diffusion coefficient of polymer chains near the wall [52, 53].

- **Capillary fluctuations:** thermal fluctuations of the free surface of a thin film deposited on a solid substrate are measured. The slip length is obtained by fitting the fluctuations of the surface of the film [54].

1.2 Temperature effects on dynamics of liquids

1.2.1 Temperature effects on viscosity

In order to derive a model of the temperature effect on viscosity, one has to make physical hypotheses on the microscopic dynamics of molecules inside the liquid. There are two main angles to tackle this issue. The first approach considers that the energy dissipation in the flow – the viscosity – is due to the fact that a molecule can move if and only if thermal fluctuations allow it to overcome the energy barrier created by the attraction of the surrounding molecules. This is the "activated process" view. The second approach is to consider instead that a molecule can jump for one spot to the next if and only if the next spot has "enough space". Then the key variable is the "free volume" accessible to the molecules. It is interesting to note that both derivations were carried out during the first half of the twentieth century, with Arrhenius, Andrade [55] and Eyring [56] for the activated process, and Batschinski [57], Macleod [58], Volger [59],

Fulcher [60], Tammann [61] and Doolittle [62] for the free volume approach. We will describe these two processes in the following.

1.2.1.1 Activated process

The activated process description is based on an analogy between liquid-liquid friction and kinetics of chemical reaction and is explained well in [63]. In this model, the liquid can be seen as an assembly of molecules interacting through an attractive interaction potential ϵ (Van der Waals, H-bonding...). We consider a cluster of molecules. In order to extract one molecule from its cluster, the molecule has to overcome a potential energy barrier ϵ (see Fig. 1.9) created by the attraction interactions of the surrounding molecules. Thermal fluctuations can provide enough energy to the molecule to be extracted from the cluster with a probability (or equivalently a rate)[c]:

$$\nu = \nu_0 \exp\left(-\beta\epsilon\right) \tag{1.19}$$

where $\beta \equiv 1/(k_\mathrm{B}T)$ and $\nu_0 = 1/(\beta h)$ the vibrational frequency of the molecule (h is the Planck's constant). If there is no macroscopic flow, there is an equal probability for the molecule to jump to the left and to the right. If there is a flow towards the right, then it provides a work w which facilitates the right jump and complicates the left jump. This work is given by the product of the stress σ, the average area occupied by the molecule α and the average distance between molecules ℓ: $w = \sigma\alpha\ell$. Thus, the rate of jumping becomes:

$$\nu = \nu_0 \exp\left(-\beta\epsilon\right)\left[\exp\left(\beta w/2\right) - \exp\left(-\beta w/2\right)\right] \tag{1.20}$$

If the stress is not too high compared to thermal agitation $w = \sigma\alpha\ell \ll k_\mathrm{B}T$, we can linearise this expression and it yields:

$$\nu = \frac{\sigma\alpha\ell}{h} \exp\left(-\beta\epsilon\right) \tag{1.21}$$

Now we have to link this to the macroscopic flow. The velocity gradient across two molecular layers distant by ℓ is $\Delta U/\ell = \nu$. The viscosity is the ratio of the stress and the velocity gradient: $\eta = \frac{\sigma}{\nu}$, and thus [56, 63]:

Arrhenian viscosity

$$\eta = \eta_0 \exp\left(\frac{\epsilon}{k_\mathrm{B}T}\right) \tag{1.22}$$

where $\eta_0 \equiv h/(\alpha\ell) = hN_\mathrm{a}/V_\mathrm{m}$ and V_m is the volume per mole of liquid.

ϵ can be seen as the energy required to create a hole inside the liquid, and thus it is linked to the enthalpy of vaporization L. For many liquids, we have $\epsilon \simeq 0.4L$ [63]. The 0.4 is attributed to the existence of free volume inside the liquid. Despite this rather simple view of molecular dynamics in liquid flows, Eq. (1.22) describes a huge number of

[c] This is very similar to the kinetics theory of chemical reaction: two reagents are mixed and if we bring enough energy to the system, they form an unstable activated complex which will then relax towards the desired product. The chemical reaction kinetics has been described first by Arrhenius in 1889 (leading to the well-known Arrhenius' law), and then by Eyring and Polanyi [64] in the 1930s.

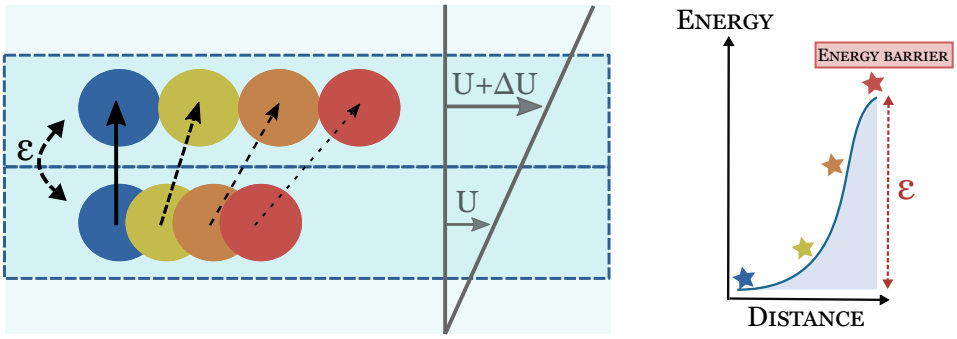

Figure 1.9: Schematic view of the energy activation barrier in liquid flows.

liquids incredibly well, especially polymer melts at high T. However, the accuracy of the physical description has been queried since, as discussed by Rizk *et al.* [65]. The second – slightly more complicated – description of the temperature effect on viscosity is based on the concept of free volume. It is described in the following section.

1.2.1.2 Free volume

When the liquid is cooled down, its density increases and steric effects start to hinder the movements of molecules. Adam and Gibbs [66] shown that, in this case, the easiest way for the molecules to move is to cooperatively rearrange, in a combination of N Arrhenian processes, where N is the number of particles which rearrange cooperatively (the **cooperativity**). A simple way to describe this crowding effect is to use the concept of free volume [62]: part of the volume is inaccessible because of these steric repulsions so that molecules have only access to a free volume V_f, which is the total volume V minus the excluded volume V_0. We often define f the fraction of the volume that is free as: $f = \frac{V-V_0}{V} \simeq \frac{V-V_0}{V_0}$. Moving a molecule inside this crowded environment requires that local voids are created in which the molecule has enough space to diffuse in (see Fig.1.10). This is the way the liquid flows: molecules move from void to void if thermal fluctuations allow the volume of the void to be large enough. Thus, the probability of having a molecule diffusing in a void is linked to the free volume, and is proportional to $\exp(-1/f) \simeq \exp(-V_0/V_\mathrm{f})$. From this, we can derive an expression for the viscosity [57, 58, 62]:

$$\eta = \eta_0 \exp(B/f) \tag{1.23}$$

where B and η_0 are constants, and $B \simeq 1$.

The VFT equation. From Eq. 1.23, we have to make an assumption to describe the temperature evolution of the free volume. Different models have been proposed (see Wang and Porter [67]), the easiest being to consider that f is related to the thermal expansion coefficient α_l of the material which evolves linearly with the temperature:

$$f = \alpha_l (T - T_\mathrm{V}) \tag{1.24}$$

where T_V is called the **Vogel temperature** and is the temperature at which the free volume becomes 0. We thus obtain:

$$\eta = \eta_0 \exp\left(\frac{B/\alpha_l}{T - T_\mathrm{V}}\right) \tag{1.25}$$

which is equivalent to the Vogel's equation: $\eta = \eta_0 \exp\left(D/(T - T_V)\right)$. This yields an apparent activation energy E^*:

$$E^*(T) \equiv R\frac{\mathrm{d}\ln\eta}{\mathrm{d}1/T} = \frac{RB/\alpha_l}{(1 - T_V/T)^2} \tag{1.26}$$

so that we can write η in an Arrhenian-like form: $\eta = \eta_0 \exp\frac{E^*(T)}{RT}$. We see that for $T \to \infty$, we reach a temperature-independent "activation energy" $E^*_\infty = RB/\alpha_l$. Yet, the physical ingredients behind this derivation are different from the ingredients used to derive the Arrhenius law of viscosity.

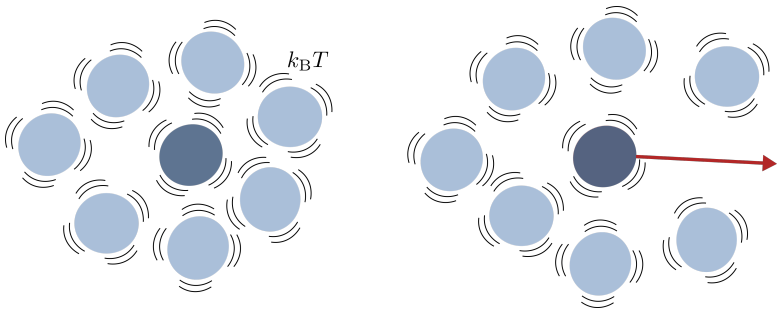

Figure 1.10: Schematic of the microscopic mechanism underlying the free volume derivation.

The temperature T_V is the temperature at which the free volume reaches 0. This temperature is related to the glass transition temperature and for many polymers $T_V = K'T_g$ with $K' = 0.77$ [67].

If we write $T = T_g + m$, with $B \simeq 1$, we have:

$$E^* = \frac{R}{\alpha_l}\frac{(T_g + m)^2}{(0.23T_g + m)^2} \tag{1.27}$$

The "high-temperature flow barrier" is taken as $E^*_c = E^*(T_g + 150)$ and writes:

$$E^*_c = \frac{R}{\alpha_l}\frac{(T_g + 150)^2}{(0.23T_g + 150)^2} \tag{1.28}$$

According to [67], $E^*_c \simeq 74$ kJ/mol for PS and $E^*_c \simeq 18$ kJ/mol for PDMS.

The WLF equation. From Eq. 1.23, we can recover the Williams-Landel-Ferry (WLF) equation [68], which relates the viscosity $\eta(T)$ to the viscosity η_{ref} taken at the reference temperature T_{ref}:

$$\ln\left(\frac{\eta}{\eta_{ref}}\right) = B\left[\frac{1}{f(T)} - \frac{1}{f(T_{ref})}\right] = \frac{B}{f_{ref}}\frac{T_{ref} - T}{T - T_V} \tag{1.29}$$

The WLF equation is:

$$\log_{10} a_T = \frac{C_1(T - T_r)}{C_2 + T - T_r} \tag{1.30}$$

with $a_T \equiv \eta/\eta_{\text{ref}}$, and C_1 and C_2 two constants. Eq. 1.30 is an empirical law valid between T_g and T_g +100 and compatible with the Doolitle's free volume description.

1.2.2 Temperature effects on friction

The effect of temperature on liquid-solid friction has not been studied extensively. We have gathered some of the results found in the literature in Fig. 1.11 from experiments with polymer melts (left) and from MD simulations (right). We plot only the slip length and not the friction coefficient since this is the parameter we can extract from the references, and we do not have access to the corresponding viscosities.

The results of the simulations are taken from [69] who describe a small Lennard-Jones polymer in a Poiseuille flow. To fit their results, they assume a two-layer model, leading to the following equation for the slip length:

$$b = \sqrt{\delta \frac{\eta_{\text{bulk}}}{\eta_{\text{surface}}} \left(\frac{\eta_{\text{bulk}}}{\eta_{\text{surface}}} - 1 \right) (\delta + 2b_s) + \left(\frac{\eta_{\text{bulk}}}{\eta_{\text{surface}}} b_s \right)^2} \tag{1.31}$$

with δ the typical size of the interfacial layer of viscosity η_{surface}, η_{bulk} the bulk viscosity and b_s the "microscopic slip length", which is the slip length at the interface between the solid surface and the boundary layer. If $\eta_{\text{surface}} < \eta_{\text{bulk}}$, then the "interfacial" layer is actually a lubrication layer, and the slip length b is larger than the microscopic slip length b_s. On the contrary, if $\eta_{\text{surface}} > \eta_{\text{bulk}}$, the interfacial layer is called "sticky", and the slip length b is smaller the b_s.

Temperature can act on η_{bulk}, η_{surface} and b_s. The authors argue that, at high temperatures, kinetic effects dominate so that $\eta_{\text{surface}} \simeq \eta_{\text{bulk}}$ and thus $b \simeq b_s$. At smaller temperatures, the behaviour of b upon cooling depends on the relative temperature dependencies between η_{bulk} and η_{surface}. They also assume that $\delta_s = \eta_s/\lambda$ diverges for $T \to T_g$ since the viscosity diverges. Therefore, they implicitly assume that λ does not depend on temperature.

As for the experimental results with polymer melts, the measurements give either increasing or decreasing slip lengths with temperature. For PS, Baümchen *et al.* [70] observe an increasing slip length upon cooling. With PMMA, Klos and Jacobs [71] have measured a non-monotonic slip length, whose shape is rather similar to the one of Servantie and Müller [69]. Hénot *et al.* [2] have measured a decreasing slip length upon cooling for PDMS melts. They have proposed to consider that friction is an activated process for the same reasons as the viscosity, described in Section 1.2.1. They have used the activated process description discussed above to model both the viscosity and the L-S friction coefficient:

$$\begin{cases} \eta &= \eta_0 \exp\left(\frac{E_{\text{a,viscous}}}{RT}\right) \\ \lambda &= \lambda_0 \exp\left(\frac{E_{\text{a,friction}}}{RT}\right) \end{cases} \tag{1.32}$$

which works well with their experimental data on PDMS melts. They conclude that the temperature dependency of the slip length depends on the relative values of $E_{\text{a,viscous}}$ and $E_{\text{a,friction}}$ and is given by a pseudo-Arrhenius law:

$$b = \frac{\eta_0}{\lambda_0} \exp\left(\frac{E_{\text{a,viscous}} - E_{\text{a,friction}}}{RT}\right) \tag{1.33}$$

The activation energy of friction $E_{\text{a,friction}}$ depends on the surface considered. They have found $E_{\text{a,friction}} = 21.3 \pm 4.0$ kJ/mol on OTS and $E_{\text{a,friction}} = 10.6 \pm 7.1$ kJ/mol on a grafted layer of PDMS. These values are to be compared with the activation energy of the viscosity $E_{\text{a,viscous}} = 16.3 \pm 2.8$ kJ/mol. Thus, the slip length decreases upon cooling for the OTS surface. On the grafted surface, we expect the reverse trend, but the slip length remains almost constant within the error bars.

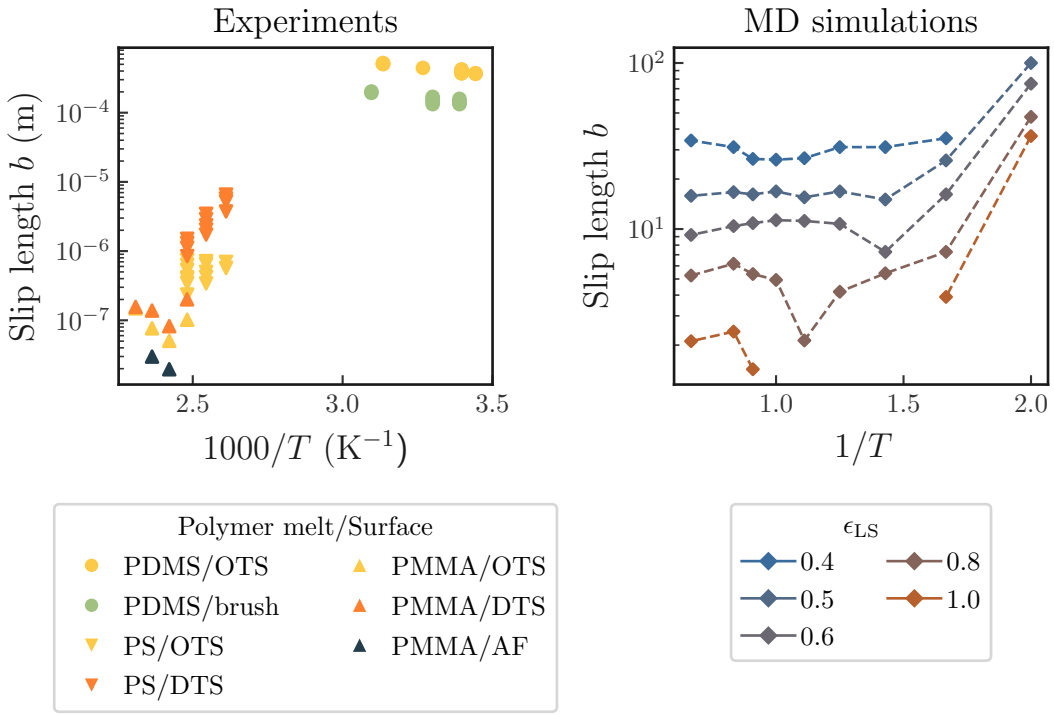

Figure 1.11: Effect of temperature on the slip length. Left: experimental data for polymer melts. PDMS data (M. Hénot PhD thesis [72]) are acquired using the Tracking of Photobleached Patterns technique, PS data (Bäumchen *et al.* [70]) and PMMA data (Klos and Jacobs [71]) are measured using dewetting experiments. Right: Molecular Dynamics simulations of a Lennard-Jones polymer at different liquid/solid interaction strengths ε_{LS}. Data are taken from Servantie and Müller [69].

As we saw, slip is likely to occur when the viscosity of the liquid is high. Therefore, liquid polymers (melts or solutions) are good candidates to display huge slip if they are flowing on a very smooth surface. In addition, because of their strong entropic nature, polymers at interfaces can adsorb onto or be depleted from the wall, leading to peculiar friction effects. Before describing slip of polymers, we briefly summarize the basis of polymer physics.

1.3 Physics of polymers

1.3.1 Generalities

A polymer is a macromolecule made of a succession of repeat units called **monomers**. The number of monomers per polymer molecule is the **polymerisation degree** and it will be called N in the present thesis. This number can vary between a hundred and thousands or even millions. Here, we will focus on **homopolymers** which are macromolecules made of only one type of monomers. In addition, we will consider **linear** polymers, which means that each monomer is connected to a maximum of two other monomers. Each polymer molecule will thus be called a **chain**.

A polymeric material contains numerous chains, which do not always have the same polymerisation degree. The distribution of polymerisation degrees is described through two average molar masses: the number average molar mass M_n and the mass average molar mass M_w . The first one is the average molar mass of the material weighted by the number of chains of each polymerisation degree, while the second one is weighted by the mass of chains of each polymerisation degree. They are defined as follows:

$$M_\mathrm{n} = \frac{\sum_{i=1}^{N} n_i N_i M_0}{\sum_{i=1}^{N} n_i} \; ; \; M_\mathrm{w} = \frac{\sum_{i=1}^{N} n_i N_i^2 M_0}{\sum_{i=1}^{N} n_i N_i} \tag{1.34}$$

where n_i is the number of macromolecules with N_i monomers and M_0 is the molar mass of one monomer. The ratio of these two average molar masses is the **dispersity index**:

$$Đ = \frac{M_\mathrm{w}}{M_\mathrm{n}} \tag{1.35}$$

The closer Đ is to 1.00, the more the material is monodisperse.

Describing the behaviour of such long statistical objects is a real theoretical challenge. Polymers have been discovered in the 1920s thanks to Hermann Staudinger, who won the Nobel Prize in 1953 "for his discoveries in the field of macromolecular chemistry" [73]. During the following decades, scientists tried to understand the physics of such long and fluctuating objects. We can mention the work of Flory in the 1950*s*, who won the Nobel Prize in 1974, and all the work related to the dynamics of polymer in the 1970s: de Gennes' view of the slithering motion of a chain in an entangled state, yielding to the **reptation** theory [74, 75], the tube model of Doi and Edwards [76] *etc.* Each monomer is a very small entity subject to thermal fluctuations and interacting with its neighbours. Therefore, describing the movement of millions of chains made of thousands of monomers is incredibly difficult, and that is when statistical physics come to our rescue: instead of describing the detailed dynamics of each component, we describe statistical average behaviours of the chains. In addition, because of their fractal nature, their physics is well caught by scaling laws [75, 77]. In the following section, we describe some of the main models: the ideal chain and the Flory chain, and we will discuss the physics of polymer solutions, since it is the centre of our experiments.

1.3.2 Polymer melts

1.3.2.1 The ideal chain

If we make the assumption that monomers of the chain do not interact with each other, the chain is called **ideal**. In particular, the orientation of one monomer is independent of the orientation of its neighbours, and thus the conformation of the chain can be described

by a 3D random walk. If we model each monomer by a rigid rode of length a, and we call R the end-to-end distance of the chain, the mean-square end-to-end distance is given by:

$$\langle R^2 \rangle \equiv R_{\text{ideal}} = aN^{1/2} \tag{1.36}$$

This description applies for both rigid polymers and flexible ones using a renormalization length b which is called the **Kuhn length** [77, 78] instead of the real monomer length a. This length takes into account the flexibility of the chain. We can then derive the same description using b instead of a.

1.3.2.2 Application to polymer melts

A polymer melt is a pure polymer in the liquid state (at a temperature higher than its glass transition temperature). It has been shown by Cotton *et al.* [79] that in this case, polymer chains are nearly ideal, because the interaction between monomers of the same chains are the same as the interaction between different chains. Thus, the mean coil size of the chains scales as $N^{1/2}$.

1.3.3 Polymer solutions

1.3.3.1 Quality of the solvent

When put in a solvent, the polymer can either completely mix to form a homogeneous solution, or it can remain in a separate phase, depending on the competition between enthalpy and entropy. Entropy tends to maximize the number of possible configurations, and therefore it goes in the direction of mixing. It is an increasing function of temperature. Enthalpy deals with the relative strength of the polymer-polymer, polymer-solvent and solvent-solvent interactions. In general, molecules "like themselves more than each other" [77] and thus enthalpy favours segregation[d]. Therefore, we can then distinguish three different cases:

- Entropy wins over enthalpy: the solution is stable. The solvent is called a **good solvent**. Toluene is a good solvent of polystyrene.

- Enthalpy wins over entropy: there is demixing into a solvent-rich phase and a polymer-rich phase. The solvent is called a **poor solvent**. Ethanol is a poor solvent of polystyrene.

- Enthaply is exactly compensated by entropy. This happens at a specific temperature called the θ-temperature. The solvent is called **θ-solvent**. In this specific case, the chain is ideal. Cyclohexane at $\theta = 34.5$ °C is a θ-solvent of polystyrene.

1.3.3.2 Concentration regimes

Once we have selected a good solvent for our polymer, another key parameter is the volume fraction ϕ of the solution. It is defined as the volume of polymer per unit volume of solution. If ϕ is small enough, polymer chains do not interact with each other. This is the

[d] In the case where molecules "like each other better than they like themselves", enthalpy favours mixing, and thus the solution is stable at any temperature and the solvent is called **athermal**. Ethylbenzene is an athermal solvent of polystyrene.

dilute regime. Upon increasing ϕ, we reach a critical concentration ϕ^* at which polymer chains start to overlap. This concentration is called the **overlap concentration**. For $\phi \geq \phi^*$, the solution is **semi-dilute**. At small length scales, the monomers are isolated in a good solvent, and we can apply Flory's theory as for the dilute regime. At larger length scales, we have an ideal chain of effective monomers of size ξ. The crossover length scale ξ is called the **blob size**. For even larger volume fractions ($\phi \geq \phi^{**}$), the blob size becomes so small that the thermal agitation within a blob becomes non-negligible. The solution is concentrated. When $\phi = 1$, we recover a polymer melt. In the next paragraphs, we will briefly introduce the main scaling laws describing these regimes in a good solvent. They are gathered in Table 1.1 and the coil size R and the correlation length ξ are plotted against the volume fraction ϕ in Fig. 1.13.

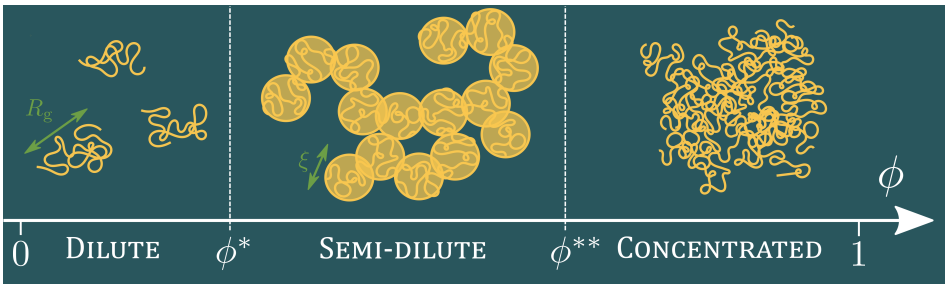

Figure 1.12: Cartoon of the three different concentration regimes.

Dilute polymer solutions. In a good solvent at small concentrations, polymer chains do not see each other. Thus, the typical size of the chain is the result of the competition between two antagonistic effects: the excluded volume interactions tends to stretch the chain[e] while the entropy decreases upon stretching (because it decreases its number of available configurations), and thus tends to minimise the end-to-end distance R of the chain.

Using a mean-field approach, Flory [78] has derived the free energy as the sum of an enthalpic $\frac{vN^2}{R^3}$ and an entropic $\frac{R^2}{Na^2}$ contribution:

$$F_{\text{Flory}} = k_{\text{B}}T \left[\frac{vN^2}{R^3} + \frac{R^2}{Na^2} \right] \tag{1.37}$$

with v a term homogeneous to a volume called the excluded volume. This equation can be minimised with respect to the coil size R to obtain the Flory radius:

$$R_{\text{Flory}} = v^{1/5} a^{2/5} N^{3/5} \tag{1.38}$$

which is the typical size of the coil in the dilute regime. The scaling law $R_{\text{Flory}} \simeq N^{\nu}$ has been verified experimentally in many systems and yielded $\nu \simeq 0.588$ which is remarkably close to the predicted 3/5.

[e] I would like to quote Tom McLeish during his lecture at the Soft Matter summer school in Cargèse in July 2022: "Self-hating chains, that's how you derive Flory's theory."

Semi-dilute polymer solutions. Upon increasing the concentration, polymer chains becomes closer and closer. When the distance between two polymer chains become of the order of R_{Flory}, they start to overlap. This happens at the overlap concentration ϕ^* defined by:

$$\phi^* \propto \frac{Na^3}{R_{\text{Flory}}^3} \propto N^{-4/5} \tag{1.39}$$

Above this concentration, there are two antagonistic effects:

- as in the dilute regime, because two adjacent monomers cannot overlap each other, the chain tends to swell (excluded volume interactions within the chain),

- but because of the excluded volume interactions coming from the surrounding chains, the chain is compressed.

Pierre-Gilles de Gennes has introduced a screening length ξ: the chain is divided into several **blobs** of size ξ, each blob containing g monomers. He assumes that ξ follows the scaling law $\xi = a\phi^n$. At the overlap concentration, the blob size is equal to the dilute coil size, and thus $\xi(\phi^*) = R_{\text{Flory}}$, which yields $n = -3/4$ and thus:

$$\xi = a\phi^{-3/4} \tag{1.40}$$

In Fig. 1.14, we plot the correlation length ξ of a solution of deuterated PS in DEP as a function of the volume fraction ϕ, from Small-Angle Neutron Scattering experiments [3]. We indeed observe an exponent close to $-3/4$.

We can now distinguish two length scales:

- Inside a blob (at length scales smaller than ξ), the interaction with other chains is negligible, and thus everything works as in the dilute case. Using Eq. 1.38, we have $\xi = ag^{3/5}$, and thus $g = \phi^{-5/4}$.

- Outside a blob (at length scales larger than ξ), the excluded volume interactions between monomers of the same chains are screened by the presence of other chains. We have an effective polymer chain made of $\frac{N}{g}$ blobs of size ξ as effective monomers, and this effective polymer chain behaves as an ideal chain, only constrained by its neighbouring chains. Using Eq. 1.36, we have $R = \xi \left(\frac{N}{g}\right)^{1/2}$ and thus:

$$R(\phi) = aN^{1/2}\phi^{-1/8} \tag{1.41}$$

Concentrated polymer solutions At very small length scales, thermal energy overcomes excluded volume interactions. At such small length scales, the chain is nearly ideal. We can define a **thermal blob size** ξ_{T} above which thermal agitation becomes negligible. It is independent of concentration. In the semi-dilute regime, $\xi_{\text{T}} \leq \xi$. Since in the semi-dilute regime, we have $\xi = a\phi^{-3/4}$, there is some concentration ϕ^{**} for which $\xi = \xi_{\text{T}}$ and thus the swollen regime disappears. This is the **concentrated regime**. In this regime,

Regime	Dilute	Semi-dilute	Concentrated
ϕ	$\phi < \phi^*$	$\phi^* < \phi < \phi^{**}$	$\phi > \phi^{**}$
ξ	$\xi = R$	$\xi = a\phi^{-3/4}$	$\xi = a\phi^{-1}$
R	$R = R_{\text{Flory}} = aN^{3/5}$	$R(\phi) = aN^{1/2}\phi^{-1/8}$	$R = R_{\text{ideal}} = aN^{1/2}$

Table 1.1: Scaling laws for the three different concentration regimes for entangled polymer solutions in a good solvent.

chains are ideal at all length scales (because excluded volume interactions are dominated by thermal agitation at small length scales and screened by overlapping chains at large length scales). Therefore, the chain radius is given by:

$$R = R_{\text{ideal}} = aN^{1/2} \tag{1.42}$$

The blob size decreases with the inverse of the volume fraction:

$$\xi = a\phi^{-1} \tag{1.43}$$

and it reaches the Kuhn length a for $\phi = 1$ (the melt state).

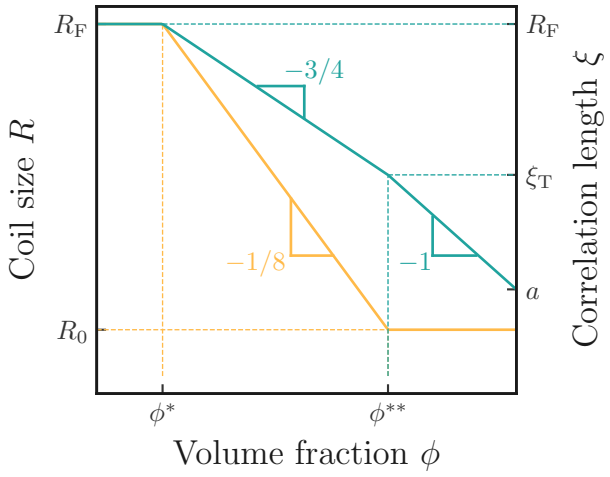

Figure 1.13: Coil size R (yellow, left-axis) and correlation length ξ (green, right-axis) as a function of the volume fraction in the three concentration regimes.

1.3.3.3 Dynamics of semi-dilute entangled polymer solutions

The dynamics of liquid polymer strongly depends on the system under consideration (melts, solutions, solvent quality, concentration, entanglements...). All these systems are well described in many books, where we can find all the corresponding scaling laws. Here, we give the main equations describing the dynamics of semi-dilute polymer solutions in a good solvent, since this is the system we have worked with. We only focus on **entangled** polymer solutions, which means that the chains are long enough to be entangled. The dynamics of unentangled polymer solutions is also well described (see [77] for example), but will not be discussed here.

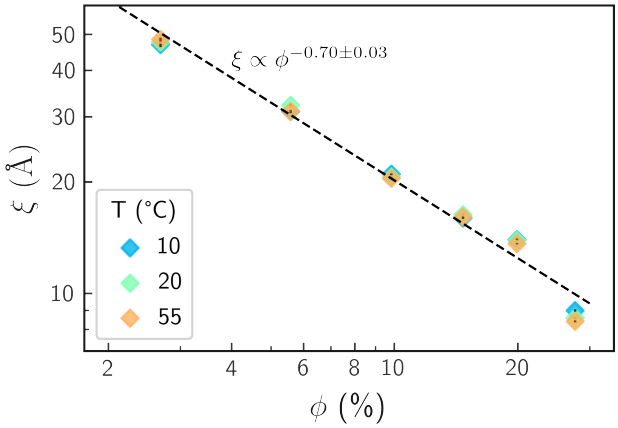

Figure 1.14: Blob size ξ as a function of the volume fraction ϕ for dPS/DEP at three different temperatures. The molar mass of dPS is $M_n = 1.33$ Mg/mol. Data taken from M. Grzelka PhD thesis [3].

At first glance, it is slightly frightening to try and describe the dynamics of semi-dilute entangled polymer solutions, since chains are long enough to be entangled and the solution is concentrated enough so that they overlap at scales larger than the blob size ξ. This implies that the movement of one chain is topologically constrained by the surrounding chains. A clever way to describe the dynamics of the chain is to use the reptation model, originally derived by de Gennes for polymer melts. The idea is that the displacement of the chain is constrained in a tube of section $S_{\text{tube}} = \xi^2$ and of length $L_{\text{tube}} = \xi N/g$.

The chain can diffuse out of the tube thanks to the thermal agitation of its extremities [74, 76]. We can define a typical relaxation time − called the **reptation time** τ_{rept} , as for polymer melts − which is the average time the chain needs to diffuse out of its tube. We can thus define a diffusion coefficient $D_{\text{tube}} = L_{\text{tube}}^2/\tau_{\text{rept}}$. The fluctuation-dissipation theorem tells us that $D_{\text{tube}} = k_B T/\zeta$, where ζ is a friction coefficient. Pierre-Gilles de Gennes has shown that the hydrodynamic friction stems from the drag of blobs inside the solvent, and the blobs are hydrodynamically decorrelated. Thus the friction coefficient can be written as follows: $\zeta = \xi\eta_{\text{solvent}}$. From these equations, we can derive the following expression for the reptation time:

$$\tau_{\text{rept}}\ (\phi) = \eta_{\text{solvent}} \frac{a^3 N^3}{k_B T} \phi^{3/2} \tag{1.44}$$

and the viscosity of the semi-dilute solution:

Viscosity of a semi-dilute entangled polymer solution in a good solvent

$$\eta(\phi) = \eta_{\text{solvent}} N^3 \phi^{15/4} \tag{1.45}$$

We see that the viscosity of the solution η strongly depends on the molar mass of the polymer and on the volume fraction of the solution. The molar mass dependency comes from the fact that the number of blobs increases with the chain length. Experimentally,

the measured exponent is around $3.3 - 3.4$. The volume fraction dependency is due to the effect of ϕ on the blob size. The experimental measurements of this exponent will be discussed in Chapter 7 for entangled semi-dilute polymer solutions.

1.3.4 Glass transition

When a liquid is cooled down, it generally crystallises at a given temperature T_c. However, if the cooling rate is too high compared to the typical time the material needs to crystallise, it stays liquid below T_c: we talk about **supercooled liquids**. When the liquid is cooled down further, the mobility of the molecules decreases until everything becomes frozen, at the glass transition temperature T_g, which depends on the cooling rate. Below this temperature, the material behaves as a solid, since it does not flow (at least during observable timescales), but its structure is amorphous: the material is in a **glassy state**. Polymers are a class of materials which easily have access to the supercooled and glassy states, because the size of the molecules prevents their crystallisation, or in other words, their relaxation time can be so large that we can cool them down more quickly than the time they need to crystallise. Some polymers, such as polyethylene (PE) are semi-crystalline: the solid is made of crystalline zones inside a global amorphous phase. On the contrary, other polymers, such as atactic[f] polystyrene (PS), never crystallise and are fully amorphous when they are below T_g .

Glass transition of polymer melts. The glass transition of polymer melts is independent of the molar mass of the polymer for high enough molar masses. This is shown in Fig. 1.15, see Novikov *et al.* [80], where they plot the glass transition of polymer melts as a function of the number of monomers per chain[g]. We see that, for many polymers, above roughly 10^3 atomic units, the glass transition becomes independent of the length of the chain.

Glass transition of a binary mixture. In a binary mixture, the dynamics of component A is affected by the presence of component B. In their paper from 2000, Lodge & McLeish [81] explain this observation for miscible polymer blends with an argument of **self concentration**: the local environment of monomer A will be on average richer in A compared to the bulk because of chain connectivity (see Fig. 1.16). We can thus define an effective concentration ϕ_{eff} such that:

$$\phi_{\text{eff}} = \phi_{\text{self}} + \phi(1 - \phi_{\text{self}}) \tag{1.46}$$

where ϕ is the bulk concentration and ϕ_{self} is the self concentration, depending *a priori* on the polymer only, but some groups have suggested that it also depends on the solvent [82]. Qualitatively, the more flexible the polymer, the smaller the self concentration effect.

[f] The **tacticity** of a linear polymer is the relative orientation of two consecutive side-groups, which is important for describing the polymer structure especially if some bonds of the chain are double or triple bonds, for which there is no free rotation of the side-groups around it. If they are on the same side of the chain, the polymer is called **isotactic**. On the contrary, if they alternate regularly, the polymer is called **syndiotactic**. If their relative position is completely random, the polymer is called **atactic**.

[g] For molecular liquids, M is the molecular mass of the molecule. Quite large values of M (up to 10^3 atomic units) can be obtained by without polymerisation, with large molecules made of a few phenyl cycles for example.

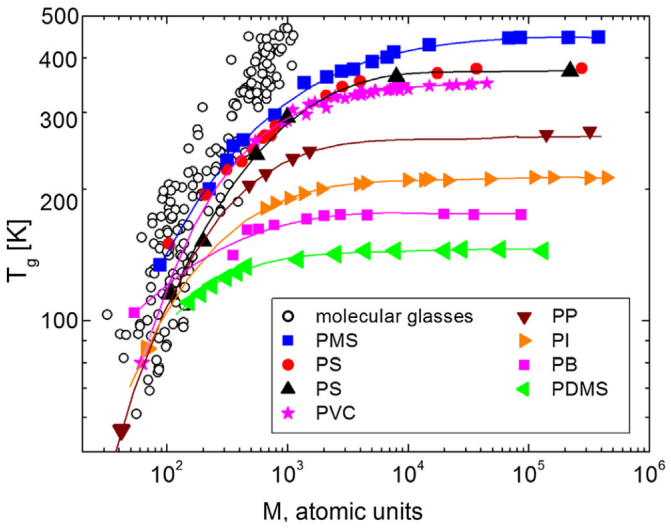

Figure 1.15: Glass transition temperature T_g as a function of the chain length of polymers (coloured filled points) and non-polymer (molecular) liquids (empty dark circles). Taken from Novikov *et al.* [80].

Thus, low-T_g polymers tend to have ϕ_{self} close to 0 while high-T_g polymers tend to have non-negligible values of ϕ_{self}. For PS, the authors have determined a value of ϕ_{self} of about 0.27.

From this equation, we can derive the effective glass transition $T_g^{eff,A}$ of compound A in a binary mixture of A and B using a Fox-Flory-like law:

$$\frac{1}{T_g^{eff,A}} = \frac{\phi_{eff}^A}{T_g^A} + \frac{1-\phi_{eff}^A}{T_g^B} \tag{1.47}$$

which relates the change of the glass transition temperature of compound A due to the presence of compound B. The only difference here is that the effect of compound B is less pronounced because locally, an A monomer sees a concentration ϕ_{eff} slightly higher than the averaged bulk concentration ϕ due to chain connectivity.

Lutz *et al.* [82] have plotted the T_g shift of the polymer between the dilute solution and the melt as a function of the T_g difference between the pure solvent and the polymer melt (see Fig. 1.17) for PS diluted in 10 different hosts. They show that the results can be understood by taking into account Eq. 1.46 with a self-concentration $\phi_{self} = 0.35$.

Now that we have introduced the notions of slip and liquid/solid friction and some fundamental results about polymer physics, polymer dynamics and glass transition of polymers, we turn to one of the main themes of this thesis: liquid polymers slip and friction. This is the subject of the following section.

1.3.5 Slip and friction of polymers

Near a solid surface, polymers can interact attractively or repulsively with the wall (see Fig. 1.18). In the case where the polymers interact repulsively, the concentration of polymers near the wall is lower than in the bulk so that there is a **depletion layer** at the surface. On the contrary, if the surface is attractive, there is a larger concentration of

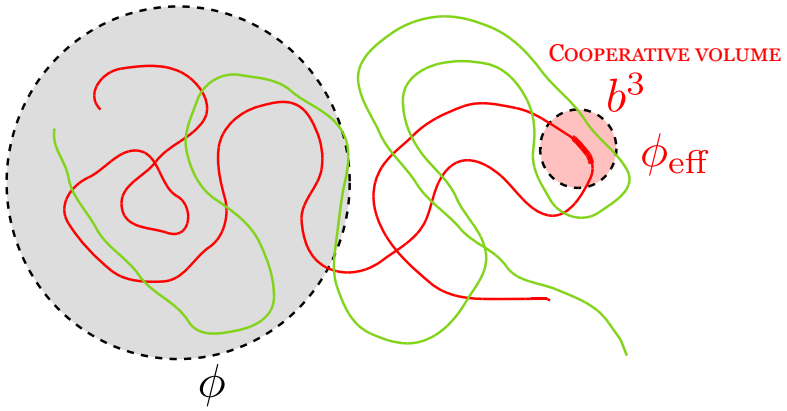

Figure 1.16: Schematic illustration of the effective volume fraction for a binary mixture of components A (red) and B (green). The volume fraction of the mixture ϕ is the volume of A over the total volume. In the vicinity of a monomer of component A, the effective volume fraction ϕ_{eff} is larger than ϕ because of chain connectivity.

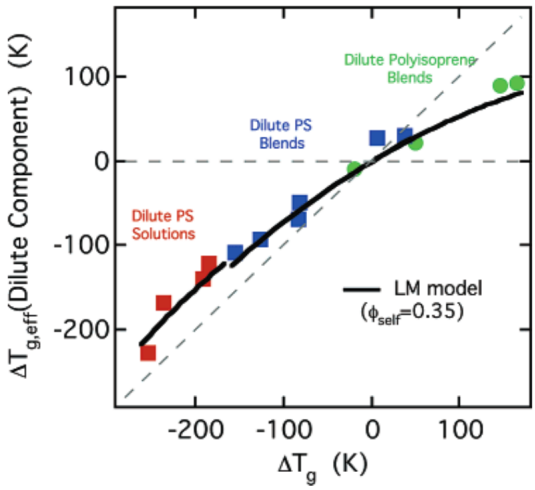

Figure 1.17: Shift of T_g between the polymer in dilute solution and the polymer melt as a function of the difference of T_g between the pure solvent and the polymer melt. Taken from Lutz *et al.*. [82]

polymers near the wall. In this case, we talk about an **adsorbed layer**. The third possible situation is when the extremities of the polymer chain are chemically attached to the surface: we say that the polymer is **grafted** to the surface. If the surface is grafted with many polymer chains, the chains are stretched, and we talk about a **polymer brush**. In the following, we describe these regimes and their link with slip and friction of polymer solutions on solid surfaces.

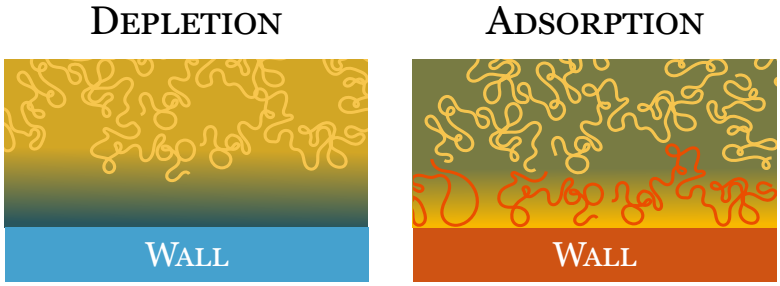

Figure 1.18: Depletion VS adsorption of a polymer solution near a solid wall.

1.3.5.1 Depletion

The first mentions of depletion of polymers near a solid wall date back to the 1980s [83]. At the time, oil companies were investing a lot of money for fundamental research on flow in microchannels in order to improve oil extraction. In this context, Chauveteau [84] observed that the viscosity deduced from flow measurements of xanthan solutions in fine pores was significantly smaller than the bulk viscosity. He attributed this to a depletion of xanthan chains near the surface of the pore, creating a layer of lower viscosity η_{wall} near the wall. By measuring the effective viscosity in the pore η_{pore} as a function of the pore radius r, he could extract the viscosity of the depleted layer η_{wall}. He found that $\eta_{\text{wall}}/\eta_{\text{bulk}} \simeq 0.4$. This depletion layer seemed to depend on neither the pore shape nor the chemical nature of the wall, and thus was attributed to a steric effect of the wall. This was further discussed in the 90s by Ausserré *et al.* [85] who directly measured depletion of polystyrene/toluene solutions near a silanised glass using Total Internal Reflection Fluorescence (TIRF) microscopy. They related this steric depletion to an entropic repulsion near the wall.

At the same time, theoretical polymer physicists were developing models to describe polymer configurations near surfaces. To properly describe the physics behind this, we need to distinguish charged and non-charged systems.

Non-charged systems. If the system is non-charged, a "repulsive" surface means that the polymer/wall interactions are weaker than the solvent/wall ones. Near the wall, there is a layer of liquid with a lower concentration than in the bulk. For a semi-dilute polymer solution, de Gennes has shown that the size δ of the depletion layer scales with the blob size of the solution [83]:

Size of the depletion layer of a semi-dilute neutral polymer solution

$$\delta(\phi) \propto \xi \propto a\phi^{-3/4} \tag{1.48}$$

This scaling law has been verified experimentally at the liquid/air interface by Lee *et al.* [86] for polystyrene in toluene using neutrons reflectivity. It has also been studied by Ausserré *et al.* [87] for aqueous solutions of xanthane near a silica surface using TIRF. This is discussed in Chapter 6.

Charged systems. If the system is charged, we have to distinguish two configurations. If the polymer and the wall share the same charge, there is a truly repulsive interaction between the two and thus a pure solvent layer is formed near the surface. In this case, the size of the layer is given by [51]:

$$\delta = \xi + 2\lambda_D \tag{1.49}$$

where λ_D is the Debye length of the solution. On the contrary, if the polymer and the wall have an opposite charge, there is first an electrostatic adsorption of the polyelectrolyte on the wall [88, 89]. This layer is very thin, and is given by:

$$\delta_{\text{adsorbed}} = a\left(\frac{2\lambda_D}{a^{1/3}\ell_B^{2/3}f^{4/3}}\right)^{1/3} \tag{1.50}$$

where ℓ_B is the Bjerrum length and f is the fraction of charged monomers in the polyelectrolyte. The accumulation of charged polymers will effectively charge the wall with the opposite sign, and thus create an electrostatic depletion on top, the size of which will be given by Eq. 1.49.

Consequence on slip and friction. The depleted layer has a lower viscosity than the bulk. In many experiments, we measure the velocity profile in the solution, and we linearly extrapolate it to obtain the slip length b. In reality, the velocity profile near the wall is affected by the variation of viscosity in the depletion layer, and it reaches almost zero at the wall (see Fig. 1.19) since usually the solvent has a negligible slip length ($b \gg b_{\text{solvent}}$). The measured slip length is thus an "effective" or "apparent" slip length that we call b_{app} here, and is given by:

$$b_{\text{app}} = \delta\left(\frac{\eta}{\eta_{\text{solvent}}} - 1\right) \tag{1.51}$$

This equation has often been used [19, 51, 89, 90] but – to our knowledge – no simultaneous measurement of both b_{app} and δ has been reported so far.

1.3.5.2 Adsorption

The reverse situation is when the polymer-wall interaction is stronger than the solvent-wall one. In this case, not only there is a larger concentration of polymers near the wall compared to the bulk, but also many polymer chains will be adsorbed on the surface.

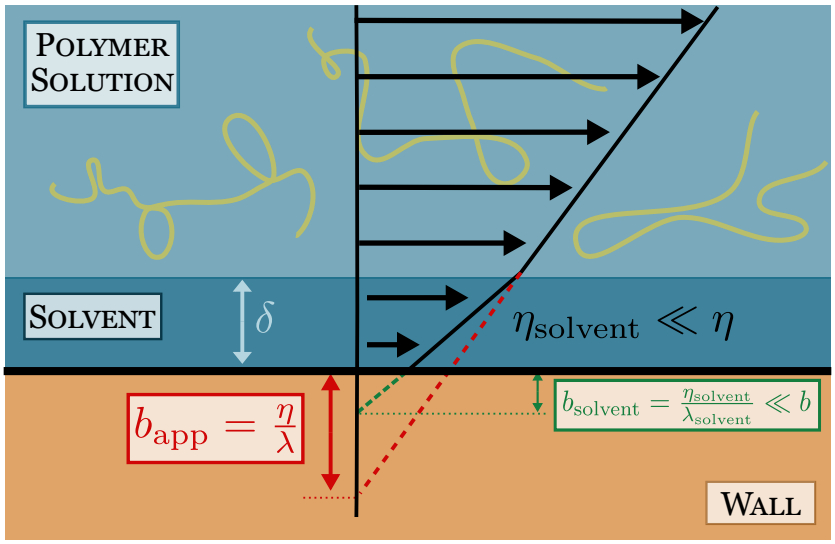

Figure 1.19: Slip on a depleted layer.

Adsorption of polymers on surfaces is quasi-irreversible. This situation is discussed in depth in Chapter 8. As the polymer solution (or melt) is in contact with the surface, more and more chains adsorb onto the wall, until it reaches a saturation density. The saturation adsorbed density of polymers ν – defined as the number of adsorbed chains per unit surface – is then given by [91]:

$$\nu = a^{-2} N^{-1/2} \phi_{\text{bulk}}^{7/8} \tag{1.52}$$

We can also define a dimensionless adsorbed density $\Sigma = \nu a^2$.

Consequences on slip and friction. The presence of adsorbed chains has a strong influence on the slippage of the solution. The first consequence that we can think of is that the interface is not a neat solid/solution interface so that the solution flows on a not-so-dense and rather flexible "carpet" of polymer chains. In particular, the adsorbed chains are entangled with the bulk chains, and this strongly reduces slip. Yet, if the flow is strong enough (above a critical shear rate $\dot{\gamma}_c$) bulk chains disentangle from the adsorbed layer and the slip abruptly increases. The transition between these two regimes is called the **slip transition** and has been observed in many polymeric systems [29, 30, 92–95]. It depends on the amount of adsorbed chains.

A second consequence of adsorption on slip is that the longer the contact between the solution and the wall, the higher and the denser the adsorbed layer. Thus, the slip length and the friction coefficient depend on the contact time between the solid and the solution. This was shown by M. Hénot in his PhD thesis [72]. Therefore, experimentally, one has to ensure that the kinetics of adsorption is much slower than the time of the experiment, or that the adsorbed layer has already reached its saturation state. In particular, heating the system speeds up the adsorption kinetics, so in order to study the effect of temperature on slip, it is safer to use a substrate that has been adsorbed with the polymer solution until saturation before conducting the experiment.

1.3.5.3 Locality of friction

Contrary to "molecular" liquids (water, alcanes...), polymers are very large objects whose behaviour is really dependent on the length scale we are looking at. Therefore, we might wonder what the relevant scale to describe liquid/solid friction is. In [96], de Gennes made the hypothesis that, for a polymer melt on a non-adsorbing surface, friction happens at the scale of the monomer. Therefore, the friction coefficient λ is the same for a fluid of monomers (of viscosity η_0) and for an entangled melt made of the same monomers (of viscosity η_N), with N monomers per chain. The slip length b_0 of the fluid of monomer is given by $b_0 = \eta_0/\lambda$ and, for the polymer melt of chain size N, the slip length is $b_N = \eta_N/\lambda$. This yields:

$$b_N = b_0 \frac{\eta_N}{\eta_0} \tag{1.53}$$

with $\eta_N \propto N^3$ for an entangled melt (and $\eta_N \propto N$ for an untangled one).

Hénot *et al.* in 2018 [2] have compared the friction coefficient of a PDMS melt and a PDMS elastomer, which is a material made of reticulated PDMS chains. For the melt, the friction coefficient λ is defined as $\lambda_{\text{melt}} = \eta/b$ where the slip length b is directly measured using the Tracking of Photobleached Patterns (TPP) technique. For the elastomer, they measure the stress σ exerted by a moving PDMS lens on the surface as a function of the velocity of the lens V. The friction coefficient $\lambda_{\text{elastomer}}$ is defined as $\sigma = \sigma_0 + \lambda_{\text{elastomer}} V$. They show that both the melt and the elastomer share the same friction coefficient, which experimentally corroborates de Gennes' theoretical prediction.

For semi-dilute entangled polymer solutions, Grzelka *et al.* [97] measured the friction coefficient λ of PS/DEP solutions as a function of ϕ (see Fig. 1.20). They observed that $\lambda \propto \phi^{1.6}$ (bare wafer) and $\phi^{1.9}$ (grafted PS layer). This is compatible with a friction at a semi-local scale, either with a monomer friction ($\lambda \propto \phi^{1.6}$) or a blob friction ($\lambda \propto \phi^{2.3}$).

1.4 Conclusion

This first chapter aims at introducing the main concepts that will be used throughout this thesis. In Section 1.1, we have given the definition of the liquid/solid friction, defining two important quantities: the **slip length** b, and the **friction coefficient** λ. Since we are interested in the temperature effects on the near-wall dynamics of the liquid, in Section 1.2, we have given the main laws describing temperature effects on the viscosity η, and the state-of-the-art about the temperature-dependence of the friction coefficient λ. Finally, in Section 1.3, we give some basic results about polymer physics, polymer dynamics and polymers at interfaces. This will be useful in Part II, where we focus on the friction of liquid polymers.

The rest of this thesis is divided into two distinct parts. In Part I, we present results about the effect of temperature on λ using molecular simulations of a bi-disperse Lennard-Jones (LJ) fluid (Chapter 3), and some ongoing simulations of the shear-rate dependence of λ for a monodisperse LJ fluid (Chapter 4). Then, in Part II, we focus on the slip and

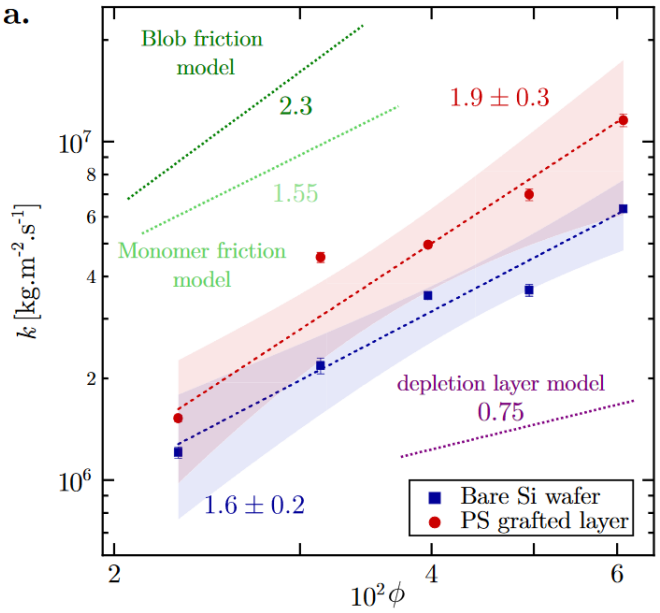

Figure 1.20: Friction coefficient (called k instead of λ here) as a function of the volume fraction of the PS/DEP solution ($M_n = 10\,\mathrm{Mg.mol^{-1}}$). Measurements have been done using TPP. Taken from Grzelka *et al.* [97].

friction of PS semi-dilute entangled solutions in a good solvent. First, we study the near-wall concentration profile using neutrons reflectivity (Chapter 6), and we show that there is both polymer depletion and adsorption at the surface. Then, we conduct some rheology experiments on our solutions (Chapter 7). We first discuss the effect of temperature on the bulk rheology. In a second section, we present some slip length measurements using the Tracking of Photobleached Patterns technique. Finally, we introduce a new method to measure friction using a rheometer. We use this to study the shear-rate and temperature dependences of λ. In the last Chapter (Chapter 8), we discuss the specificities of the adsorption kinetics of PDMS melts compared to other polymers. We combine these results to dielectric spectroscopy measurements of the relaxation times of the melts. Finally, we conclude this thesis by the General Conclusion.

Part I

Numerical Simulations

"God made the bulk, surfaces were invented by the devil" is a famous quote attributed to the Nobel laureate Wolfgang Pauli. Those who have done surface science probably all agree with this sentence. Surfaces are temperamental: as soon as we look at them closely, everything starts to matter: the way we have cleaned them, the air quality, the air humidity, any roughness, any impurity, any everything can significantly change what we are trying to measure. A question that many of us might have asked themselves is: "What if everything was perfectly controlled? This would require an experiment in which the experimentalist itself controls everything. The only way to do this is to use numerical simulations: the experiment is created and controlled by the scientist itself. If this is done correctly, it gives access to an easier and above all quicker way of measuring a surface phenomenon, getting rid of all the experimental artefacts. Of course, there is always the risk that the scientist ill-designs its numerical experiment, or designs an experiment that has absolutely no physical meaning, and thus, numerical results have to be compared with experimental results at the end of the day.

This is why we have devoted the first part of this thesis to numerical simulations. We will try to tackle the scientific questions explained in the introduction for the simplest system possible: a model liquid, interacting with one of the simplest interaction possible: the Lennard-Jones potential. In this system where we control everything, we would like to provide models to describe the effect of temperature on the slip length, which would be useful to understand the experimental measurements of Part II. Of course, getting rid of experimental artefacts is not for free: we are now exposed to numerical artefacts. In Chapter 2, we give the main ingredients used to run the simulations. In Chapter 3, we describe the slip and friction of a bi-disperse Lennard-Jones (Kob-Andersen) fluid on a crystalline FCC LJ wall. Chapter 4 – the third and last chapter of this first part – is ongoing work, which focuses on the friction coefficient λ of a pure Lennard-Jones fluid. In particular, we discuss the shear-rate dependency of λ and the non-validity of the Cox-Merz rule. We also try to probe the interfacial behaviour of the fluid near its melting temperature.

All the work presented in Part I have been done in close collaboration with Laurent Joly and Samy Merabia from the Institut Lumière Matière, in Lyon.

Chapter 2

Methods

Contents

In this first chapter, we describe the methods used throughout Part I. We start by describing how we prepare the simulated system (Section 2.1). Then, we describe the way we conduct our numerical measurements (Section 2.3). Finally, we briefly discuss our choice of the parameters (Section 2.4).

2.1 System

In this section, we describe the way we implement our system. We describe how we create the model liquid and the model walls.

2.1.1 Liquid

All the simulations have been conducted using LAMMPS [98]. The liquid is either a pure Lennard-Jones (LJ) liquid, or a bi-disperse Lennard-Jones liquid, which is also called a Kob-Andersen (KA) [99] liquid. Both liquids are made of atoms of size σ, which interact with a Lennard-Jones interaction potential:

$$\begin{cases} V^{\mathrm{LJ}}(r < r_{\mathrm{cut}}) = 4\epsilon[(\frac{\sigma}{r})^{12} - (\frac{\sigma}{r})^{6}] \\ V^{\mathrm{LJ}}(r \geq r_{\mathrm{cut}}) = 0 \end{cases} \tag{2.1}$$

where V^{LJ} is the interaction potential between two atoms, r is their relative distance, r_{cut} is the cut-off distance over which we consider that atoms do not interact anymore and ϵ is the typical interaction energy. This is called the $12-6$ Lennard-Jones potential. It stems from the following considerations:

- at long distances, there is an attractive interaction between induced dipoles created by spontaneous fluctuations of electronic clouds. We can explicitly calculate this interaction using quantum physics, and the dominating term[a] decreases as $1/r^6$.

- at short distances, we need to implement a repulsive potential modeling the steric (or electronic clouds) repulsion. A potential varying as $\exp(-r/r_0)$ would work, but it is easier to compute power laws $r^{-\alpha}$. It can be shown that α has to be between 9 and 15, and choosing 12 makes the calculations easier (since $x^{12} = (x^6)^2$).

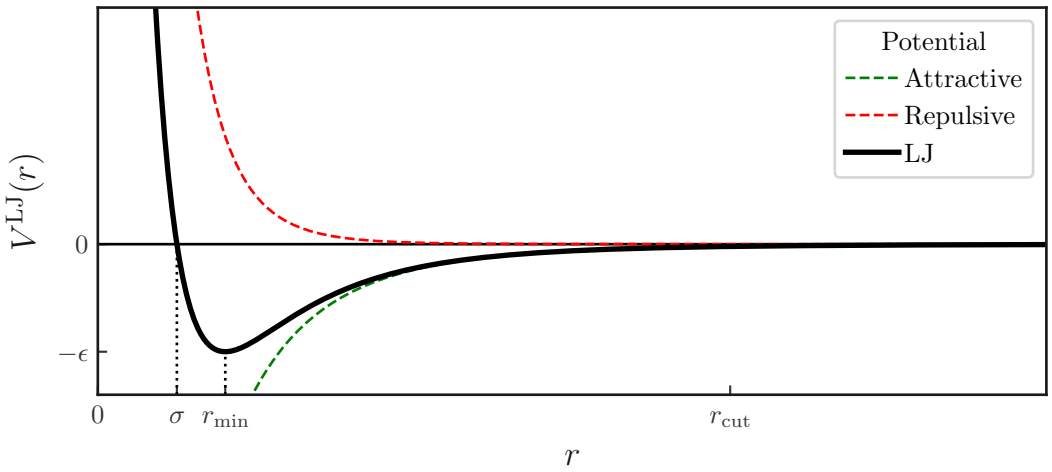

Figure 2.1: Lennard-Jones (LJ) potential as a function of the inter-particle distance r.

A schematic LJ profile is illustrated in Fig. 2.1. We need to choose a set of $(m, \sigma, \epsilon, r_{\mathrm{cut}})$ for all type of interactions. For all our simulations, we the same mass for all atoms, and the cut-off distance r_{cut} is always 2.5σ. We call 1 and 2 the two types of atoms in the KA simulations, and 3 will always refer to the wall particles. Parameters are given in Table 2.1 for the KA fluid.

We take m, σ_{11} and ϵ_{11} as references for all masses, lengths and energies. All other units can be built thanks to these three references, such as time $\tau_{\mathrm{ref}} = \sigma\sqrt{m/\epsilon}$ and temperature $T_{\mathrm{ref}} = \epsilon/k_{\mathrm{B}}$. We take $k_{\mathrm{B}} \equiv 1$ for simplicity. In the following, all quantities will be expressed in reduced units, which means that they are implicitly expressed *as a function of* the references units.

2.1.2 Wall

Unless otherwise stated, the liquid is confined between two alls. Each wall is a 8.0 unit cells $\times$ 8.0 unit cells assembly of atoms in a crystalline FCC lattice of density ρ. The density is related to interatomic distances in the crystal Therefore, playing with the density of the wall, we can tune its *corrugation*. Unless otherwise stated, we always use a density of 4.0, which implies that the mesh parameter a is equal to σ, and the contact distance d is given by $a/\sqrt{2}$. The liquid is sandwiched between two identical walls.

[a] Multipoles interactions (dipoles-quadrupoles, quadrupoles-quadrupoles etc.) are in general negligible.

ij	ϵ_{ij}	σ_{ij}
11	1.0	1.0
12	1.5	0.8
22	0.5	0.88
13	0.15 $\rightarrow$ 1.00	1.0
23	0.15 $\rightarrow$ 1.00	1.0
33	1.0	1.0

Table 2.1: Parameters used in the simulations. Lines in orange correspond to the second type of liquid atoms, used in the KA simulations only

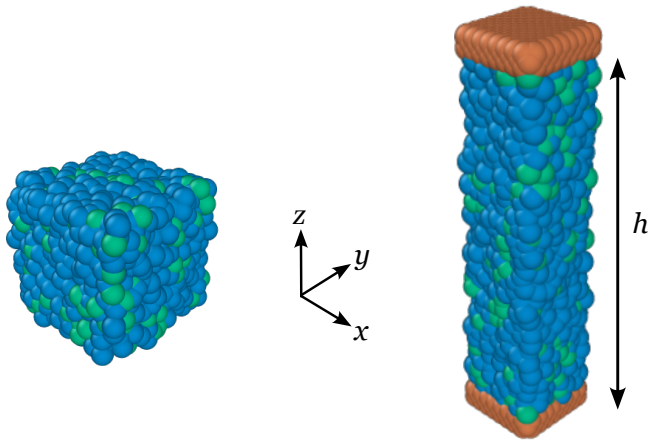

Figure 2.2: Kob-Andersen fluid. Left: system with no walls. Right: system with walls. The distance between the walls is h.

Atoms of the wall interact with the liquid through a Lennard-Jones potential, which parameters are given in Table 2.1. The key parameter is the typical liquid-solid energy ε_{LS}.

2.2 Preparation of the system

The generated systems are shown in Fig. 2.2 for the KA fluid. Now that we have generated our systems, we need to bring them to equilibrium. This is what is described in this section, first for the system with walls, then for the fully-periodic system, with no walls.

System with walls. The initial height h of the box along the z direction is at least 200.0 and is increased up to 450.0 for high temperatures. We impose periodic boundary conditions along x and y. Inside this box, the initial positions of atoms are randomly generated with a Gaussian distribution corresponding to an initial temperature $T_0 = 10$. In a first stage, the system is cooled down to the desired temperature T in the (N, V, T)

ensemble, using a Nose-Hoover thermostat with a damping time of 100 time steps. The damping time is the typical time over which the thermostat brings the temperature of the system back to the imposed temperature. A small damping time will generate huge temperature fluctuations, while a large damping time will require a very long equilibration. 100 time steps is a common choice for damping times. During this stage, the top wall is allowed to move along the z direction. For the systems with walls, in a second stage, the temperature is fixed, and the piston oscillates to reach the desired pressure P. The piston is then fixed at its equilibrium position and the thermostat removed so that the system is in the (N, V, E) ensemble. The evolution of T, P and the distance between the walls h are shown in Fig. 2.3 during the two steps of equilibration.

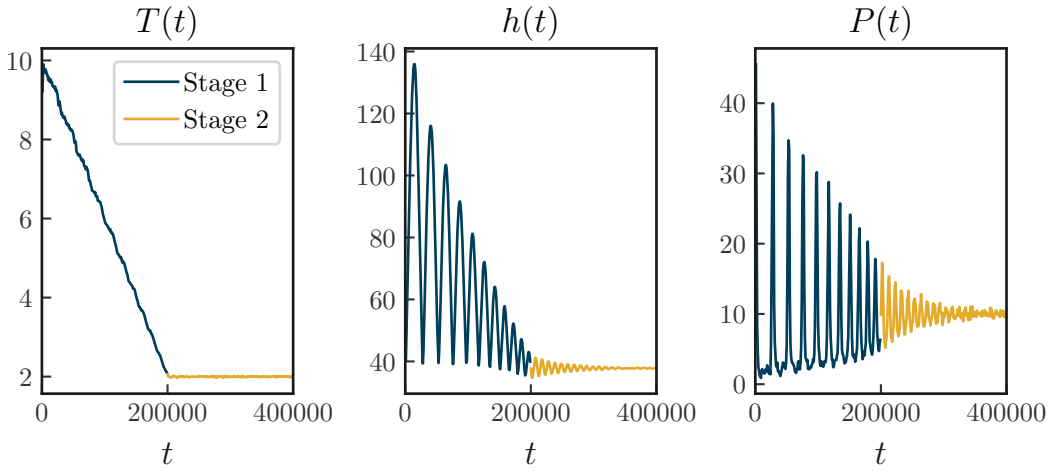

Figure 2.3: Equilibration of a KA liquid with $T = 2.0$ and $P = 10.0$.

System with no walls. For the system with no walls, we impose periodic boundary conditions along x, y and z. The box has a size $200 \times 200 \times 200$ in unit cells. As for the system with walls, the liquid is first equilibrated in the (N, V, T) ensemble using a Nose-Hoover thermostat with a damping time of 100 time steps. Then, the pressure is fixed by equilibrating the liquid in the (N, P, T) ensemble using a Nose-Hoover for both T (with a damping time of 100 time steps) and P (with a damping time of 1000 time steps). Finally, the system is maintained in the (N, V, E) ensemble.

2.3 Measurements

Once the system has been equilibrated, we need to extract the quantities we are interested in. We will distinguish two different cases: in Section 2.3.1, the system is maintained at equilibrium, and we look at the fluctuations of the stress both in bulk and at the interface. In Section 2.3.2, the liquid is sheared by the walls, and we measure the wall stress and the velocity profile inside the liquid. This configuration is called the "Out-of-equilibirum simulation".

2.3.1 Equilibrium simulations

The first method to measure the viscosity η and the friction coefficient λ is to look at the stress fluctuations of the liquid which is kept at equilibrium. From the bulk fluctuations, we can extract η, and from the fluctuations of the force near the wall, we can extract λ, both using the Green-Kubo formula described below.

2.3.1.1 Viscosity

To measure the viscosity, we simulate the liquid without the walls, in a fully periodic box. The preparation of the system is similar to the one described above. Once equilibrium is reached, we measure the viscosity using Eq. 2.2 [14] :

$$\eta = \frac{V}{k_B T}\frac{1}{5}\sum_i \lim_{t\to+\infty}\int_0^t \langle\sigma_i(0)\sigma_i(\tau)\rangle d\tau \tag{2.2}$$

where V is the volume, k_B is the Boltzmann constant (here taken equal to 1), T is the temperature of the system, and the $\sigma_i = \sigma_{xy}, \sigma_{xz}, \sigma_{yz}, (\sigma_{xx}-\sigma_{yy})/2, (\sigma_{yy}-\sigma_{zz})/2$ are the traceless components of the stress tensor inside the liquid. The correlations and their integral are plotted in Fig. 2.4 at various temperatures. At high temperatures, the correlations $C(\tau)$ have a single relaxation time, which corresponds to a single jump (see left graph). When the liquid is supercooled, we observe a second jump and thus a second relaxation time. The viscosity η is given by the limit of $I(t)$ when $t \to +\infty$ (plateau value in the right graph). As the temperature is decreased, the correlation time of the liquid increases and the plateau value is reached for a larger t, and thus it is necessary to do the simulation over a longer time to reach it.

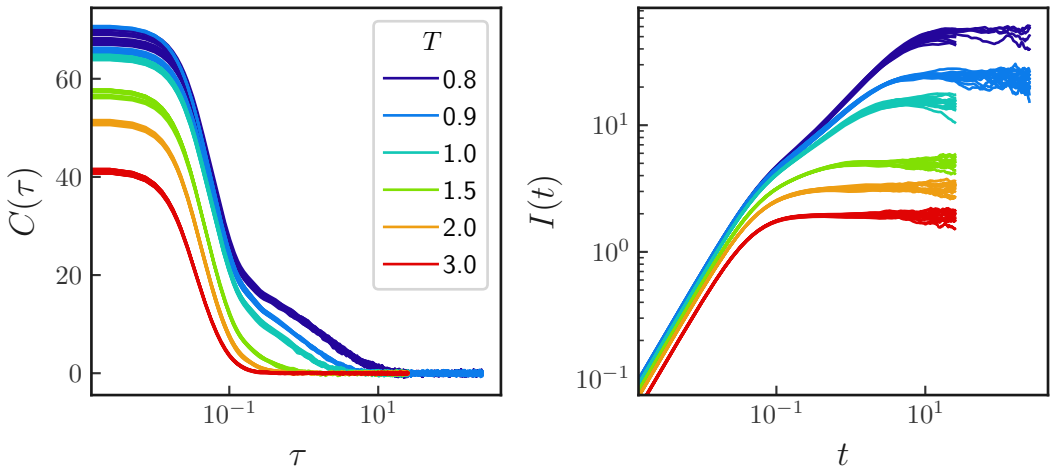

Figure 2.4: Left: correlations $C(\tau) = \frac{V}{k_B T}\langle\sigma_i(0)\sigma_i(\tau)\rangle$ with the σ_i described in the text, and for various temperatures of the liquid. Right: integral of the correlations $I(t) = \int_0^t C(\tau)d\tau$. The viscosity η is given by the plateau value of $I(t)$ for $t \to +\infty$. This has been done for a KA fluid.

2.3.1.2 Friction coefficient

The measurement of the friction coefficient is done in the system with walls, described above. The walls are immobile. λ is calculated using the Green-Kubo equations (Eq. 2.3):

$$\lambda = \frac{S}{k_B T} \frac{1}{2} \sum_j \lim_{t \to +\infty} \int_0^t \langle \sigma_j(0) \sigma_j(\tau) \rangle d\tau \tag{2.3}$$

where $S = L_x L_y$ is the surface of the wall, and the $\sigma_j = \sigma_{\text{LS, top}}, \sigma_{\text{LS, bottom}}$ are the liquid-solid friction forces per unit surface along the x direction at the two liquid-solid interfaces.

An example of such measurement is displayed in Fig. 2.5. As for the viscosity, $C(\tau)$ denotes the correlations $C(\tau) = \frac{S}{k_B T} \langle \sigma_j(0) \sigma_j(\tau) \rangle$, and $I(t)$ is the integral of these correlations: $I(t) = \int_0^t C(\tau) d\tau$. For each temperature T, we plot the correlations on both walls, and for systems generated with three different initial conditions. The plateau value is ill-defined, especially when the liquid is cooled down. This has been discussed by Español and Zúñiga [100], who explain that the plateau would be reached in the thermodynamic limit, but since the number of atoms in the simulations is limited, we never reach a real plateau in practice. In addition, as we reach the supercooled state ($T \leq 1.0$), a second characteristic time appears [99, 101], as predicted by the mode-coupling theory of supercooled liquids [102]. We observe that, for temperatures lower than 1.0, the correlation profile becomes non-physical and the measurement is not reproducible from one set of initial conditions to the other. For all these reasons, we will use the measurement at equilibrium for the friction only at high temperatures. In this regime, the value of λ is taken as the maximum of the "plateau". Therefore, it will always be a little bit overestimated.

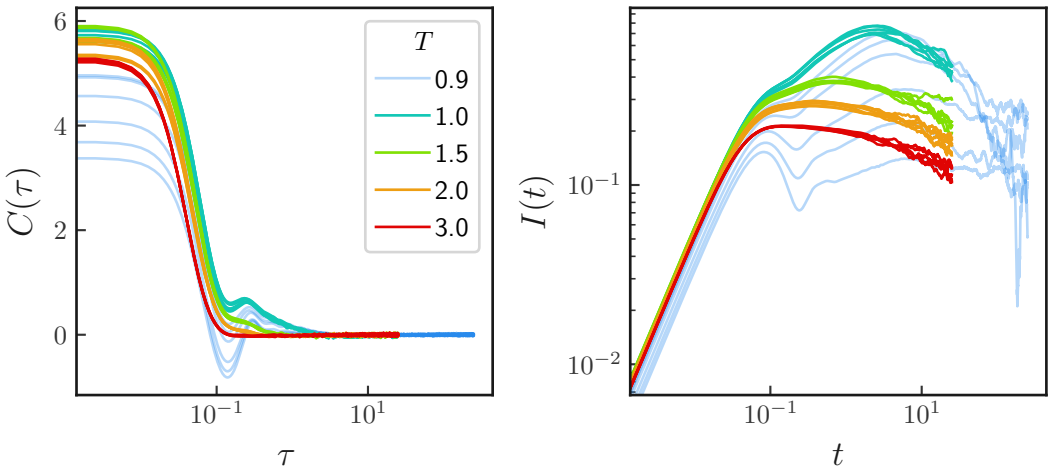

Figure 2.5: Left: correlations $C(\tau) = \frac{S}{k_B T} \langle \sigma_j(0) \sigma_j(\tau) \rangle$ for various temperatures. Right: integral of the correlations : $I(t) = \int_0^t C(\tau) d\tau$.

2.3.1.3 Complex viscosity and friction coefficient

We can also calculate the complex spectra $\eta^*(\omega)$ and $\lambda^*(\omega)$. We use the same calculations as in Yamaguchi *et al.* [103] for the viscosity, and thus the complex viscosity is calculated using:

Complex equilibrium viscosity $\eta^*(\omega)$

$$\eta^*(\omega) = \frac{V}{k_B T} \int_0^{+\infty} dt e^{-j\omega t} \langle \sigma(0)\sigma(t) \rangle \tag{2.4}$$

where $j^2 = -1$, V is the volume and σ is one of the traceless components of the stress tensor, as defined for Eq. 2.2.

Similarly, we calculate $\lambda^*(\omega)$ using:

Complex equilibrium friction coefficient $\lambda^*(\omega)$

$$\lambda^*(\omega) = \frac{S}{k_B T} \int_0^{+\infty} dt e^{-j\omega t} \langle \sigma(0)\sigma(t) \rangle \tag{2.5}$$

with $S = L_x L_y$ the surface of the wall and σ the shear stress on a wall, as defined by Eq. 2.3.

2.3.2 Out-of-equilibrium simulations

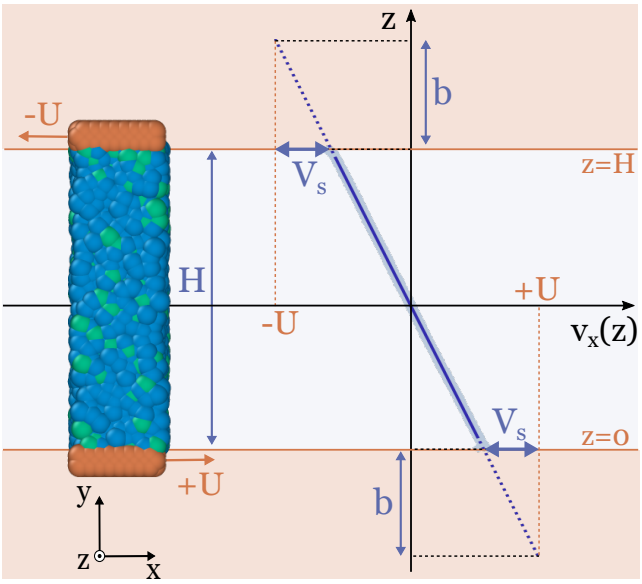

Figure 2.6: Schematic of the non-equilibrium simulation and the corresponding schematic velocity profile.

The liquid is sheared by applying of velocity $+U$ to the bottom wall and a velocity $-U$ to the top wall, both in the x direction (see Fig. 2.6). During shear, the temperature of the liquid is maintained at T by applying a thermostat in the transverse directions (y and z) only. We have access to both the density profile $\rho(z)$, the velocity profile $v(z)$ and the shear stress at the two liquid/solid interfaces $\sigma_{LS}(t)$. An example is shown in Fig. 2.7. The liquid has a homogeneous density ρ_{bulk} in bulk, and displays oscillations in the close vicinity of the wall. The hydrodynamic height h of the liquid can be identified with the Gibbs dividing plane (GDP) [104, 105]. The GDP is defined as the position of the wall so that a homogeneous density profile would have the same number of atoms than the real density profile. If we write z_0 some height inside the liquid and $n(z) = \rho(z) L_x L_y$,

the number of particles between the bottom wall and z_0 is given by: $N = \int_0^{z_0} n(z)\mathrm{d}z$. A homogeneous distribution of these N atoms would lead to $N = n^{\mathrm{bulk}}(z_0 - z_s)$ with z_s the GDP position. Thus, by equating these two equations, one can derive the GDP z_s:

$$z_s = z_0 - \frac{\int_0^{z_0} n(z)\mathrm{d}z}{n^{\mathrm{bulk}}} \tag{2.6}$$

This calculation is independent of z_0.

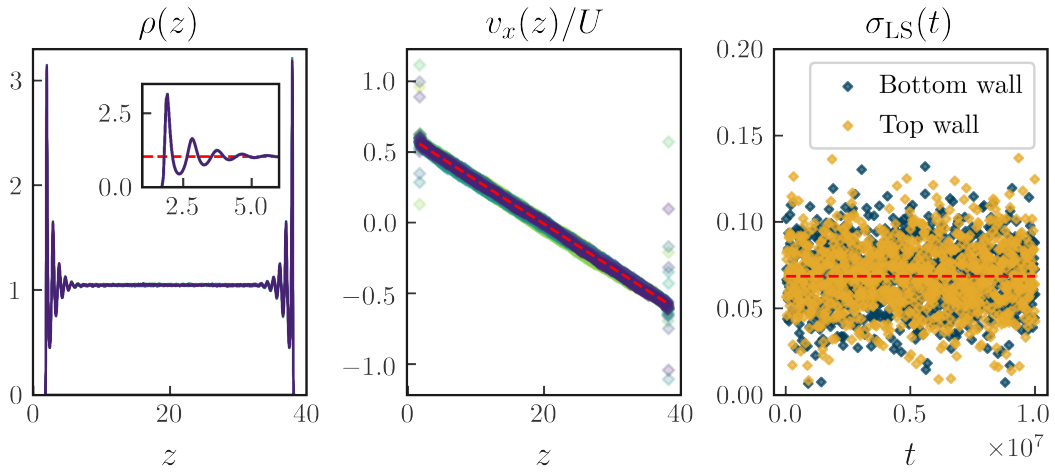

Figure 2.7: Left: density profile $\rho(z)$. Inset: zoom near the bottom wall. The red line denotes the density profile of the bulk liquid $\rho_{\mathrm{liq}} \approx 1.05$. Middle: velocity profile $v_x(z)/U$ at different times during shear. The red dotted line is a linear regression yielding $\dot{\gamma} \approx 0.022$. This corresponds to a KA liquid at $T = 2.0$, $P = 10.0$ and $\varepsilon_{\mathrm{LS}} = 0.25$. Right: stress exerted by the liquid on both walls σ_{LS} as a function of time. The red dotted line is the average over time of the shear stress $\overline{\sigma}_{\mathrm{LS}}$.

In Fig. 2.7, one can also observe that the velocity near the walls is different from the shear velocity U, which means that the liquid slips on the walls. The stress fluctuates around a mean value, which we call $\overline{\sigma}_{\mathrm{LS}}$. From the stress at the wall and the shear-rate, we can calculate the viscosity η using:

$$\eta = \overline{\sigma}_{\mathrm{LS}}/\dot{\gamma} \tag{2.7}$$

Then, we can calculate the slip velocity V_{s} with:

$$V_{\mathrm{s}} = U - \dot{\gamma}h/2 \tag{2.8}$$

Once we have obtained the slip velocity, we can easily calculate the friction coefficient λ using:

$$\lambda = \overline{\sigma}_{\mathrm{LS}}/V_{\mathrm{s}} \tag{2.9}$$

An example of the velocity profiles obtained from simulations with $\varepsilon_{\mathrm{LS}} = 0.25$, $T = 1.0$ and $U = 0.10$ but starting from various initial velocity distributions is shown in Fig. 2.8. In the left graph, we plot the velocity profile inside the liquid at different times (different

colours) during shear. As expected for a Couette flow, the velocity profile is linear. The true shear-rate $\dot{\gamma}$ is measured by linearising the velocity profile near the centre of the liquid. In the right graph, we plot $\dot{\gamma}$ at various times during the shear, and for various initial conditions (numbered 1 to 6). Initial conditions are changed by changing the seed generating the Gaussian distribution of the initial velocities. The value of the shear-rate is then averaged over all times and initial configurations, and the error bars are given by the standard deviation of these values. We do at least 3 initial conditions per measurement.

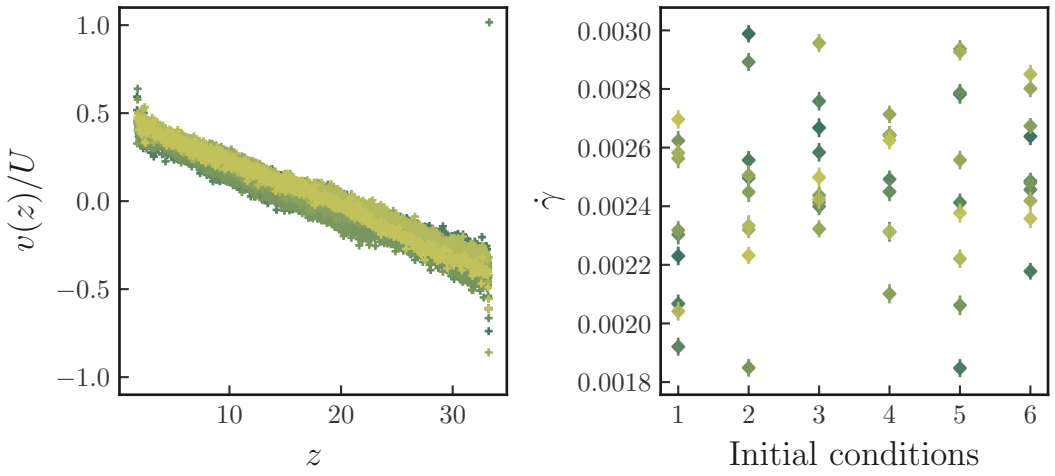

Figure 2.8: Left: velocity profile inside the liquid at different times. Right: true shear-rate $\dot{\gamma}$ for several initial conditions. The colours correspond to different times during the shear. These simulations have been done for $\varepsilon_{\text{LS}} = 0.25$ and $T = 1.0$.

The error bars on λ are given by the sum of the relative error bars on $\overline{\sigma}_{\text{LS}}$ and on $\dot{\gamma}$.

2.3.3 Structure factor

It can be useful to calculate the 2D structure factor of the liquid. This structure factor is calculated inside a given layer of liquid, perpendicularly to the wall, and as a function of the x and y components of the wavevector $\vec{q}$: q_x and q_y using [20]:

Calculation of the 2D structure factor $S(\vec{q})$

$$S(\vec{q}) = \frac{1}{N}\left[\left(\sum_{\text{i}=0}^{N}\cos(\vec{r}_{\text{i}}\cdot\vec{q})\right)^2 + \left(\sum_{\text{i}=0}^{N}\sin(\vec{r}_{\text{i}}\cdot\vec{q})\right)^2\right] \tag{2.10}$$

where $\vec{r}_i = x_i\vec{e}_x + y_i\vec{e}_y$ is the position of atom i and N is the total number of atoms considered in the calculation. These atoms are either part of a thin layer near the wall (the first layer of liquid near the wall, delimited by the first non-zero minimum in the density profile in the z direction), or from the bulk. The values of q at which we calculate the structure factor are multiples of $2\pi/L$ with L the size of the box along the x and y directions.

2.4 Choice of parameters

2.4.1 Kob-Andersen fluid

In this last section, we briefly discuss our choices of the parameters. The phase diagram of the KA liquid is shown in Fig. 2.9, taken from Pedersen *et al.* [106]. We work at $P = 10.0$ and $\chi_B = 0.20$, leading to a melting temperature T_m of about 1.01.

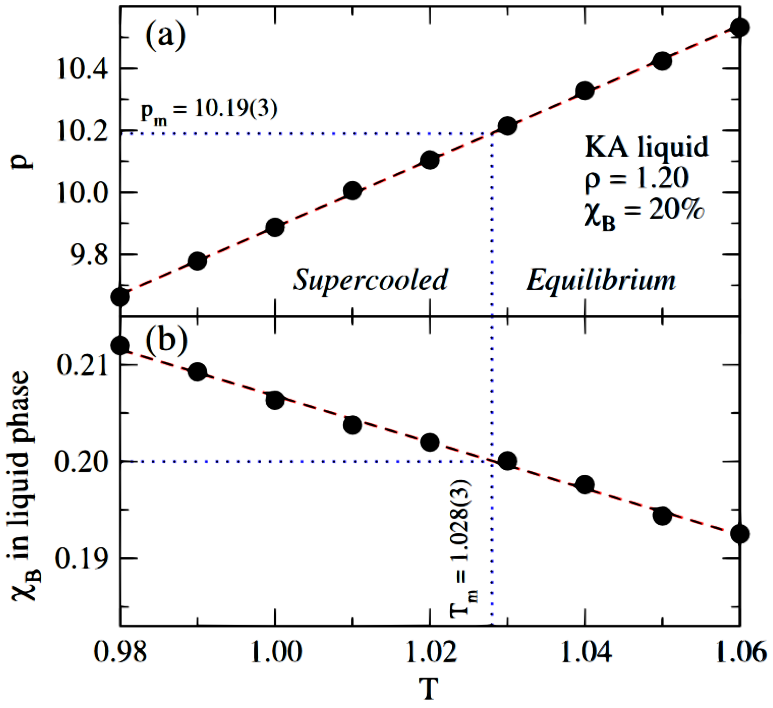

Figure 2.9: Phase diagram of the KA liquid for the pressure P (top) and the fraction of B particles inside the liquid χ_B (bottom). The blue dotted line indicates that at a liquid density $\rho = 1.20$, a fraction of B atoms $\chi_B = 0.20$ and a pressure $P = 10.19$, the melting temperature is $T_m = 1.028$. Taken from Pedersen *et al.* [106]. In the following, we use $P = 10.0$ and $\chi_B = 0.20$.

Effect of pressure The effect of pressure on η and λ is shown in Fig. 2.10. Both the viscosity and the friction coefficient are increasing functions of the pressure of the liquid. Interestingly, the ratio of the two results in an almost constant slip length b.

Effect of wall density In Fig. 2.11, we plot both the friction coefficient λ and the slip length b as a function of the interatomic distance a and the reduced wall density $\tilde{\rho}$, defined as:

$$\tilde{\rho} = \rho\sigma^3 \tag{2.11}$$

We see that the density of the wall has a strong effect on the friction. Indeed, it affects the apparent wall rugosity. The reduced density $\tilde{\rho} = \rho\sigma^3$ is related to the interatomic

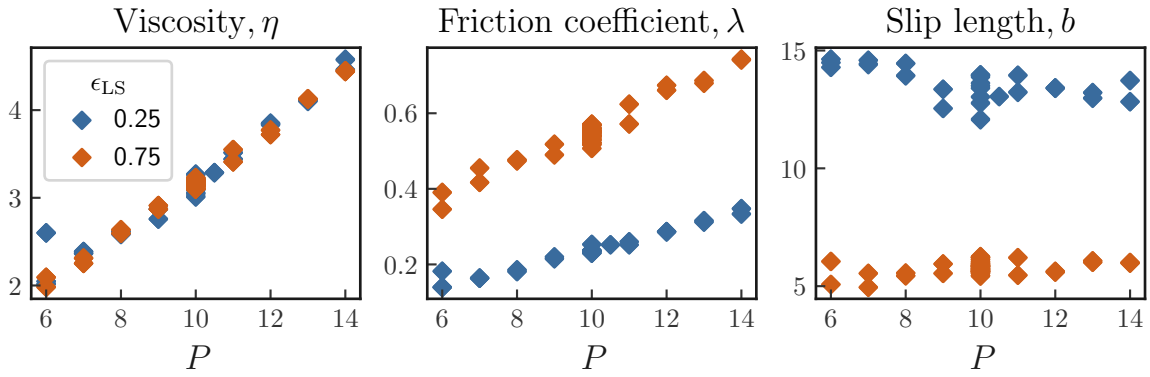

Figure 2.10: Effect of the pressure P on the viscosity (left), the friction coefficient (middle) and the slip length (right). These simulations have been done under shear, at $T = 2.0$ and $U = 0.40$. The simulations will be carried out at $P = 10$ in the rest of this chapter.

distance in the wall a by:

$$a = \left(\frac{4}{\tilde{\rho}}\right)^{1/3} \tag{2.12}$$

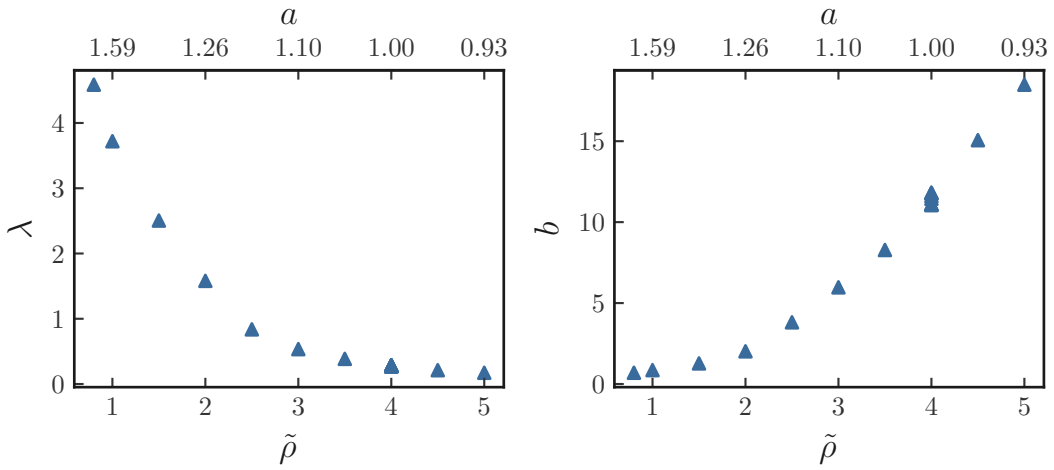

Figure 2.11: Effect of the wall density $\tilde{\rho}$ on the friction coefficient (left) and slip length (right). a is the interatomic distance, given by Eq. 2.12. These simulations have been done at equilibrium, at $T = 2.0$ and $\varepsilon_{LS} = 0.25$.

In our simulations, we have used a wall density $\tilde{\rho} = 4.0$, corresponding to $a = 1.00$.

2.4.2 Lennard-Jones liquid

For the monodisperse LJ fluid, we work at a pressure $P = 10.0$ and for temperatures between 1.0 and 3.0. The phase diagram of the LJ fluid is shown in Fig. 2.12, taken from Agrawal *et al.* [107]. We see that at $P = 10.0$, the fluid is in the supercritical state, and its melting temperature is around 1.4.

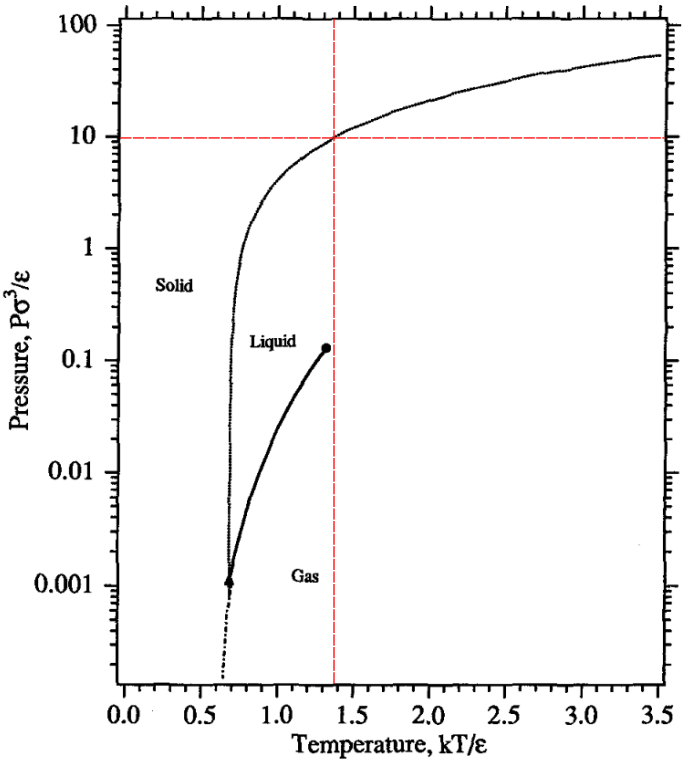

Figure 2.12: Lennard-Jones (LJ) phase diagram in the $P-T$ plane. Taken from [107] (Fig.5). The horizontal red dashed line indicates the pressure $P = 10.0$ we use in our simulations. This corresponds to a melting temperature near 1.4.

2.5 Conclusion

In this chapter, we have described the numerical methods used throughout this first part. In Chapter 3, we use the Kob-Andersen fluid to measure the effect of temperature on the slip length. In Chapter 4, the methods described here are used to probe the friction of a pure Lennard-Jones liquid near the crystallisation temperature.

Chapter 3

Kob-Andersen liquid: towards supercooled liquid/solid friction

Contents

The chapter aims at understanding the temperature dependency of the liquid/solid friction for a model liquid which is able to reach the supercooled state. We start by a brief recap of the Arrhenius law and the activated processes (Section 3.1). Then, in Section 3.2, we explore the high temperature regimes, for which the liquid is above its melting temperature. We use the activated process formalism to describe the temperature evolution of the friction. Finally, in Section 3.3, we focus on the friction of the supercooled liquid, and in particular, the effect of the structuration of the liquid near the surface.

3.1 Introduction and motivations

In this chapter, we try to unveil the dependencies of slip and friction with temperature. We want to explore a broad range of temperatures, either far from or close to the glass transition temperature T_g of the liquid. To this end, we have used a bi-disperse Lennard-Jones fluid – also called a Kob-Andersen (KA) fluid [99] – which is commonly used in the community of glass transition, since bi-dispersity prevents crystallisation and thus gives access to the supercooled state. We use the KA fluid described in [106] which is a mixture of two particle types $i = \mathrm{A}, \mathrm{B}$ in a $80-20$ ratio (see Fig. 3.1). Details about the parameters of the simulations are described in Chapter 2. The results of the present chapter have been published in [108].

As described in the introduction, different models have been proposed in order to rationalize the temperature dependence of the viscosity η, the friction coefficient λ, and the slip length b. A simple description is Eyring's theory, which assumes that flow is an activated process: in order to jump from one position to a neighbouring one, a given molecule has to overcome an energy barrier E_a. In this case, we can derive the temperature

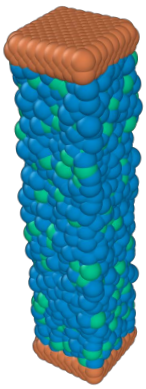

Figure 3.1: Schematic illustration of the cell. The walls are made of a crystalline FCC lattice. The liquid is composed of 80 % A particles (blue) and 20 % B particles (green).

dependency of the viscosity $\eta(T)$ (the derivation is well explained by Tabor in [63], chapter 12, pp.228-232):

$$\eta(T) = \eta_0 \exp\left(E_{a,\eta}/T\right) \tag{3.1}$$

where $E_{a,\eta}$ is the typical energy barrier of the flow, which characterizes somehow its "cohesion" and thus is related to the latent heat of vaporization of the liquid.

Although Eq. 3.1 is a good approximation for $\eta(T)$ for many liquids, the accuracy of this simple view has been challenged. In [65], Ritz *et al.* compare the Arrhenius dependency with a free volume model, and conclude that the microscopic mechanisms underlying movement of liquid particles are better described by the free volume model. This model relies on the hypothesis that each particle is confined inside a "cage" by the surroundings particles. In practice, because of thermal fluctuations, the free volume accessible to the particle is larger, and sometimes large enough that a "void" is created, allowing another particle to diffuse inside. This microscopic description yields another temperature dependency for the viscosity, which is well-described by the VFT law [59–61] (see Section 1.2).

Even if the barrier-hoping mechanism is not actually accurate, Eyring's theory is still useful to compare the general temperature dependence of η and λ in ordinary liquids. It can be applied both to the bulk flow, leading to an Arrhenian viscosity $\eta \propto \exp\{E_{a,\eta}/(k_B T)\}$ [109], and to the flow near the wall, leading to an Arrhenian friction coefficient $\lambda \propto \exp\{E_{a,\lambda}/(k_B T)\}$ [110, 111]. Therefore, the slip length also follows an Arrhenius law [109, 112–115], which can be expressed as:

$$b \propto \exp\left(\frac{E_{a,\eta} - E_{a,\lambda}}{k_B T}\right), \tag{3.2}$$

and one cannot know *a priori* its variation with temperature, since we do not know whether the energy difference $E_{a,\eta} - E_{a,\lambda}$ is positive or negative. Recently, Hénot *et al.* [2] have used this formalism to discuss the effect of temperature on the slip length of PDMS melts measured with a velocimetry technique. Equation 3.2 fits well their data, and depending on the surface, $E_{a,\lambda}$ was either larger than or equal to $E_{a,\eta}$, implying that the slip length was increasing or constant with temperature, respectively.

3.2 High-temperatures regime

We first look at the temperature evolution of both η and λ in the liquid regime, for $T \leq T_{\mathrm{m}} = 1.01$.

3.2.1 Comparison between Green-Kubo and shear simulations

We start by comparing the measurements of η and λ between the study of fluctuations at equilibrium (using Green-Kubo's formula) and the velocity profile inside the sheared liquid. The results are shown in Fig. 3.2 for $T > 1.0$, at various values of the liquid-solid interaction energy $\varepsilon_{\mathrm{LS}}$. We can observe that the viscosity is independent of $\varepsilon_{\mathrm{LS}}$, which is expected since it is a bulk property of the liquid. Both measurements yield the same values of η. For the friction coefficient λ, there is a rather good but not perfect agreement between the shear and the Green-Kubo (equilibrium) procedures. With the latter, λ is measured as the maximum of the integral of the fluctuations [116–118], since the plateau value is not always clearly defined (see Section 2.3.1 and [100]). This explains the fact that the Green-Kubo procedure slightly overestimates λ.

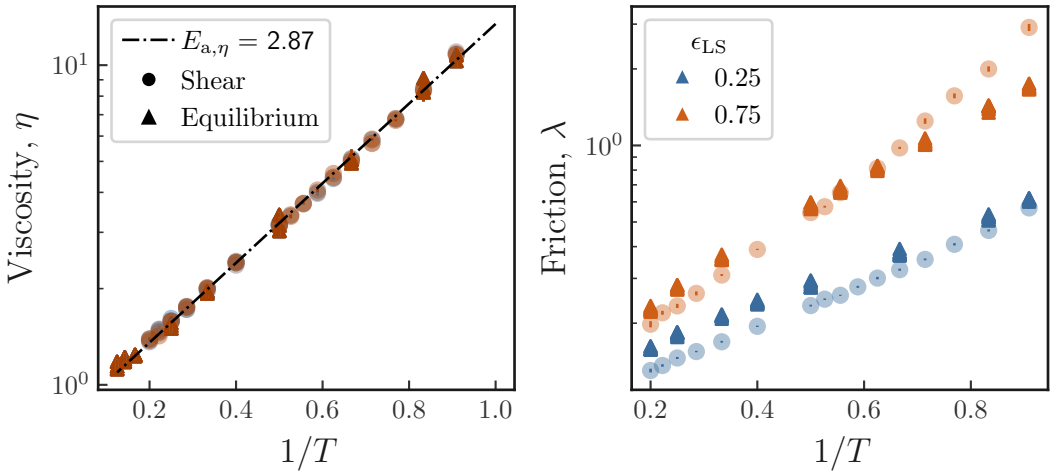

Figure 3.2: Comparison between the viscosity (left) and friction coefficient (right) as a function of temperature measured under shear (circles) and at equilibrium (triangles). The black dotted line corresponds to Arrhenian regression for the viscosity, yielding $E_{a,\eta} = 2.87 \pm 0.01$.

3.2.2 Effect of temperature

In Fig. 3.2, the data are plotted with a logarithmic vertical scale and as a function of $1/T$ to enhance the fact that we can model the temperature dependence of η and λ using an Arrhenius-like law:

$$x(T) = x_0 \exp\left(E_{a,x}/T\right) \tag{3.3}$$

where x stands for either η or λ and $E_{a,x}$ is a typical activation energy.

The fit gives $E_{a,\eta} \approx 2.87 \pm 0.01$ for the viscosity. For the friction coefficient λ, the fit is done using the values from the shear measurements only. We find $E_{a,\lambda} = 2.01 \pm 0.02$ for

$\varepsilon_{LS} = 0.25$ and $E_{a,\lambda} = 3.67 \pm 0.08$ for $\varepsilon_{LS} = 0.75$. We already see that, depending on the value of ε_{LS}, the activation energy of λ can be smaller or larger than $E_{a,\eta}$. The slip length is given by the ratio η/λ, and thus it can be fitted by an Arrhenius law $b(T) \propto \exp(E_{a,b}/T)$, with a formal activation energy of slip $E_{a,b} = E_{a,\eta} - E_{a,\lambda}$, which can be either positive or negative. Therefore, the value of ε_{LS} controls the temperature-dependency of the slip length. In Fig. 3.3, we plot $b(T)$ (left) and $E_{a,b}(\varepsilon_{LS})$ (right). For high values of ε_{LS}, $E_{a,\lambda}$ becomes larger than $E_{a,\eta}$. Thus, far from the glass transition temperature, the variation of $b(T)$ is governed by the parameter ε_{LS}, which controls the wettability of the system. This is consistent with previous work on LJ liquids [115].

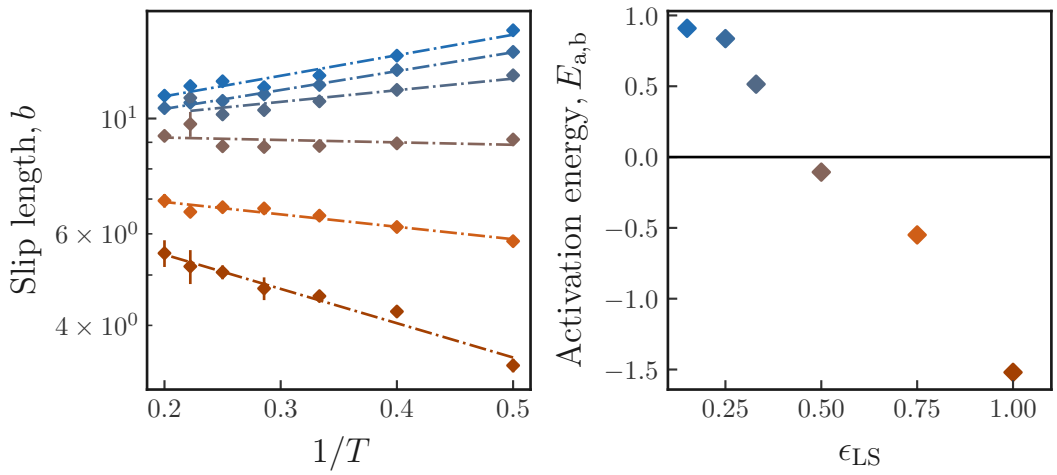

Figure 3.3: Effect of temperature on the slip length in the "high temperatures" regime. Left: slip length b as a function of temperature. Dashed-dotted lines correspond to Arrhenian regressions. Right: activation energy extracted from an Arrhenian fit of $b(T)$ as a function of the liquid-solid interaction potential ε_{LS}. The colours are the same in both graphs, so the colour scale is given by the x-axis of the right graph.

3.2.3 Effect of ε_{LS}

As discussed in the introduction of this chapter, λ is expected to be proportional to ε_{LS}^2. This is indeed what we observe in Fig. 3.4. We find a temperature-independent limit at low ε_{LS} of 0.17 ± 0.01.

3.3 Slip and friction in the supercooled regime

We now explore lower temperatures. At these temperatures, the measurement of the friction coefficient λ using the Green-Kubo formula becomes delicate because of the so-called plateau problem [100]. Therefore, in this regime, λ is measured with shear simulations only.

The viscosity is independent of the value of ε_{LS}, as observed in Fig. 3.5 where the points correspond to measurements at different ε_{LS}. At high temperatures, $\eta(T)$ is well described by an Arrhenius law (red dashed curve) with an activation energy of 2.87, as mentioned above. At lower temperatures, $\eta(T)$ can be fitted with a VFT model (blue

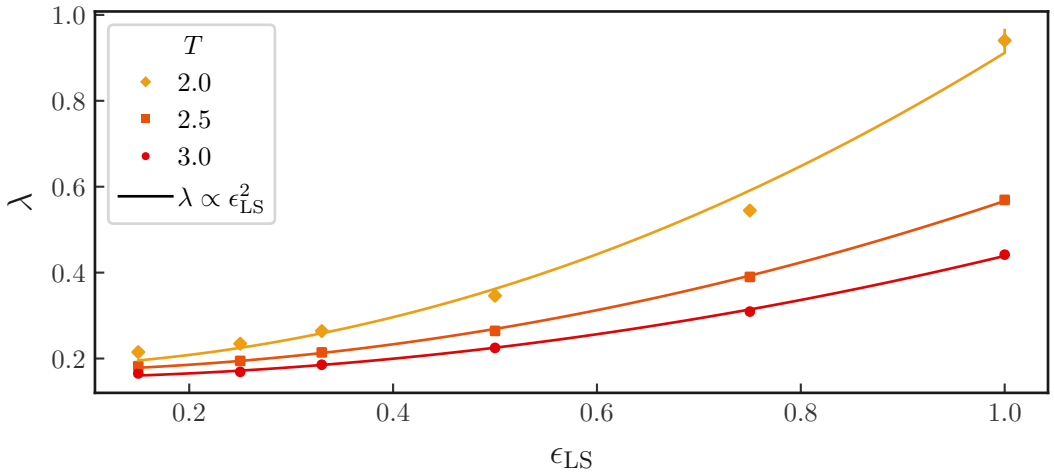

Figure 3.4: Effect of ε_{LS} on the friction coefficient λ. A quadratic dependence on ε_{LS} $\lambda \propto \varepsilon_{LS}^2$ describes well the data.

dashed-dotted curve) [59–61]: $\eta = \exp(A + \frac{B}{T-T_{VFT}})$ with $A = 0.27 \pm 0.06$, $B = 1.45 \pm 0.06$ and $T_{VFT} = 0.41 \pm 0.01$.

For the friction coefficient λ, we focus on a subset of values for ε_{LS} (0.25, 0.50 and 0.75) for clarity. The results are shown in Fig. 3.6. We observe two different behaviours. For $\varepsilon_{LS} = 0.75$, λ becomes super-Arrhenian while decreasing the temperature below 1.5. This slightly dominates the increase of η upon cooling and thus results in a slip length which keeps decreasing while approaching the glass transition. However, for $\varepsilon_{LS} = 0.25$ and 0.50, the friction coefficient suddenly drops by at least one order of magnitude for $T < 1$. This corresponds to a strong increase of the slip length at low temperatures by more than one order of magnitude.

Servantie *et al.* [69] observe the same behaviour for the slip length of a LJ polymer slipping on a LJ surface, and attribute it to a difference of mobility between the bulk and the interfacial liquid. In addition, Herrero *et al.* [105] study the slip length of water on graphene and LJ walls. They observe a moderate increase of the slip length at low temperatures for water on LJ walls, and a strong increase of b for water on graphene, and they relate it to the subtle differences in the temperature evolution of the static and dynamic contributions to viscosity and friction.

Structure factor To further explore this point, and to understand the fast decrease of λ at low temperatures, we have calculated the two-dimensional structure factor $S_{liq}(\vec{q})$ of the interfacial liquid and compared it to the structure factor $S_{wall}(\vec{q})$ of the solid wall. The structure factor is calculated by:

$$S(\vec{q}) = \frac{1}{N}\left[\left(\sum_{i=0}^{N}\cos(\vec{r_i}\cdot\vec{q})\right)^2 + \left(\sum_{i=0}^{N}\sin(\vec{r_i}\cdot\vec{q})\right)^2\right] \tag{3.4}$$

where $\vec{r_i} = x_i\vec{e}_x + y_i\vec{e}_y$ is the position of atom i and N is the total number of atoms considered in the calculation (in the first layer of liquid near the wall, delimited by the first non-zero minimum in the density profile in the z direction). The values of q at which we

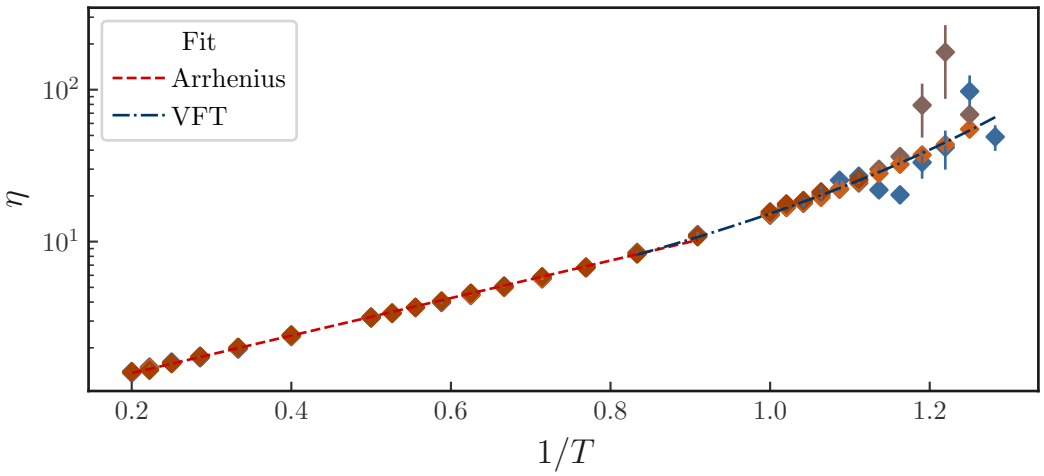

Figure 3.5: Viscosity as a function of temperature for various $\varepsilon_{\mathrm{LS}}$. The red dashed curve is an Arrhenian fit, giving an activation energy of 2.87. The blue dashed-dotted curve is a VFT [59–61] regression $\eta = \exp(A + \frac{B}{T-T_{\mathrm{VFT}}})$ yielding $A = 0.27 \pm 0.06$, $B = 1.45 \pm 0.06$ and $T_{\mathrm{VFT}} = 0.41 \pm 0.01$.

calculate the structure factor are multiples of $2\pi/L$ with L the size of the box along x and y directions. The commensurability between the local structure of the liquid interfacial layer and the wall structure is a key factor controlling friction. This commensurability can be quantified by the value of the two-dimensional structure factor of the liquid interfacial layer at the smallest characteristic wavevector of the wall interaction energy landscape, $S_{\mathrm{liq}}(\vec{q}_{\mathrm{wall}})$, where $\vec{q}_{\mathrm{wall}}$ is the position of the first peak in the wall structure factor [17, 24].

The structure factors of the wall and the interfacial liquid layer for $\varepsilon_{\mathrm{LS}} = 0.25$ and $\varepsilon_{\mathrm{LS}} = 0.75$ are shown in Fig. 3.7 for $T = 0.80$. The wall has a square lattice. The interfacial liquid layer is that of an isotropic liquid for $\varepsilon_{\mathrm{LS}} = 0.75$, but interestingly, for $\varepsilon_{\mathrm{LS}} = 0.25$, the interfacial layer displays a hexagonal crystalline order. On the same figure, we show snapshots of the layer over which the structure factor is calculated. We clearly see that for $\varepsilon_{\mathrm{LS}} = 0.25$, the interfacial layer contains only A particles. In contrast, for stronger L-S interaction ($\varepsilon_{\mathrm{LS}} = 0.75$), type B particles remain at the interface and prevent the interfacial liquid to structure itself, and thus its structure factor remains that of a liquid. In this case, $S(\vec{q}_{\mathrm{wall}})$ remains on the order of 1, and that is why we do not observe a sudden decrease of the friction coefficient at $\varepsilon_{\mathrm{LS}} = 0.75$ in Fig. 3.6.

To quantify this depletion, we have calculated the concentration of A particles c_{A} in a thin layer of thickness 0.1 near the bottom wall. The result is shown in Fig. 3.8. We observe that c_{A} is always larger near the wall than in the bulk. This difference is slightly stronger for low values of $\varepsilon_{\mathrm{LS}}$. As the temperature is decreased, the interface becomes richer and richer in A particles, especially at low $\varepsilon_{\mathrm{LS}}$. It even reaches 100 % below 1.0 for $\varepsilon_{\mathrm{LS}} = 0.25$. Since the ability of the liquid to be supercooled is due to its bidispersity, when the layer becomes almost monodisperse, it cannot maintain the supercooled state and crystallises.

Here, superlubricity is possible because of the structure of the interface, and is reminiscent of solid-solid superlubricity, as evidenced experimentally e.g. for graphite [119].

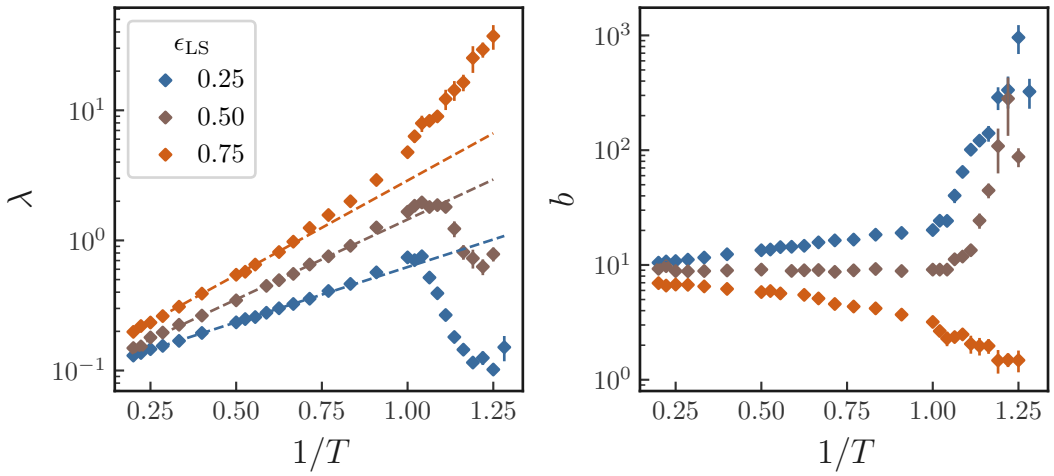

Figure 3.6: Friction coefficient (left) and slip length (right) as a function of temperature for various ε_{LS}. Dotted lines correspond to Arrhenian fits at high T.

Indeed, the role of incommensurability in reducing the friction between two solids has been reported by Zhang *et al.* [120] and Franchini *et al.* [121] for Al/Al and Xe/Cu interfaces respectively. In addition, Cieplak *et al.* [122] have observed a strong reduction of friction from a fluid to a crystallized layer of krypton adsorbed on gold because of incommensurability between the crystallized krypton layer and the gold lattice.

3.4 Conclusion

In this chapter, we have used a model Kob-Andersen liquid to study the effect of temperature on the friction coefficient λ. Above the melting temperatures, λ follows an Arrhenius law with an activation energy depending on the liquid-solid interaction potential ε_{LS}. In particular, depending on ε_{LS}, the activation energy of λ can be either smaller or larger than the activation energy of the viscosity. Therefore, ε_{LS} controls the temperature-dependence of the slip length b in this regime. In the supercooled regime, at large ε_{LS}, the friction coefficient becomes super-Arrhenian, similarly to the viscosity. On the contrary, at low ε_{LS}, B particles are depleted from the interface, allowing the very first layers of liquid to crystallise. The crystalline structure of these layers being incommensurate with wall structure, the friction coefficient is strongly reduced, leading to giant slip lengths. All these measurements have been done in the linear regime, where both η and λ are independent of the shear velocity U. In the next chapter (Chapter 4), we study a pure LJ liquid and try to probe the high-U regimes and relate this to the local relaxation of the liquid. In addition, because a pure LJ easily crystallises, we look at the wall stress near the crystallisation temperature.

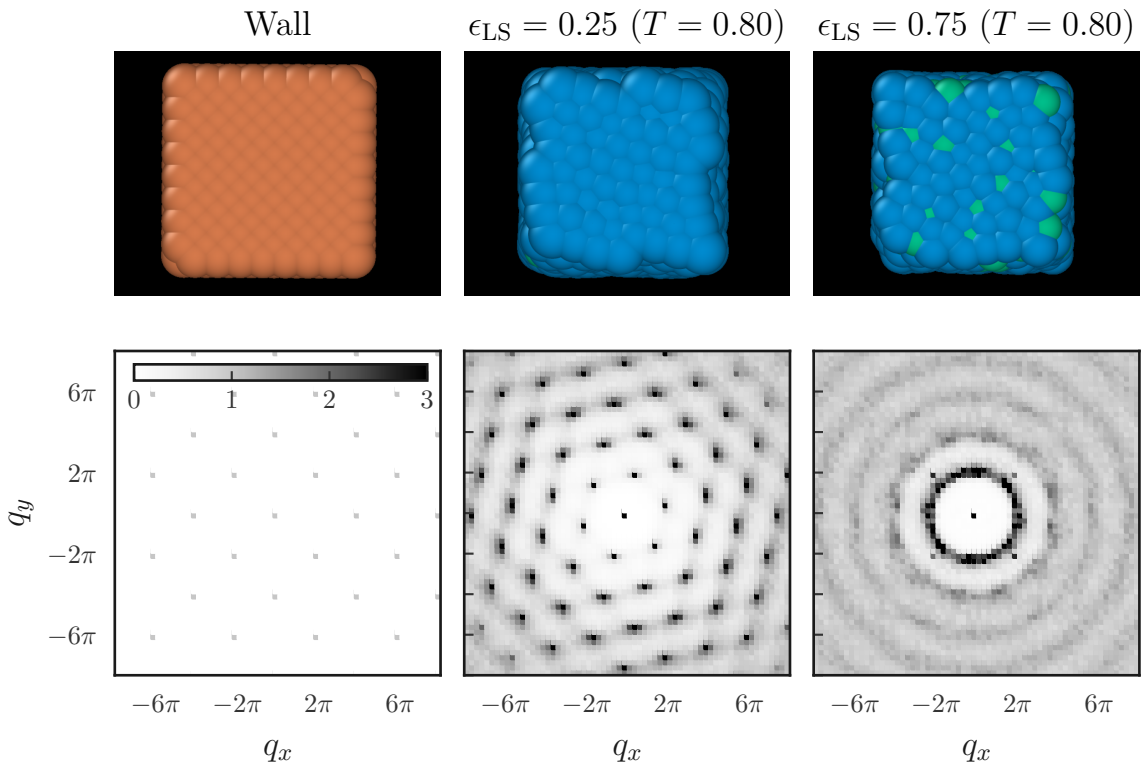

Figure 3.7: Structure factor of the wall (left) and of the liquid layer in contact with the wall (middle and right). The colormap corresponds to the value of the structure factor at each pair (q_x,q_y) and is the same for the three plots.

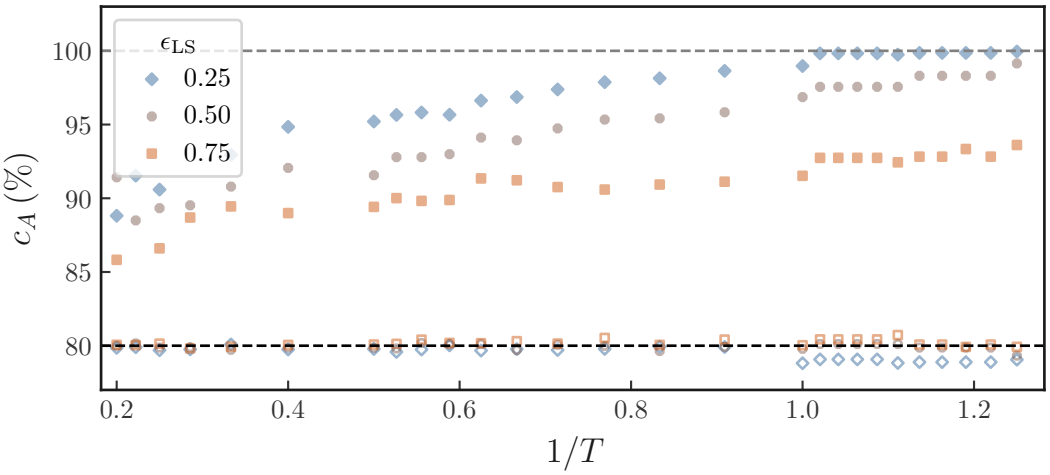

Figure 3.8: Percentage of A particles with respect to the total number of particles for various temperatures T and liquid-solid interaction energies ε_{LS}. Filled symbols correspond to the concentration inside a layer of thickness 0.1 near the bottom wall whereas empty symbols correspond to the bulk concentration.

Chapter 4

Lennard-Jones liquid: from liquid/solid to solid/solid friction

Contents

In this chapter, we study the liquid/solid friction of a pure Lennard-Jones (LJ) liquid on a crystallised FCC LJ wall. In Section 4.1, we use the methodology derived in Chapter 2 and used for the KA liquid to measure the viscosity and the friction coefficient. We first describe the effect of shear-rate on the friction and the viscosity of the fluid. We also discuss the validity of the Cox-Merz rule for both parameters. In Section 4.2, we measure the stress exerted by the fluid on the wall near the melting temperature and the transition between liquid/solid and solid/solid friction.

4.1 Effect of shear-rate on viscosity and friction

In this first section, we remain in the fluid domain ($T \geq 1.5$). We extract the viscosity and the friction coefficient from the stress at the wall and the velocity profile, as we have done for the Kob-Andersen (KA) fluid in Chapter 3. Details about the procedure are given in Section 2.3.2.

4.1.1 Bulk shear-thickening and interfacial shear-thinning

We are interested in the shear-rate dependence of η and λ. The shear-rate is controlled by the velocity $(U, -U)$ applied to the bottom and top walls, respectively. The height h of the liquid is fixed during the equilibration procedure, and is approximately the same for a given temperature T and L-S interaction energy ϵ_{LS}. The value of the shear-rate is obtained by linearising the velocity profile at the centre of the fluid. In Fig. 4.1, we plot the viscosity η and the friction coefficient λ as a function of the applied shear-rate.

We observe that, at approximatively the same shear velocity U (around 1 at $T = 2.0$), the viscosity increases (around 40 % over the considered range of U) and at the same time the friction coefficient significantly decreases (around 60 % over the same range of U). In

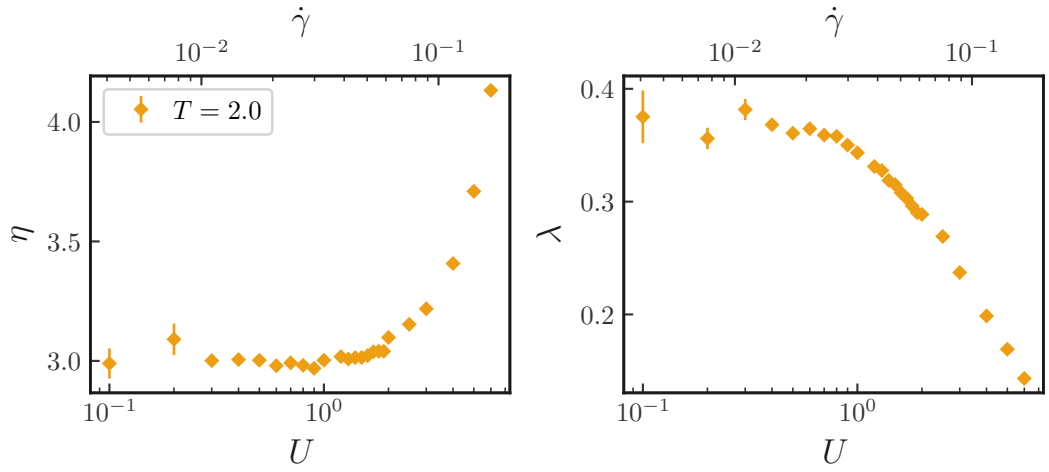

Figure 4.1: Shear velocity U dependence of the viscosity η (left) and the friction coefficient λ (right) for a LJ liquid at $T = 2.0$ and $\varepsilon_{\text{LS}} = 0.75$. The top axis in both graphs is the shear-rate $\dot{\gamma}$ computed at the centre of the liquid.

Chapter 3, we have focused on the linear regime only. Here, we would like to understand what happens at high shear-rates.

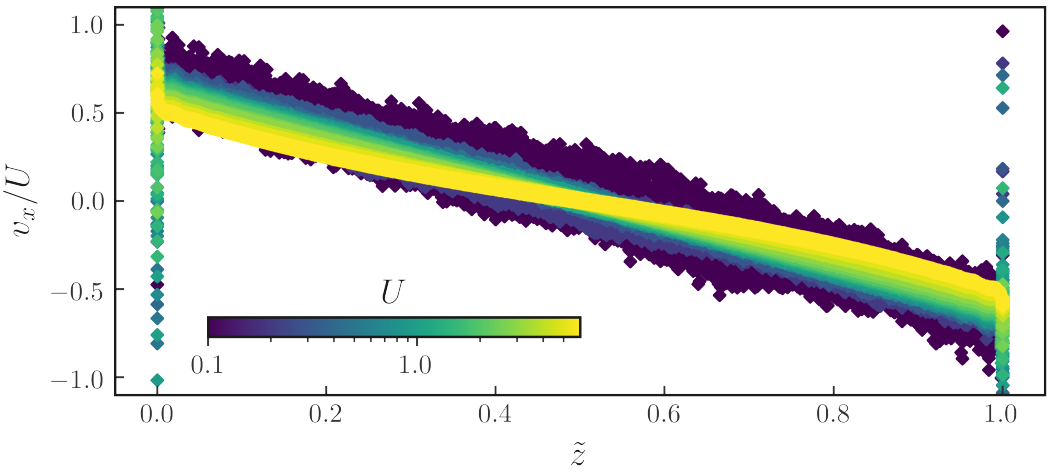

Figure 4.2: Velocity profile inside the liquid as a function of the applied shear velocity U. $\tilde{z}$ is the dimensionless height inside the liquid. This is done for $T = 2.0$ and $\varepsilon_{\text{LS}} = 0.75$.

Velocity profiles. We first look at the velocity profile inside the liquid as a function of the velocity $(-U, U)$ applied to the top and bottom walls in the x-direction, respectively. The results are shown in Fig. 4.2. In this graph, $\tilde{z}$ is the dimensionless height inside the liquid, defined so that $\tilde{z} = 0$ is at the bottom wall and $\tilde{z} = 1$ is at the top wall. At small velocities, the velocity profile is noisy but linear. As we increase U, it becomes less and less noisy, but at very high U, it also becomes non-linear. The shear-rate we measure is the slope at the centre of the liquid. We see here that the shear-rate is actually non-homogeneous, and more precisely, it is smaller at the middle of the liquid than at the interfaces. Such a non-linear velocity profile is unexpected, and could be the consequence of an inhomogeneous density profile.

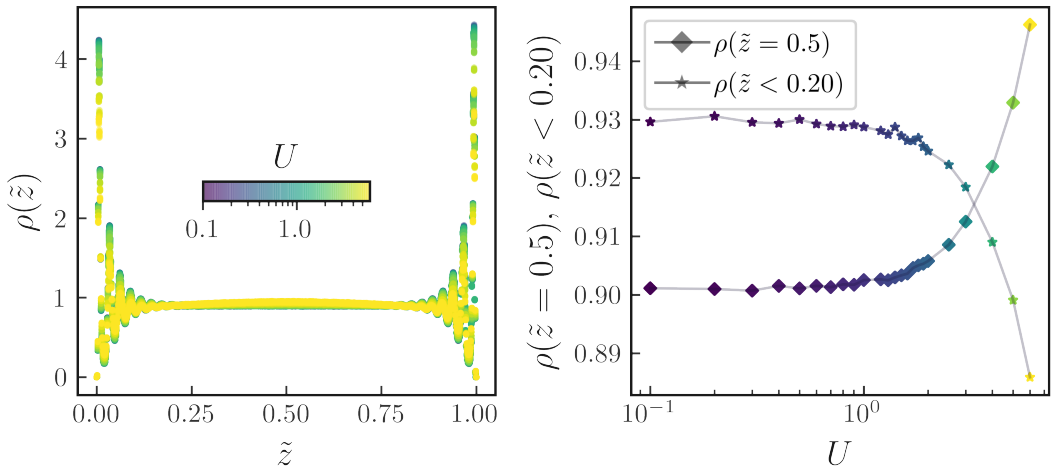

Figure 4.3: Left: density profile inside the liquid as a function of the applied shear velocity U. $\tilde{z}$ is the dimensionless height across the liquid. Right: density at the centre of the liquid $\rho(\tilde{z} = 0.5)$ and average density near the bottom wall $\rho(\tilde{z} < 0.20)$ as a function of U. This is done for $T = 2.0$ and $\varepsilon_{\text{LS}} = 0.75$.

Density distribution. In Fig. 4.3, we show the density profile inside the liquid as a function of U. Again, $\tilde{z}$ is the dimensionless height inside the liquid. Near the walls, the density profiles oscillate, and reaches a constant value in the bulk. We see that at high U, the density at the centre of the liquid slightly increases, while the density near the walls slightly decreases. In the right graph, we plot the density at the centre of the liquid $\rho(\tilde{z} = 0.5)$ and the average density near the bottom wall $\rho(\tilde{z} < 0.20)$ as a function of the shear velocity U. We indeed see that for $U > 1$, these two densities are affected by the flow, which suggests that the shear-thickening of η and the shear-thinning of λ are correlated to this change of density profile. In addition, the mean temperature inside the liquid increases slightly at high shear-rates, as illustrated in Fig. 4.4.

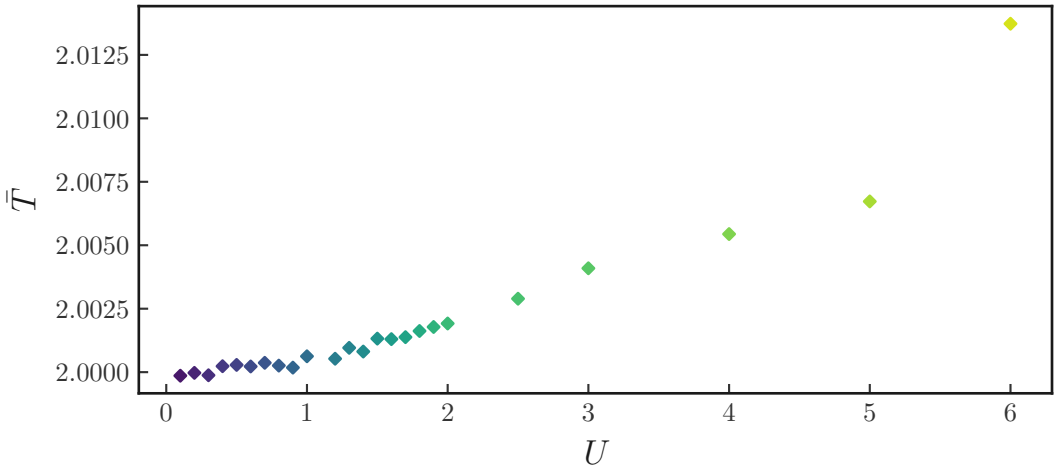

Figure 4.4: Average temperature T inside the liquid as a function of the shear velocity U. This is done at $\varepsilon_{\text{LS}} = 0.75$.

Structure factor. We look at the 2D structure factor inside the liquid. The calculation is described in Section 2.3.3. We calculate $S(q_x, q_y)$ for various heights inside the liquid. In Fig. 4.5, we plot the structure factor near the bottom wall (first layer of liquid atoms) and at the centre of the bulk liquid, for two different shear-rates $\dot{\gamma} = 0.06$ ($U = 1.90$) and $\dot{\gamma} = 0.22$ ($U = 7.00$). The temperature is 2.0 and we are in the wetting situation ($\varepsilon_{\text{LS}} = 0.75$). We see that in both cases, the liquid remains isotropic both in bulk and near the walls. The shear-rate has thus no effect on the structuration of the liquid.

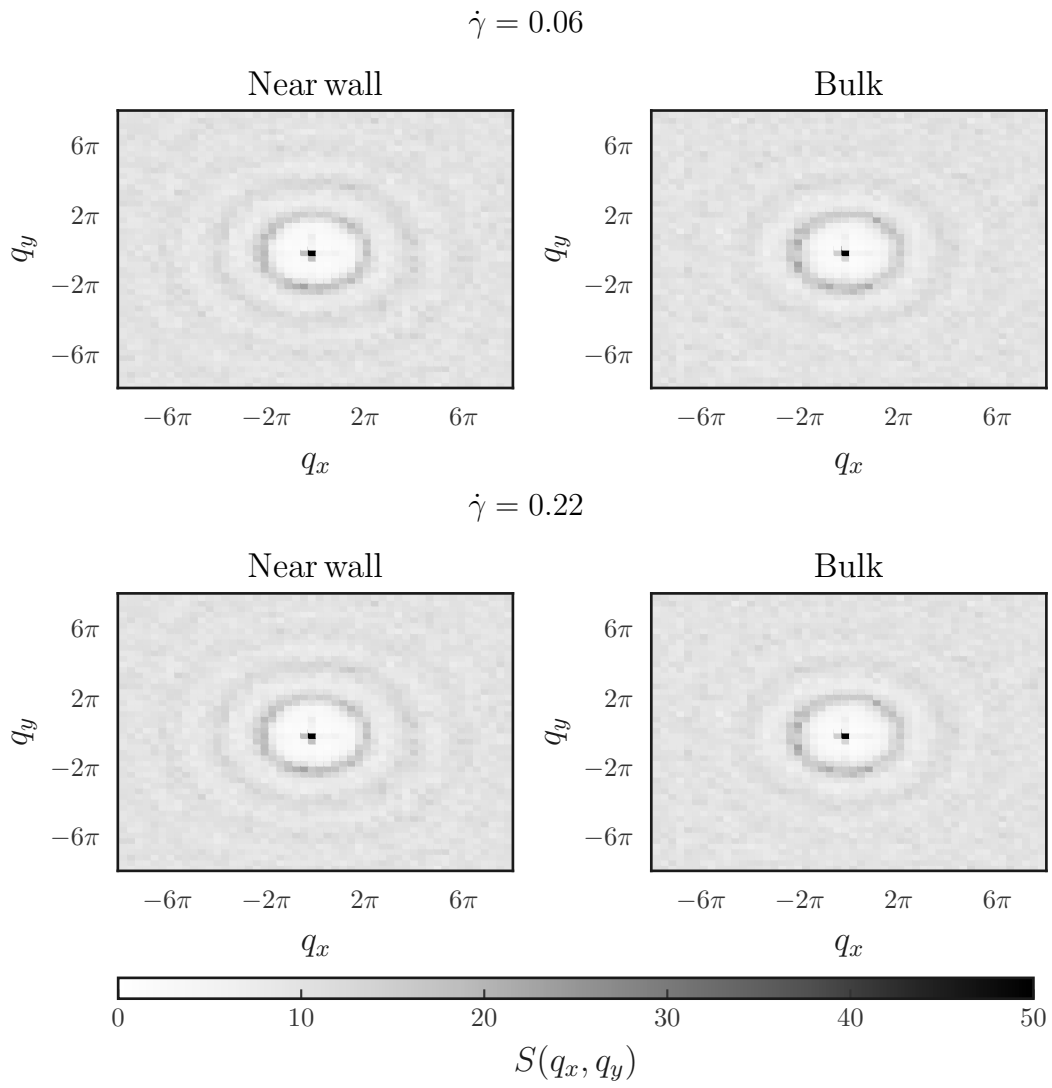

Figure 4.5: 2D structure factor $S(q_x, q_y)$ for $\dot{\gamma} = 0.06$ (top) and $\dot{\gamma} = 0.22$ (bottom). Left figures correspond to the structure factor of the first layer in contact with the solid. Right figures correspond to the structure factor at the centre of the liquid. The colorbar correspond to the amplitude of $S(q_x, q_y)$ and is the same for all plots.

It is possible that at high shear-rates, the pressure inside the liquid becomes inhomogeneous, leading to an inhomogeneous density in the bulk liquid. To check this, we would need to look at the dependency of η with the pressure or the liquid density. We could also look at the effect of the size of the box. These are ongoing simulations. Another possi-

bility would be the failure of the thermostat at high shear-rates. To test this hypothesis, we would need to use another thermostat to see whether the results are the same.

4.1.2 Validity of the Cox-Merz rule

We now make a brief detour to discuss the inapplicability of the Cox-Merz rule in our system. We first discuss this for the viscosity (Section 4.1.2.1) and then for the friction coefficient (Section 4.1.2.2).

4.1.2.1 Viscosity

The Cox-Merz rule [123] relates the non-linear viscosity of the liquid under steady shear flow $\eta(\dot{\gamma})$ to the frequency-dependent linear complex viscosity of the liquid under oscillatory shear flow $\eta^*(\omega)$. The Cox-Merz rule states that:

$$\eta(\dot{\gamma}) = |\eta^*(\omega)| \tag{4.1}$$

This rule is very often verified in polymeric liquids. Nonetheless, several deviations have been observed [124], in particular for LJ [103] and supercooled liquids [125]. The reasons why these liquids do not follow the Cox-Merz rule are still under investigation. Bair *et al.* [124] argued that the Cox-Merz rule works when there is a coupling between the shear stress and the conformation of the molecules. This is true for elongated molecules such as polymers, but not for spherical molecules. When the coupling is weak, a reasonable hypothesis is to say that strong shear-rates induce structural distortions in the liquid: it creates a compression along the axis of the flow, and in particular, it can locally change the density of the liquid. This may modify the structural relaxation time, which strongly depends on the density for supercooled liquids. Furukawa [125] indeed related the threshold shear-rate above which the fluid becomes shear-thinning $\dot{\gamma}_c$ to the dependence of the α-relaxation time with the density ρ:

$$\dot{\gamma}_c = [\rho(\partial\tau_\alpha/\partial\rho)]^{-1} \tag{4.2}$$

This can explain the breakdown of the Cox-Merz rule: compared to the equilibrium fluid, the flow is likely to modify the structural relaxation time of the fluid. This changes $\dot{\gamma}_c$ and thus shifts the $\eta(\dot{\gamma})$ curve. Experimentally, a good technique to probe this effect is the rheo-dielectric spectroscopy: by adding a dielectric spectroscopy device on a rheometer, one has access to the relaxation spectrum of the liquid under shear. Some examples of such measurements on polymer melts and nematic liquid crystals can be found in [126,127].

In Fig. 4.6, we plot both the shear viscosity $\eta(\dot{\gamma})$, with $\dot{\gamma}$ the slope of the velocity profile at the centre of the liquid, and the real part of the complex viscosity $\mathrm{Re}\,(\eta^*(\omega))$ as a function of the pulsation ω. The calculation is given in Section 2.3.1.3.

For the equilibrium spectrum, the viscosity displays a shear-thinning behaviour for $\omega > 1$. The low-frequency value is in agreement with the low shear-rate value obtained from out-of-equilibrium simulations. As expected, the slightly shear-thickening regime is only visible for the sheared liquid. We can compare these results to the work of Yamaguchi *et al.* [103], who have also plotted the non-equilibrium viscosity $\eta(\dot{\gamma})$ and the equilibrium frequency-dependent shear-viscosity $\eta^*(\omega)$ of a LJ fluid near the triple point (see Fig. 4.7). Their out-of-equilibrium simulations are conducted with a periodic system without walls.

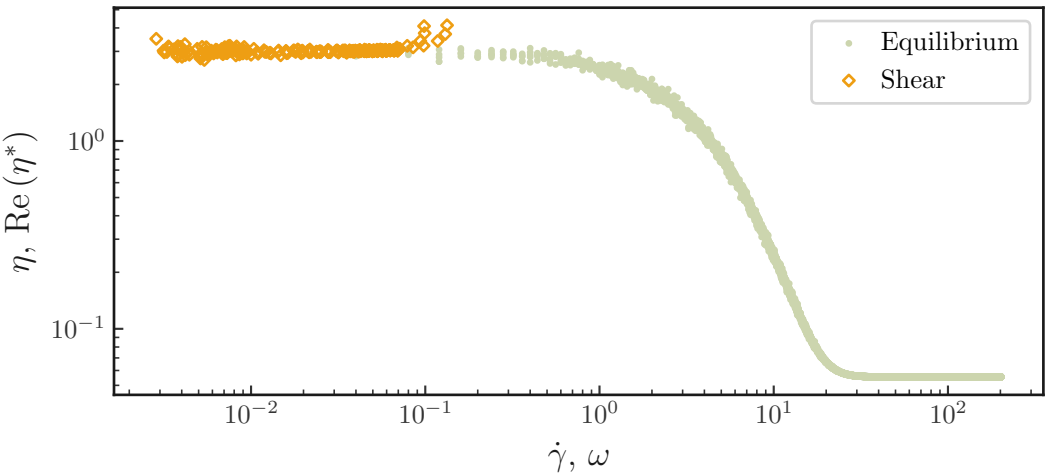

Figure 4.6: Shear viscosity $\eta(\dot{\gamma})$ and real part of the complex viscosity $\mathrm{Re}\,(\eta^*(\omega))$ for $T = 2.0$.

They do not observe a shear-thickening behaviour, but a shear-thinning viscosity instead. The shear-thinning regime is reached much sooner in the out-of-equilibrium simulations compared to the equilibrium simulations, and thus the Cox-Merz rule is violated.

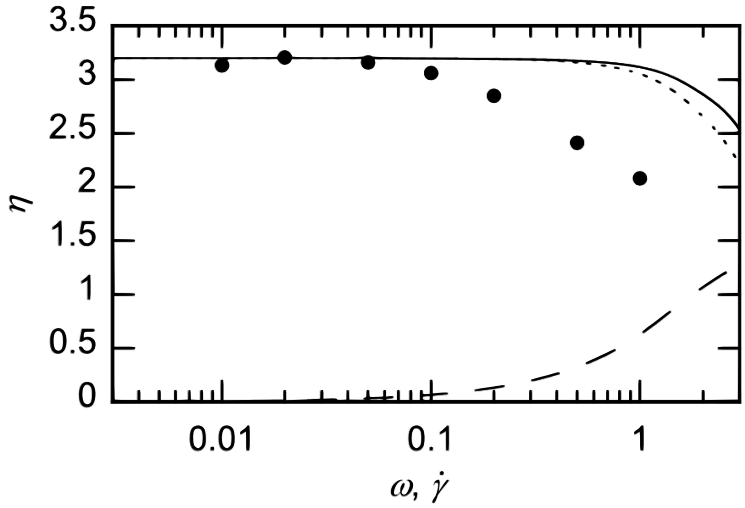

Figure 4.7: Comparison between the non-equilibrium shear-rate dependent viscosity $\eta(\dot{\gamma})$ (filled circles) and the equilibrium frequency-dependent complex viscosity $\eta^*(\omega)$. The real part is dotted, the imaginary part is dashed, and the amplitude is solid. Taken from [103].

Since the Cox-Merz rule does not hold for the viscosity of the LJ liquid, it is very likely that it does not work for the friction coefficient as well. This is the purpose of the next subsection.

4.1.2.2 Friction coefficient

In the same way, we can calculate the real part of the complex friction coefficient $\lambda^*(\omega)$ and compare it to the friction coefficient obtained for the sheared liquid. This is shown in Fig. 4.8. Similarly to the viscosity, the low-frequency value of $\mathrm{Re}\,(\lambda^*(\omega))$ matches the low

shear-rate value of $\lambda(\dot{\gamma})$. We observe a shear-thinning behaviour of both coefficients, yet, shear-thinning happens sooner for the out-of-equilibrium λ compared to the equilibrium one. As discussed in Section 4.1.1, the shear-thinning behaviour observed for the out-of-equilibrium simulations is likely to be due to the distortion of the density profile because of the flow.

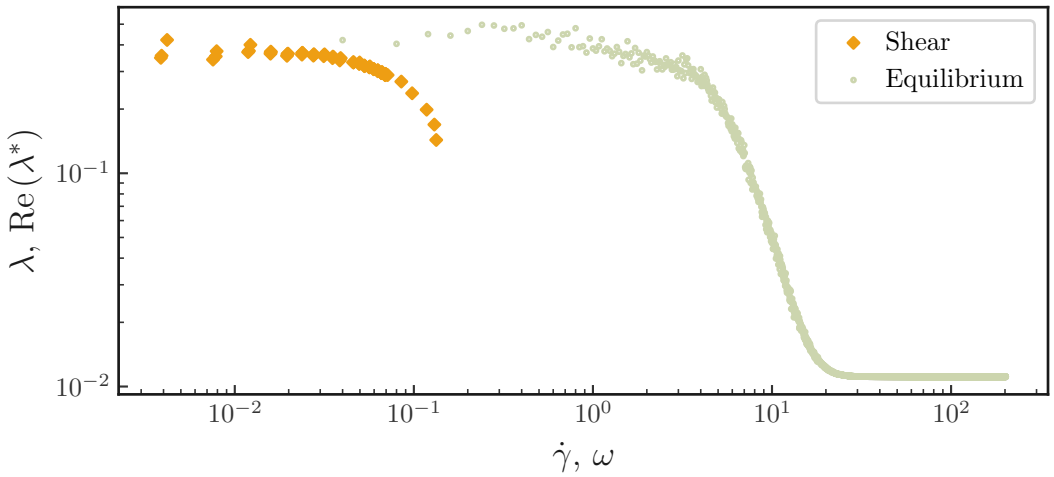

Figure 4.8: Shear friction coefficient $\lambda(\dot{\gamma})$ and real part of the complex friction coefficient Re $(\lambda^*(\omega))$ for $\varepsilon_{\text{LS}} = 0.75$ and $T = 2.0$.

4.2 Stress at the wall: from liquid/solid to solid/solid friction

In this section, we are focusing on the stress at the liquid-solid interface as the temperature crosses the melting temperature of our LJ fluid.

4.2.1 Crystallization

When the liquid is cooled down below 1.5, it crystallises. Velocity profiles at $T = 1.5$ and $T = 1.2$ are plotted in Fig. 4.9. When the LJ is crystallised, it does not move with the walls and the velocity profile is flat, with underlying oscillations stemming from the crystalline structure. There is thus a discontinuity of behaviour between the sheared liquid and solid.

4.2.2 Wall-stress

In Fig. 4.10, we show the stress at the wall σ_{wall} exerted by the fluid (left) and by the crystallized LJ (right). In the latter case, the solid is immobile and undistorted, and thus we cannot define a shear-rate. In order to have comparable units, we plot the wall stress as a function of an "apparent" shear-rate which is defined by the velocity difference between the two sliding walls $2U$ divided by the height of the solid h. For the fluid, σ_{wall} is proportional to $\dot{\gamma}$, as $\sigma_{\text{wall}}/\dot{\gamma} = \eta$ which remains Newtonian. As the temperature of the fluid is decreased, η increases and thus the curve is steeper. For the crystallised LJ, the wall stress σ_{wall} is proportional to the apparent shear-rate $2U/h$. This is unexpected for solid/solid friction. The slope $\mu \equiv \sigma_{\text{wall}}/(2U/h)$ decreases slightly as the solid is cooled

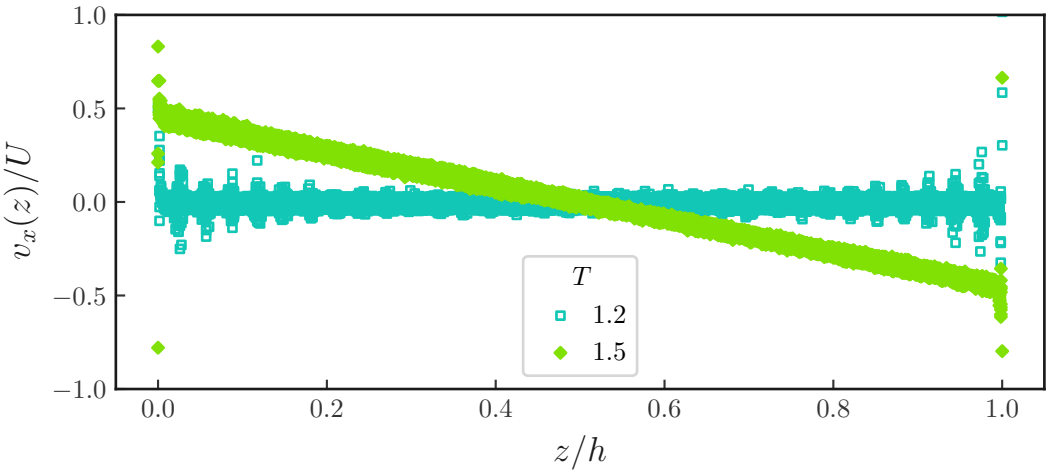

Figure 4.9: Velocity profile of the LJ at two different temperatures.

down.

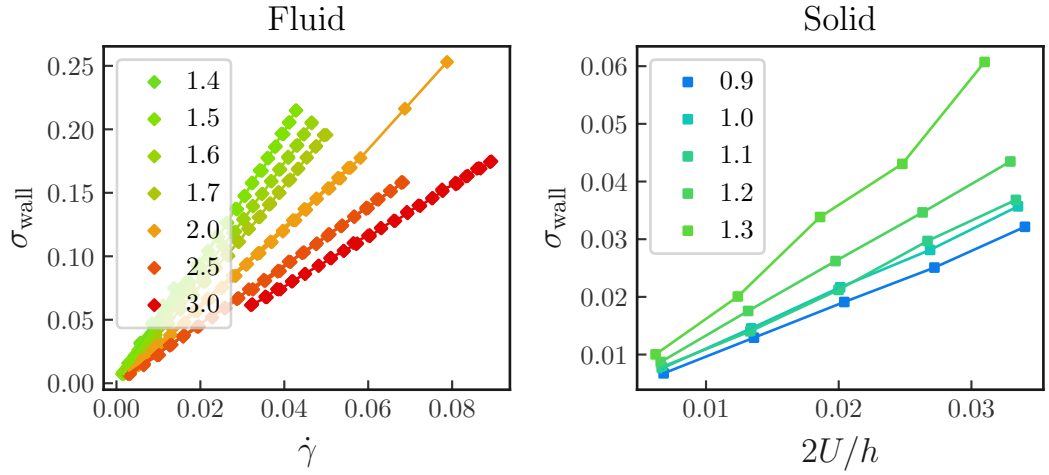

Figure 4.10: Wall stress as a function of (left) the shear-rate applied to the liquid, and (right) the "apparent" shear-rate $2U/h$ to which the solid is submitted. Colours correspond to temperatures.

The temperature dependences of η and μ are shown in Fig. 4.11. As expected, the viscosity follows an Arrhenius law $\eta \propto \exp(E_a/T)$ with $E_a = 2.71 \pm 0.01$. On the other hand, $\mu(T)$ is an increasing function of the temperature, and cannot be fitted by neither an Arrhenius law nor a linear function.

4.3 Conclusion

This chapter contains ongoing work on the interfacial behaviour of a LJ fluid. In Section 4.1, we have focused on the shear-rate dependency of the viscosity η and the friction coefficient λ. In particular, we have observed an increase of η simultaneously to

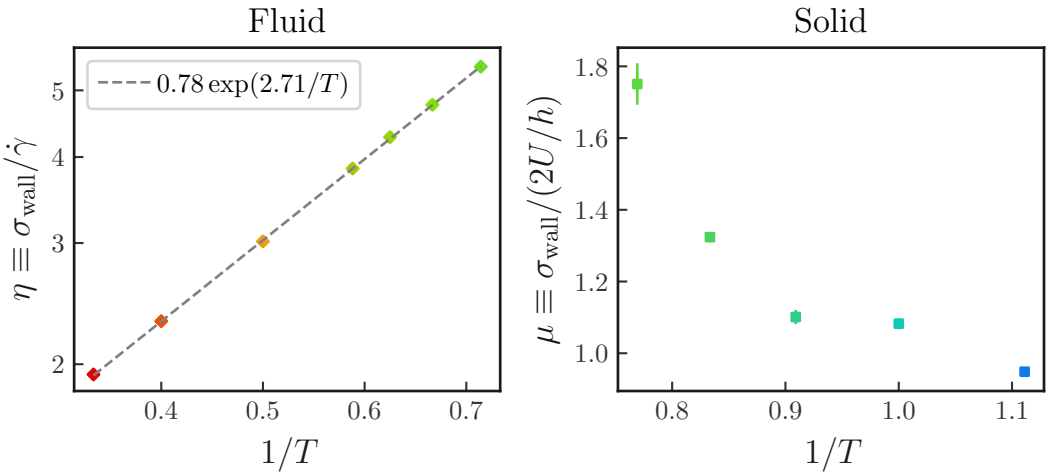

Figure 4.11: Left: viscosity of the LJ fluid as a function of temperature. Right: proportionality coefficient between σ_{wall} and $2U/h$ for the crystallized LJ, as a function of temperature.

a decrease of λ at high shear-rates. We have shown that these behaviours are likely to be due to a distortion of the density profile $\rho(z)$ at high shear-rates. This inhomogeneity of the bulk density profile might explain the violation of the Cox-Merz rule observed for both η and λ, in line with previous work. Finally, we have briefly looked at the evolution of the stress at the liquid-solid interface as the liquid crystallises. We have seen that, surprisingly, the stress between the wall and the crystallised LJ depends on the shear velocity applied. This is unexpected for common solid-solid friction, and it would require more time to understand these results.

Conclusion of Part I

In this first Part, we have used Molecular Dynamics simulations to explore the effect of temperature on the slip and the friction coefficient of a model liquid. In the first and main chapter of this section (Chapter 3), we have used a Kob-Andersen liquid in order to study the slip of a supercooled liquid. We have shown that at high temperatures, the friction is activated, and from this we could rationalise the various temperature dependencies of the slip length reported in the literature. Then, we have observed that the supercooled liquid can display two different behaviours upon cooling: either the friction coefficient becomes super-Arrhenian, or there is a phase separation near the surface and thus a crystalline layer is formed at the wall, which strongly reduces friction, yielding to giant slip lengths. This work has been published recently in [108]. The second and last chapter of this first part, Chapter 4, focuses on the friction between a model wall and a monodisperse Lennard-Jones fluid. In a first section, we look at the shear-rate dependency of the viscosity and the friction. We observe a bulk shear-thickening and an interfacial shear-thinning, attributed to density inhomogeneities at high shear-rates. The consequence of this is the violation of the Cox-Merz rule. In a second part, we briefly mention the evolution of the stress at the wall as we cross the melting temperature. In particular, we observe that the temperature dependency of the wall stress changes as we go from the liquid to the solid regime. All the results of this chapter are very recent, and we are still conducting simulations in order to understand them.

Part II

Experimental

The second part of this thesis is devoted to the experimental study of the liquid/solid interface. In Part I, we have looked at friction at the liquid-solid interface for two different model Lennard-Jones liquids. Now, we are focusing on the behaviour of polymers near solid surfaces. This part contains experiments conducted with various techniques. In Chapter 5, we detail the materials and methods used throughout the rest of the thesis. The near-surface behaviour of polymer solutions relies on the concentration profile near the substrate. Therefore, in Chapter 6, we present neutrons reflectivity experiments designed to probe the concentration profile of a flowing polymer solution in the vicinity of the solid wall. Then, we have dedicated an entire chapter to the bulk and near-surface rheology of our polymer solutions. This is detailed in Chapter 7. Finally, we conclude this experimental part with Chapter 8, where we describe the adsorption kinetics of a PDMS melt on a silicon surface. In particular, we study the effect of temperature on the kinetics, which is very different from kinetics of other polymers because of the strong interaction of PDMS with oxidised surfaces.

Chapter 5

Methods

Contents

In this chapter, we present the materials and methods used for the experiments described in Part II. We first present the various polymers, solvents and surfaces used (Section 5.1). Then, we briefly mention the characterisation of the thermal and rheological properties of polymers (Section 5.2). In a third section, we explain the techniques used to clean and functionalise our surfaces (Section 5.3). Finally, we describe the reflectivity techniques we have used (ellipsometry, X-Ray and neutron reflectivity) (Section 5.4).

5.1 Materials

This section aims at presenting the materials and techniques used for most of the experiments. We start by describing the polymers and solvents used, and their physical properties. Then, we present two techniques of polymer characterisation, namely rheology and Differential Scanning Calorimetry (DSC). Afterwards, we explain the processes we have used to prepare surfaces, either to clean them or to graft polymers on them. Finally, we detail two techniques of surface characterisation: ellipsometry and X-Ray reflectivity. Neutrons reflectivity is described in details later, in Chapter 6.

	M_0 [g/mol]	ρ [g/cm^3]	a [nm]	M_e [g/mol]	T_g [K]
PS	104	1.04	0.55	13000	373
PDMS	74	0.965	0.50	9600	150

Table 5.1: Physical parameters of PS and PDMS [128]. M_0 is the molar mass of the monomer, ρ is the density (at room temperature and ambient pressure), a the monomer size (estimated using $a^3 = \frac{M_0}{\rho \mathcal{N}_A}$), M_e is the molar mass above which polymer chains start to entangle [129] and T_g is the glass transition temperature of the polymer in the high molar masses limit [130].

5.1.1 Polymers

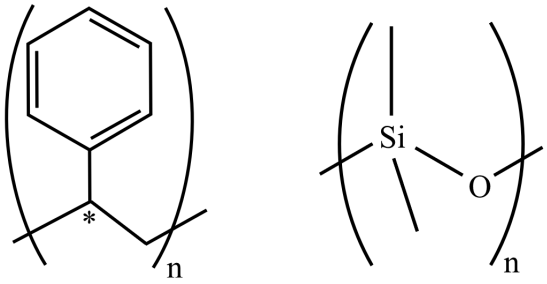

Figure 5.1: Left: polystyrene (PS) molecule. The star indicates the asymmetric carbon. Right: polydimethylsiloxane (PDMS) molecule.

Polystyrene (PS). Polystyrene (PS) is a linear neutral polymer of formula $(C_8H_8)_n$ made from styrene (C_8H_8) monomers. Its molecular structure is shown in Fig. 5.1 (left). We have only used atactic polystyrene, which means that the relative orientation of phenyl groups of two successive monomers is random. This prevents crystallisation of polystyrene, which can only overcome a glass transition temperature, around 110 °C for $N > 10^4$ monomers. High molar masses PS is thus a solid at room temperature. Its physico-chemical properties are summarised in Tab. 5.1. It is relatively chemically inert, but it can be oxidized by UV light in the presence of oxygen[a]. Polystyrene is used in a broad range of applications, especially packaging and building insulation, and thus the worldwide annual production was estimated around a few million tonnes in 2007 [131].

Our choice to use polystyrene is motivated by the fact that it is a suitable model polymer, well characterised, commercialized with a low dispersity index, and available in a deuterated form, where all (PSd8), or some hydrogen atoms have been replaced by a deuterium atom. This is useful for neutron experiments.

Polydimethylsiloxane (PDMS). Polydimethylsiloxane (PDMS) is also a linear neutral polymer of raw formula $(C_2H_6OSi)_n$ obtained by anionic polymerization of octamethylcyclotetrasiloxane. The structure is shown in Fig. 5.1 (right). Its physico-chemical properties are summarised in Tab. 5.1. It has a very low glass transition temperature (around

[a]This leads to a yellowing of PS, which is a visual clue of the oxidation of the chains.

Polymer	Name	M_n [Mg/mol]	Đ	Provider
PS	PS10M	10.2	1.08	Agilent
	PS8M	8.42	1.10	TOSOH
	PS20M	20.6	1.15	TOSOH
PDMS	PDMS345k	0.345	??	??

Table 5.2: Description of the polymers used in the following chapters.

−127 °C), which makes it liquid at room temperature. Its chain ends (α and ω) can be various chemical groups, such as hydroxyl, silanol, methyl, vinyl... The choice of these two groups has strong consequences on the adsorption of PDMS onto surfaces, and is discussed in Chapter 8. Except when it is explicetly specified, the PDMS we use is a α,ω-dihydroxyl-terminated PDMS (that we also cal OH-terminated PDMS for simplicity).

PDMS is rather resistant to oxidation, and can be cross-linked to create soft materials with a controlled elastic modulus. This is often used to create microfluidics chips, seals, molds etc. [132]. In addition, it is biocompatible, and therefore it can be used as medical implants or in cosmetics[b].

Table 5.2 recapitulates the various polymers used during this thesis.

5.1.2 Solvents

Diethylphtalate (DEP). We use diethyl benzene-1,2-dicarboxylate also known as diethylphtalate (DEP) as a solvent of polystyrene (PS). This choice is motivated by the fact that DEP is a good solvent of PS, non-volatile (P_{sat} = 0.27 Pa at 25 °C ; T_{boil} = 295 °C), non-toxic [133] and rather viscous (12.5 mPa.s at 20 °C), which enhances slippage. It is an organic liquid, polar and non-miscible with water. It is used either as a plasticiser or as a vehicle for perfumes [133]. The overlap volume fraction of PS in DEP is estimated to be $\phi^* = 0.025N^{-4/5}$ (see [3] Section 5.1.2).

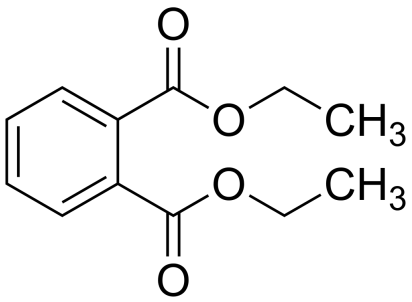

Figure 5.2: Diethylphtalate molecule.

The DEP we use has been purchased from Carlo Erba (RPE, for analysis) and used without further distillation.

5.1.3 Surfaces

[b]PDMS belongs to the large group of "silicones", which use in cosmetics has been debated.

Silicon wafer. A silicon wafer is a slice of monocrystalline silicon which surface has been polished down to a roughness below 0.5 nm. The wafers used in this work are either (001) (for slip measurements) or (111) (for adsorption). They are purchased from Silicon Materials Inc.. The surface presents a native silicone dioxide layer which thickness is around 2 nm. Therefore, the exposed surface has SiOH groups, which density is usually around $1-10$ OH/nm^2. The surface was freshly polished by Fichou and cleaned with the procedures described in Section 5.3.1.

Sapphire. We call a "sapphire surface" a surface of amorphous Al_2O_3. The surface we use has been polished. The density of SiOH is quite similar to silicon wafers and is about $1-10$ OH/nm^2 [134,135]. The sapphire surface was used for Neutrons Reflectivity (NR).

5.2 Polymer characterisation

5.2.1 Differential Scanning Calorimetry (DSC)

Differential Scanning Calorimetry (DSC) is a thermal analysis used to probe phase transitions of materials. It consists in two samples (of typically 10 mg): the material of interest and a reference sample. The idea is to heat up (or cool down) both samples at the same time, and measure the difference of heat flux required between the two. If the sample of interest undergoes an endothermic process, the heat flux required for it increases, while it decreases for an exothermic process. By choosing relevant temperature ramps, one can thus determine phase transitions temperatures, glass transitions temperatures and reaction enthalpies.

In our case, we use DSC to determine the glass transition temperature of our polymer solutions. This is what we describe in the following. We use a DSC Q-100 from TA instruments equipped with a liquid nitrogen cooling system which allows us to reach temperatures down to 143 K. Around 10 mg of our solution is deposited inside a small aluminium hermetic capsule which is loaded in the DSC apparatus. We then perform a cooling at -10 K/min and a heating at $+10$ K/min prior to the measurement. After that, we perform successive cooling/heating cycles at various rates. We measure the differential heat flow as a function of temperature. This is shown in Fig 5.3. The peak on the cooling curves probably originate from the crystallisation of an impurity (maybe water). The jump corresponds to the glass transition. This transition is also visible on the heating curve. The glass transition temperature is obtained as the temperature of the inflexion point of the cooling curves[c].

5.2.2 Rheology

Rheology is "the science of deformation and flow"[d] [136]. Here, we use shear rheology to measure the shear viscosity η of our polymer solutions. The principle is to shear a liquid between two rotating plates, and measure the corresponding torque. There are two ways of measuring η. The first one is called a **flow experiment**: we scan a range of shear rates defined as $\dot{\gamma} \equiv \partial v/\partial z$, and we measure the resulting torque Γ exerted by the

[c] The heating step is used to erase the thermal history of the sample.
[d] It comes from ancient greek *rheo*: to flow and *logos*: study, science.

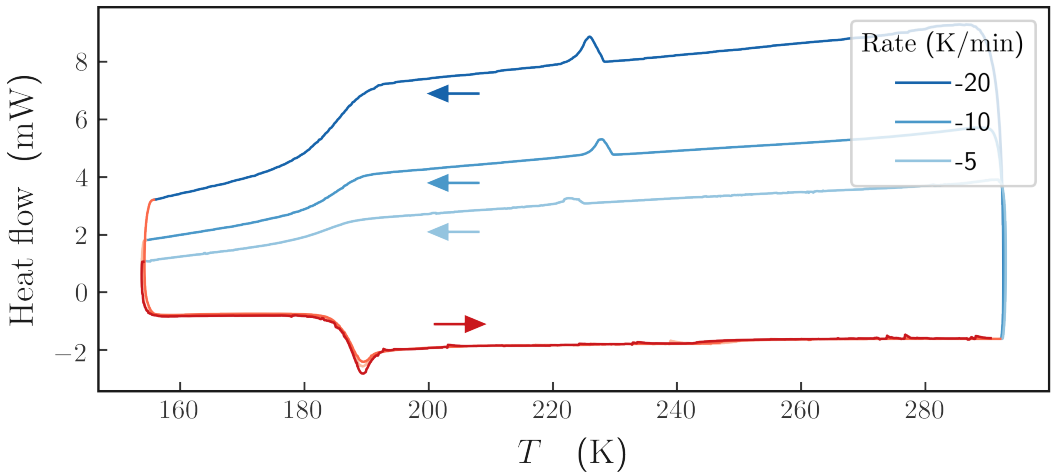

Figure 5.3: DSC thermograph of a 2.3% 10M PS/DEP solution. Blue (red) curves denote cooling (heating) ramps. Arrows show the sense of evolution of the temperature. The jump around 185 K correspond to the glass transition. The small peak on the cooling curves around 223 K correspond to the crystallisation of an impurity.

liquid on the top geometry. In a cone-plate geometry, the shear rate is homogeneous in the whole sample (if there is no slip and no shear-banding) and writes:

$$\dot{\gamma} \equiv \partial v/\partial z = \frac{2\pi\Omega}{\tan\alpha} \tag{5.1}$$

with Ω the rotational velocity and α the cone angle. Then the viscosity is calculated using:

$$\eta(\dot{\gamma}) = \frac{3\Gamma}{2\pi\dot{\gamma}R^3} \tag{5.2}$$

with R the radius of the geometry.

The second method is called **oscillatory rheology**: the cone oscillates periodically. Assuming a linear response between the strain and the stress allows us using a complex notation. The periodic complex deformation $\gamma^* = \gamma_0 e^{j\omega t}$ with γ_0 the amplitude of oscillations, ω the frequency, the stars denote complex quantities and $j^2 = -1$. The resulting torque Γ^* can be decomposed in an in-phase and an out-of-phase components with respect to the deformation: $\Gamma^* = (G' + jG'')\gamma^*$. G' and G'' are the storage and loss moduli, respectively. The complex viscosity can then be calculated by:

$$|\eta^*(\omega)| = \frac{G'(\omega) + jG''(\omega)}{\omega} \tag{5.3}$$

This gives access to reptation times for semi-dilute entangled polymer solutions. The smaller frequency ω_{rept} such that $G'(\omega_{\text{rept}}) = G''(\omega_{\text{rept}})$ gives the reptation time $\tau_{\text{rept}} = 1/\omega_{\text{rept}}$. This is illustrated in Fig. 5.4. In practice, the two moduli cross several times, corresponding to various relaxation times of the system. The reptation time is the longest relaxation time, written τ in Fig. **??**, and shorter timescales can be observed, such as the Rouse time of an entanglement strand τ_e and the relaxation time of a Kuhn segment τ_0.

The phenomenological Cox-Merz' law [123] stipulates that the two methods measure the same viscosity, provided that:

$$|\eta^*(\omega)| = \eta(\dot{\gamma}) \tag{5.4}$$

A superposition of viscosity measurements with these two techniques is shown in Fig. 5.4 for a PS/DEP solution with a molar mass $M_n = 10$ Mg/mol and a volume fraction $\phi = 6.15$ %. The curves superimpose nicely provided that $\omega \equiv \dot{\gamma}$.

Weissenberg number. The dimensionless number which compares the elastic and viscous forces is called the Weissenberg number Wi. In this thesis, we define it as the ratio of the shear-rate $\dot{\gamma}$ over the critical shear-rate $\dot{\gamma}_c$ at which the fluid becomes shear-thinning[e]. Using the Cox-Merz' law, we have $\dot{\gamma}_c = \omega_{rept} = 1/\tau_{rept}$. This is used in Chapter 6.

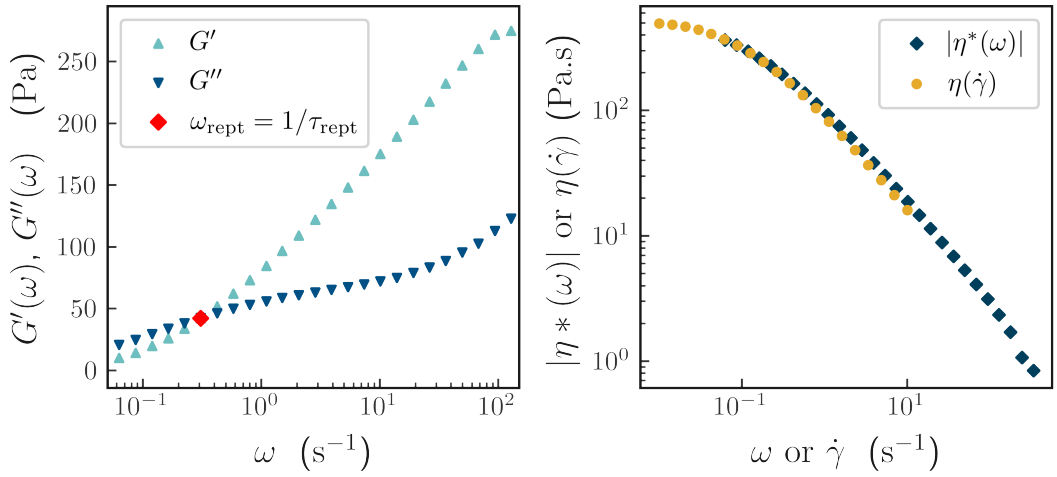

Figure 5.4: Rheology of a PS/DEP solution (10 Mg/mol, $\phi = 6.2$ %) using a sand-blasted cone-plate geometry ($R = 25$ mm, $\alpha = 2°$). Left: oscillatory measurement. We find $\tau_{rept} \approx 1/0.3 \approx 3.3$ s. Right: comparison of the viscosity measurements in flow rheology $\eta(\dot{\gamma})$ and oscillatory rheology ($|\eta^*(\omega)|$).

5.3 Chemistry of surfaces

5.3.1 Cleaning of surfaces

Surface science requires an extreme attention on the state of cleanliness of the surface. The first role of a cleaning process is to dissolve all the residues (inorganic and organic) on the surface. In addition, silicon surfaces exposed to air spontaneously form an oxide layer, which grows with time until reaching an equilibrium height. On top of this oxide layer, there can be different amounts of hydroxyl groups (-OH) depending on the cleaning process used. The total amount of -OH can change the reactivity and "attractiveness" of

[e] $\dot{\gamma}_c$ can be obtained by fitting $\eta(\dot{\gamma})$ or $|\eta^*(\omega)|$ by a function of the type Carreau-Yasuda. We come back to this in Chapter 7.

the surface (this will be discussed in Chapter 6). Therefore, one has to carefully chose the way it cleans its surface.

5.3.1.1 Cleaning surfaces under UV/ozone

The first and simplest way of cleaning the surface is to use a UV/ozone lamp. The surface is first thoroughly rinsed during 30 s successively with acetone (to dissolve organic residues), ethanol (to dissolve inorganic residues) and acetone, using wash bottles. Both solvents have been purchased from Sigma Aldrich (analytical standards). Between each rinsing, the surface is dried with nitrogen (a non-reactive gas). Then the surface is exposed to strong UV with a UV/ozone lamp (ProCleaner^{TM} *Plus*, Bioforce Nanosciences) during at least 45 minutes. This lamp emits UV light at $\lambda_1 = 185$ nm and $\lambda_2 = 254$ nm. λ_1 light dissociates O_2 molecules, producing ozone O_3, whereas λ_2 light dissociates organic chemical molecules on the surface. The residues of this reaction and ozone produce volatile molecules (CO_2, H_2O, N_2) which are eliminated in the hood [137].

5.3.1.2 Cleaning with Piranha

Piranha solution is a mix of sulfuric acid 99 % (H_2SO_4) (ACS reagent, Sigma Aldrich) and hydrogen peroxide 30 % (H_2O_2) (for analysis). We usually take a 3:1 ratio, freshly prepared before use. Piranha solutions have a dual role: they are strong acidic and oxidizing agents, so that they dissolve many organic residues, and they hydroxylate surfaces (adding OH groups) [138]. It is therefore dangerous to manipulate because it can generate severe chemical burns. The reaction between H_2SO_4 and H_2O_2 being very exothermic, one has to prepare the solution carefully, by gently pouring sulfuric acid into hydrogen peroxide in a proper glassware. The cleaning has to be done under a hood, with thick gloves, a visor and an apron in addition to the regular lab equipment. The surface is put inside the piranha between 20 minutes and 1 hour, depending on its dirtiness. It is then thoroughly rinsed with distilled water. After cleaning, the piranha solution has to be put in a dedicated chemical trash, labeled accordingly.

5.3.1.3 Etching of silicon wafers with hydrofluoric acid

It is sometimes necessary to regenerate completely the surface. This is done using hydrofluoric acid, which is a solution of hydrogen fluoride (HF) that dissolves the oxide layer. This operation has been done with the help of Nathalie Bardou at C2N, using the following process:

- we put the surface in a PTFE beaker and put it during 2 minutes in a 7:1 Buffer Oxide Etch (BOE) (Sigma Aldrich) which is a HF solution buffered with ammonium fluoride.
- we plunge the beaker in flowing milliQ water during 1 minute.
- we plunge it in Piranha solution 5:1 ratio during 5 minutes to regenerate the oxide layer.
- we dry the surface with nitrogen

This procedure is repeated twice. Chemical burns of the skin by HF are extremely dangerous, therefore it is mandatory to manipulate it with all the regular personal protective equipments (PPE) plus specific gloves, an apron and a visor, close to a source of water and close to calcium gluconate, which is an antidote in case of HF burns.

5.3.2 Surface functionalization

5.3.2.1 Adsorption

The easiest way to attach polymer chains onto surfaces is to let the polymer spontaneously adsorb onto the substrate. This method is used either to adsorb polystyrene from PS/DEP solutions or polydimethylsiloxane from PDMS melts. The process is always the same: we take a freshly cleaned silicon wafer, and we deposit the polymer on it, with a spatula. This is done in a white room, under a laminar flow hood. We incubate the wafer at a temperature T during a certain time Δt. Then, we rinse it thoroughly with toluene in order to remove non-anchored chains, we put it inside toluene for 1 hour, remove it from toluene, and dry it under vacuum for at least 3 hours. In case of PDMS, the thickness h of the adsorbed layer reaches high values, and therefore toluene is easily trapped inside the layer and difficult to remove. Therefore, for $h > 10$ nm, we let it dry under vacuum at least one night.

5.3.2.2 Grafting a PS brush

The *grafting-to* method is a two-steps process: first, the surface is silanised using a specific silane, and then, amino-terminated PS chains are grafted to the exposed silanes.

Silanisation Silanes self-assembled monolayers (SAMs) are popular chemicals, allowing to functionalize various surfaces. Silanes have usually a tail and head structure, the tail being an organosilicon of the type SiR_4 and the tail can vary (linear carbon chains or more complicated structures). The choice of silane depends on the desired use of the surface, and it conditions the recipe used to prepare the coating. A good silanisation requires forming a single homogeneous layer of silane over the whole surface. This is a real experimental challenge, and every team - or even every experimentalist - has its own recipe to form a nice silane coating. In our case, we want to use a silane that enables us to covalently bond NH_2-terminated PS molecules on it through the opening of the epoxy head. The silane we use is 3-Glycidyloxypropyl trimethoxysilane (Sigma Aldrich) (see Fig. 5.5).

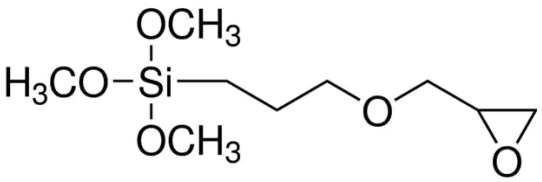

Figure 5.5: 3-Glycidyloxypropyl trimethoxysilane.

We use vapour phase silanization which requires very clean and dry glass wares. The surfaces are cleaned using Piranha. We put our sample inside a desiccator flushed with argon. We deposit a few drops of silane at the bottom of the desiccator, below the surfaces. We put the desiccator under vacuum, and we heat it using a hot plate and a heat gun, until all the silane has been evaporated (we can see vapours condensing on the walls of the desiccator). This can take between 10 and 30 minutes, depending on the size of the desiccator and on the temperature. Once the vapour has reached the top of the desiccator, we stop heating and let the whole thing rest during the night.

Then, the surface is thoroughly rinsed with toluene (reagent, Sigma Aldrich) in an ultrasonic bath during 5 minutes. Finally, we rinse it with toluene and isopropanol (reagent, Sigma Aldrich), and dry it with argon or nitrogen between each step.

Grafting-to Using the reactivity of (3-Glycidyloxypropyl) trimethoxysilane with amine terminations of PS, we can graft PS chains onto our silanised surface. The protocol starts right after the end of the silanisation. We put a 10 mg/mL solution of PS amino-terminated (Polymer Source) inside THF or toluene (reagent, Sigma Aldrich) on the whole silanised surface. We dry it under vacuum at 130 °C during $3-4$ hours. We finally rinse it in toluene, and we flush it with argon. The grafting density of the brush is measured by ellipsometry and/or X-ray reflectivity, as described in the following section.

5.4 Reflectivity techniques

5.4.1 General description and calculations

During this thesis, we have used three different reflectivity techniques, namely ellipsometry, X-ray and neutrons reflectivity. Since the calculations are very similar for these three techniques, we will derive the main ones in this section.

Reflection on a dioptre. We consider an interface between a medium 0 and a medium 1 characterised by their index n_0 and n_1 which are linked with the nature of the wave (neutrons or photons). A plane wave hits the surface with an angle i_0 with respect to the normal[f]. This wave can be a polarised light wave (ellipsometry), a X-ray wave (X-Ray reflectivity) or the wave function of neutrons (neutron reflectivity). In any case, when the wave hits the interface, some of it can be reflected in medium 0 and the rest is transmitted in medium 1 with an angle i_1 with respect to the normal. We can define an amplitude reflection coefficient r_{01} and an amplitude transmission coefficient t_{01} which describe the attenuation of the reflected and transmitted waves with respect to the initial one, respectively. If the wave is characterised by a quantity E (typically the electric field for light propagation) and if we call $E_{0,i}$, $E_{0,r}$ and $E_{1,t}$ the initial, reflected and transmitted waves, we have $r_{01} = \frac{E_{0,r}}{E_{0,i}}$ and $t_{01} = \frac{E_{1,t}}{E_{0,i}}$. These coefficients can be expressed as a function of the parameters of the system, depending on the technique used. They will be specified explicitly for each of the three techniques.

Reflection on a thin film. Now we consider a thin film of thickness d and index n_1 which is sandwiched between medium 0 (of index n_0) and medium 2 (of index n_2). The quantity we are interested in is the total amount of reflected beam. As before, the incident beam hits the surface with an angle i_0 with respect to the normal of the interface. Part of it is directly reflected, part of it is transmitted. The transmitted beam hits the second interface, part of it is transmitted (and will not contribute to the total reflected intensity), and the rest is reflected. Then it hits again the first interface, and again, part of it is transmitted, which generates another contribution to the total reflected intensity,

[f] For X-ray reflectivity, the incident angle θ is defined as $\pi/2 - i_0$.

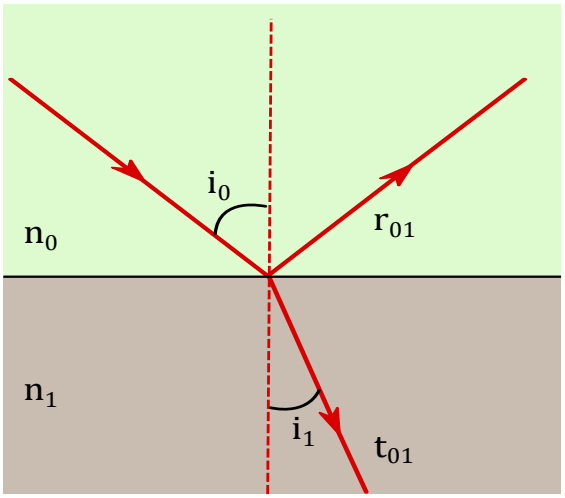

Figure 5.6: Reflection and refraction on a dioptre.

and the rest is reflected inside the film etc. Thus, the total reflected light contains the contribution of an infinite number of beams, which have undergone various numbers of transmission/reflection/transmission processes at the two interfaces. Two consecutive emerging beams have both a phase and an intensity differences. The phase difference is 2Φ with $\Phi = \frac{2\pi}{\lambda} d(n_1^2 - n_0^2 \sin^2 \Phi_0)^{1/2}$. In terms of intensities, the beam directly reflected has an intensity attenuated by a factor r_{01}, and then all the beams have an intensity attenuated by $t_{01}t_{10}$ and a factor $r_{12}^m r_{10}^{m-1}$ for the $m-th$ reflected beam. Thus, the total reflection coefficient R writes:

$$R = r_{01} + \sum_{m=1}^{+\infty} t_{01} t_{10} r_{10}^{m-1} r_{12}^m e^{-2m\mathrm{j}\Phi} \tag{5.5}$$

with $\mathrm{j}^2 = -1$. This is a geometric sum of common ratio $r_{10}^{-1} r_{12} e^{-2\mathrm{j}\Phi}$, and we can easily show that $r_{10} = -r_{01}$ and $t_{01}t_{10} = 1 - r_{01}$ and thus, we can calculate explicitly R:

$$R = \frac{r_{01} + r_{12} e^{-2\mathrm{j}\Phi}}{1 + r_{01} r_{12} e^{-2\mathrm{j}\Phi}} \tag{5.6}$$

with $\Phi = \frac{2\pi}{\lambda} d(n_1^2 - n_0^2 \sin^2 i_0)^{1/2}$.

Reflection on a multilayered film. The value of R (or R_p/R_s for ellipsometry) contains all the information about the system. Yet, it is usually impossible to inverse the system and to calculate exactly the desired quantities from the measurement of R. In this case, one has to postulate a model with a certain number of layers (each of them being described by a certain number of parameters), calculate the corresponding reflectivity, and adjust the parameters to match the calculated and the measured reflectivities. Of course, the larger the number of parameters, the more difficult it is to find the good adjustments. Thus, it is paramount to really think about a realistic description of the system before struggling with the fits.

5.4.2 Ellipsometry

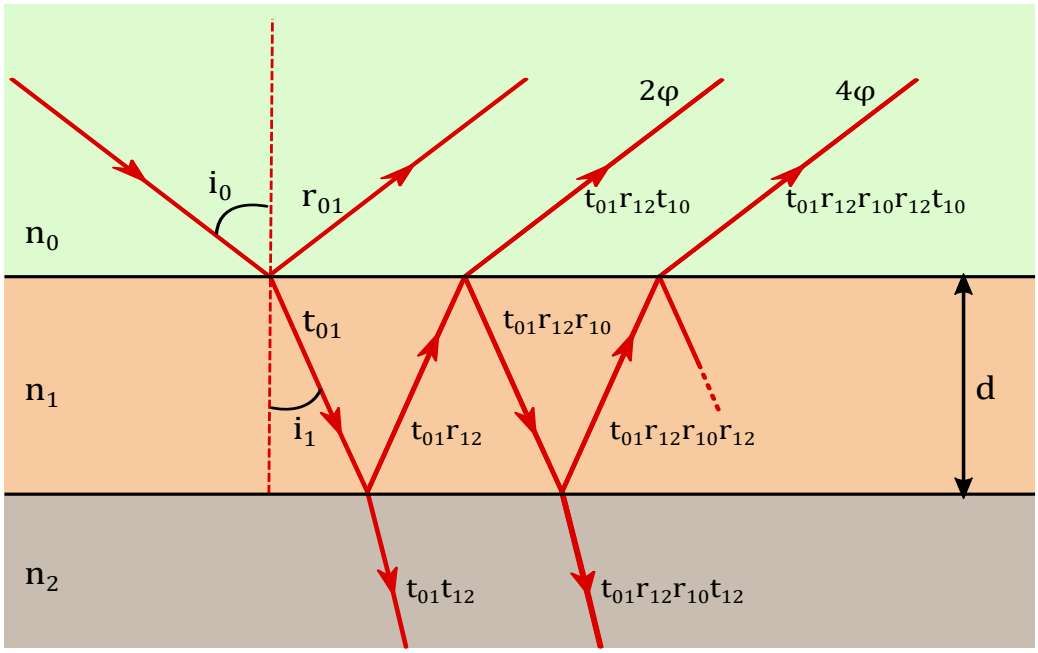

Figure 5.7: Successive reflection and refraction for a one-layer system.

Ellipsometry is a powerful technique to quickly characterize transparent thin films, especially when they are deposited on a reflective flat substrate [139]. The principle is to send an elliptically polarised light on the sample and measure the polarisation of the light after reflection on the surface. The comparison between the initial and the final polarisation allows determining the thicknesses and the refraction indexes of the different layers deposited on the substrate.

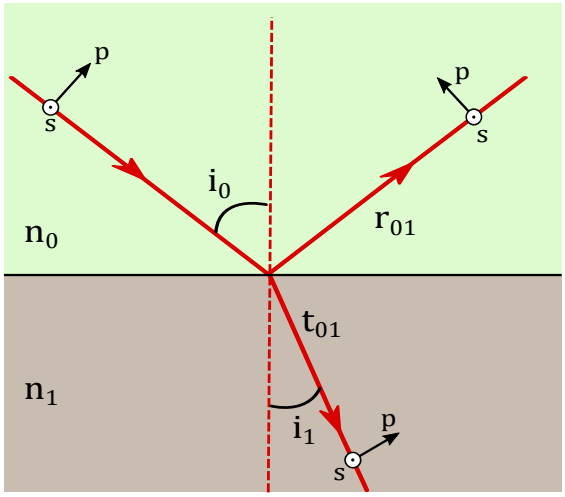

Figure 5.8: Reflection of a polarized light on a dioptre. p and s denotes the parallel and perpendicular vectors with respect to the plane of incidence, so that $\vec{p} \wedge \vec{s}$ is in the same direction and sense than the direction of propagation.

Reflection on a dioptre. We will start by the case of a dioptre: a polarised light beam hits a flat interface delimiting two semi-infinite isotropic media 0 and 1. The wave is described by its propagating electric field $\overrightarrow{E}$ which we can decompose into two *eigenstates* s and p: $\overrightarrow{E} = \overrightarrow{E}_s + \overrightarrow{E}_p$. We write $(E_{i,s}, E_{i,p})$ and $(E_{r,s}, E_{r,p})$ and $(E_{t,s}, E_{t,p})$ the complex amplitudes of the two components of the incident, reflected and transmitted waves, respectively. Matching conditions of the tangential $\overrightarrow{E}$ and $\overrightarrow{H}$ fields (with $\overrightarrow{H}$ the magnetic field) yields the following complex amplitude reflection and transmission coefficients:

$$\begin{cases} r_s \equiv \frac{E_{r,s}}{E_{i,s}} = \frac{n_1 \cos i_0 - n_0 \cos i_1}{n_1 \cos i_0 + n_0 \cos i_1} \\ r_p \equiv \frac{E_{r,p}}{E_{i,p}} = \frac{n_0 \cos i_0 - n_1 \cos i_1}{n_0 \cos i_0 + n_1 \cos i_1} \\ t_s \equiv \frac{E_{t,s}}{E_{i,s}} = \frac{2 n_0 \cos i_0}{n_1 \cos i_0 + n_0 \cos i_1} \\ t_p \equiv \frac{E_{t,p}}{E_{i,p}} = \frac{2 n_0 \cos i_0}{n_0 \cos i_0 + n_1 \cos i_1} \end{cases} \tag{5·7}$$

Ellipsometry measurement gives access to the ratio: $\rho = \frac{r_p}{r_s}$ which is often written $\rho = \tan \psi e^{\mathrm{j}\Delta}$ where ψ and Δ are called the **ellipsometric angles**.

Reflection on a thin film. Now, we consider a thin film of thickness d and index n_1 sandwiched between the two semi-infinite isotropic media 0 and 2. As before, we can define complex amplitude reflection and transmission coefficients for the two interfaces ($(0,1)$ and $(1,2)$).

Using Eq. 5.6, we can show that the total reflection coefficients are:

$$\begin{cases} R^p = \frac{r_{01}^p + r_{12}^p e^{-2j\phi}}{1 + r_{01}^p r_{12}^p e^{-2j\phi}} \\ R^s = \frac{r_{01}^s + r_{12}^s e^{-2j\phi}}{1 + r_{01}^s r_{12}^s e^{-2j\phi}} \end{cases} \tag{5·8}$$

with $\phi = \frac{2\pi}{\lambda} d (n_1^2 - n_0^2 \sin^2 i_0)^{1/2}$.

Experimentally, we measure the ratio ρ which is defined as before:

Ellipsometric angles

$$\rho \equiv \frac{R^p}{R^s} \equiv \tan \psi e^{j\Delta} \tag{5·9}$$

Ψ and Δ are functions of λ, i_0, n_0, n_1, n_2 and the thickness of the film, d. If we know everything except d, with a measurement at a single incidence angle i_0, we can inverse this system and find the value of the thickness of the film, d (see [140], chapter 4). If several parameters have to be measured at the same time, one has to do the measurement at various i_0 and/or various λ. In practice, we will always be looking for d only, but since our ellipsometer allows to easily vary the angle of incidence, we vary the range of i_0. The sensitivity of the measurement being larger when i_0 is near the Brewster angle i_B, we perform the measurement near $i_0 = i_\mathrm{B}$.

Material	$n(658\,\text{nm})$	Reference
PS	1.586	[141]
PDMS	1.400	[128]
SiO_2	1.456	[142]
Si	$3.833 + 0.014j$	[143]

Table 5.3: Complex refractive indexes at room temperature for $\lambda = 658$ nm for the materials used here.

Nulling ellipsometry. We use an EP3 ellipsometer from Accurion, with a laser at $\lambda = 658$ nm. On the path of the LASER beam, there is a polariser, a quarter-wave plate, the sample, an analyser and a CCD detector. We can control independently the three angles P, C and A. The angles P and C are adjusted so that the beam reflected on the sample is linearly polarised, and then the angle A is varied until it blocks completely the beam. This is the so-called *nulling ellipsometry*.

In reality, there are four possible triplets (P, C, A) for which we can obtain extinction. The measurement of one of these triplets is sufficient to characterise the sample, but it is also possible to find the four triplets to have an even better description of the sample. This is the so-called *four-zones* method. Considering the amount of measurements we have to do, we only do the *one-zone* method, which is quicker. We use a fixed angle $C = 45°$, and we vary the pair (P, A) until we reach extinction. The measurement of the triplet (P, C, A) at which we have extinction allows us to measure the values of Ψ and Δ.

Example. With this technique, we measure both Ψ and Δ as a function of the angle of incidence (AOI). A typical example is shown in Fig. 5.9. Silicon wafer are themselves made of bulk crystalline silicon and an oxyde layer on top of thickness around 2 nm. We measure the thickness of this layer for all the wafers used prior to each experiment. The complex refraction indexes used are given in Table 5.3. Thus, the only unknown of our system is the thickness of the adsorbed layer d, which is easily obtained by fitting the measurements of $\Psi(i_0)$ and $\Delta(i_0)$. The fit is done using the *refellips* package in Python [144] which uses the *scipy* package for data fitting.

5.4.3 X-ray reflectivity

Very similarly to ellipsometry, X-ray reflectivity is a powerful technique to study surfaces. The experiment is a bit more delicate to do compared to ellipsometry, but it has the great advantage to give access to both thicknesses and roughnesses. We use a Xeuss 2.0 from XENOCS with a Cu source emitting X-ray at $\lambda = 1.54\,\text{Å}$. X-ray interact with the electronic clouds of atoms, and thus the scattering length density, which governs the index of the material, depends on its electronic density. We use a $\theta/2\theta$ configuration, illustrated in Fig. 5.10. We measure the specular reflectivity R as a function of the angle of incidence θ.

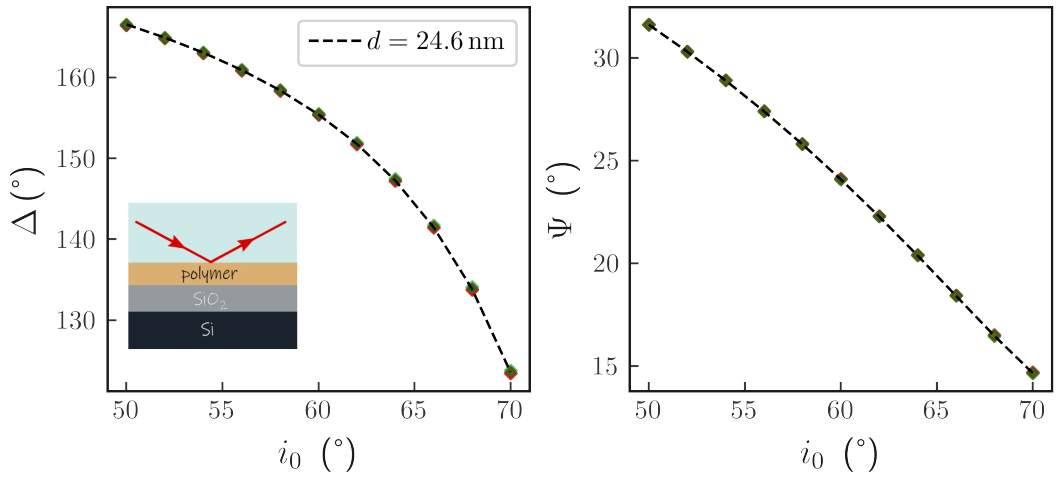

Figure 5.9: Ellipsometric angles Ψ and Δ as a function of the incidence angle i_0 for a silicon wafer adsorbed with PDMS. Diamonds represent experimental measurements, each color corresponds to a different location on the surface. The black dotted line is a fit assuming a index 1.400 for PDMS and resulting in a thickness $d = 24.6$ nm for the adsorbed layer.

5.4.4 Neutron reflectivity

The calculations for X-ray and neutron reflectivity are very similar. The formalism is exactly the same, the only difference is that the scattering length density (SLD) for X-ray depends on the electronic density of the material, whereas neutrons interact with the atomic nucleus, and thus the neutronic SLD depends on the isotope. This is the great advantage of neutron reflectivity: we can change the isotopes to change the contrast. In addition, we use a $\theta/2\theta$ configuration for the X-ray reflectivity while we use Time-of-Flight (TOF) for the neutron reflectivity. Since we discuss in depth neutron reflectivity in Chapter 6, we derive these calculations with the formalism of neutron in that chapter, together with the results of the experiment. The derivation is very similar to what is written here, except that for light reflectivity, the wave is an electromagnetic wave obeying the Maxwell equations while for neutron reflectivity, the propagating wave is the wave-function ψ of neutrons, obeying the Schrödinger equation. In both cases, we can write an index n, which depends on the coupling between the propagating electromagnetic field with electronic clouds of atoms in the case of light reflectivity, whereas n is related to the strength of the interaction between neutrons and the nuclei of atoms in the case of neutron reflectivity.

5.5 Dielectric Spectroscopy

The last chapter of this manuscript deals with adsorption kinetics of PDMS melts. These measurements are compared to relaxation measurements obtained using dielectric spectroscopy (DS) on PDMS thin films. These measurements were performed by Erik Thoms and Simone Napolitano at ULB, Bruxelles, Belgium. The experimental protocol is the same as the one described in [145]. In a nutshell, a PDMS thin film is sandwiched between two aluminium electrodes. The bottom electrode is a 50 nm thick film (oof roughness below 2 nm) deposited on a glass substrate by thermal evaporation of aluminium.

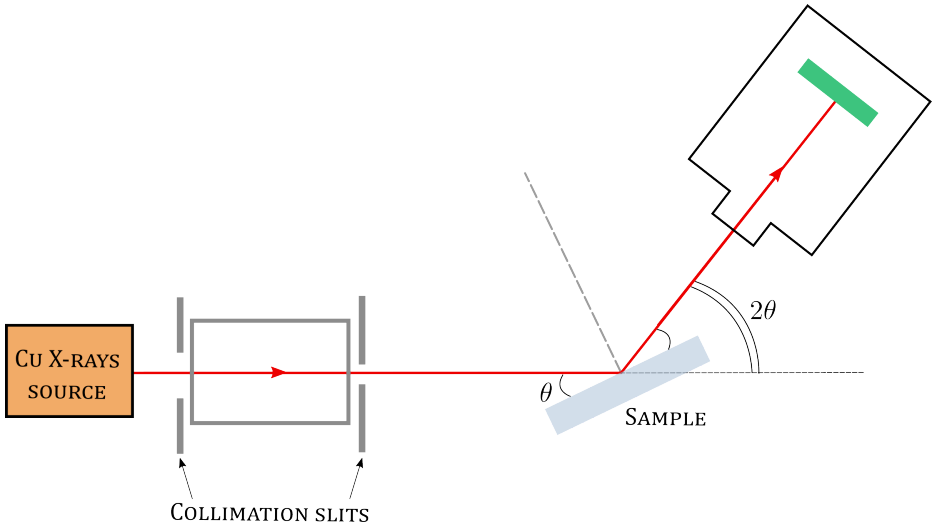

Figure 5.10: Principle of X-Ray reflectivity in the $\theta/2\theta$ configuration.

The PDMS film is obtained by spin-coating at 3000 rpm a concentrated solution of PDMS in n-heptane. The cell is then closed by the top aluminium electrode. The thickness h of the polymer film is obtained by the measurement of the capacitance at room temperature, assuming a parallel plate geometry:

$$h = \epsilon_\infty \epsilon_0 S / C_\infty \tag{5.10}$$

with C_∞ and ϵ_∞ the capacitance of the film and the dielectric constant of the polymer, respectively, ϵ_0 the vacuum permittivity and S the surface area of the electrodes.

Then, an impedance analyser measures the complex capacitance, which yields dielectric spectra $\epsilon(f) = C(f) h \epsilon_0^{-1} S^{-1}$.

Chapter 6

Depletion and adsorption of polymer solutions near a solid surface with neutrons reflectivity

Contents

As discussed in the introduction, slippage depends on the behaviour of the liquid near the substrate. Indeed, the presence of the wall affects the concentration profile of the liquid at its vicinity. Thus, a precise measurement of the near-surface concentration profile is necessary in order to understand slip measurements. To this end, this chapter is devoted to the study of PS/DEP solutions near solid surfaces using neutrons reflectivity. The results presented here have been submitted for publication. The preprint is accessible on Arxiv [146]. These results will be useful to discuss the slip measurements of Chapter 7.

6.1 State of the art about adsorption and depletion

6.1.1 Static

As explained in the introduction, polymers at interfaces can behave in two different ways: either there is an attraction between the chains and the wall, resulting in an adsorption of chains on the surface, or there is a repulsive interaction between the two, leading to a depletion layer at the interface. Both cases happen on very small length scales (a few tens of nanometres) so that only a few techniques are able to measure concentration profiles at these scales. Since adsorption is described in depth in Chapter 8, here we focus mainly on depletion.

The first hint of the existence of depletion is the flocculation of colloidal particles immersed in a solution containing non-adsorbing polymers [147–149]. This is attributed to the existence of an osmotic attraction between the particles, due to a depletion of polymer chains in between them if they are close enough. At the end of the 70s, Joanny, Leibler and de Gennes [150] have derived a scaling argument for the depleted concentration profile near a solid wall: $\phi(z) \propto z^{5/3}$, with a typical extent around the correlation size ξ of the polymer solution. Further away from the wall, the concentration smoothly reaches the bulk concentration ϕ_b at larger distances.

This theoretical prediction had called for experiments, and the first direct measurement of polymer depletion near a solid surface was achieved by Allain *et al.* [151] in 1982. They studied a dilute solution of PS in ethyl acetate near a silanized glass surface using evanescent waves microscopy and measured a depletion layer of size 4.5 nm. Yet, it is delicate to relate this size with the R_g (11 nm) of the solution, since the penetration depth in their experiment was large compared to the coil size.

A few years later, Marra *et al.* [152] inferred again a depletion, this time with SFA[a] on a sodium polystyrene sulfonate (PSSNa) solution near a mica surface, having an unexpected large electrical double layer. During the same decade, Chauveteau *et al.* [153] measured anomalously low viscosities of polymer solutions in capillaries. The anomaly can be resolved by assuming the existence of a low-viscosity layer near the wall, and then a proper fit of their data resulted in a measurement of the size of the depletion layer, which is related to the correlation length of the polymer solution. In 1991, Lee *et al.* [86] have used neutrons reflectivity at the liquid-air interface to show the existence of a depletion of polystyrene chains at the interface between air and a PS/toluene semi-dilute solution. They experimentally verified for the first time the scaling law $\delta \propto \phi^{-3/4}$ as predicted by de Gennes *et al.* [83,150]. In the case of a polyelectrolyte near a charged surface, if both share the same sign, there is an additional contribution to depletion due to the electrostatic repulsion, which depends on the Debye length [154]. Thus, if the charges are poorly screened, the size of the depletion layer can be much larger compared to the neutral case.

6.1.2 Dynamics

[a] surface force apparatus

The above description has been derived for non-flowing liquids. Another part of the topic is to describe the effect of the flow on the adsorbed/depleted layer. Here, we focus on semi-dilute polymer solutions.

Effect of the flow on brushes and adsorbed chains. For a solvent flowing on a brush, it has been reported theoretically [155,156] and experimentally [157] that the thickness of the brush increases when the flow is strong enough, and more precisely, when the shear rate $\dot{\gamma}$ is larger than the typical relaxation time τ of the blobs of the brush, which corresponds to a Weissenberg number $\mathrm{Wi} \equiv \dot{\gamma}\tau > 1$. This swelling is attributed to the chain stretching because of the flow. In addition, the Harden and Cates model enhances that the shear is not uniform along the brush. In the case when the brush is exposed to a flowing semi-dilute polymer solution, Korolkovas *et al.* [158] have shown that at high Wi, the thickness of the brush collapses because of disentanglements between bulk chains and grafted chains. In their case, the shrinking of the brush is proportional to the square of the applied shear rate, and they observe the same behaviour for both a long-sparse and a short dense brushes.

Effect of the flow on depleted layers. The case of a depleted layer has been less extensively studied under flow, because the low contrast between the depleted layer and the solution makes the measurement difficult. A few theoretical [159,160] and experimental [87] works have reported a depletion layer becoming thicker when the Weissenberg number is increased. Ausserré *et al.* [85, 87] have used a dumbbell model, which aligns with the flow at low flow rates and starts to rotate quickly at high flow rates, so that the volume occupied by the dumbbell is larger, and thus it flows further away from the wall. This argument has also been used by Park *et al.* [161], who measure the depletion layer of a polystyrene sulfonate (PSS) solution near fused silica, using STED-anisotropy imaging. Even if one has to be cautious regarding their derivations of the scaling laws for the relaxation times and concentration regime, they do observe a change in the interfacial anisotropy with the flow, from which they derive a shrinking of the thickness of the depletion layer, especially for Wi above 1.

Following all these considerations, we aim at studying the evolution of the interfacial structure of a semi-dilute entangled PS/DEP solution up to high Weissenberg (Wi) number, without being bothered by the Weissenberg effect. To this end, we have designed a cell which can carry Poiseuille flows at high Weissenberg numbers during a neutrons reflectivity experiment. In Section 6.2, we introduce the principle of neutrons reflectivity (NR). In Section 6.3, we present the materials used and the cell designed. The first results are shown in Section 6.4. We show that there is a depletion layer at the interface between the solution and the sapphire surface. In particular, we look at the effect of the volume fraction ϕ on the depletion layer. Then, in Section 6.5, we show that a depletion layer is not incompatible with adsorption. Finally, in Section 6.6, we look at the effect of the flow on the near-surface concentration profile.

6.2 Neutron reflectivity: introduction and principle

6.2.1 A brief history of neutrons reflectivity

The discovery of nuclear fission dates back to the late 30s, following the work of Otto Hahn, Fritz Strassmann [162] and Lise Meitner[b]. Sadly, some scientists realised that this discovery might be used to create nuclear weapons, and conveyed this information to the USA president F. Roosevelt, who launched a secret research program about nuclear weapon, under the name "Project Manhattan". It was in this context that the first high-flux reactor, X-10, was created in Oak Ridge in 1943. At the end of the war, X-10 became dedicated to (disinterested and non-lethal) scientific research. In 1972, the highest neutron flux was achieved with the creation of the Institut Laue-Langevin (ILL) in Grenoble, France. Since then, neutron scattering techniques, and especially neutrons reflectivity, have been developed and used in many different fields of science, including soft matter. The ILL still has one of the most powerful neutron flux in the world.

The formalism of neutrons reflectivity is actually very close to the one used for light reflectivity. The principle is the following: a beam of neutrons is sent onto a sample with an incident angle θ, and the reflected beam intensity is measured by a He^3 detector. Similarly to light, we can define a neutronic refractive index, which depends on the material. Thus, at an interface between two different media, the amount of refracted (and thus reflected) neutrons depends on the composition of the two materials. If there is a variation of chemical composition near the interface, the measured reflectivity contains information on the detailed composition of the medium perpendicular to the surface, and thus neutrons reflectivity is a powerful technique to study concentration profiles near interfaces on a typical range of $0.5 - 500$ nm in thickness. In addition, it has the great advantage of being non-destructive, and contrary to light reflectivity, it allows contrast variation through the use of isotopes. In the following, we describe the physics behind neutrons reflectivity. We will neglect magnetic properties of neutrons, and we will assume that there is no adsorption of neutrons by the medium they pass through.

6.2.2 Neutron interaction with matter

Contrary to X-rays (which interact with electrons), neutrons interact with nuclei of atoms. This interaction can be modelled by a sum of point-like Fermi pseudo-potentials, centred on each atom i:

$$V_{\mathrm{F}} = \frac{2\pi\hbar^2}{m} \sum_i b_i \delta(r - r_i) \tag{6.1}$$

where $\hbar$ is the reduced Planck constant, m is the mass of a neutron, $\delta(r)$ is the Dirac function, r_i is the position of the nucleus of the i atom and b_i is its coherent scattering length. The latter describes the amplitude of interaction between a neutron and the nucleus. In general, it is a complex quantity, and the imaginary part accounts for adsorption of neutrons by the nucleus. Here, we make the hypothesis that adsorption is negligible, and thus b_i can be considered as a real number.

It is worth mentioning that b_i can be either positive or negative, and that its value

[b] Lise Meitner, even if she had an important role in the discovery, was not even mentioned in the first publication, and - contrary to Otto Hahn - she never won the Nobel Prize for it (although she had been nominated 49 times for it).

is really dependent on the considered isotope. In particular, for hydrogen, we have $b_{\mathrm{H}} = -0.374\,.10^{-12}$ cm while for deuterium - which is the isotope of hydrogen - we have $b_{\mathrm{D}} = 0.667\,.10^{-12}$ cm. This is one of the reason why Neutrons Reflectivity (NR) is a powerful technique: we can play with the contrast using either hydrogenated or deuterated materials, or a mix of the two. Since chemical interactions are mainly dictated by electronic properties, using perdeuteration[c] allows rendering contrast between species without significantly altering their chemical interactions.

Since the typical length scales probed by NR is much larger than an atom ($1 - 1000$ nm), in the following, we will consider a mean Fermi potential V_{F} which is the average of the Fermi potential over a homogeneous layer of atoms:

$$V_{\mathrm{F}} = \frac{2\pi\hbar^2}{m}\mathcal{N}b \equiv \frac{2\pi\hbar^2}{m}\mathrm{SLD} \tag{6.2}$$

where $\mathcal{N}$ is the number of atoms per volume unit, b their coherent scattering length, and we define the Scattering Length Density (SLD) as $\mathrm{SLD} \equiv \mathcal{N}b$.

6.2.3 Definition of the neutronic refractive index n

Let us consider a beam of neutrons propagating in air with a wavelength λ. Their energy is $E = \frac{\hbar^2 k^2}{2m}$ where $k = \frac{2\pi}{\lambda}$ is the corresponding wave-vector and ψ is their wave function. We now put a flat homogeneous semi-infinite material on their way, and we write z the distance perpendicular to the surface of the material, imposing $z = 0$ at the interface. In both media, propagation of neutrons can be described by a wave-function ψ which obeys the Schrödinger's equation:

$$\frac{\hbar^2}{2m}\frac{d^2\psi_z}{dz^2} + (E - V_{\mathrm{F}})\psi_z = 0 \tag{6.3}$$

Now, at the interface, we consider that there is an elastic scattering, meaning that there is no exchange of energy. Therefore, we can write the conservation of energy:

$$\frac{\hbar^2 k^2}{2m} = \frac{\hbar^2 k_n^2}{2m} + V_{\mathrm{F},n} \tag{6.4}$$

with $k_n = \frac{n2\pi}{\lambda}$ the wave-vector of neutrons in the material and $V_{\mathrm{F},n} = \frac{2\pi\hbar^2}{m}\mathrm{SLD}$ is the potential created by atoms of the material. From this equation, we can calculate the index of refraction n of the material, defined as:

$$n^2 \equiv |\frac{k_n}{k}|^2 = 1 - \frac{\lambda^2}{\pi}\mathrm{SLD} \tag{6.5}$$

We can see that the refractive index n depends on the wavelength λ of the neutrons beam, and it is a decreasing function of the SLD of the material.

6.2.4 Reflection and refraction at an interface

Assuming that our interface is a dioptre, it is possible to write the Snell-Descartes law of refraction between two homogeneous media of indexes n_1 and n_2:

[c] replacement of all the hydrogen atoms of the molecule by a deuterium atom.

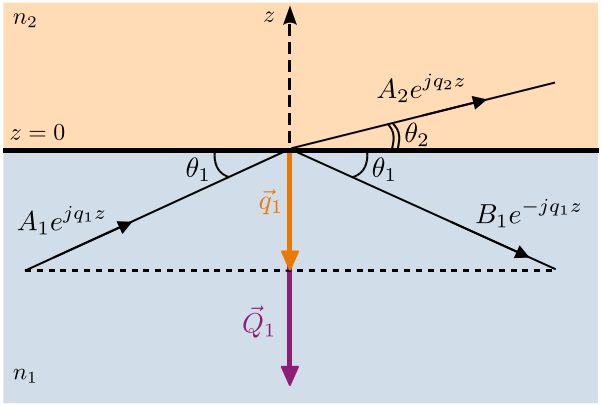

Figure 6.1: Reflection and refraction at an interface. An incident neutron beam propagates in the medium 1 and hits the interface in $z = 0$ with an angle θ_1 with the surface. A part of the beam is reflected and propagates in medium 1 with the same angle and in the direction of decreasing z. The other part is refracted inside medium 2 with refracted angle $\theta_2 = \arccos \frac{n_1}{n_2} \cos\theta_1$ (Snell-Descartes' law) and propagates in the direction of increasing z. We define $Q_1 \equiv 2q_1$, the scattering vector.

$$n_1 \cos\theta_1 = n_2 \cos\theta_2 \tag{6.6}$$

where θ_1 (θ_2) is the angle between the interface and the incident beam (refracted beam).

Total reflection One can see that if $\frac{n_2}{n_1} < 1$, $\exists\, \theta_c / \cos\theta_c = \frac{n_2}{n_1}$. For $\theta < \theta_c$, there is total reflection: the neutron beam is not transmitted inside medium 2 but only reflected at the interface. Using the previous equations, we can derive:

$$\sin\theta_c = \lambda\sqrt{\frac{\mathrm{SLD}_2 - \mathrm{SLD}_1}{\pi}} \tag{6.7}$$

Thus, for a given wavelength λ of the beam, the value of θ_c only depends on the contrast, *i.e.* on the difference of SLD between the two media. Therefore, if the SLD of one of the material is known, the measurement of θ_c gives access to the SLD of the other material.

Definition of the reflection coefficient R Assuming that the interface is located at $z = z_0$ and that the two media are homogeneous, a general solution of the Schrödinger equation (Eq. 6.3) in medium i is the superposition of two plane waves, one propagating in the $+z$ direction (of amplitude A_i) and the other propagating in the $-z$ direction (of amplitude B_i):

$$\begin{cases} \psi_1(z) = A_1 e^{jq_1 z} + B_1 e^{-jq_1 z} & \text{for } z < z_0 \\ \psi_2(z) = A_2 e^{jq_2 z} + B_2 e^{-jq_1 z} & \text{for } z > z_0 \end{cases} \tag{6.8}$$

with $q_i \equiv |k_i| \sin\theta$ is the projection of $\vec{k}_i$ on the direction perpendicular to the interface, and $j^2 = -1$. The reflectivity at this interface $(1, 2)$ is defined by:

$$R_{1,2} \equiv |r_{1,2}|^2 \equiv \frac{|B_1|^2}{|A_1|^2} \tag{6.9}$$

where $r_{1,2}$ is the complex reflection coefficient, which can be calculated using the continuity conditions of the wave and its derivative at the interface, written as:

$$\begin{cases} \psi_1(z_0) = \psi_2(z_0) \\ \psi_1'(z_0) = \psi_2'(z_0) \end{cases} \tag{6.10}$$

Fresnel reflectivity In the case where both media are semi-infinite and the interface between the two is perfectly smooth, the reflectivity coefficient is called the **Fresnel reflectivity** R_F, and is given by:

$$R_\mathrm{F} \equiv |r_{1,2}^\mathrm{F}|^2 = \frac{|q_2 - q_1|^2}{|q_2 + q_1|^2} = \frac{|1 - \sqrt{1 - (q_c/q)^2}|^2}{|1 + \sqrt{1 - (q_c/q)^2}|^2} \tag{6.11}$$

with $q_c \equiv \frac{2\pi}{\lambda} \sin\theta_c$ the critical scattering vector and $q \equiv q_1 = 2\pi/\lambda$. One can see that $R_\mathrm{F}(q < q_c) = 1$ *i.e.* the reflectivity has a plateau at small q values. This is illustrated in Fig. 6.2 (blue curve) where we plot the simulated SLD profile and the corresponding Fresnel reflectivity for a perfectly smooth interface between sapphire and D_2O (SLD = 5.77 and $6.36\,10^{-6}$ Å^{-2}, respectively). We observe a plateau at small $Q = 2q$ values because $\mathrm{SLD}_{D_2O} > \mathrm{SLD}_\mathrm{sapphire}$.

In the case of a more complex interface, the calculation of R requires a more detailed analysis. We will give the calculation procedures of R first for a rough interface and then for a multilayered material. In practice, the two can be combined.

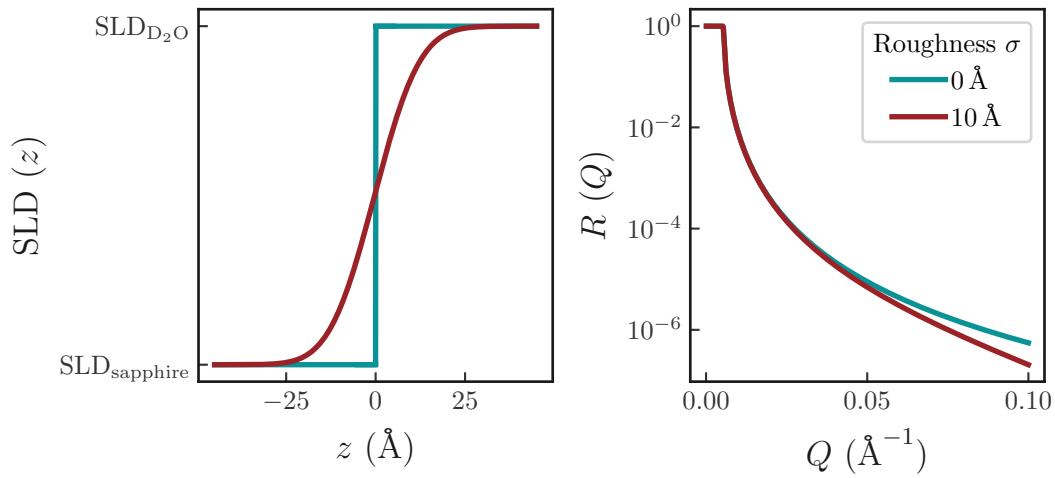

Figure 6.2: Simulated SLD profiles (left) and corresponding calculated reflectivity curves (right) of the sapphire/D_2O interface. Blue: perfectly smooth interface. Red: interface with a roughness $\sigma = 10$ Å.

Roughness and interdiffusion Roughness describes the fact that a given interface is not infinitely flat, and thus the distance from this interface is not perfectly defined. Interdiffusion describes the fact that, at an interface between two materials, there is a slight mutual diffusion of the two media inside each other. They are both modelled by an error function in the postulated SLD profile:

$$\mathrm{SLD}(z) = \mathrm{erf}((z - z_{i,i+1})/\sigma_{i,i+1}) \tag{6.12}$$

where $(i, i+1)$ is the considered interface, $z_{i,i+1}$ is the position of the interface and $\sigma_{i,i+1}$ is a parameter describing the roughness of this interface. erf is the error function defined by $\mathrm{erf}(x) = 2/\sqrt{\pi}\int_0^x \mathrm{e}^{-t^2}\mathrm{d}t$. For very smooth solid substrates, σ is typically on the order of a few Å. Fig. 6.2 compares the simulated profile for a perfectly smooth sapphire/D_2O interface and the same interface but with a roughness $\sigma = 1.0$ nm. We can see that the increase in roughness induces a steeper decrease in the reflectivity signal.

In terms of reflectivity, introducing roughnesses is equivalent to multiply the Fresnel reflectivity between layers i and $i+1$ by a Debye-Waller factor that writes:

$$\mathrm{DW} = \exp\left(-4q_i q_{i+1}\sigma_{i,i+1}^2\right) \tag{6.13}$$

using the previous notations.

Reflection on a succession of layers If the chemical composition of the material of interest is not homogeneous perpendicularly to the interface, we have to decompose it in a succession of N layers $\{i\}_{i\in[1,N]}$ of homogeneous concentrations (and thus homogeneous refractive indexes). We have N layers, and each layer i has a refractive index n_i and a thickness d_i. At each interface $(i-1, i)$, there is a reflected beam and a transmitted beam. This transmitted beam will then hit the above layers and the reflected part will end up hitting again the $(i-1, i)$ interface, be partially transmitted and interfere with the first reflected beam on the $(i-1, i)$ interface. Therefore, the derivation has to be done recursively, taking into account all the layers.

Firstly, energy conservation yields:

$$\forall i \in [1; N],\ q_i^2 = q_{i-1}^2 - 4\pi(\mathrm{SLD}_{i-1} - \mathrm{SLD}_i) \tag{6.14}$$

If we write q_0 the wave vector in the initial medium, we obtain by recurrence that:

$$\forall i \in [1; N],\ q_i = \sqrt{q_0^2 - 4\pi(\mathrm{SLD}_i - \mathrm{SLD}_0)} \tag{6.15}$$

At each interface $(i-1, i)_{i\in[1;N]}$, we can define $r_{i-1,i}^F$ such that:

$$r_{i-1,i}^F \equiv \frac{q_{i-1} - q_i}{q_{i-1} + q_i} \tag{6.16}$$

Similarly to the derivation of Eq. 5.6, the complex reflection coefficient $r_{i-1,i}$ can be expressed as [163]:

$$r_{i-1,i} = \frac{r_{i-1,i}^F + r_{i,i+1}\mathrm{e}^{2jq_i d_i}}{1 + r_{i-1,i}^F r_{i,i}\mathrm{e}^{2jq_i d_i}} \tag{6.17}$$

The last medium $N+1$ is homogeneous and semi-infinite (it can be air, a solid substrate, a bulk solution...). Therefore, at the last interface $(N, N+1)$ we have $r_{N,N+1} = r_{N,N+1}^F = \frac{q_N - q_{N+1}}{q_N + q_{N+1}}$. Thus, we can calculate all the $\{r_{i-1,i}\}_{i\in[1;N]}$ by recurrence, starting from the

$(N-1, N)$ interface. This is done using the Parratt algorithm [164] and we end up with a calculated reflectivity $R_{\text{calc}}(Q)$ defined as:

$$R_{\text{calc}}(Q) = |r_{0,1}|^2 \quad \text{with} \quad Q \equiv 2q_0 \quad \text{the incident wave-vector} \tag{6.18}$$

Finally, the parameters of the model (N, $\{d_i\}_{i\in[1,N]}$, $\{n_i\}_{i\in[1,N]}$...) have then to be adjusted so that the calculated and the measured reflectivities are as close as possible: $R_{\text{calc}}(Q) \approx R_{\text{exp}}(Q)$. This is discussed in the next paragraph.

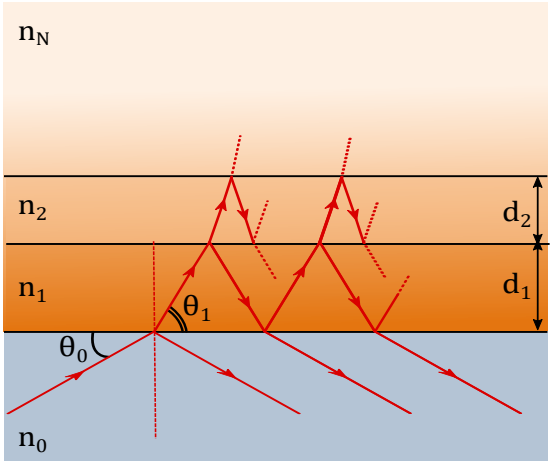

Figure 6.3: Successive reflection and refraction on a succession of layers. The total reflectivity measured is the sum of the contribution of all the possible sequences of refraction-reflection at each interfaces.

6.2.5 Data analysis

At the end of the experiment, we obtain a reflectivity curve $R_{\text{measured}}(Q)$ where $Q = 2q = \frac{4\pi}{\lambda}\sin\theta$ is the scattering vector. Ideally, we would like to invert this curve in order to obtain the corresponding near-surface concentration profile. Yet, we do not have access to the phase of the neutrons but only the reflected intensity. Therefore, several concentration profiles might lead to the same NR curve, and we cannot directly invert the NR curve. We have to postulate a realistic concentration profile, simulate its resulting NR curve and adjust its parameters so that it fits well the experimental data.

Assuming a volume fraction profile $\phi_{\{\alpha_i\}}(z)$, where $\{\alpha_i\}$ are the parameters of the postulated profile, we can calculate the corresponding $R_{\text{calc}}(Q)$ using the procedure described in the previous paragraphs. We then determine the ensemble $\{\alpha_i\}$ that minimises the reduced $\tilde{\chi}^2$ defined as:

$$\tilde{\chi}^2 \equiv \frac{1}{N_{\text{points}} - N_{\text{adjustable parameters}}} \sum_{m=1}^{N_{\text{points}}} \left(\frac{R_{\text{exp}}(Q) - R_{\text{calc}}(Q)}{dR_{\text{exp}}(Q)} \right)^2 \tag{6.19}$$

with N_{points} the number of experimental points, $R_{\text{exp}}(Q)$ and $R_{\text{exp}}(Q)$ the measured and calculated reflectivity at the scattering vector Q and $dR_{\text{exp}}(Q)$ the corresponding uncertainty on the experimental reflectivity[d]. Of course, the more adjustable parameters we

[d] Using the central limit theorem, the uncertainty on the experimental reflected intensity R_{exp} is proportional to $1/\sqrt{N_{\text{hit}}}$ with N_{hit} the number of neutrons that hit the detector.

have, the more difficult it is to minimise this quantity. In addition, we are never sure that we find the global minimum and not a local one. But if the experimental NR curve is well fitted ($\tilde{\chi}^2$ values is around 1) and if the result of the fit gives reasonable physical parameters, then we can reasonably trust the result. The fitting procedure is done using the *refnx* Python module [165], which uses the *scipy.optimize* library.

It is tempting to use machine learning to improve the fitting procedure of the reflectivity data. The first results are promising, but still fail to fit more than very simple profiles [166, 167]. This will probably be developed in the future.

6.3 Materials

6.3.1 Time-of-Flight reflectivity

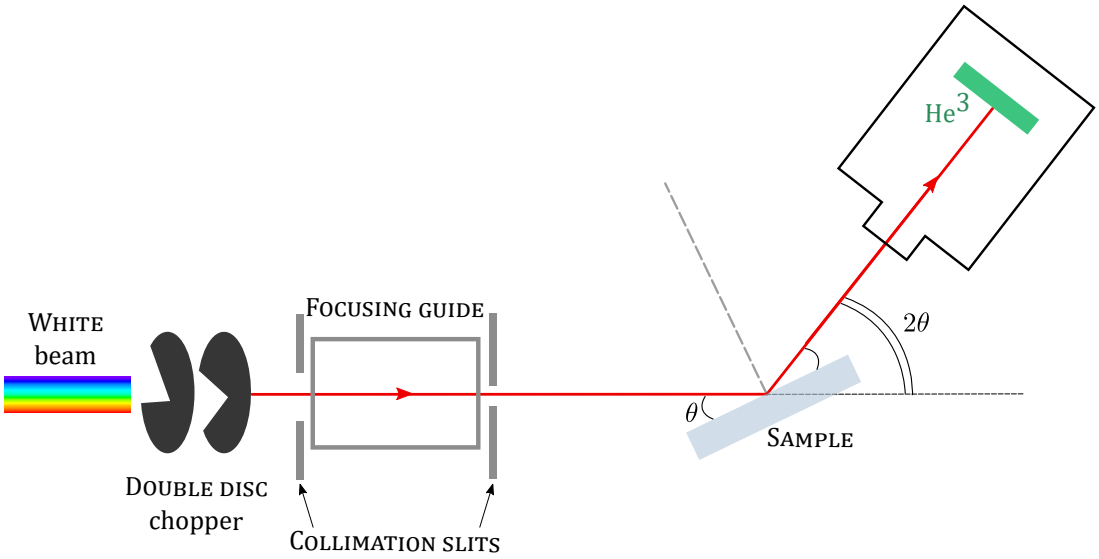

Figure 6.4: Schematic illustration of the D17 instrument.

The experimental setup is illustrated in Fig. 6.4. Experiments have been conducted on the D17 instrument [168] at Institut Laue-Langevin (ILL)[e] in Grenoble, France. Neutrons are produced inside the reactor by fission of uranium nuclei. The outgoing beam is "white" *i.e.* it is polychromatic. Disc choppers create a polychromatic neutron pulse between 2 and 27 Å. The beam is then collimated using two slits of widths d_1 and d_2 and hits the sample with an angle θ with respect to the surface. The reflected beam is collected by a He^3 detector. The principle of **Time-Of-Flight** (TOF) reflectivity is that the beam hitting the surface contains neutrons of various wavelengths, and thus of various speeds, which will hit the detector at different times t depending on their wavelength: a neutron of wavelength λ travels the distance L during a time $t = mL\lambda/h$. Therefore, the time of

[e]The reactor produces a flux of $1.5\,10^{15}$ neutrons /s/cm^2 with a thermal power of 58.3 MW, which makes it one of the most intense neutron reactor in the world. This flux is shared between several instruments to conduct various neutron experiments. Each instrument and its environment form a beam-line. Our NR experiments have been done on the D17 beam-line, which is one of the two beam-lines allowing to do Time-Of-Flight (TOF) reflectivity.

arrival on the detector is directly linked to the wavelength of the neutron, and thus for a single beam of neutrons, we obtain the reflectivity as a function of $q = 2\pi/\lambda \sin\theta$. θ is fixed during the acquisition, and we do the measurement at two different θ (0.5 and 2.5 °) during the experiment in order to obtain a broader range of q.

6.3.2 Substrate: sapphire

The substrate of interest is a $4 \times 8 \times 2$ cm rectangular block of sapphire which has been polished down to roughnesses smaller than 2 nm, as measured by X-ray reflectivity.

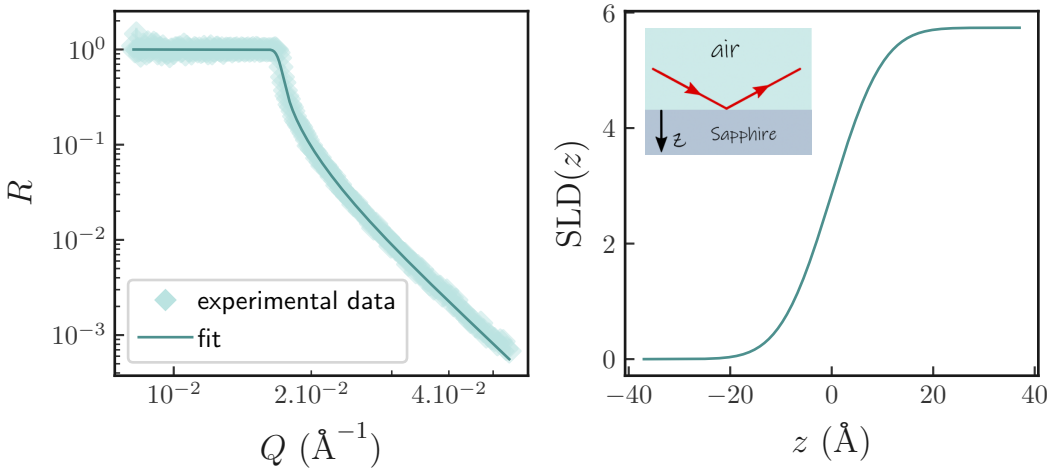

Figure 6.5: Reflectivity at the air/sapphire interface.

In Fig. 6.5, we show the reflectivity curve at the air/sapphire interface. The dark blue solid line corresponds to a fit with an SLD of $5.77.10^{-6}$ Å $^{-2}$ for the sapphire and a roughness of 2.3 Å (the SLD of air is fixed at 0 Å $^{-2}$), leading to the SLD profile shown on the right. Because the SLD of sapphire is larger than the SLD of air, we observe a total reflectivity plateau on the $R(Q)$ curve. The roughness of the interface leads to a smooth jump of the SLD profile.

6.3.3 dPS/DEP entangled semi-dilute solutions

In the continuity of the neutrons reflectivity measurements of M. Hénot [72] (chapter 5) and M. Grzelka [3] (chapter 7), we use solutions of fully-deuterated polystyrene (dPS) inside diethyl phtalate (DEP). We chose to work with deuterated chains inside a hydrogenated solvent because deuterated DEP is not commercially available. dPS has been purchased from Polymer Source, at two molar masses M_n = 195 kg/mol and M_n = 1.56 Mg/mol larger than the entanglement molar mass (see Tab. 5.1), and with a dispersity index Đ = 1.17. The volume fractions of the prepared solutions are 3 and 6 %, both larger than the overlap volume fraction ϕ^*, given in Section 5.1. Solutions are homogenized under gentle stirring during two weeks prior to the experiment. Details of the solutions are given in Tab. 6.1.

[g] N is the average number of monomers per chain. The molar mass of the dPS polymer is often measured using Gel Permeation Chromatography. calibrated with hydrogenated polymers. Therefore, it is common to calculate N by dividing the molar mass of the polymer by the molar mass of the corresponding **hydrogenated** monomer. Thus, even for dPS, we divide the polymer molar mass M_n by the molar mass of a hPS monomer, which is 104 g/mol.

[g] Not Measured.

M_n (10^6 g/mol)	N[f]	ϕ_b (%)	η_0 (Pa.s)	τ_{rept} (s)
0.195	1875	3	NM[g]	NM
0.195	1875	6	0.184 ± 0.006	NM
1.56	15000	6	11.0 ± 0.4	0.23 ± 0.01

Table 6.1: Details of the dPS/DEP solutions used for the NR experiment. Rheological properties are measured using shear oscillatory rheology (see Section 5.2.2) at $T = 20°$ C. η_0 is the Newtonian viscosity.

6.3.4 Cell

The cell is shown in Fig. 6.6. The bottom surface is the sapphire (4x8x2 cm), the top surface is a PTFE[h] block. The height of the sandwiched liquid is controlled by a rectangular Viton frame of thickness $h = 1$ mm. The resulting sapphire/liquid/PTFE block is sandwiched between two large blocks of aluminium. The cell is then sealed by forcefully screwing blocks together. The top surface is pierced at the two extremities so that we can inject the solution through the holes. The flow is applied with a Chemyx Fusion 6000 syringe pump with 50 mL steel syringes. Measurements are done either with a constant flow or with an alternating injection/withdrawal flow, in which case the acquisition is synchronised with the frequency of the flow. We call the latter process the "stroboscopic" measurement.

The configuration of the cell is such that we generate a Poiseuille flow. Similar NR measurements have been done using a rotating rheometer [158], but in that case, if there is slip, the shear rate is not homogeneous inside the sample. By using a Poiseuille flow we avoid this issue, and even if there is slip on the surface, the flow remains homogeneous.

Using a Comsol simulation (not shown here), we have checked that the flow at the centre of the cell - where the 3 cm wide neutron beam arrives - is relatively uniform.

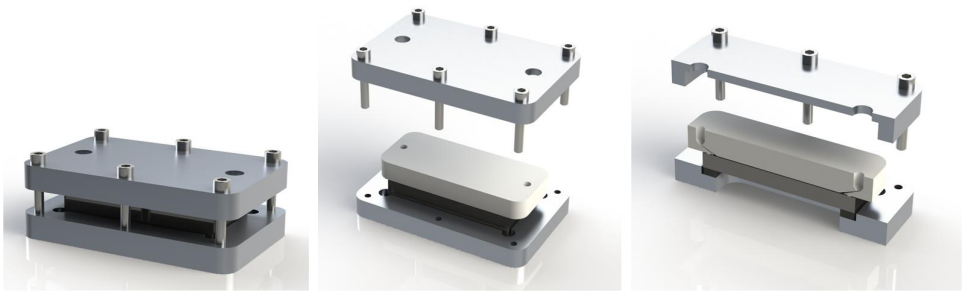

Figure 6.6: Illustrations of the cell. Pictures created by Arnaud Hélary.

6.4 Depletion and effect of volume fraction

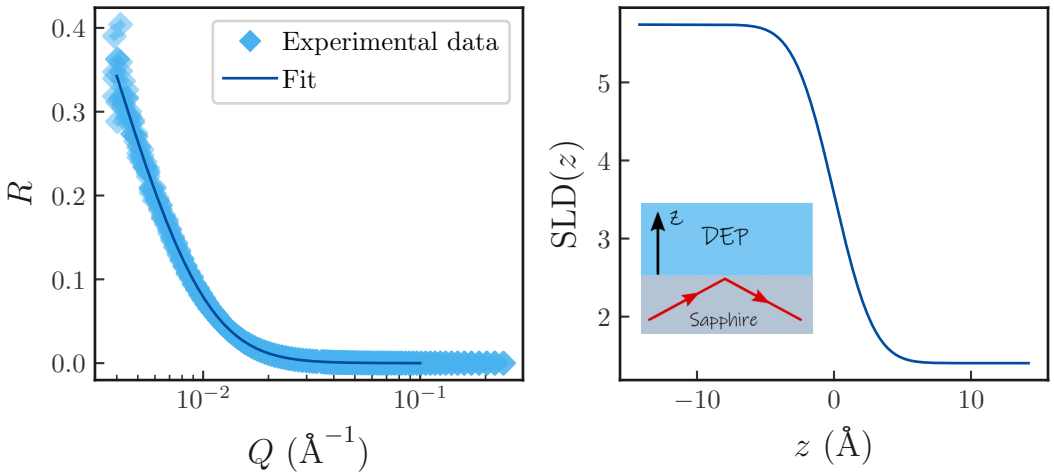

Figure 6.7: Reflectivity at the sapphire/DEP interface.

We first acquire the reflectivity of DEP/sapphire. The curve is shown in Fig. 6.7. Light blue points are experimental data and their error bars, and the blue solid line is the fit corresponding to an SLD of $1.46.10^{-6}$ Å $^{-2}$ for the DEP and an SLD of $5.77.10^{-6}$ Å $^{-2}$ for the sapphire, and a roughness of 2.4 Å.

Fig. 6.8 (left) shows the NR curves of two static solutions at different volume fractions ϕ_{bulk} but same molar mass $M_{\text{n}} = 195$ kg/mol. We chose to show the results using the Porod representation (RQ^4 vs Q) in order to enhance the differences between the curves. Error bars on Q arise from the experimental resolution on the wavelength λ and the angle of incidence θ, related to the collimation. As mentioned before (see Section 6.2.5), error bars on R come from statistics of neutrons hitting the detector[i].

Using the procedure described above, we fit the experimental data assuming an exponential variation of the concentration from the wall [83]:

$$\phi(z) = \phi_{\text{bulk}} + (\phi_{\text{wall}} - \phi_{\text{bulk}})\text{e}^{-z/d} \tag{6.20}$$

where z is the distance from the sapphire surface, ϕ_{wall} and ϕ_{bulk} are the surface and bulk volume fractions, respectively, and d is the typical size over which the polymer concentration differs from the bulk one. $\phi_{\text{wall}} > \phi_{\text{bulk}}$ corresponds to adsorption, while $\phi_{\text{wall}} < \phi_{\text{bulk}}$ corresponds to depletion. The precise function used is not very important as long as it catches the required dependencies (continuous monotonous function with a width given by a typical parameter d).

The resulting volume fraction profiles are plotted in Fig. 6.8 (right). In the vicinity of the interface, data fitting shows unambiguously a polymer depletion which characteristic

[h] PTFE = polytetrafluoroethylen $(C_2F_4)_n$

[i] There is a subtlety for the error bars in the Porod representation. Logic would say that $\delta(RQ^4) = RQ^4\sqrt{(\delta R/R)^2 + 4(\delta Q/Q)^2}$. But in reality, the value of R already contains the error on Q, because the experimental measurement of R is given by the convolution of the real reflected intensity with the experimental resolution of Q: $R(Q_0) = \int dQ R_{\text{real}}(Q) e^{-(Q-Q_0)^2/\delta Q}$ and we do not have access to R_{real}. Therefore, it is not correct to take into account δQ in the error bars of RQ^4 and thus we only consider δR.

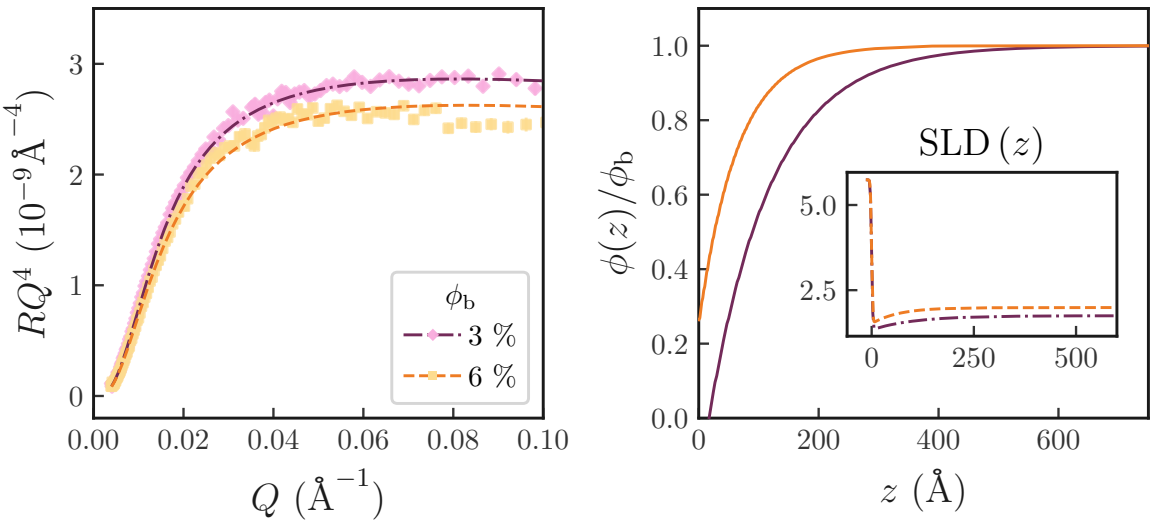

Figure 6.8: Effect of bulk volume fraction ϕ_{bulk} . Left: reflectivity curves. Dashed and dash-dotted lines correspond to the Fresnel reflectivity if the solution was homogeneous until the solid surface. Dashed lines correspond to fits from which the volume fraction profiles (right) are extracted.

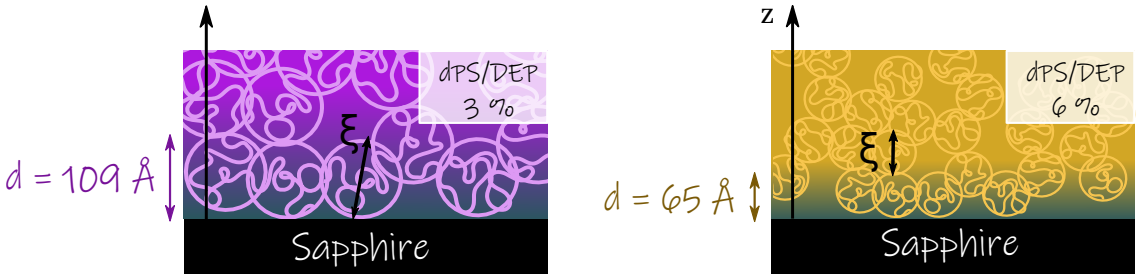

Figure 6.9: Cartoon of the interface. The size of the depletion layer is typically the size of the blob, which depends on the bulk volume fraction ϕ_{bulk} .

size decreases from $d = 109 \pm 18$ Å for $\phi = 3$ % to $d = 65 \pm 12$ Å for $\phi = 6$ %. These characteristic distances can be compared to the bulk blob size ξ measured using Small Angle Neutron Scattering (see Fig. 1.14). This is schematically illustrated in Fig. 6.9. We find that the characteristic depletion distance d is twice larger than ξ, and is in agreement with the bulk scaling law $\xi \propto \phi^{-3/4}$. Lee *et al.* [86] had already a factor 2 between d and ξ at the liquid/air interface. This is in good agreement with theoretical predictions which state that the size of the depletion layer is the blob size [83,150,169] and consistent with previous measurements at liquid/air interface [86].

6.5 Depletion does not prevent adsorption

As discussed in Section 1.3.5, observing depletion is always associated with "repulsive" surfaces (the solvent/substrate attractive interaction is much larger than the polymer/substrate one) and thus we usually discard any possible adsorption. However, in Fig. 6.8 we can see that, even if there are less polymer chains near the surface than in the bulk, the polymer volume fraction at the interface can still be larger than zero. It

means that some monomers are in contact with the surface, but the profiles do not allow concluding whether they are physically adsorbed or not.

In order to probe potential adsorption, we have put the dPS/DEP solution ($\phi = 6\,\%$, $M_n = 1.56$ Mg/mol) in contact with the sapphire for a certain time, then we have rinsed it, and we have injected pure clean DEP inside the cell. The resulting NR curve is plotted in Fig. 6.10 (top left), together with the NR curve of DEP on a clean sapphire. One can see that at large Q values, the profiles are significantly different. If there was no adsorption of dPS chains on the substrate, the two profiles would be the same. Our measurement suggests that some dPS chains remain adsorbed on the interface. However, due to the low quantity of adsorbed chains and their large coil size, it is impossible to extract quantitative information from this measurement.

To confirm this hypothesis, we have conducted X-ray reflectivity on air/sapphire interface for a sapphire which has been in contact with a hPS/DEP solution during one hour and then thoroughly rinsed with DEP and dried. The details of the X-ray reflectivity techniques are given in Section 5.4.3. The corresponding reflectivity curve is plotted in Fig. 6.10 (bottom left) and shows a clear Kiessig fringe between $Q = 0.15$ Å^{-1} and $Q = 0.3$ Å^{-1}. A single layer model with roughness at both interfaces fits well the data and confirms the presence of a dry adsorbed layer of thickness $h_{dry} = 24$ Å. Assuming that these chains are swollen over their Flory radius (320 nm), the mean volume fraction of adsorbed chains is estimated to be 0.7 %. Such change in concentration is too small for NR fitting, which further confirms that it is nearly impossible to fit the NR reflectivity data of Fig. 6.10 (top).

It is quite surprising to see both depletion and adsorption as they are usually excluding *scenarii*. The measurement of depletion is rather robust since the neutron flux of the ILL is strong enough to give precise measurements and we could not fit any adsorption profile on our data while depletion profiles were easily fitted with good $\tilde{\chi}^2$ values. As for adsorption, both the qualitative NR measurements and the quantitative X-ray ones leave little doubts on the presence of remaining chains on the surface. In addition, Barraud *et al.* [89] have mentioned an adsorption/depletion situation for a charged polymer on a charged surface: they observed a depletion layer of the polyelectrolyte above its own adsorbed layer. However, in their case, adsorption was the result of the favorable electrostatic attraction between the surface and the chains, and depletion was the consequence of the electrostatic repulsion between the adsorbed layer and the bulk chains. These arguments do not apply to our neutral system.

From a chemical point of view, the surface of the sapphire has hydroxyl groups with a surface density in the range of $1-10$ OH/nm^2 [134,135]. Contrary to PS (hydrogenated or deuterated), DEP is able to make hydrogen bonds with these exposed OH groups, which is likely to favour the DEP-surface interaction compared to the dPS-surface interaction, which further corroborates the depletion scenario. However, adsorption of PS chains onto sapphire surfaces has already been mentioned in the literature for PS melts [170], which means that PS can also interact favourably with the surface. A first possibility would be a π-H interaction between the π orbitals of the styrene and the labile H of the exposed hydroxyl groups. This interaction should be around -0.11 eV [171,172]. However, a DFT

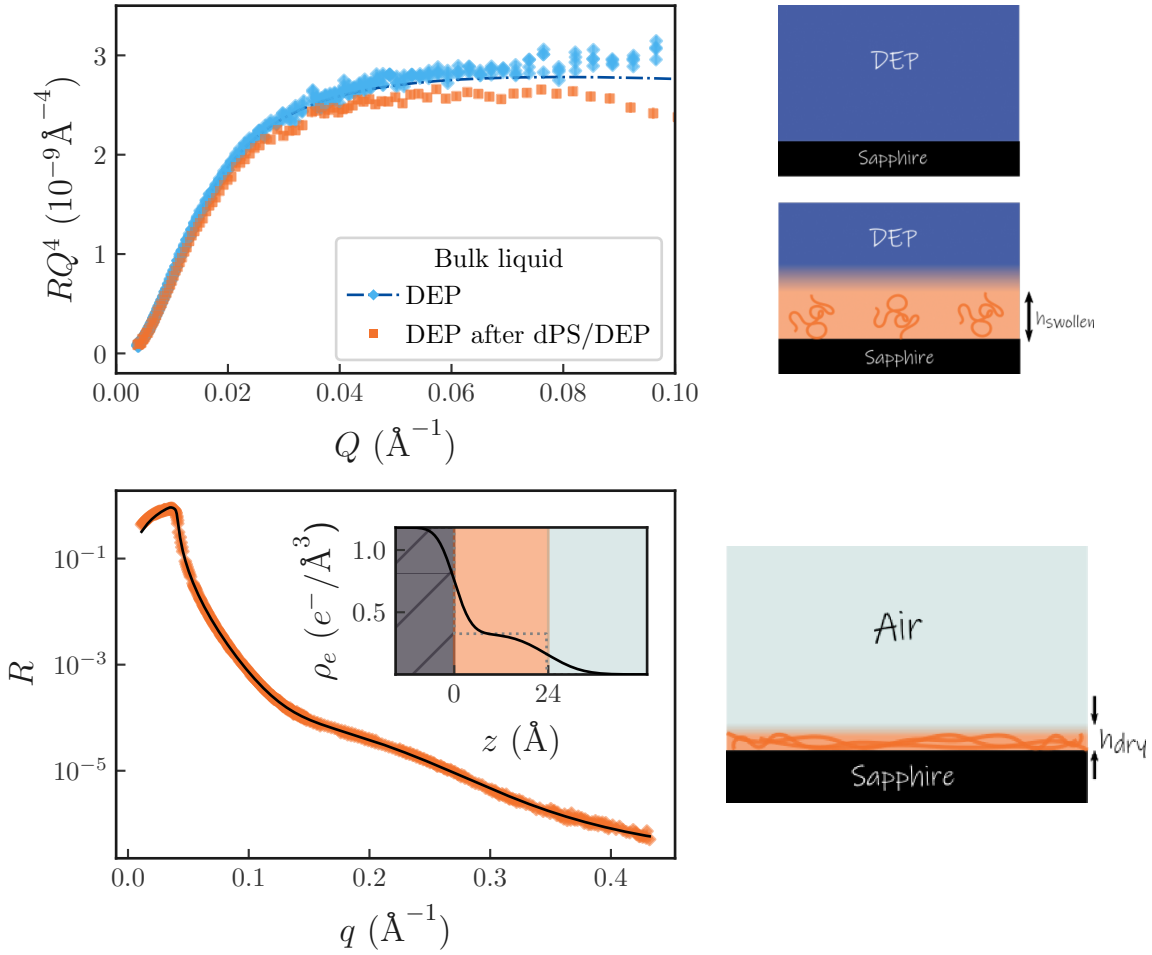

Figure 6.10: Top: Neutron reflectivity curves of DEP on clean sapphire (blue diamonds, fit is the blue-dashed line) and on sapphire which has been incubated with dPS/DEP solution prior to the experiment (orange squares). Bottom: X-ray reflectivity curve of the sapphire surface that has been incubated with hPS/DEP solution ($\phi = 6$ %, $M_n = 708$ kg/mol), and then rinsed and dried. The black line is a fit with a rough interfacial layer. Inset: Electronic density as a function of the distance from the interface. Corresponding cartoons are plotted on the right.

calculation performed by Dominique Costa[j] with a styrene monomer in the vicinity of a sapphire surface has shown a purely Van der Waals attraction, with an adsorption energy of -0.63 eV (see Fig. 6.11). Thus, the adsorption of dPS on sapphire is not governed by a specific chemical interaction but rather by Van der Waals forces, and we could expect that this is a rather general result for polymer solutions near a surface which interact more favourably with the solvent.

6.6 Effect of the flow

Finally, we have studied the effect of a Poiseuille flow on the concentration profiles of the dPS/DEP solutions near the sapphire surface. The results are plotted in Fig. 6.13,

[j]PCS team, IRCP, Chimie ParisTech, PSL University, Paris, France.

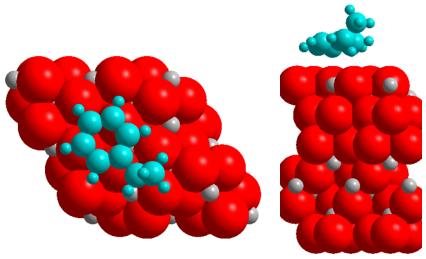

Figure 6.11: Snapshot of the DFT calculation of a styrene molecule (in blue) facing a sapphire surface Al_2O_3 (in red and white).

for a solution with a 6 % volume fraction and a 1.56 Mg/mol molar mass. The strength of the flow is characterized by the Weissenberg number Wi, which is the dimensionless number comparing the typical relaxation time of the polymer solution τ and the typical timescale of the flow. For the relaxation time, we take the reptation time of our solution $\tau_{\text{rept}} = 0.037$ s, which has been measured in oscillating rheology (see Fig. 6.12). In our geometry, we have $\text{Wi} = 6Q\tau_{\text{rept}}/(\ell h^2)$ with Q the flow rate imposed by the pump, and ℓ and h the width and the height of the cell, respectively.

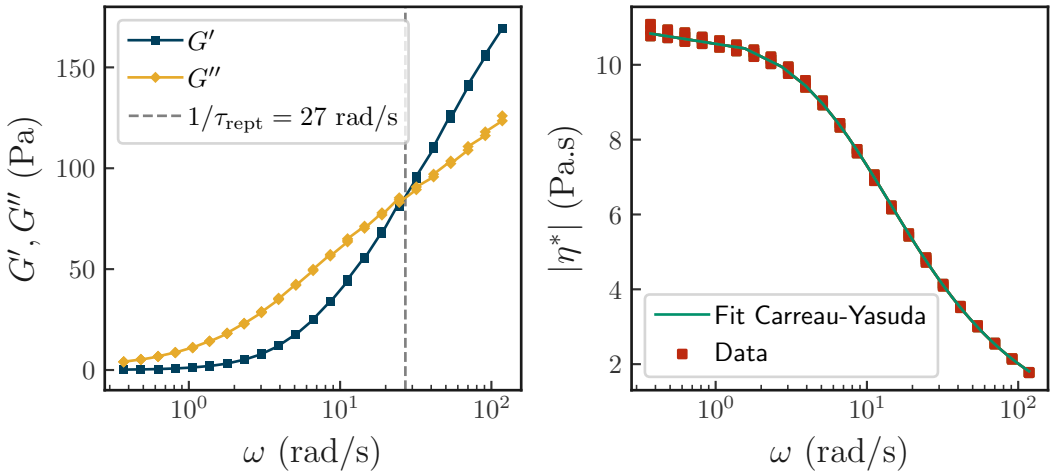

Figure 6.12: Oscillating rheology of the dPS/DEP 1.56 Mg/mol 6 % used. The reptation time τ_{rept} is given by the crossover between G' and G'', and yields $\tau_{\text{rept}} = 0.037$ s.

The reflectivity curves are very similar for both the static solution and the flowing ones, and the fit yields the same SLD profiles, with $\tilde{\chi}^2$ between 1 and 2. The size of the depletion layer does not vary significantly with the Weissenberg number up to $\text{Wi} = 0.1$. Reaching higher values of Wi was challenging because it requires both a highly viscous liquid (high τ) and a strong flow rate Q, and we were limited by the total amount of solution we had, which conditions the emptying time of the syringe.

The flow rate can have an effect on both the depletion layer and the adsorbed chains. Previous works on the effect of flow rate on the size of the depletion layer report interesting behaviours. For rigid rodlike particles, Ausserré *et al.* showed that the depletion size d increases with the flow rate due to hydrodynamics lift [85]. For dilute polymer solutions,

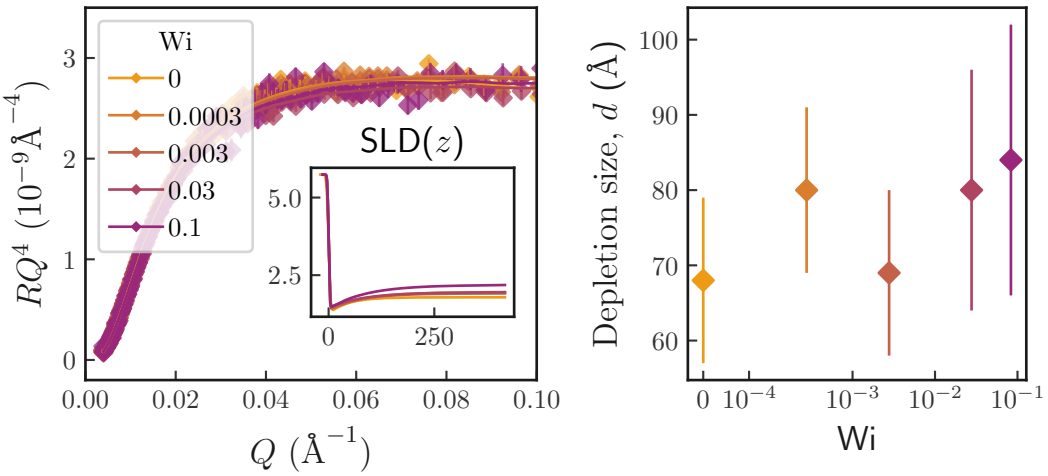

Figure 6.13: Effect of the flow on the reflectivity profiles. Left: reflectivity curves and corresponding SLD profiles in the inset. Right: Size of the depletion layer extracted from the fits as a function of the Weissenberg number Wi. These measurements have been done with 1.56 Mg/mol dPS/DEP at a volume fraction $\phi = 6$ %.

de Pablo *et al.* predicted a decreasing d with the flow rate at moderate flow rates and an increasing d at large flow rates [159], which corroborates the experiment done by Ausserré *et al.*. They used a dumbbell model, which aligns with the flow at low flow rates and starts to rotate quickly at high flow rates, so that the volume occupied by the dumbbell is larger, and thus it flows further away from the wall. However, the flow rate starts to affect the depletion profile for Wi > 1. On the contrary, in our experiments, the dispersed polymers are flexible so their description does not apply to our system, and we are always at Wi $<< 1$. The depletion size might change if the flow has an effect on the blob size of the solution. Here, we see that up to Wi $= 1$, no effect of the flow is visible and thus the size of the blobs remains constant. As for the adsorbed layer, Korolkovas *et al.* [158] used neutrons reflectivity to study the effect of flow rate on the interface between a dPS/DEP solution and PS brushes in a cone-plate rheometer. They showed that the thickness of the brush decreases when increasing the Weissenberg number, which in their case was $\dot{\gamma}\tau$, with $\dot{\gamma}$ the applied shear rate. However, the grafting density of their brushes varied between 0.04 and 0.4 nm^{-2}, which is much higher than the density of the adsorbed chains we have estimated for our system (about 0.002 nm^{-2}). Therefore, in our experiment, the effect of the flow on the adsorbed chains is negligible.

A logical continuation of this work would be to reach higher Wi values. A first possibility to do so would be use longer dPS chains, increasing the reptation time of the solution. Another possibility would be to close the circuit to make the sample flow permanently, thus getting rid of the problem of syringe emptying. We have tried the latter possibility using a gear pump. Yet, it is very difficult to not introduce air bubbles inside the solution while closing the circuit. In addition, some residues from the gears polluted our solutions, even after a careful rinsing of the circuit.

6.7 Conclusion

In this chapter, we have studied the polymer concentration profile in dPS/DEP solutions near a polished sapphire surface. The first result is that there is a depletion of polymer chains near the surface, and the size of this depletion layer is typically the blob size of the semi-dilute solution. This corroborates the scalings predicted by de Gennes, which has been experimentally observed only at the liquid/air interface before. The second − and main result − of this experiment is that depletion does not exclude adsorption. Indeed, the concentration of polymer chains inside the depletion layer is not zero, and there is an attractive interaction between the polymer and the wall. This attractive interaction is smaller than the solvent/wall attraction, which explains the depletion, but it allows some chains to still adsorb on the substrate. This is an important result as in general depletion and adsorption are two excluding *scenarii*. The last result is that, up to Wi ≈ 0.01, the flow has no effect on the near-surface concentration profile. This is expected for such low Weissenberg numbers, and calls for experiment at larger Wi.

To put our results in the context of depletion/adsorption between a semidilute polymer solution and a solid surface, we have recapitulated the different configurations in Fig. 6.14. If the system is charged and if the wall and the polymer share the same type of charge (both positive or both negative), there is a true depletion, on a typical length-scale which depends on the blob size and the Debye length. This is observed for example in Guyard *et al.* [51]. In the case where the wall and the polymer have opposite charges, there is adsorption of a polymer layer of thickness d_a, which collapse onto the wall, and therefore a depletion because of the electrostatic repulsion between the adsorbed chains and the bulk ones. The size of the depletion layer is also given by the blob size and the Debye length. This situation is observed by Barraud *et al.* [89].

In the case where the system is neutral, we can distinguish two different cases. The first one is when the surface has a neat preference for the polymer compared to the solvent. In that situation there is pure adsorption, and we can estimate an adsorbed surface density σ, which depends on the molar mass of the chains and on the bulk volume fraction. This is observed for PDMS in [91]. We do not give the typical thickness of the adsorbed layer, as it depends on the solvent it is immersed in. Lastly, there is the situation we are looking at, which is a neutral system with a wall which interact more favourably with the solvent. In that situation, we have shown that there is a depletion, which size scales with the blob size, and there is also adsorption of a few chains. Since there is only a few amounts of adsorbed chains, we could not extract the typical characteristics of the adsorbed layer, and this calls for future experiments.

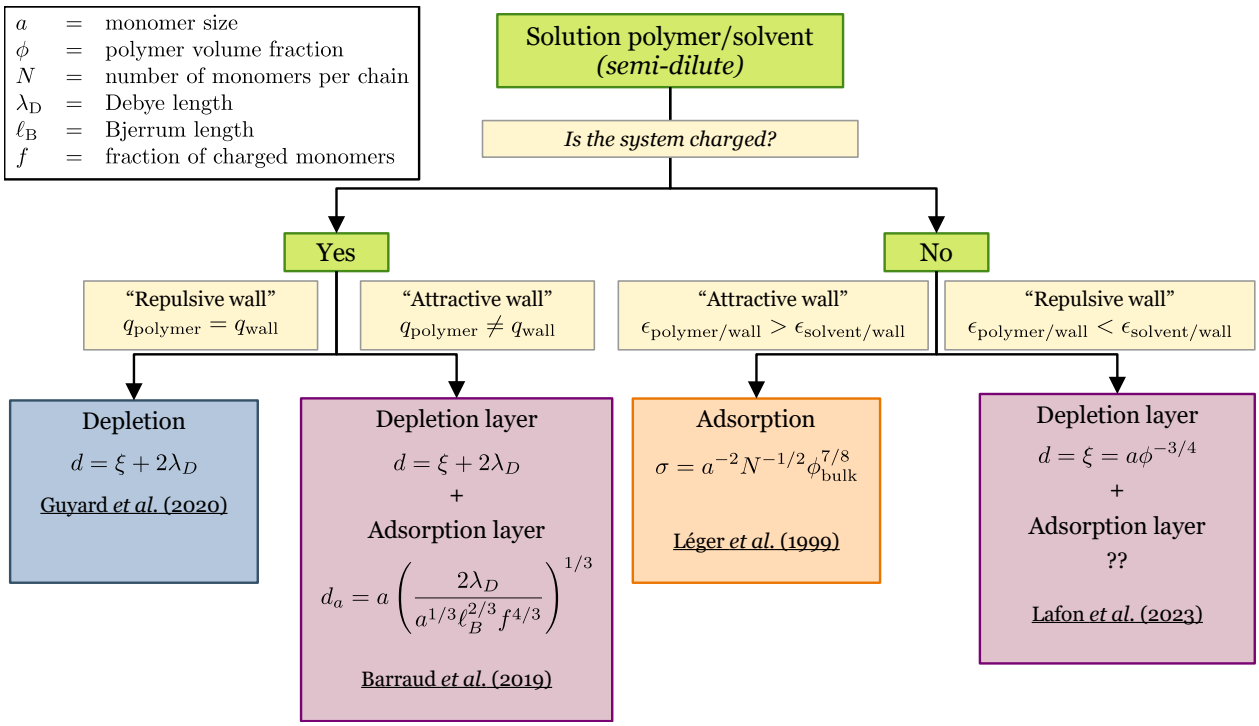

Figure 6.14: Chart summarizing the different situations encountered for a semi-dilute solution of polymers facing a solid substrate. The reference are Guyard *et al.* [51], Barraud *et al.* [89], Léger *et al.* [91] and Lafon *et al.* [146]

Chapter 7

Rheology and friction of semi-dilute entangled polymers solutions

Contents

As we have seen in Chapter 1, the slip length is usually very small, and thus it is delicate to measure it quantitatively. Since the slip length is proportional to the viscosity, we choose to use very viscous liquids, and polymers are good candidates to this end. Because we are interested in probing temperature effects on the slip length, we have opted for polymer solutions, for which the choice of the solvent controls the glass transition temperature of the solution. We have chosen to work with semi-dilute solutions, as they are relatively viscous, and the scaling laws regarding their dynamics are well established.

In this whole chapter, we work with semi-dilute solutions of high molar mass polystyrene (PS) in diethylphtalate (DEP). In Section 7.1, we discuss the bulk rheology of our solutions. Indeed, we have noticed a deviation from the expected scaling laws for our system, and thus we compare it to semi-dilute polystyrene solutions in other good solvents to understand the origin of this discrepancy. In Section 7.2, we present results of slip lengths measurements using the Tracking of Photobleached Patterns (TPP) technique. We present the current version of this technique, developed in our lab, and we show some friction measurements we have done with it. Finally, in Section 7.3, we discuss in depth how to measure slip lengths using a rheometer, and we focus on the shear-rate dependency of the friction coefficient. In particular, we derive a new approach, which might be used to experimentally measure the oscillatory response of the friction coefficient $\lambda(\omega)$.

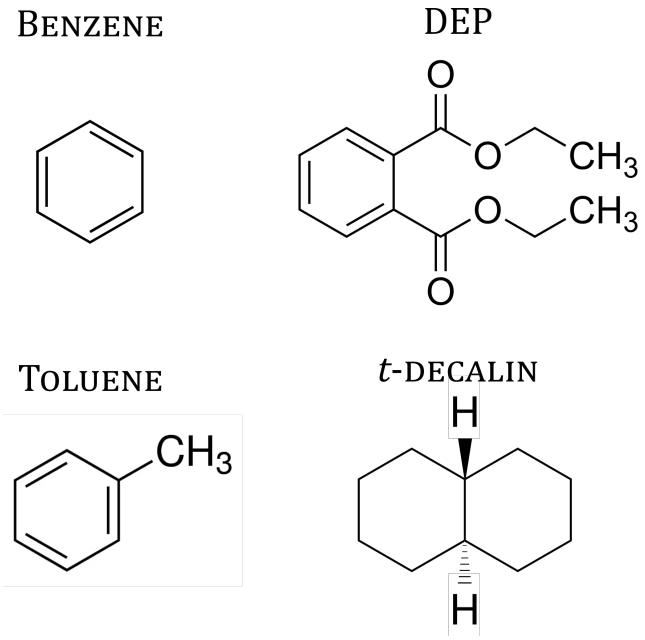

Figure 7.1: Solvents discussed in this chapter.

7.1 Bulk rheology

We start with the bulk rheology of polystyrene (PS) semi-dilute solutions in good solvents. We are especially interested in the effect of temperature on the relation between the viscosity η of the solutions and their volume fraction ϕ.

As described in the general introduction of this manuscript (Eq. 1.45), the viscosity of entangled semi-dilute polymer solution is expected to obey the following scaling law [75,173]:

$$\eta(\phi) = \eta_{\text{solvent}} N^3 \phi^{15/4} \tag{7.1}$$

This equation stems from the fact that the viscosity of the semi-dilute solutions emerges from the reptation of polymer chains confined in "tubes" due to the presence of surrounding chains. The higher the concentration, the narrower the tube and the higher the viscosity. The larger the molar mass, the larger the time needed to escape the reptation tube (τ_{rept}) and thus the higher the viscosity too.

This scaling law has been experimentally confirmed by many groups [174–176] in benzene and toluene at room temperature. Yet, a deviation from the exponent 15/4 has been observed by several groups [3,46,97,177–179] for PS in DEP. They observe a steeper slope in the dependency of η with ϕ. An unexpectedly large exponent has also been observed by Kulicke *et al.* [175] for PS in *t*-decalin.

In Fig. 7.2, we plot the data from these various papers. In the left graph, we fit a power law $\eta = \phi^{\alpha}$ solvent per solvent, and the resulting exponents α are shown in the right graph. From Eq. 7.1, we expect $\alpha = 15/4$, which is the value found for benzene. However, *t*-decalin and even more DEP have indeed a larger exponent than expected.

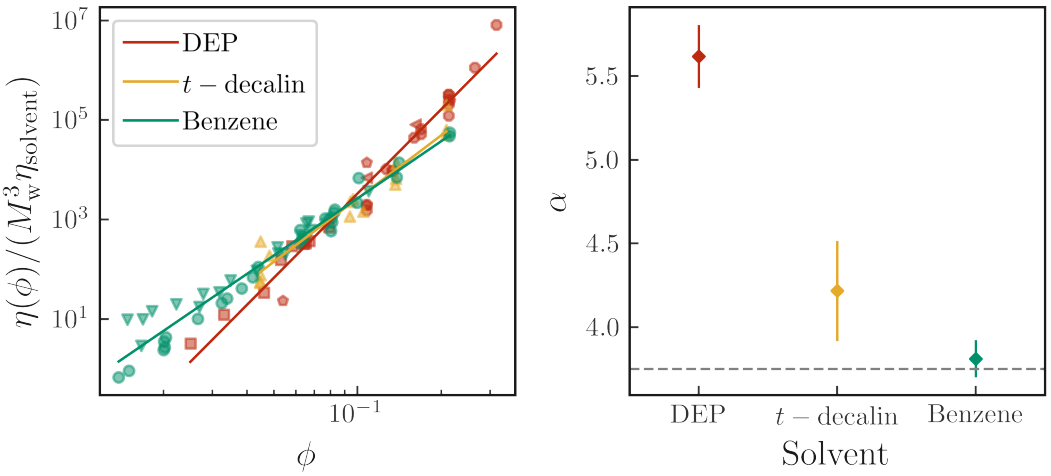

Figure 7.2: Left: Zoom on the viscosity dependence on the volume fraction ϕ for three different solvents for which there is a discrepancy between the expected and measured scaling laws. (red: DEP, green: benzene, yellow: t-decalin). Data are taken from the following references: ◁ are from Bhattacharjee *et al.* [177], ⬠ are from Mhetar *et al.* [178], ∘ are from Osaki *et al* [179], □ are from Sanchez-Reyes *et al.* [46], ◯ are from Adam *et al.* [174], ▽ are from Raspaud *et al.* [176] and △ are from Kulicke *et al.* [175]. Right: measured exponent for the three different solvents.

For t-decalin, Kulicke *et al.* [175] suggest that this might be due to the proximity of the θ-temperature: at 25 °C, t-decalin would not be such a good solvent. The θ-temperature of t-decalin has been estimated around 20 °C [180]. θ effects should arise in the range $\theta(1 \pm \frac{1}{N})$ [77] (p.172), and in the data from [175], the minimum molar mass is 266 kg/mol, so that θ effects should happen between 14 and 26 °C. The experiments being conducted at 25 °C, the deviation of the exponent is likely to be caused by θ effects. In addition, the scaling law for entangled semi-dilute polymer solutions in θ-solvent is:

$$\eta(\phi) \propto \eta_{\text{solvent}} N^3 \phi^{14/3} \tag{7.2}$$

so we expect an exponent around 4.7 for an entangled semi-dilute solution in a θ solvent.

However, for PS/DEP solutions, SANS[a] experiments show that the correlation length ξ follows the expected scaling law for semi-dilute entangled polymers in a good solvent (see Fig. 1.14). Even if these experiments do not provide a measurement of the second virial coefficient A_2, the fact that $\xi \propto \phi^{-3/4}$ at 10, 20 and 55 °C is a good sign that DEP is a good solvent of PS. In addition, the measured exponent is around 5.6, so it is much larger than the 4.7 predicted for a θ-solvent.

If the quality of the solvent is not the cause of the observed deviation of exponent α, we have to look for another explanation. In [97], Grzelka *et al.* have attributed the deviation to the proximity of the glass transition temperature T_g of the polymer solution and more specifically to the dependence of T_g on ϕ. We will discuss this hypothesis in the following paragraphs.

[a] Small-Angle Neutrons Scattering.

The range of volume fractions explored by M. Grzelka is between 1 and 8 %. Savin *et al.* [181] have measured the T_g of polystyrene solutions in three solvents very similar to DEP: dimethylphtalate (DMP), dibutylphtalate (DBP) and dioctylphtalate (DOP). They have studied the evolution of the DSC glass transitions as a function of the weight fraction of PS. Their results are reproduced in Fig. 7.3. They notice three regions:

1. at low PS concentrations (blue region), the T_g of the solution is almost the T_g of the solvent. The dynamics is mainly given by the motion of solvent molecules, slightly hindered by the PS.

2. at intermediate PS concentrations (purple region), two glass transitions are observable with DSC. A lower T_g , corresponding to the relaxation of solvent molecules, and a higher T_g , corresponding to the dynamics of the solvent slaved to the dynamics of the polymer matrix.

3. at high PS concentrations (orange region), the relaxation of the solvent is completely slaved to the dynamics of the PS matrix, which itself strongly depends on the amount of solvent - acting as a plasticizer - adding free volume to the chains.

In our case, the range of considered concentrations is located at very small concentrations of PS so that there is only one glass transition, and it is nearly at the T_g of the solvent (around 193 K) (see Appendix).

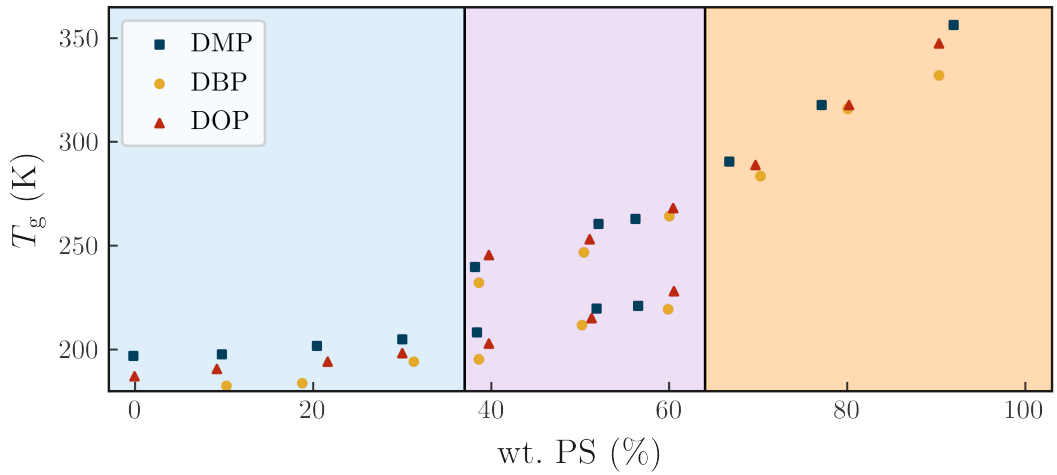

Figure 7.3: Glass transition temperatures measured by DSC in various polystyrene solutions, as a function of the weight percent of PS, in dimethylphtalate (DMP), dibutylphtalate (DBP) and dioctylphtalate (DOP). Adapted from [181].

In order to get more insight on these observations, we have measured $\eta(\phi)$ at various temperatures to obtain the dependency of the exponent α with temperature. We have used high molar masses PS/DEP solutions with volume fractions ranging from 1 to 8 %, for temperatures between 5 and 90°C. The results are shown in Fig. 7.4. We fit the viscosity by the scaling law $\eta \propto \phi^{\alpha}$ and we plot the exponent $\alpha(T)$ on the right graph.

We observe that α tends to reach the expected 15/4 values at high temperatures, yet we did not reach large enough temperatures in order to observe a plateau. On the contrary, as the solution is cooled down, the deviation from the expected scaling law increases. In Fig. 7.5, we compare $\alpha(T)$ from our measurements as well as the exponent extracted from data from the literature [46,174–176]. The exponent found for PS in benzene solutions is around the expected 15/4 value. For *t*-decalin, the value is a little bit larger than expected, even if the error bars are quite large. The exponent for PS in DEP are always larger than expected. The point at 301 K is taken from [46] and the other data points are our own results from Fig. 7.4. On the right graph of Fig. 7.5, we have plotted α as a function of $T - T_g^{\text{solvent}}$. We observe that the data seem to follow a common trend, the exponent 15/4 being reached at least at $T > T_g^{\text{solvent}} + 180$ K. We could not observe any levelling at the highest temperatures studied here, and performing experiments at higher temperatures would be useful to see if the exponent indeed saturates around the expected 15/4 value.

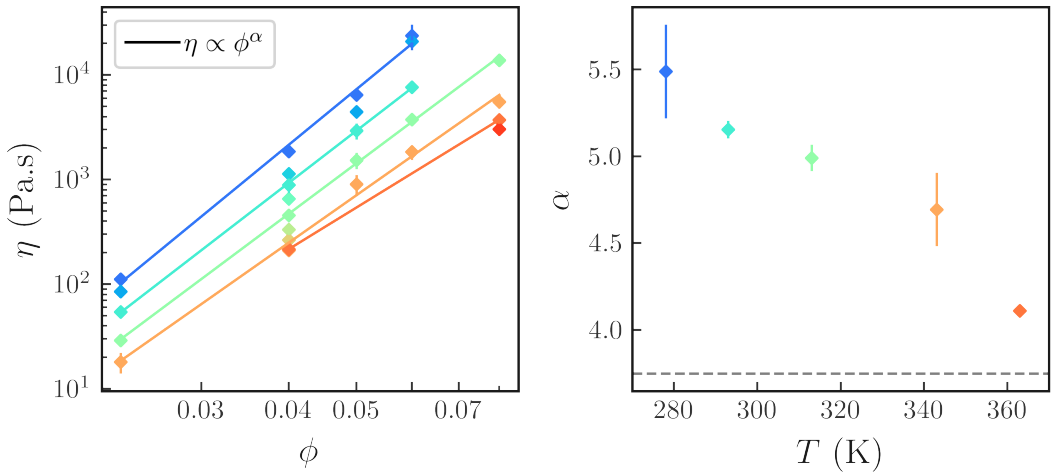

Figure 7.4: Results of rheology of semi-dilute entangled PS/DEP solutions at various temperatures. The molar mass is the same for all the solutions: $M_n = 10.153$ Mg/mol. Left: $\eta(\phi)$ for temperatures between 5 °C and 90 °C. Solid lines correspond to power-law regressions $\eta \propto \phi^\alpha$. Right: $\alpha(T)$. The gray dashed line correspond to the expected exponent 15/4.

To conclude this first section, we have seen that PS/DEP semi-dilute solutions do not follow the expected scaling law $\eta \propto \phi^\alpha$. This observation is consistent with other experiments from the literature. This deviation could be due to the proximity of a θ-temperature, but it is very unlikely for DEP. Another possibility would be glassy effects over a much wider range than expected (usually we consider that above T_g +100 there are no reminiscent effects of the glass transition). We have measured the temperature dependence of the exponent $\alpha(T)$ and we saw that it is a decreasing function of temperature. Deeply understanding the reason why we observe such a temperature-dependent deviation would require more experiments to 1) check if there is a deviation from the 15/4 exponent in all good solvents as soon as the temperature of the solution if below T_g +180[b] ; and 2) look for a potential θ-temperature for PS in DEP. Ideally, we would need

[b] We have started to do these experiments, but many good solvents of polystyrene are toxic and volatile,

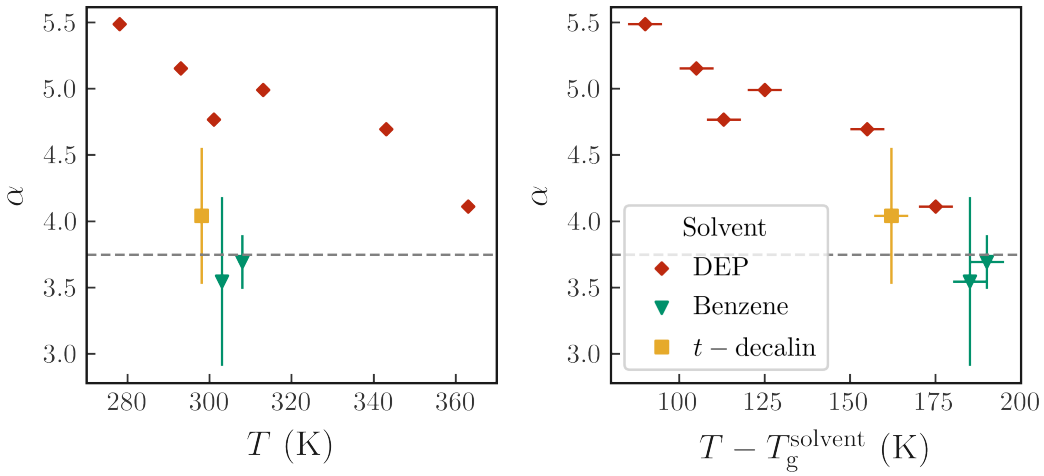

Figure 7.5: Exponent α from Eq. 7.1 for semi-dilute entangled solutions of PS in various good solvents. Data in toluene and t-decalin are taken from Kulicke *et al.* [175], data in benzene are taken from Raspaud *et al.* [176] for $T = 303$ K and Adam *et al.* [174] for $T = 308$ K. Data in DEP are taken from Sanchez-Reyes *et al.* [46] for $T = 301$ K and are our own results for the rest of the data points.

to measure the second virial coefficient A_2 for all the solvents used in order to be sure that they are good solvents of PS.

For the following sections of this chapter, we use the exponent we have measured for our solutions instead of the 15/4 expected exponent. We now focus on measuring the slip length of our PS/DEP solutions as a function of temperature. Since the slip length depends on both the viscosity and the friction coefficient, we use our measurements of $\eta(\phi, T)$ to determine the temperature dependency of the friction coefficient $\lambda(T)$. In Section 7.2, we use the TPP technique to try and measure $b(T)$. In Section 7.3, we derive a new analysis to measure the friction coefficient using a rheometer. This allows us to extract the dependency of λ with the shear-rate $\dot{\gamma}$ over a very broad range, and we discuss these results in light with the measurements done with our MD simulations of a LJ liquid.

7.2 Slip measurement using tracking of photobleached patterns (TPP)

First, we use the technique developed in Liliane Léger's group in Collège de France to measure slip length of liquid polymers [29, 31, 182, 183]. For simplicity, we call this technique "TPP" for Tracking of Photobleached Patterns. This method has been used by M. Hénot [72] and M. Grzelka [3] to measure slip lengths of PDMS melts and PS/DEP solutions. We have upgraded the set-up to implement a temperature control.

7.2.1 Fluorescence and photobleaching

A fluorescent molecule is a molecule which is able to emit a photon of wavelength λ_e after absorbing a photon of wavelength $\lambda_i < \lambda_e$. The incident photon excites some

which makes the experiments delicate, and we did not have time to push the experiments further for now.

electrons at an energy $E_1 = \frac{hc}{\lambda_i}$. Then, there is a non-radiative transition which brings the electrons to the energy $E_2 < E_1$. Finally, they relax back to their initial state of energy E_0, emitting a photon of energy $\lambda_e = \frac{hc}{E_2}$. As soon as the incident intensity is not too large, the concentration of fluorescent molecules not too high and the thickness of the sample smaller than the absorption length of the medium, the intensity of the emitted fluorescent light I_e is proportional to the initial intensity of light I_i. The quantum yield Φ is defined as the ratio of the number of photons emitted over the number of photons absorbed. This quantum yield depends on the fluorescent molecule, and can also depend on temperature [184].

If the incident intensity of light is too high, the fluorescence of the molecule is destroyed. This is called **photobleaching**. A consequence of this is that the emitted fluorescent intensity I_e (at λ_e) depends on the illumination time as:

$$I_e \propto e^{-KI_i t} \tag{7.3}$$

where K is a constant depending on the molecule and I_i is the intensity of the incident light.

In our case, we use PS-diNBD labels (see [185]) synthetized by Eric Drockenmuller from Université Claude Bernard, Lyon 1. They consist of small PS chains labelled with NDB groups (7-nitrobenz-2-oxa-1,3-diazole). Fluorescence of NDB is excited at $\lambda_i = 453$ nm (blue light) and they fluoresce at $\lambda_e = 510$ nm (green light). In practice, we incorporate a small amount of PS-diNBD in our PS/DEP solutions so that the concentration of fluorescent PS labels is below 0.5 mg/mL.

7.2.2 Experimental technique

This technique has been evolving since 1991 when it has first been developed in the group of Liliane Léger at Collège de France [29, 31, 182, 183, 186]. The configuration we use is the same as the configuration used by M. Hénot [72] and M. Grzelka [3] during their PhD. A schematic of the experimental set-up is shown in Fig. 7.6. We sandwich the labelled polymer solution between the slipping surface and a flat prism. The prism has been grafted with PS chains in order to prevent slip on its surface. The thickness of the liquid is controlled by Mylar spacers. We look at our sample from the top, using a home-made microscope with a x10 objective (Mitutoyo), a high-pass filter (Edmund) and a Nikon D780 camera. z is the direction perpendicular to the surface.

In what we call the "reading mode", a laser beam ($\lambda = 458$ nm, Coherent, Sapphire LP) hits the liquid and excites the fluorescent labels. This is done at the minimal power (7 mW) and adding an attenuator, which reduces the intensity to prevent photobleaching. Then, we use a convergent lens ($f = 10$ cm) to focus the laser along a thin line (in the y direction) inside the sample at the maximum power (75 mW, no attenuator) and thus photobleach the fluorescent labels along this line. We call that the "writing mode". We come back to the reading mode to observe the fluorescent green background, in which there is now a black bleached line. The liquid is then sheared perpendicularly to the bleached line, and both the displacement and the deformation of the photobleached line are followed.

Shear is achieved along the x direction thanks to a stepper motor (Radiospares, hybrid bipolar 1.6 nm 1.8° 4 wires 24V) controlled by a stepper motor controller (Sanmotion, BS1D200). We use a 5 : 1 speed reducer (Radiospares) to smoothly change the accessible velocity range. We have calibrated the set-up using a resistive position sensor. We can reach shear velocities between 0.1 and 30 µm .s^{-1}.

The displacement of the black line gives us a direct visualisation of the velocity profile inside the liquid, and in particular it gives us direct access to the velocity of the liquid on both surfaces. This requires that the diffusion time inside the liquid is much larger than the shearing time so that the bleached line is not significantly modified by diffusion during the shear.

One experiment follows the following protocol:

- in reading mode, we take a picture of the background.
- in writing mode, but still at low power (7 mW) and with the attenuator, we take a picture of the focused beam using a long exposure time (4 s) and a high gain.
- in writing mode, we bleach the sample along a line at maximum power (75 mW) without attenuator.
- in reading mode and at low power, we take a picture of the sample with the photobleached line.
- we shear our sample at a velocity U during a time t_{shear}. We take pictures during the shear, with exposure times much smaller than t_{shear} and we adapt the gain accordingly.

Temperature control. We have upgraded the set-up used by M. Hénot [72] and M. Grzelka [3] to add a precise temperature control. The design has been done by Vincent Klein, from LPS, Orsay. The wafer is placed inside a copper furnace, which is connected to a Peltier system and regulated with a PID. This allows us to reach temperatures between 0 and 100 °C with an accuracy of ±2 °C due to the temperature loss between the inner furnace and the surface of the wafer.

7.2.3 Analysis

The image analysis procedure has been developed by M. Hénot during his PhD [72] and published in [187]. He has developed two different analysis procedures: 1) the z-integrated method, more suitable for small slip lengths and 2) the z-resolved method, more adapted for large b. We briefly describe the two types of analysis.

7.2.3.1 The z-integrated method

For this analysis, we consider the integral of the intensity over the whole thickness of the liquid (see Fig. 7.7). x is the direction of the shear, and z the height inside the liquid. We write $I(x, z)$ the intensity at position (x, z) and we will use the calligraphic letter $\mathcal{I}(x) = \int_0^h I(x, z)\frac{dz}{h}$ to refer to the integral of the intensity over the whole thickness of the liquid. After photobleaching, in reading mode, the sample has a green fluorescent

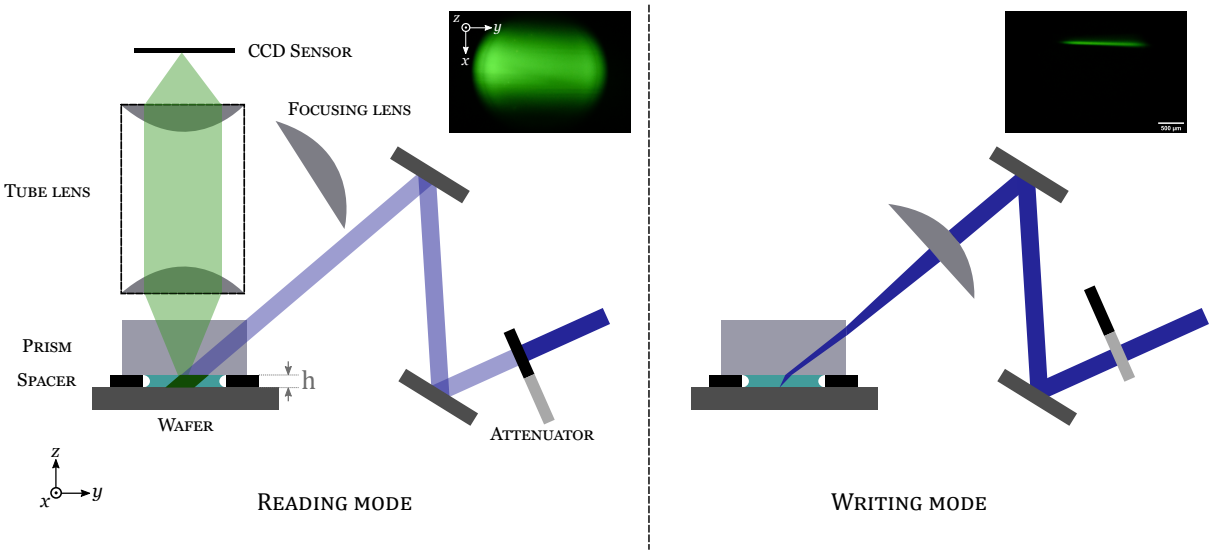

Figure 7.6: Schematic of the TPP set-up used to measure the slip length of polymer solutions on wafer surfaces. The gain and exposure times on both pictures are different, and in practice, the focused beam is much more intense than the non-focused field. The scale-bar on the pictures is 500 µm.

background and a dark photobleached line at a position x_0 and along the z direction. Before shearing, at any height z, the thickness of the bleached line along the x direction is Gaussian:

$$I_0(x,z) = \mathcal{I}_0(x) = I_\mathrm{i} - A\exp\left(-\frac{(x-x_0)^2}{2\sigma_0^2}\right) \tag{7.4}$$

where I_i, A and σ_0 are constant depending on the laser, the focus and the photobleaching process[c]. These parameters are obtained by fitting the initial profile.

When the liquid is sheared, each layer at a position $z \in [0,h]$ is displaced of a distance $d(z)$. Because we are in a laminar flow, the intensity profile along x, at the height z is given by:

$$I_\mathrm{sh}(x,z) = I_0(x-d(z)) \tag{7.5}$$

In particular, in $z=h$, if there is no slip on the prism, the displacement is $d(h) = d_\mathrm{t} = U\Delta t$, and we write d_b the displacement on the wafer (at $z=0$). Thus, the integrated intensity is given by:

$$\mathcal{I}_\mathrm{sh} = \frac{1}{h}\int_0^h I_0(x-d(z))dz = I_\mathrm{i} + B\left[\mathrm{erf}\left(\frac{x-x_0-d_\mathrm{t}}{\sqrt{2}\sigma_0}\right) - \mathrm{erf}\left(\frac{x-x_0-d_\mathrm{b}}{\sqrt{2}\sigma_0}\right)\right] \tag{7.6}$$

with $B = \frac{A\sigma_0\sqrt{\pi/2}}{d_\mathrm{t}-d_\mathrm{b}}$ and erf the error function[d]. The only unknown is d_b and thus we can obtain it by analysing the $\mathcal{I}_\mathrm{sh}(x)$ profile. The slip length b is finally determined using:

$$b = \frac{h}{d_\mathrm{t}/d_\mathrm{b} - 1} \tag{7.7}$$

[c] In our case, $\sigma_0 \approx 20$ µm.
[d] $\mathrm{erf}(x) = \frac{2}{\pi}\int_0^x e^{-t^2}dt$.

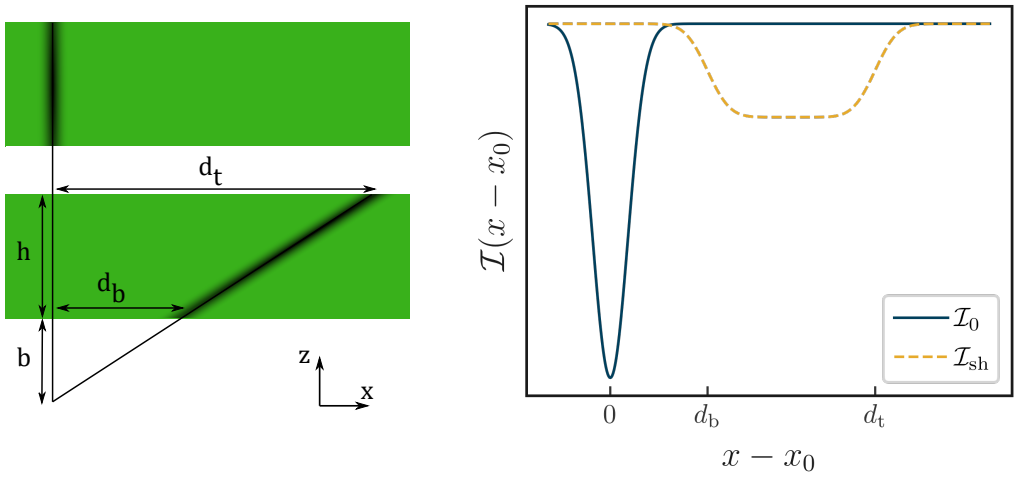

Figure 7.7: The bleached line is sheared (left). The integrated intensity over the thickness of the liquid $\mathcal{I}$ is plotted on the right for the initial bleached line (blue solid line) and for the sheared one (yellow dashed line). In $z = h$, the liquid has been displaced over a distance d_t. In $z = 0$, the liquid has moved (and thus slipped) over a distance d_b. This is a numerical simulation of the result.

7.2.3.2 The z-resolved method

This method is described in [187] and the current analysis is described in M. Grzelka PhD thesis [3]. For this method, we do not integrate over the z direction. In the writing mode, the focused laser beam hits the fluid from the top with an angle θ. Thus, the photobleached line follows the equation:

$$z = (y - y_0)\tan\theta \tag{7.8}$$

with y_0 the position along the y axis where the beam hits the top of the liquid. If we integrate the intensity profile along the x direction, we obtain the intensity profile

$$I(y) = I_1(y)I_2(y) \tag{7.9}$$

where $I_1(y)$ is given by:

$$I_1(y) = \left(\left[\operatorname{erf}\left(\frac{y-y_0}{\sqrt{2}\sigma}\right) - \operatorname{erf}\left(\frac{y-y_0+d}{\sqrt{2}\sigma}\right)\right] + R\left[\operatorname{erf}\left(\frac{y-y_0+d}{\sqrt{2}\sigma}\right) - \operatorname{erf}\left(\frac{y-y_0+2d}{\sqrt{2}\sigma}\right)\right]\right) \tag{7.10}$$

with $\sigma \equiv \sigma_0/\theta$, σ_0 the width of the laser beam, R the reflection coefficient on the wafer and $d \equiv h/\tan\theta$ the projected length of the line along y. $I_2(y)$ is a correction due to the fact that the beam is attenuated as it penetrates inside the liquid. A Beer-Lambert law with an absorption coefficient κ yields:

$$I_2(y) = \mathrm{e}^{-\kappa(y-y_0)} \tag{7.11}$$

Using a picture of the focused laser beam, we fit Eq. 7.9 to obtain the parameters σ_0, θ, κ and R.

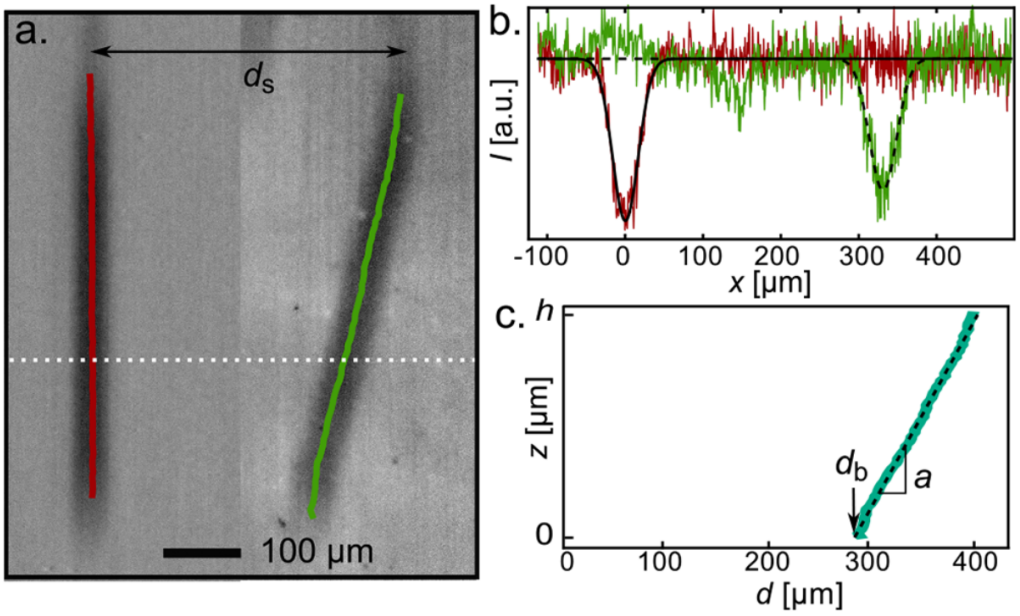

Figure 7.8: Determination of the displacement profile inside the liquid $d(z)$. Figure taken from M. Hénot *et al.* [187] (fig. 4). (a): bleached line (left) and sheared line (right). The coloured solid lines correspond to centres of Gaussian fits along x, illustrated in (b) taken at the position y plotted with the white dotted line in (a). (c): displacement profile deduced from the fitting of (a). d_s is the sheared distance, called d_t in the text, and d_b is the distance slipped on the wafer. The displacement field leads to $b = 239 \pm 7$ µm.

Now, to obtain the displacement profile $d(z)$ inside the liquid, we compare the initial photobleached line and the one after shear (see Fig. 7.8). The pictures are in the (x, y) plane. For each value of y, we fit a Gaussian to the intensity $I(x)|_y$ and we spot the centre of the Gaussian (solid lines in Fig. 7.8). Using Eq. 7.9, we can determine d for each y. We can thus reconstruct the profile $d(z)$ using Eq. 7.8 (Fig. 7.8 (c)). The distance slipped on the wafer d_b and the sheared distance on the prism d_t are determined by linearly fitting $d(z) = (d_t - d_b)z/h + d_b$. Assuming not slip at the prism/solution interface, the slip length at the wafer/solution interface is then deduced as before, using:

$$b = \frac{h}{d_t/d_b - 1} \tag{7.12}$$

7.2.4 Results

We apply this technique to measure the slip length b as a function of the temperature T of PS/DEP semi-dilute solutions of molar mass 10.2 Mg/mol. For the more concentrated solutions (5 and 6 %), we have used the z-resolved method, while for the 2.3 %, we have used the z-integrated method. The results are plotted in Fig. 7.9.

For both the 5 and the 6 % solutions, the slip length seems to be relatively independent of temperature. On the right graph, we have plotted the friction coefficient λ as a function of temperature. This has been done using the viscosity measured independently using a cone-plate rheometer, which values are shown in the inset. Contrary to the slip length, the friction coefficient seems to decrease significantly with temperature.

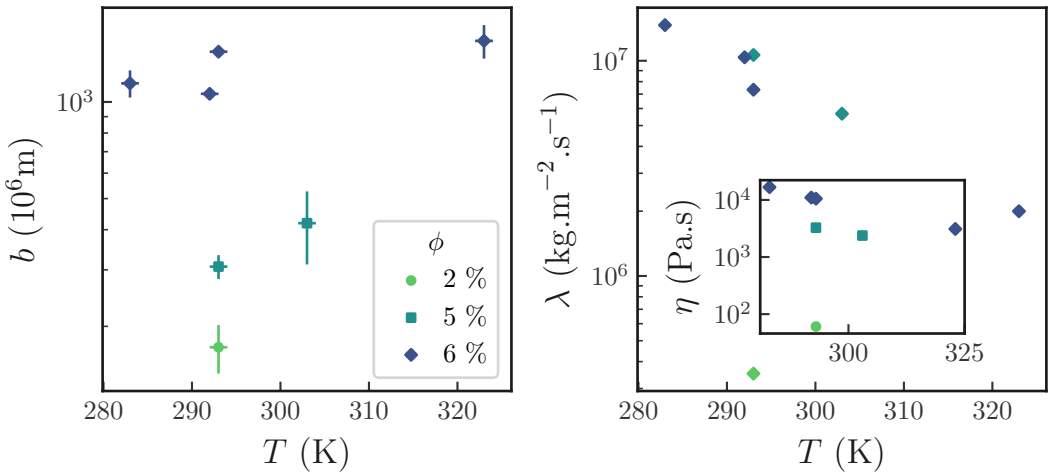

Figure 7.9: Slip length (left) and friction coefficient (right) as a function of temperature for PS/DEP solutions ($M_n = 10$ Mg/mol) at various volume fractions ϕ. The corresponding Newtonian viscosity $\eta(T)$ is plotted in the inset.

However, it is quite difficult to obtain precise measurements of the slip length as a function of temperature using this technique because the fluorescence of our label decreases significantly as the temperature is increased (see Fig. 7.10). To compensate this loss of fluorescence, we could increase the power of the laser in the reading mode, but this accelerates the photobleaching of the sample, and thus quickly reduces again the fluorescence. This strong effect of temperature is something that, unfortunately, was not anticipated, despite reported in the literature.

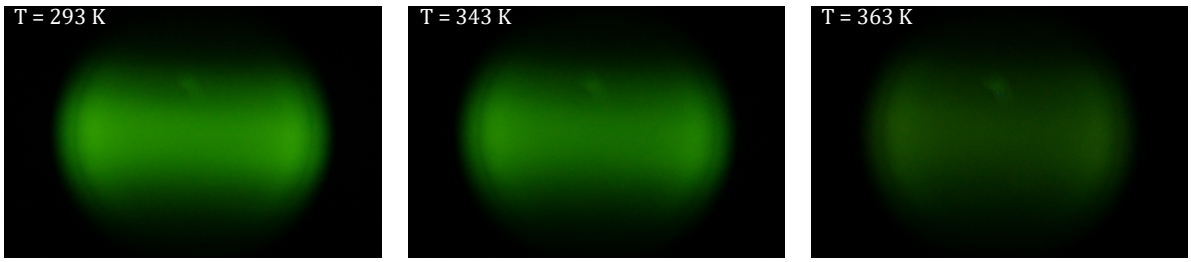

Figure 7.10: Fluorescent PS/DEP solution observed in FRAP at various temperatures.

To quantify the decrease of fluorescence, we have measured the absorbance spectrum (Cary Eclipse Spectrophotometer, Varian) of the fluorescent label (PS-diNBD) diluted in DEP, as a function of temperature. This is shown in Fig. 7.11. We can see that the intensity of the absorbance peak decreases as the temperature is increased. When the liquid is cooled down to 20 °C after being heated, it does not fully recover its original fluorescence.

Since the precision of the TPP technique is directly linked to the ability to distinguish a neat bleached line inside the sample, a decrease of the fluorescence as the temperature is increased is a strong drawback. Therefore, we have tried to derive a new experimental protocol in order to measure slip lengths using a rheometer, since this does not require

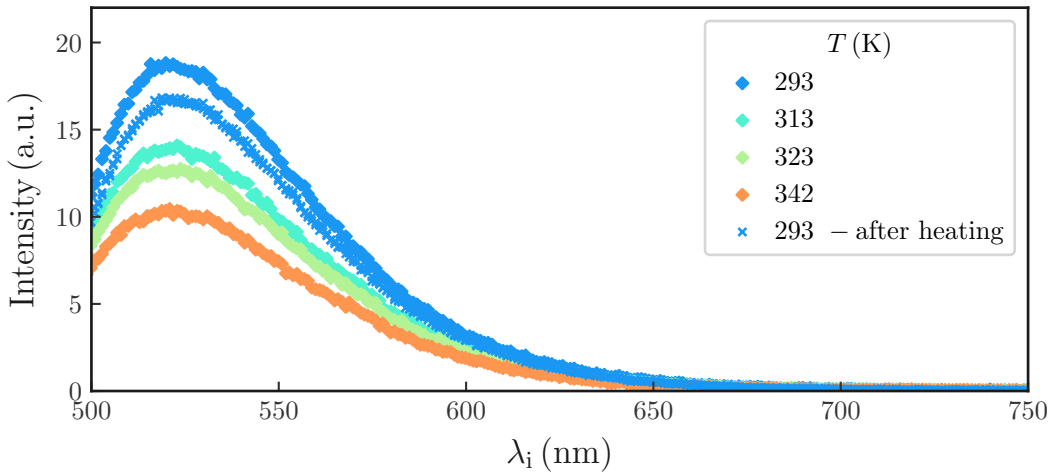

Figure 7.11: Absorbance spectra of PS-diNBD fluorescent label in DEP at various temperatures.

any use of fluorescent labels. In addition, the temperature control of the rheometer has proved its worth. Nonetheless, the TPP technique is extremely powerful in the sense that it allows one to have access to the slip length and the true shear-rate during the shear, while with a rheometer, we have only access to an average slip length and the apparent shear-rate. This will be discussed in the following section.

7.3 Measuring slip with a rheometer

Measuring a slip length requires high sensitivity techniques. The increasing performances of rheometers give access to precise measurements of the force required to make a liquid flow, and therefore, a tiny change in the boundary condition at the wall can detected on the measurement of these forces. In many cases, this is a drawback and results in errors on the measurements if one wants to determine a quantity such as the viscosity. That is why, in general, in shear rheology, scientists use rough surfaces if they suspect slippage in order to prevent it. On the contrary, we can take advantage of this great sensitivity and use it to measure the slip length.

In the 1930s, Melvin Mooney developed the so-called "Mooney" analysis [44] in order to measure the slip length with a shear rheometer. It was originally designed by Melvin Mooney to measure slip in capillaries and Couette geometries, and later adapted by Yoshimura and Prud'homme [45] for parallel disks. It has then been used by several groups [46, 188–191] as the reference technique to measure the wall slip as a function of the shear-stress using a rheometer. In particular, Sanchez-Reyes and Archer [46] have used this method to extract the slip length of PS/DEP solutions as a function of an effective stress σ_R. We start this section by the derivation of the simplified Mooney's analysis as described in [45] and discuss the results of Sanchez-Reyes and Archer. In a second part, we will derive our own analysis to try and extract the friction coefficient as a function of both the shear-rate and the temperature.

7.3.1 Historical measurement: the Mooney's analysis

Let us consider two parallel plates, the bottom one is a fixed wafer on which we expect slip, while the top one is a rough non-slipping surface rotating at the rotational velocity Ω. The original derivation has been conducted for a symmetrical system in which both surfaces are assumed identical, both with slippage, but in our case only the bottom surface slips, and thus we will derive the equations with the latter assumption (it basically changes the results by a factor of 2). The distance between the two plates is h, and their radius is R. The liquid is sandwiched between the two. Since there is slip on the bottom surface, the true shear-rate $\dot{\gamma}$ and the apparent shear-rate $\dot{\gamma}_{\mathrm{a}}$ are not equal, and, in addition, they vary along the geometry. They are given by:

$$\dot{\gamma}(r) = \frac{\Omega r - v_{\mathrm{s}}(r)}{h} = \frac{r\Omega}{h+b} \; ; \; \dot{\gamma}_{\mathrm{a}}(r) = \frac{r\Omega}{h} \tag{7.13}$$

with r the distance from the centre of the geometry, b the slip length on the slippery wall and $v_{\mathrm{s}}(r)$ the slip velocity on the wafer, which is the velocity of the liquid at the wall. This velocity *a priori* depends on r. In the following, we will use $\dot{\gamma}_{\mathrm{aR}} \equiv R\Omega/h$ the apparent shear-rate at the edge of the geometry, and similarly $\dot{\gamma}_{\mathrm{R}} \equiv (R\Omega - v_{\mathrm{s}})/h$ the true shear-rate at the edge of the geometry.

Now, the torque Γ applied to the top geometry is related to the stress inside the liquid $\sigma(r)$ through [192]:

$$\Gamma = \int_0^R 2\pi r^2 \sigma(r) \mathrm{d}r \tag{7.14}$$

if we apply the change of variable $r \to h\dot{\gamma}_{\mathrm{a}}(r)/\Omega$, we obtain:

$$\Gamma = \frac{2\pi R^3}{\dot{\gamma}_{\mathrm{aR}}^3} \int_0^{\dot{\gamma}_{\mathrm{aR}}} \dot{\gamma}_{\mathrm{a}}^2 \sigma(\dot{\gamma}_{\mathrm{a}}) \mathrm{d}\dot{\gamma}_{\mathrm{a}} \tag{7.15}$$

which we can differentiate with respect to $\dot{\gamma}_{\mathrm{aR}}$:

$$\frac{\mathrm{d}\Gamma}{\mathrm{d}\dot{\gamma}_{\mathrm{aR}}} = 2\pi R^3 \left[\frac{-3}{\dot{\gamma}_{\mathrm{aR}}^4} \int_0^{\dot{\gamma}_{\mathrm{aR}}} \dot{\gamma}_{\mathrm{a}}^2 \sigma(\dot{\gamma}_{\mathrm{a}}) \mathrm{d}\dot{\gamma}_{\mathrm{a}} + \frac{1}{\dot{\gamma}_{\mathrm{aR}}} \sigma_R \right] \tag{7.16}$$

with $\sigma_R \equiv \sigma(\dot{\gamma}_{\mathrm{aR}})$. Then it follows that:

$$\sigma_R = \frac{\Gamma}{2\pi R^3} \left(3 + \frac{\mathrm{d}\ln\Gamma}{\mathrm{d}\ln\dot{\gamma}_{\mathrm{aR}}} \right) \tag{7.17}$$

Eq. 7.17 is a common rheology equation and can be used to obtain the stress σ_R by measuring the torque Γ as a function of the apparent shear-rate $\dot{\gamma}_{\mathrm{aR}}$ (see Fig. 7.12, left). We obtain a curve $\sigma_R(\dot{\gamma}_{\mathrm{aR}})$ which will be more convenient to plot as $\dot{\gamma}_{\mathrm{aR}}(\sigma_R)$ (see Fig. 7.12, right). We need to have this curve for at least two different liquid thicknesses h_1, h_2.

Then, the idea is, for each stress σ_R, to compare the apparent shear-rates $\dot{\gamma}_{\mathrm{aR}_1}$ and $\dot{\gamma}_{\mathrm{aR}_2}$ corresponding to the two thicknesses h_1 and h_2. Using Eq. 7.13, this can be written as:

$$\dot{\gamma}_{\mathrm{aR}_1}(\sigma_R) = \dot{\gamma}_R(\sigma_R) + \frac{2v_{\mathrm{s}}(\sigma_R)}{h_1} \tag{7.18}$$

$$\dot{\gamma}_{\mathrm{aR}_2}(\sigma_R) = \dot{\gamma}_R(\sigma_R) + \frac{2v_{\mathrm{s}}(\sigma_R)}{h_2} \tag{7.19}$$

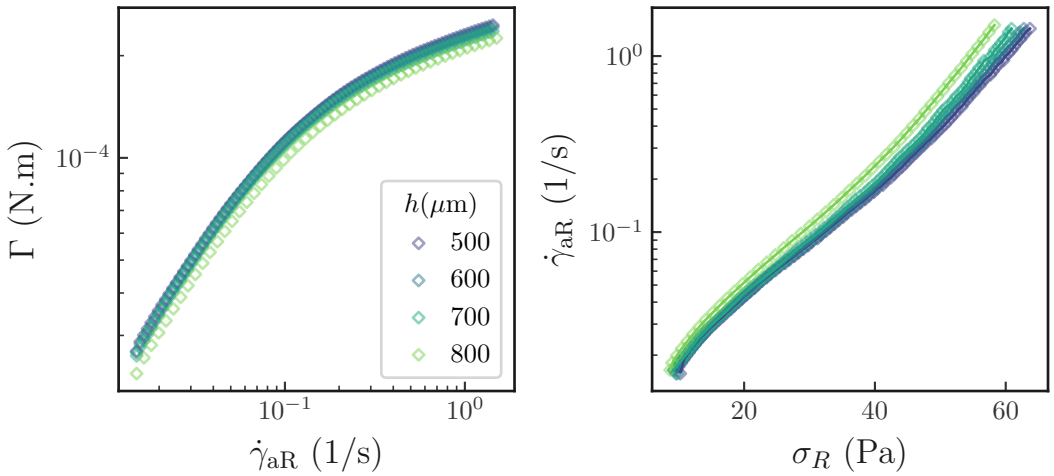

Figure 7.12: Rheology measurement of a PS/DEP solution (10Mg/mol, 4%) on a bare silicon wafer. Left: torque Γ as a function of the apparent shear-rate at the edge of the disk $\dot{\gamma}_{aR}$. Right: $\dot{\gamma}_{aR}$ as a function of the calculated stress σ_R using Eq. 7.17.

Since we work with a stress-imposed configuration, the true shear-rates $\dot{\gamma}_R$ are the same for a given σ_R.

Now we make the hypothesis that $v_s(\sigma_R)$ is independent of h. This can be understood by considering the Navier's hypothesis $\sigma = \lambda v_s$: at an imposed stress σ, if λ is a constant, v_s is independent of h. Thus we can combine Eqs. 7.18 and 7.19 to obtain the slip velocity v_s:

$$v_s = \frac{\dot{\gamma}_{aR1} - \dot{\gamma}_{aR2}}{1/h_1 - 1/h_2} \tag{7.20}$$

The slip velocity is related to the slip length by:

$$\dot{\gamma}_R = \frac{\Omega R - v_s}{h} = \frac{\Omega R}{h + b} \tag{7.21}$$

and thus it follows that:

$$b = \frac{(\dot{\gamma}_{aR1} - \dot{\gamma}_{aR2}) h_1 h_2}{h_2 \dot{\gamma}_{aR2} - h_1 \dot{\gamma}_{aR1}} \tag{7.22}$$

The results of the calculations are shown in Fig. 7.13 for a PS/DEP solutions (10Mg/mol, $\phi = 4$ %). As a comparison, in Fig. 7.14, we plot the results found by Sanchez-Reyes and Archer [46] for PS/DEP semi-dilute solutions of high molar masses on bare smooth substrates (silicon and titanium surfaces). The shape of their curves are relatively the same as ours, although they observe a bell shape for the slip length b while we observe only an increasing curve. Nonetheless, the solution we use has already been studied by M. Grzelka during her PhD thesis using the tracking of photobleached patterns technique, and she had found a slip length between 300 and 400 µm (see [3] fig.5.5 and [97] fig.2). Sanchez-Reyes and Archer argued that their bell-shaped curve has the following origin: at low stresses, because of adsorption of PS chains onto the surface, there is a slip transition as the shear-rate (and thus the stress) is increased. For higher stresses, the viscosity enters

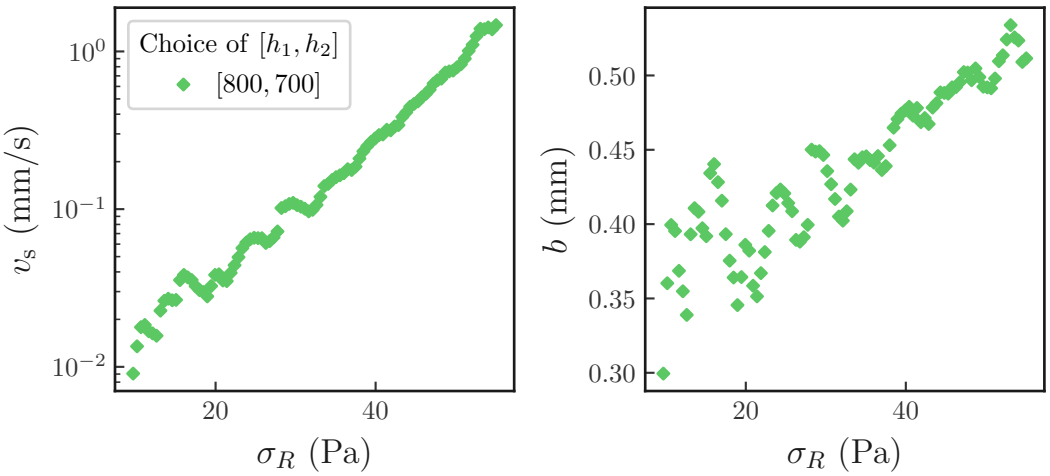

Figure 7.13: Calculated slip velocity v_s (left) from Eq. 7.21 and b (right) from Eq. 7.22. The calculation has been done by comparing the $h = 800$ and $h = 700$ µm curves.

a shear-thinning regime, and thus the slip length decreases. We cannot reach this regime, since the Weissenberg effect starts to empty our geometry approximately when the fluid becomes shear-thinning (for the Weissenberg number $\mathrm{Wi} \equiv \dot{\gamma}/\omega_{\mathrm{rept}} \approx 1$). Several details may explain why we could not reproduce exactly the same results as Sanchez-Reyes and Archer [46], who :

- do not mention any issue regarding the $\mathrm{Wi} > 1$ regime.
- do not mention the acquisition time they choose for each data point. This is an important parameter, not only because the acquisition time has to be much larger than $1/\dot{\gamma}$ but also because it has recently been shown that viscoelastic polymer solutions has an onset of the slip length [7]. A handy criterion is that a constant slip length is reached after a time larger than 5 times the reptation time of the solution. This can be a very large time for semi-dilute solutions of high molar masses.
- implicitly assume that the friction coefficient, $\lambda = \eta/b$, does not have any shear-thinning effect. This is not always the case, as shown in Chapter 4, where we have shown that the friction coefficient can display a shear-thinning behaviour at high shear-rates. This is discussed below.
- in addition, the fact that b depends on σ and thus on $\dot{\gamma}$ implies that b is not homogeneous over the whole geometry. Thus, the hypothesis of a homogeneous b taken in the calculation is questionable.

In addition, if we try to compare the slip velocity and slip length profiles obtained for various choices of the pair $[h_1, h_2]$, the curves have very different shapes (see Fig. 7.15). This might be the consequence of the fact that the previous derivation assumes a **homogeneous slip length b over the whole disk**, which is likely to be incorrect at least due to the presence of adsorbed chains at the interface. b is thus $\dot{\gamma}$-dependent and therefore b is r-dependent. Another possibility for the discrepancy of these curves might be the lack

of parallelism of our two disks. In the work of Sanchez-Reyes and Archer, parallelism is achieved by glueing the plates *in situ*, pressing them in contact with each other using the rheometer itself. In our case, we have glued only the bottom geometry by manually applying a pressure, outside the rheometer. This might lead to a slightly less parallel system.

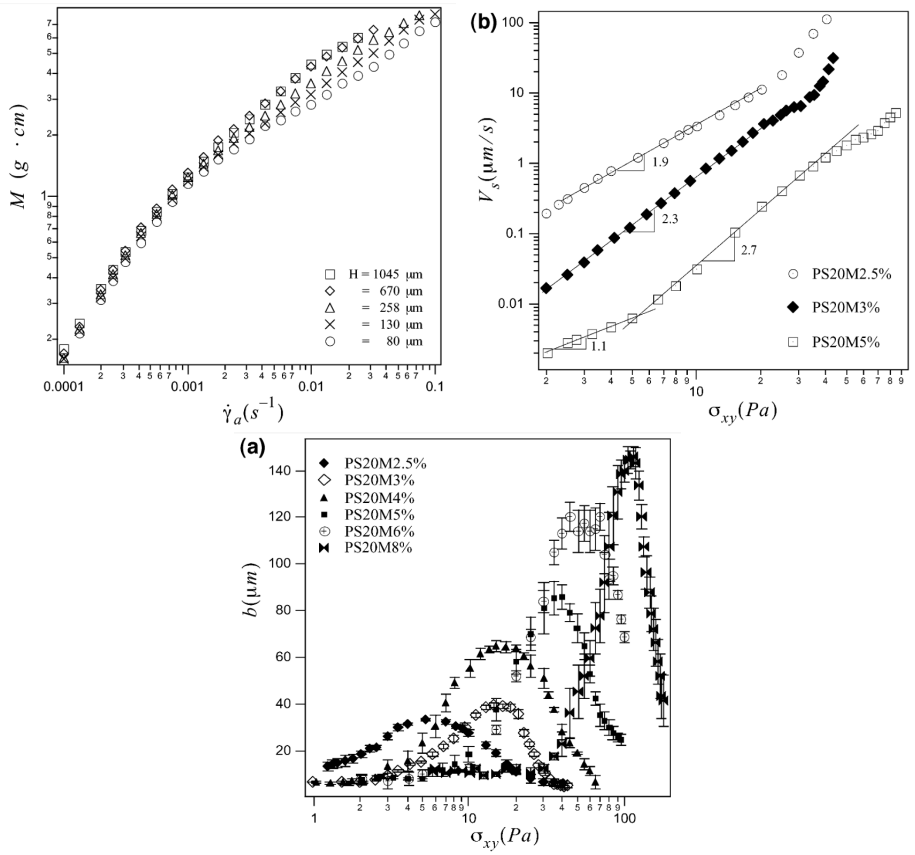

Figure 7.14: Results of slip measurement using the Mooney analysis for PS/DEP solutions of molar mass 20 Mg/mol at various volume fractions. The surfaces are bare titanium or silica. Top left: torque M as a function of $\dot{\gamma}_{\mathrm{aR}}$ for various gaps H. Top right: deduced slip velocity V_{s} as a function of the stress σ_{xy} (σ_R in our derivation). Bottom: slip length as a function of σ_{xy}. Taken from [46].

In any case, it seems questionable to use this analysis in our case. In particular, the slip length is extracted from the tiny torque difference between two gaps. It is likely that the torque difference is actually smaller than the torque resolution of the rheometer, as illustrated by the contested results of Choi and Kim [193], which raised the discussion reported in [194, 195]. In this paper, the authors have used a Mooney-like analysis to measure slip lengths using a cone-plate geometry. The additional problem of using a cone-plate geometry is the very small amount of liquid that is sheared. Thus, not only the torques are small, but some edge effects might appear. In our case, after many failed attempts to obtain similar curves as Sanchez-Reyes and Archer, we have not persisted in reproducing this analysis with our samples, and we have decided to derive our own approach to the problem instead. This is explained in the following section.

7.3.2 Derivation of a new analysis

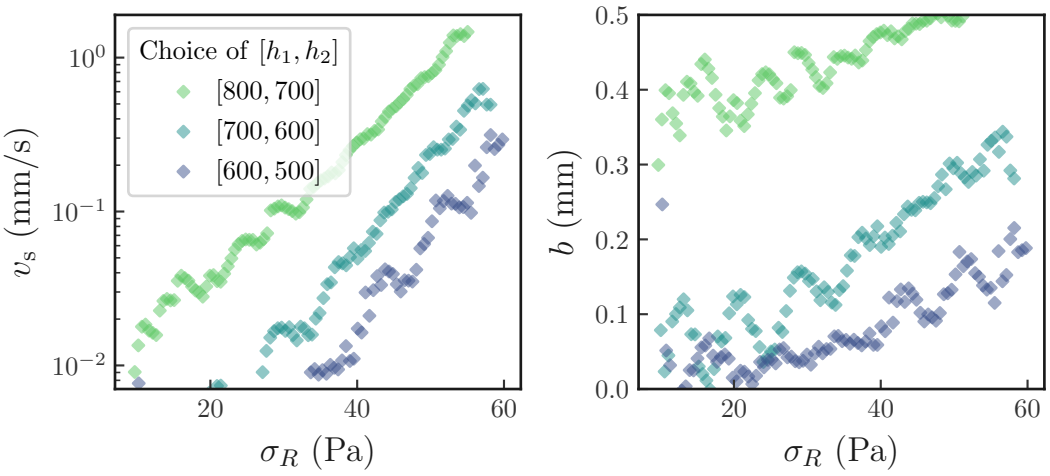

Figure 7.15: Same as Fig. 7.13 but for various choices of the pair $[h_1, h_2]$.

The derivation of this analysis is illustrated by a measurement for a PS/DEP solution (20.6 Mg/mol, 5 %) slipping on a bare silicon wafer, and thus on its own adsorbed layer. The set-up is the same as before: we use a plane-plane geometry, the top geometry is sand-blasted to prevent slip, the bottom geometry is a fixed wafer. Only the top geometry is rotating, and we measure the torque Γ as a function of the rotational velocity Ω. The error due to the lack of parallelism is estimated in Appendix , and is less than 0.5 %. The analysis requires a precise determination of the viscosity $\eta(\dot{\gamma})$ profile. We thus start by the viscosity measurement, in a cone-plate geometry with both surfaces sandblasted. This is Section 7.3.2.1. Then, in Section 7.3.2.2, we derive our calculation of the friction coefficient from the torque measurement at a single liquid thickness h. In Section 7.3.3, we show the dependency of λ with the shear-rate and the temperature, and we compare our slip measurements to measurements done using the TPP technique. Finally, in Section 7.3.4, we try to provide a physical description of the shapes of the curves obtained for $\lambda(\dot{\gamma})$, and we discuss the possible link with an interfacial viscosity.

7.3.2.1 Viscosity measurement

For the viscosity, an independent measurement in a cone-plat geometry gives us access to the dependency of η with $\dot{\gamma}$, which is well described by a Carreau-Yasuda (CY) [196–198] model:

$$\eta = \eta_0(1 + (\tau_\eta \dot{\gamma}_{\text{app}})^a)^{(n-1)/a} \tag{7.23}$$

The CY works well for shear-rates $\dot{\gamma}$ up to 1 s^{-1} (which correspond to Weissenberg numbers $\text{Wi} = \dot{\gamma}\tau_\eta$ up to 10^2) (see Fig. 7.16). An Arrhenius model (see Section 1.2.1.1) describes well the temperature dependency of both η and τ_η, which share a common activation energy $E_a \simeq 20 \pm 1$ kJ/mol for the PS/DEP 20.6 Mg/mol 5 % shown in Fig. 7.16. The exponents n and a (not shown here) do not depend on temperature and are 0.24 ± 0.02 and 2.0 ± 0.2, respectively.

7.3.2.2 Calculation of the friction coefficient

Now that we have access to the viscosity for any $\dot{\gamma}$, we can derive our calculation of the friction coefficient λ. As previously, the torque Γ is given by the integral of the stress

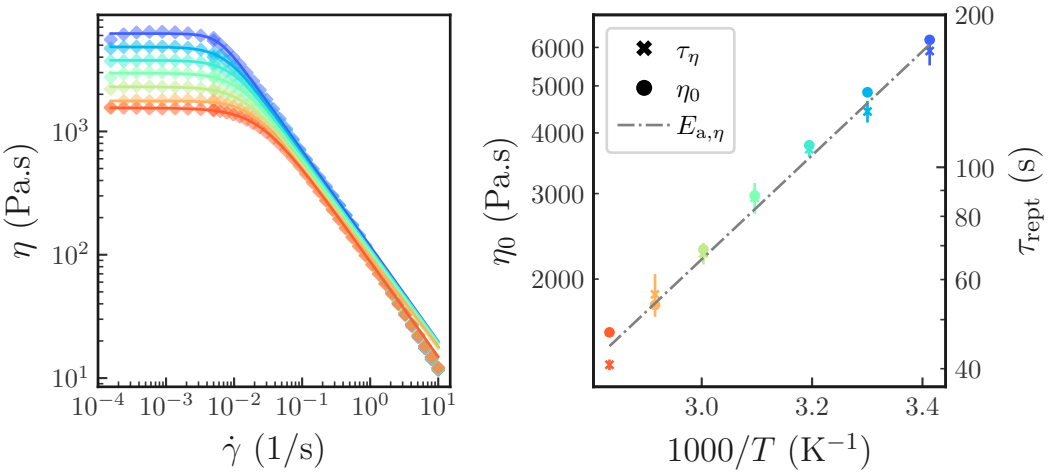

Figure 7.16: Viscosity measurement of a PS/DEP solution (20.6Mg/mol, $\phi = 5$ %) from a cone-plate geometry (no slip). Left: viscosity as a function of the (true) shear-rate $\dot{\gamma}$. Solid lines correspond to Carreau-Yasuda (CY) regressions. Colours correspond to the temperature of the liquid, from 20 °C to 80 °C by steps of 10 °C. Right: η_0 and τ_{rept} obtained from the CY fit on the viscosity. The Arrhenius fit gives the same activation energy for both η and τ_{rept} : $E_a \simeq 19.7 \pm 0.9$ kJ/mol.

$\sigma(\dot{\gamma}) = \eta(\dot{\gamma})\dot{\gamma}$ over the whole surface:

$$\Gamma = \int_0^R 2\pi r^2 dr \sigma(\dot{\gamma}) \tag{7.24}$$

where R is the radius of the geometry and η is the viscosity of the liquid. If there is no slip, at any r, the shear-rate is $\dot{\gamma} = \frac{r\Omega}{h}$ with Ω the rotational velocity of the top geometry and h the thickness of the liquid layer, and thus, we can calculate explicitly the torque Γ_{calc}. In Fig. 7.17, we plot the measured torque, and we compare it to this calculated torque Γ_{calc} using the no-slip boundary condition on both surfaces.

We clearly see that the calculated torque is much higher than the measured torque, and their difference is much larger than the error on the torque measurement, which is a good sign of the existence of slip on the wafer. Our idea is now to calculate the torque including the slip boundary condition. In case of slip, at any point r, the shear-rate is given by :

$$\dot{\gamma} = \frac{r\Omega}{h+b} = \frac{r\Omega}{h + \frac{\eta}{\lambda}} \tag{7.25}$$

Both η and λ could depend on the local shear rate, and thus on the position r inside the geometry, resulting in a very complicated explicit calculation of the torque. To simplify, we assume a constant friction coefficient $\bar{\lambda}$ over the whole geometry. The function $\eta(\dot{\gamma})$ has already been precisely determined in an independent cone-plane oscillatory measurement with rough geometries, described in Section 7.3.2.1.

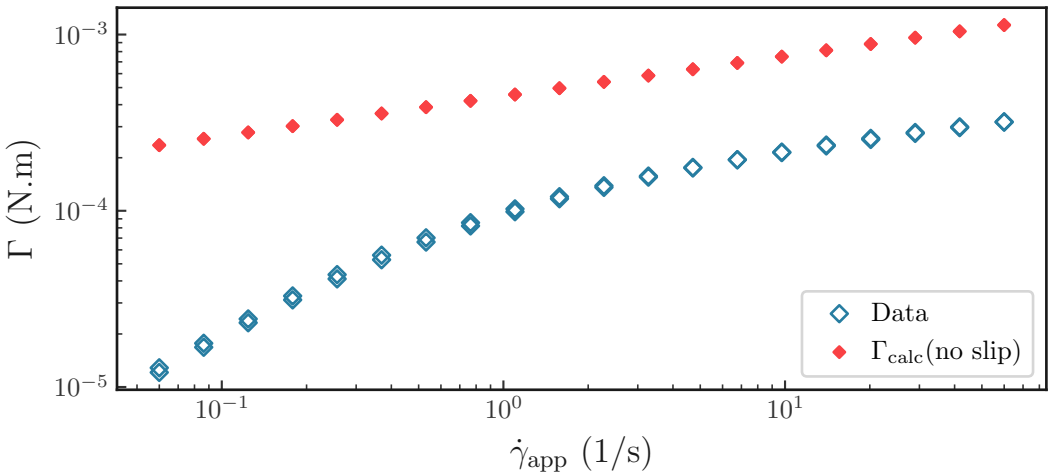

Figure 7.17: Torque Γ as a function of the applied rotational velocity Ω for a PS/DEP 20.6M 5 % at 20 °C flowing on its own adsorbed chains. Empty blue diamonds correspond to experimental measurements, and red squares to the calculated torque assuming $b = 0$.

Now, to calculate the resulting torque, we discretise the integral 7.24 using the constitutive equation $\sigma(\dot{\gamma}) = \eta(\dot{\gamma})\dot{\gamma}$:

$$\Gamma = \sum_{i=1}^{N} 2\pi r_i^2 \Delta R \eta(\dot{\gamma}_i)\dot{\gamma}_i \tag{7.26}$$

with $\Delta R = R/N$, $N = 1000$ the number of discretized points and $r_i = i\Delta R$. The delicate part is that, in $r = r_i$, the shear-rate $\dot{\gamma}_i$ depends on the slip length b_i which itself depends on $\dot{\gamma}_i$ and so on. To avoid this loop, we make the hypothesis that the shear-rate in r_i is given by the slip length in r_{i-1}: $\dot{\gamma}_i = \frac{r_i \Omega}{h+b_{i-1}}$ with $b_{i-1} = \eta(\dot{\gamma}_{i-1})/\bar{\lambda}$. We need an initial condition for this recursion. We make the hypothesis that $b_0 = 0$. We make this hypothesis because at the centre of the geometry, the applied shear-rate is 0, and thus the slip length is expected to be small near $r = 0$. We write $\eta(0) = \eta_0$ the Newtonian viscosity known from the Carreau-Yasuda fit. All the parameters are known except $\bar{\lambda}$ and thus, we look for the value of $\bar{\lambda}$ that minimises the difference between the calculated torque Γ_{calc} and the measured torque $\Gamma_{measured}$. This calculation is done for each value of the rotational velocity Ω, and thus, we obtain a curve $\bar{\lambda}(\Omega)$ or equivalently $\bar{\lambda}(\dot{\gamma})$.

In Fig 7.18, we plot the measured torque (blue diamonds), the calculated torque with the no-slip boundary condition (red diamonds) and the calculated torque taking into account the slip boundary condition (green crosses) as described above. The previous derivation allows us to calculate a torque which is really close to the experimentally measured torque ($(\Gamma_{exp} - \Gamma_{calc,\ slip})/\Gamma_{exp}$ is less than 2 %).

7.3.3 Results

7.3.3.1 Effect of the applied shear-rate

In Fig. 7.19, we plot the friction coefficient averaged over the whole geometry $\bar{\lambda}$ (top) and the averaged slip length $\bar{b}$ (bottom) derived with the previous calculation, as a function of the applied rotational velocity. This experiment has been done for two different

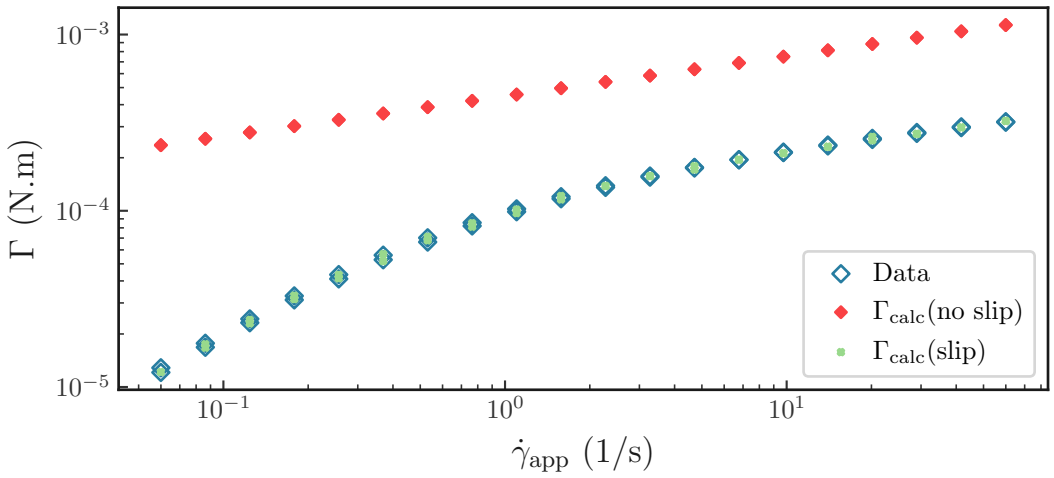

Figure 7.18: Torque Γ as a function of the applied rotational velocity Ω for a PS/DEP 20.6M 5 % at 20 °C flowing on its own adsorbed chains. Empty blue diamonds correspond to experimental measurements, red squares to the calculated torque assuming $b = 0$ and green crosses to the torque calculated taking into account slip using the method described in the text.

samples:

- a PS10M/DEP solution of volume fraction $\phi = 4.0$ % on its adsorbed layer (light blue).
- a PS20M/DEP solution of volume fraction $\phi = 5.0$ % on its adsorbed layer (dark blue).

First, we observe that the measured friction coefficient $\bar{\lambda}$ decreases with the apparent shear-rate $\dot{\gamma}_{app}$. For the PS20M5%, it seems to reach a plateau at low shear-rates, while no inflexion is visible for the PS10M4%. The decrease is steeper for PS10M4%, with an exponent -0.8 while we find an exponent around -0.6 for PS20M5%. Combining $\bar{\lambda}$ and the viscosity previously obtained η, we can plot the shear-rate dependency of $\bar{b}$. Surprisingly, both samples yield to completely different profiles. The less viscous sample (PS10M4%) shows an increasing slip length with the shear-rate, while the PS20M5% has a decreasing slip length. The top axis in each plot indicates the apparent bulk Weissenberg number, defined as $\mathrm{Wi}_{app}^{bulk} \equiv \dot{\gamma}_{app}\tau_{rept}$ where τ_{rept} is the (longest) relaxation time obtain by the CY fit of the viscosity $\eta(\dot{\gamma})$[e]. Ideally, we would like to plot $\bar{\lambda}$ and $\bar{b}$ as a function of the interfacial stress, or even the slip velocity v_s but our analysis does not give access to these parameters.

For the more viscous solution, we are in a regime of higher Wi_{app}^{bulk} compared to the less viscous solution, which might explain the difference of behaviour for the slip length. Indeed, the behaviour of $\bar{b}(\dot{\gamma}_{app})$ depends on the relative shear-rate dependencies of η and $\bar{\lambda}$. If we are in a "low" Wi regime (PS10M4%), the viscosity does not decrease quickly yet, while $\bar{\lambda}$ already decreases significantly, resulting in an increase of the slip length. On the

[e] identified with the reptation time τ_{rept} of the solution.

contrary, if we are in a "high" Wi regime (PS20M5%), the viscosity is already strongly decreasing, whereas the friction coefficient decreases slowly at the beginning of the curve, which indeed results in a decreasing slip length. The Weissenberg number compares the applied shear-rate to a typical relaxation time. Here, we only discuss our data using the "bulk" Weissenberg number because we only have access to the typical relaxation time of our bulk solution. It is not obvious that this relaxation time is the same for the bulk and the interfacial liquid. Indeed, in Chapter 6, we have seen that near the surface, we have a depleted layer and some adsorbed chains on the substrate[f]. Besides, we see that, for PS10M4%, $\bar{\lambda}$ has no visible plateau even if $\mathrm{Wi}_{\mathrm{app}}^{\mathrm{bulk}} < 1$, where η is constant. This already suggests that the relaxation time of the interface is different than the bulk relaxation time. To extract this information, we need to look at the effect of temperature on the friction coefficient $\bar{\lambda}$. This is the goal of the next section.

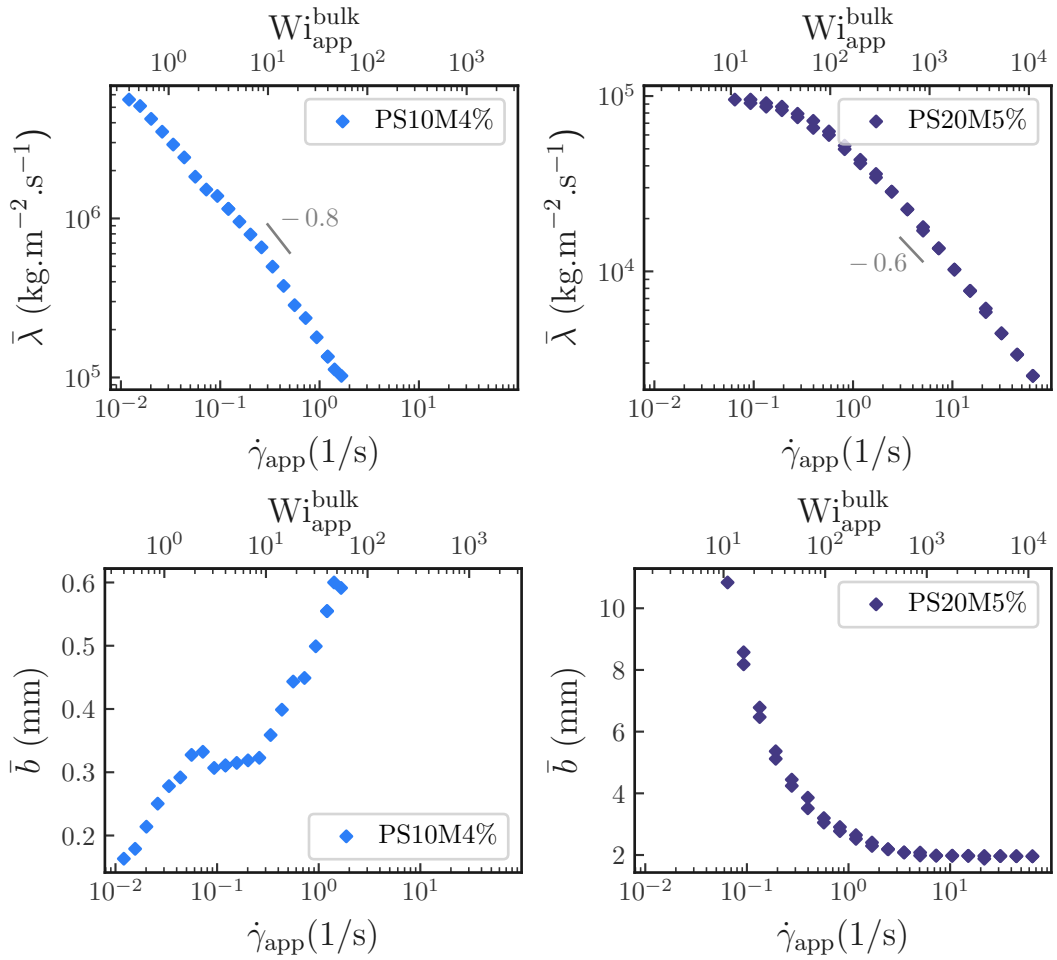

Figure 7.19: Comparison between PS/DEP 10 Mg/mol 4 % (left, light blue) and PS/DEP 20.6 Mg/mol 5 % (right, dark blue) flowing on their own adsorbed layer. Top: friction coefficient $\bar{\lambda}$. Bottom: slip length $\bar{b}$. Both are taken at $T = 293$ K. Top axis indicate the bulk apparent Weissenberg number, defined in the text.

[f]Actually, this has been done for a sapphire substrate, but the surface of the wafer is likely to behave in the same way, since chemically, the oxidised layer is similar, and there is *a priori* no reason why PS would interact differently with Si compared to Al.

7.3.3.2 Effect of temperature

We use the method derived in Section 7.3.2 to determine the slip length and the friction coefficient as a function of temperature. This is done with a PS/DEP solution of 20.6 Mg/mol and $\phi = 5$ %. The results are shown in Fig. 7.20, in which we plot $\bar{\lambda}$ and $\bar{b}$ as a function of $\dot{\gamma}_{\text{app}}$ (top graphs) For comparison, the viscosity as a function of the true shear-rate is also shown (bottom graph). It corresponds to the same solution, but from an independent measurement using a cone-plate geometry with no-slip boundary conditions. The Carreau-Yasuda regression of $\eta(\dot{\gamma})$ works well until $\dot{\gamma} = 1$ s^{-1}, but slightly overestimates the viscosity at higher shear-rates. This implies that the slip length $\bar{b}$ is calculated with a larger uncertainty at high shear-rates.

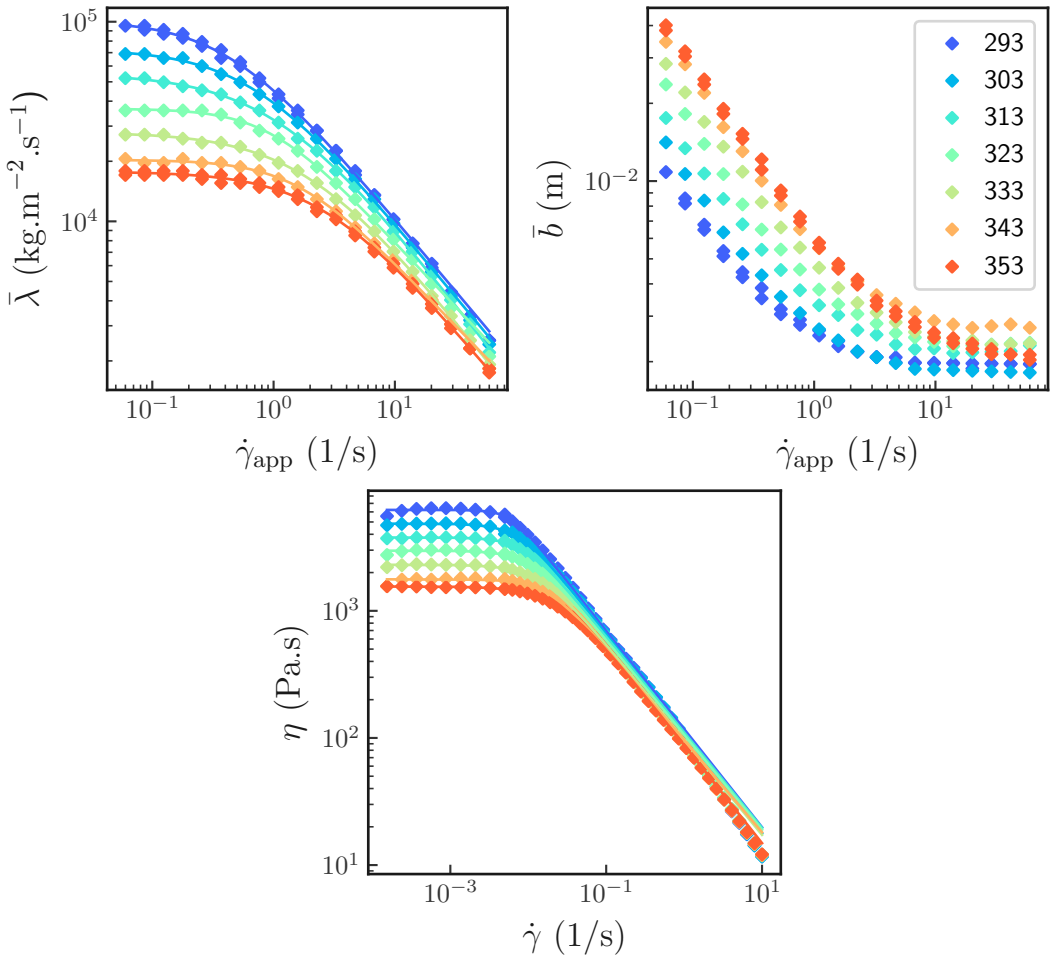

Figure 7.20: Top: Effect of temperature on the measured friction coefficient $\bar{\lambda}$ and slip length $\bar{b}$. Solid lines correspond to a CY fit. Bottom: viscosity as a function of the applied shear-rate, from an independent measurement using a cone-plate geometry with no-slip boundary conditions. The legend is the same for the three plots, indicating the temperature in Kelvins. This is done for the PS20M5% solution.

We fit both $\bar{\lambda}(\dot{\gamma})$ and $\eta(\dot{\gamma})$ with a Carreau-Yasuda function:

$$x = x_0 \left(1 + (\dot{\gamma}\tau)^a\right)^{(n-1)/a} \tag{7.27}$$

We obtain the plateau values of the viscosity (η_0) and the friction coefficient (λ_0) as a function of temperature, as well as the corresponding relaxation times τ_η and τ_λ. These four parameters are plotted as a function of the temperature in Fig. 7.21. They all follow an Arrhenius law, with the same activation energies for the plateau values and the relaxation times (20.5 ± 0.5 kJ/mol and 19.7 ± 0.9 kJ/mol for η_0 and τ_η, respectively ; and 26.1 ± 0.8 kJ/mol and 23.6 ± 3.5 kJ/mol for λ_0 and τ_λ, respectively). The exponents do not depend on temperature and are not shown here. We obtain $n = 0.24 \pm 0.02$ and $a = 2.03 \pm 0.19$ for the viscosity, and $n = 0.28 \pm 0.05$ and $a = 1.18 \pm 0.11$ for the friction coefficient. The activation energy of the friction coefficient is larger than the one of the viscosity, which implies that the slip length is a decreasing function of temperature, as we can indeed observe in Fig. 7.20 (top right). This corroborates the results from Hénot *et al.* [2] for PDMS melts and elastomers. In addition, we see that the relaxation time of the friction coefficient τ_λ is much smaller than the relaxation time of the bulk viscosity τ_η.

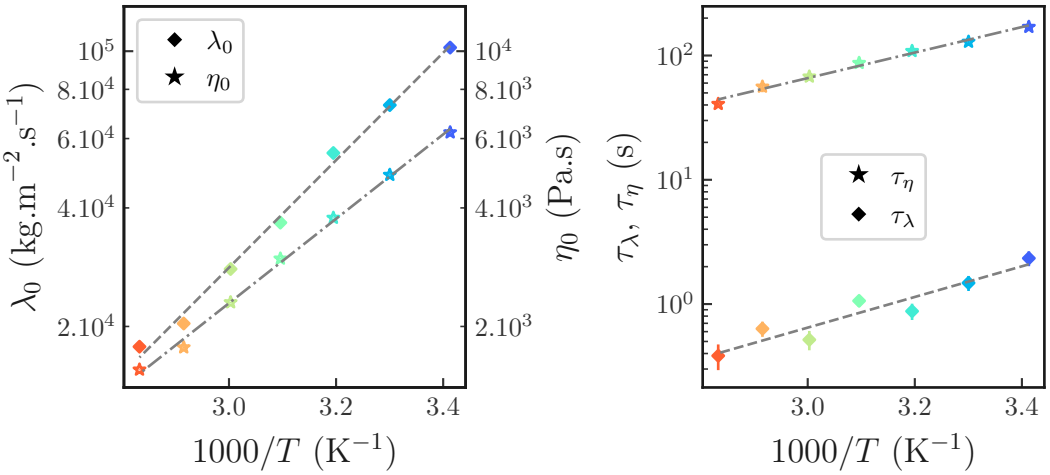

Figure 7.21: CY parameters for the friction and the viscosity as a function of the temperature. Each parameter is fitted with an Arrhenius law. We obtain $E_{a,\lambda_0} = 26.1 \pm 0.8$ kJ/mol and $E_{a,\eta_0} = 20.5 \pm 0.5$ kJ/mol for the activation energies of λ_0 and η_0, respectively, and $E_{a,\tau_\lambda} = 23.6 \pm 3.5$ kJ/mol, $E_{a,\tau_\eta} = 19.7 \pm 0.9$ kJ/mol for the relaxation times τ_λ and τ_η, respectively. This is obtained from data of the PS20M5% solution shown in Fig. 7.20.

In addition, from Fig. 7.20, we plot $\bar{\lambda}(T)$ at various apparent shear-rates $\dot{\gamma}_{app}$. This is shown in Fig. 7.22. Colours correspond to the values of $\dot{\gamma}_{app}$, and are indicated in the scale bar in the left graph. At a given $\dot{\gamma}_{app}$, we fit $\bar{\lambda}(T)$ by an Arrhenius law, and we plot the activation energy obtained from the fit as a function of the apparent shear-rate $\dot{\gamma}_{app}$ in the right graph. At low shear-rates, the activation energy is around 25 kJ/mol, and as the shear-rate increases, the activation barrier is lowered. This reminds the derivation of Eyring's theory described by Tabor in [63], where the flow lowers the energy barrier for the probability for molecules to move in its direction.

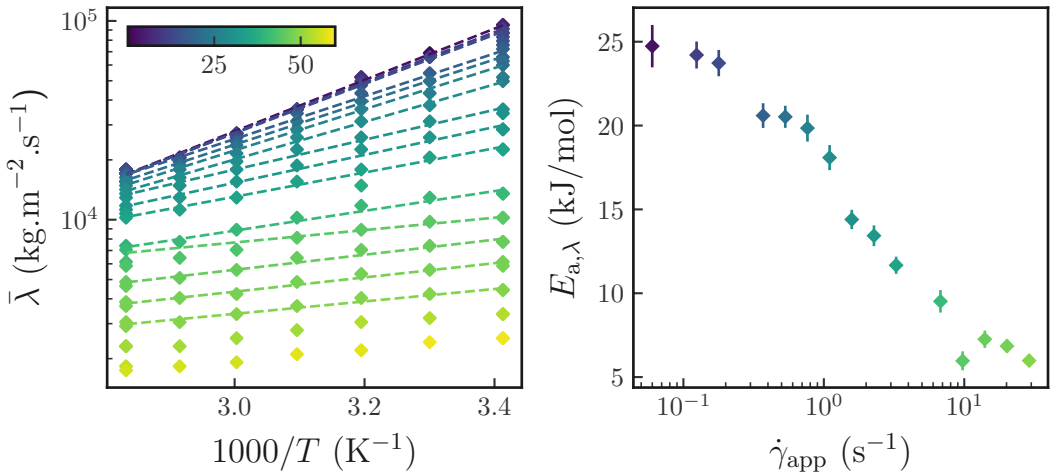

Figure 7.22: Left: friction coefficient $\bar{\lambda}$ as a function of temperature, for different apparent shear-rates $\dot{\gamma}_{app}$. Dashed lines correspond to Arrhenius fits at each shear-rate. The colour bar indicates the value of $\dot{\gamma}_{app}$. Right: activation energy $E_{a,\lambda}$ (obtained from the Arrhenius fit) as a function of $\dot{\gamma}_{app}$. The colours are the same for both plots.

7.3.3.3 Comparison with TPP experiments

In order to check the consistency of our measurements, we have measured the friction coefficient of a PS/DEP solution at 10 Mg/mol 4 % for which we had trustable TPP data to compare with. Two differences has to be enhanced:

- there is a difference between the surface studied in TPP and the one studied with the rheometer: for the TPP measurement, the solution has been freshly deposited on the wafer, and therefore the amount of adsorbed chains is low. For the rheology experiment, the solution has been kept in contact with the wafer for weeks at 52 °C in order to reach the saturation of the adsorbed layer. Therefore, there are much more adsorbed chains for the rheology experiment compared to the TPP measurement.

- with TPP, the friction coefficient λ is homogeneous over the whole surface, whereas we have access to a friction coefficient averaged over the whole geometry $\bar{\lambda}$ using the rheometer measurement.

The results are plotted in Fig. 7.23. Green open circles correspond to TPP measurements of λ and b taken from [3] and blue filled diamonds correspond to the results obtained using our rheology measurements, both plotted as a function of the bulk Weissenberg number $\mathrm{Wi}^{\mathrm{bulk}} \equiv \dot{\gamma}\tau_\eta$. We have indeed a good agreement between the values of λ and b with the two experiments, although the rheometer gives us access to an average friction coefficient $\bar{\lambda}$. We observe a slip transition for the $b(\mathrm{Wi})$ curves in both cases, but the transition happens at a lower Wi for the TPP experiment. We can imagine two reasons for this discrepancy.

First, it might be due to the fact that the Weissenberg number Wi in the x-axis is the true Wi in TPP, defined by $\mathrm{Wi}_{\mathrm{true}} = \frac{U}{h+b}\frac{1}{\omega_{\mathrm{rept}}}$ where U is the velocity applied at the top of the liquid. On the contrary, for the rheology measurement, we have only access to

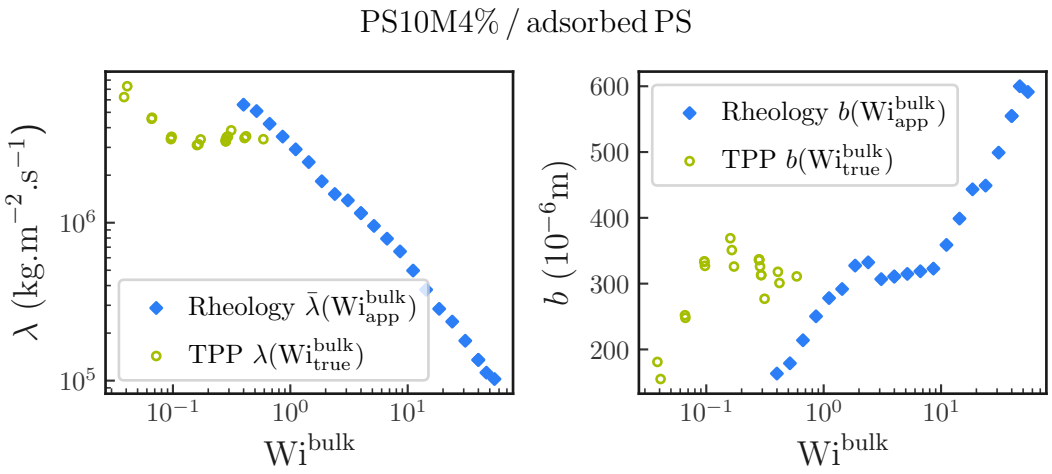

Figure 7.23: Friction coefficient λ and slip length b as a function of the Weissenberg number $\mathrm{Wi}^{\mathrm{bulk}} = \dot{\gamma}\tau_\eta$ from TPP (green open circles) and rheology (blue filled diamonds) experiments with the same solution (PS/DEP 10.2 Mg/mol 4 %) at room temperature. The shear-rate obtained from the TPP experiment is the true shear-rate $\dot{\gamma}_{\mathrm{true}}$ felt by the fluid, while in rheology we have only access to the apparent shear-rate $\dot{\gamma}_{\mathrm{app}}$.

the apparent Wi defined as $\mathrm{Wi}_{\mathrm{app}} = \frac{R\Omega}{h\omega_{\mathrm{rept}}} > \frac{R\Omega}{h+b}\frac{1}{\omega_{\mathrm{rept}}} = \mathrm{Wi}_{\mathrm{true}}$. Yet, this is probably not the only reason for this shift: if we introduce our measurement of $\bar{b}$ to calculate a "true" shear-rate $\dot{\gamma} = \frac{R\Omega}{h+\bar{b}}$, since the maximum value of $\bar{b}$ is 600 µm and $h = 650$ µm, the "true" shear-rate is at best shifted by a factor 2, and thus does not match the shear-rates of the TPP experiment.

The shift in the slip transition could also be due to the difference in the amount of adsorbed chains between the two experiments. Indeed, the critical shear-rate at which the slip transition occurs $\dot{\gamma}^*$ grows linearly with the surface density of adsorbed chains ν [28, 31, 95]. Since we have much more adsorbed chains in our rheology experiment, we expect a higher slip transition compared to the TPP measurement. In Fig. 7.24, we have shown the slip length as a function of the true shear-rate $b(\dot{\gamma}_{\mathrm{true}})$ for a PS5M18% solution in DEP flowing on its own adsorbed layer. This figure is taken from M. Hénot's PhD thesis [72]. Different colours correspond to different contact times between the surface and the solution. We see that the shear-rate $\dot{\gamma}^*$ at which we observe a slip transition increases significantly with the contact time. In particular, the transition is shifted by a factor of 10 between 54 h and 222 h of contact times. Thus, the shift we observe in Fig. 7.23 is likely to be due to the difference in contact time between the TPP and the rheometer experiment.

7.3.4 Discussion

7.3.4.1 Physical origin of the shear-rate dependency of the slip length

The understanding of the $\bar{\lambda}(\dot{\gamma})$ profile is not straight-forward. The choice of Ω imposes the range of velocities applied by the top surface $v(r) = r\Omega$ over the whole geometry, and thus the range of shear-rates to which the fluid is *a priori* subjected. Because the friction coefficient and the viscosity (and thus the slip length) depend on $\dot{\gamma}$, they all depend on r.

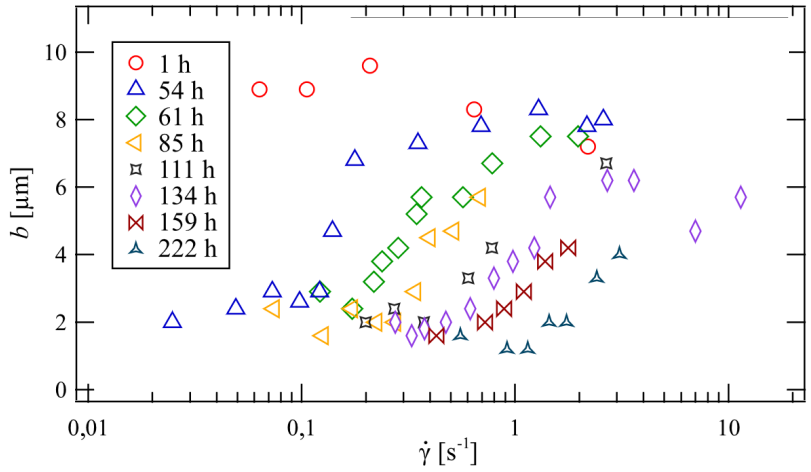

Figure 7.24: Slip length of a PS/DEP solution with M_n = 4.5 Mg/mol and ϕ = 18 % flowing on its own adsorbed layer as a function of the true shear-rate, obtained by TPP. Different colours correspond to different contact times between the solution and the surface, and therefore to different thicknesses of the adsorbed layer. The temperature of incubation is the room temperature. Figure taken from M. Hénot's PhD thesis [72].

Thus, the measured value of the torque Γ contains the average effect of the $b(\dot{\gamma})$ profile over the whole geometry. In order to discuss the average profiles $\bar{\lambda}(\Omega)$ and $\bar{b}(\Omega)$, we need first to describe what would be the expected profiles along the geometry.

Theoretical predictions and experimental measurements suggest a slip transition $b(\dot{\gamma})$ at $\dot{\gamma} = \dot{\gamma}^*$: at $\dot{\gamma} < \dot{\gamma}^*$, entanglements between the bulk and adsorbed chains lead to a strong friction (and thus a small slip). At $\dot{\gamma} = \dot{\gamma}^*$, both disentangle, and the friction coefficient abruptly decreases (and thus the slip increases) to reach a lower (larger) constant value. In addition, at higher shear-rates, the liquid becomes shear-thinning, and thus there is a transition at $\dot{\gamma} = 1/\tau_{\text{eta}}$ above which the viscosity decreases. This would result in a decrease of the slip length. Altogether, we would expect a bell-shaped $b(\dot{\gamma})$ curve, as observed by Mhetar *et al.* and Sanchez-Reyes and Archer [46,178]. These descriptions are usually given in terms of slip lengths only, since it is the quantity which is experimentaly accessible. Yet, with our derivation, we have access to the friction coefficient profile $\bar{\lambda}$. Our results suggest that $\lambda(\dot{\gamma})$ follows a shear-thinning behaviour, with a typical relaxation time τ_λ different from the bulk relaxation time τ_η.

For the PS20M5% solution, the friction coefficient $\bar{\lambda}$ displays a plateau, and thus a CY fit gives a typical relaxation time $\tau_\lambda = 2.3$ s much smalller than the bulk relaxation time $\tau_\eta = 170$ s at $T = 293$ K. This would imply that, as the shear-rate $\dot{\gamma}$ is increased, there is a regime where the viscosity decreases while the friction coefficient is constant, and thus the slip length decreases[g]. And indeed, we do observe a decreasing $\bar{b}(\dot{\gamma})$ in Fig. 7.19 (bottom right). On the contrary, for the PS10M4%, the friction coefficient $\bar{\lambda}$ has no plateau visible, and decreases over the whole range of $\dot{\gamma}_{\text{app}}$ studied. This means that its characteristic time τ_λ is at least the inverse of the minimum shear-rate considered, so it is at least 100

[g]It would be followed by a regime where both η and λ decrease, and thus the slip length evolution would depend on the relative decrease of both quantities.

s. However, the caracteristic time for the viscosity τ_η is 33 s. Therefore, for this solution, there is a regime where the viscosity is constant while the friction coefficient decreases, and this results in an increasing slip length, as observe in Fig. 7.19 (bottom left). To summarize, it seems that the shape of the $b(\dot{\gamma})$ depends on the ratio τ_η/τ_λ. If $\tau_\eta > \tau_\lambda$, the slip length decreases (PS20M5%) whereas if $\tau_\eta > \tau_\lambda$, the slip length decreases. The reason why the ratio would be smaller or larger than 1 are not yet clear. In case of grafting, the relaxation time of the grafted chains is much larger than the bulk relaxation time [199], because their dynamics is rather that of a star-arm polymer than a reptation dynamics. For adsorbed chains, to our knowledge, there is no clear answer to that question.

7.3.4.2 Averaging over the whole geometry

Now that we have postulated this $\lambda(\dot{\gamma})$ profile, we can discuss the values we measure under the assumption of a homogeneous $\bar{\lambda}$. The choice of Ω conditions the range of explored $\dot{\gamma}$ over the whole geometry. Thus, the average $\bar{\lambda}$ is the average of λ over a range of $\dot{\gamma}$ that is Ω-dependent. This is schematically illustrated in Fig. 7.25 where the coloured regions correspond to the range of $\dot{\gamma}$ explored over the geometry (for the case where $\tau_\eta \ll \tau_\lambda$). From (1) to (3), the rotational velocity is increased. We describe what happens region per region:

0. If $\Omega R/h < \dot{\gamma}^*$, we are before the slip transition: the friction coefficient is constant and high everywhere and the slip length is constant and small everywhere. Thus, $\bar{\lambda}$ and $\bar{b}$ are constant.

1. For $\dot{\gamma}^* < R\Omega/h < 1/\tau_\lambda$, we have crossed the slip transition: λ starts to decrease at the edge of the geometry and progressively everywhere along the geometry as we increase Ω (case (1) in yellow).

2. For $1/\tau_\lambda < R\Omega/h < 1/\tau_\eta$, λ starts to decrease at the edge of the geometry, and progressively decreases along most of the geometry as Ω in increased. Thus, $\bar{\lambda}$ decreases progressively, and since the bulk iquid is still Newtonian, $\bar{b}$ increases in the same way (case (2) in green).

3. Finally, when $R\Omega/h > 1/\tau_\eta$, the bulk liquid becomes shear-thinning, and thus the viscosity start to decrease. If we assume that λ and η are two independent quantities, λ still decreases in the same way as before. Therefore, b can either increase more slowly or even decrease in this region (case (3) in blue).

In the reverse situation where $\tau_\eta \gg \tau_\lambda$, at stage (2), the slip length starts to decrease at the edge of the geometry because of the bulk shear-thinning, and at stage (3), it either decreases more slowly or it increaes, depending on the relative decrease of η and λ at high shear-rates.

Becausein our derivation, we only have access to an average friction coefficient over the whole geometry, it is necessary that these transitions are rather far from each other in order to see them properly while averaging. Indeed, what we measure is the integration of the friction from $\dot{\gamma} = 0$ to $\dot{\gamma} = R\Omega/h$. Therefore, the transitions are smoothed in the $\bar{\lambda}$ profiles. In particular, if τ_λ and τ_η are to close to each other, their transitions will overlap in the $\bar{b}$ profile. We were lucky that this was not the case for the two solutions we have studied here. Maybe, to improve this discussion, it would be interesting to look

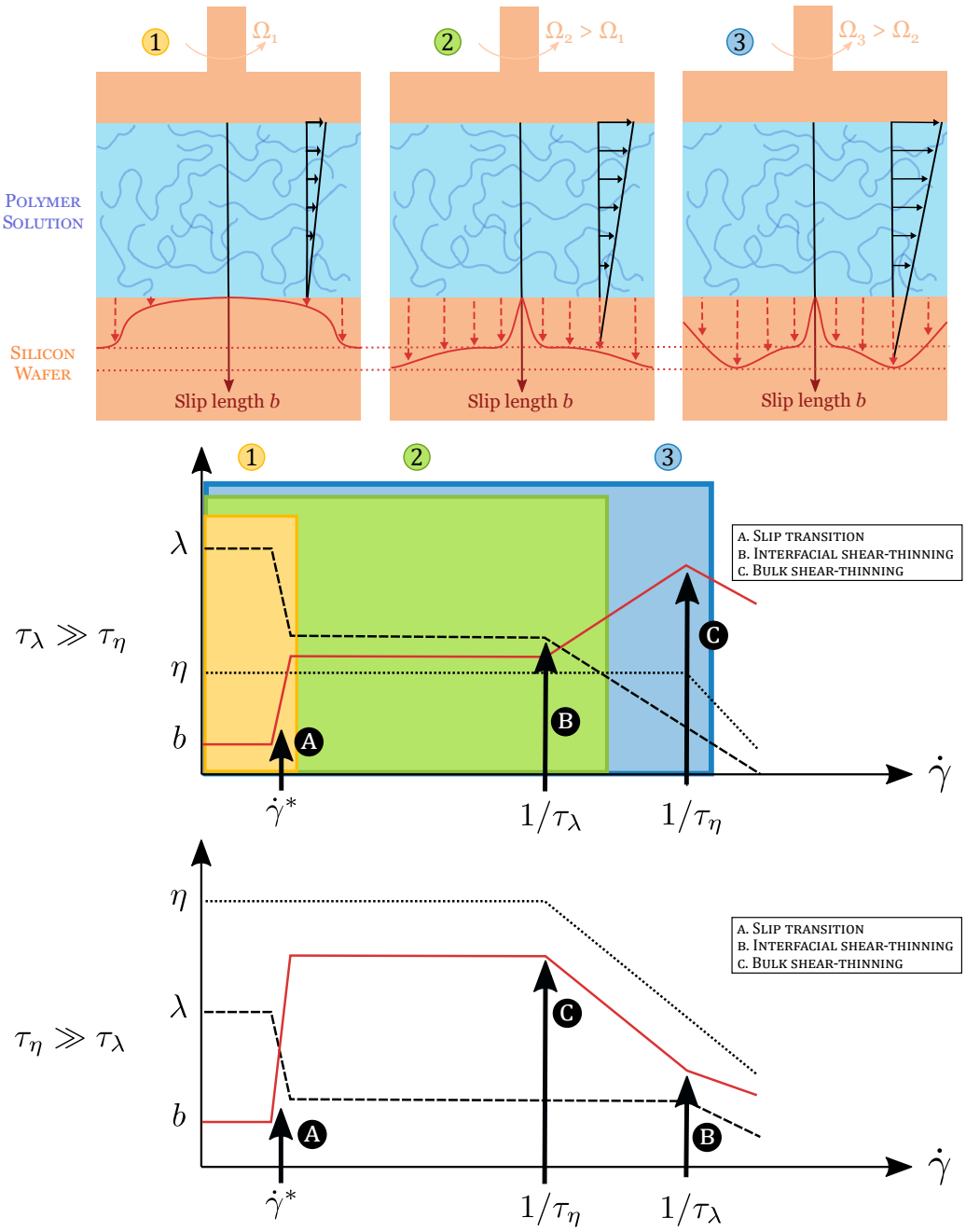

Figure 7.25: Schematic of the different b profiles experienced by the fluid over the whole geometry, depending on the applied rotational velocity Ω.

at the effect of the liquid thickness h on the $\bar{\lambda}(\dot{\gamma})$ and $\bar{b}(\dot{\gamma})$ profiles. These are ongoing experiments.

7.3.4.3 Interfacial viscosity?

Cohen *et al.* [199] have measured the friction of PDMS elastomers sliding on a silica surface. They measure the stress σ as a function of the sliding velocity V. They use a single-layer model to describe the bulk PDMS lens sliding on an adsorbed or grafted PDMS chains layer. This layer has an effective viscosity η_{eff} related to the shear stress σ by $\sigma = \eta_{\text{eff}} V/h$ where h is the thickness of the interfacial layer. They estimate this thickness using the JKR analysis, and thus calculate η_{eff}. They observe that η_{eff} follows the same shear-thinning behaviour as the corresponding bulk PDMS melt (see Fig. 7.26). The only difference is the absence of the Newtonian plateau for η_{eff}, which they attribute to a much longer relaxation time for the grafted chains compared to the corresponding melt (and thus a shear-thinning that starts at much smaller $\dot{\gamma}$). More precisely, they attribute the long relaxation time of the grafted chains to the fact that they were attached to the surface, leading to a star-arm polymer dynamics instead of a reptation dynamics for polymer chains.

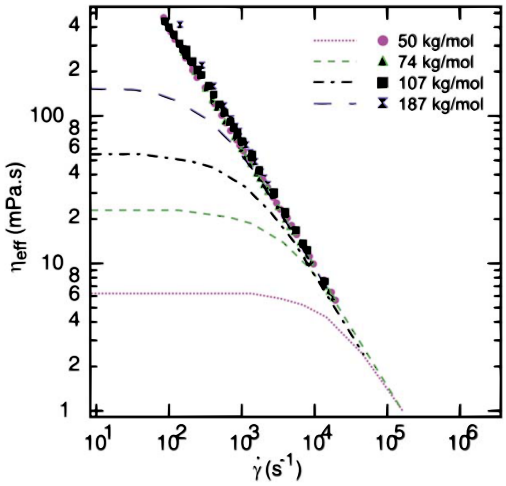

Figure 7.26: Effective viscosity of the sheared grafted layer as a function of the applied shear-rate $\dot{\gamma}$ described in the text. The viscosities of the corresponding bulk melts are shown as full lines. Taken from [199].

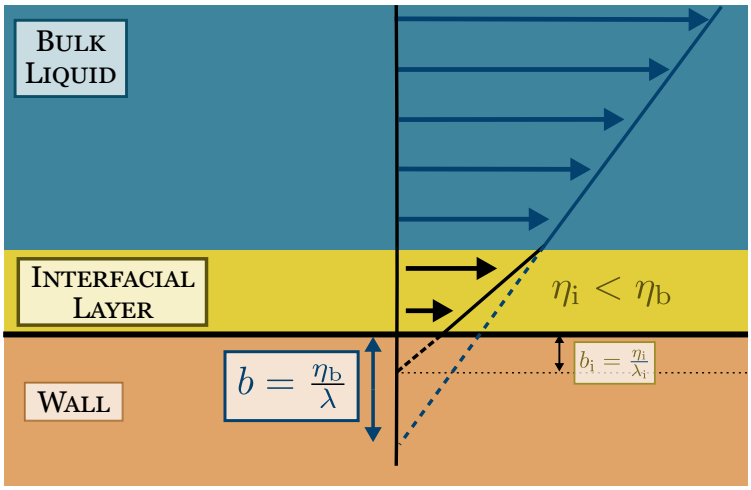

Figure 7.27: Schematic of the two-layers model. The bulk liquid (blue) and the wall (orange) are separated by a liquid interfacial layer (yellow) of viscosity η_i lower than the bulk viscosity η_b. The measured slip length b is given by the ratio η_b/λ. We neglect the slip at the interfacial layer/wall interface b_i.

Following the same idea, we could use a two-layers model to describe our system: the bulk solution, of viscosity η_b and the interfacial layer of viscosity η_i (see Fig. 7.27). Contrary to Cohen *et al.*, both the bulk and the interfacial layer are polymer solutions, and in particular, we do not know the concentration of PS near the surface. Our measurements of neutron reflectivity (see Chapter 6) suggest that the interfacial layer is made of a few adsorbed chains inside a globally depleted solution of viscosity much smaller than the bulk viscosity. A stress balance at the interface between the bulk and the interfacial layer leads to:

$$b = \delta \left(\frac{\eta_b}{\eta_i} - 1 \right) \tag{7.28}$$

with δ the size of the interfacial layer. Thus, the friction coefficient $\lambda = \eta_b/b$ can be rewritten as:

$$\lambda = \frac{\eta_b/\delta}{\eta_b/\eta_i - 1} \overset{\eta_i \ll \eta_b}{\approx} \frac{\eta_i}{\delta} \tag{7.29}$$

Up to a prefactor (which is the thickness of the interfacial layer), λ is equivalent to an interfacial viscosity. Therefore, it is interesting to plot in the same graph the bulk viscosity and the friction coefficient. This is shown in Fig. 7.28. On the left graph, we plot the bulk viscosity η_b as a function of the true shear-rate $\dot{\gamma}$ (stars) as well as the friction coefficient $\bar{\lambda}$ as a function of the apparent shear-rate $\dot{\gamma}_{app}$. On the right graph, we plot η_b and $\bar{\lambda}$ as a function of $\dot{\gamma}\,\tau_\eta$ and $\dot{\gamma}_{app}\,\tau_\lambda$, respectively. They can be interpreted as the bulk and interfacial Weissenberg numbers. τ_η and τ_λ are the relaxation times extracted from the CY fits in Fig. 7.20 and shown in Fig. 7.21.

We see that the shapes of the curves are really similar, suggesting that λ can indeed be related to an effective viscosity of the interfacial layer. To quantitatively extract the viscosity of the interface, we need to know the thickness of the interfacial layer δ. According to our measurements of neutron reflectivity, we know that δ should scale with

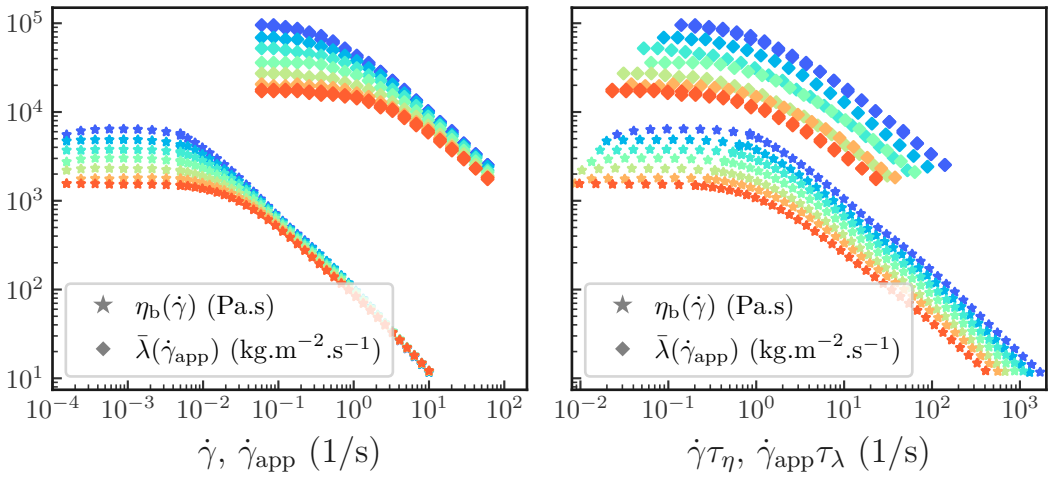

Figure 7.28: Bulk viscosity η_b and average friction coefficient $\bar{\lambda}$ as a function of the shear-rates $\dot{\gamma}$ and $\dot{\gamma}_{app}$ (left) and the bulk and interfacial Weissenberg numbers (right).

the blob size of the solution. We can infer the blob size of our bulk solution using the SANS measurements described in Fig. 1.14:

$$\delta \propto \xi \simeq a e^{1.4} \phi^{-0.7} \tag{7.30}$$

with $a = 0.55$ nm the monomer size of PS (see Chapter 5) and ϕ the bulk volume fraction. We find $\xi \simeq 18$ nm. If we multiply our friction coefficient $\bar{\lambda}$ by this value, we find an interfacial Newtonian viscosity η_i around 2 mPa.s at $T = 293$ K and 0.3 mPa.s at $T = 353$ K, which are both much smaller than the corresponding Newtonian bulk viscosities η_b.

We can do a very rough estimate of the volume fraction of the interfacial layer, which would correspond to a Newtonian viscosity of 2 mPa.s. In Section 7.1, we have measured the viscosity of several PS/DEP solution of 10 Mg/mol molar mass. The 5 % solution at 293 K had a viscosity around 4.10^3 Pa.s. We can express the viscosity of the solution as $\eta \propto M^3 \phi^\alpha$ with α the anomalously large exponent discussed in Section 7.1. We had $\alpha \simeq 5.1$ at 293 K. From this equation and the values measured, we can estimate the volume fraction of the interfacial layer using:

$$\phi_1 = \phi_2 \left(\frac{M_2}{M_1}\right)^{3/\alpha} \left(\frac{\eta_1}{\eta_2}\right)^{3/\alpha} \tag{7.31}$$

with $\phi_2 = 0.05$, $\eta_2 = 4.10^3$ Pa.s, $M_2 = 10.2$ Mg/mol, $M_1 = 20.6$ Mg/mol and $\alpha = 5.1$. We find $\phi_1 \simeq 0.2$ % for the volume fraction of the interfacial layer. This is of course a very rough estimation, assuming that the semi-dilute scaling law applies down to this concentration range, and that the thickness of the interfacial layer is exactly the blob size. If we had the thickness measurement of the adsorbed layer, we could deduce the density of adsorbed chains and maybe discuss it to this estimated interfacial volume fraction.

7.3.5 A short remark: using a ring instead of a plate

The difficulty of the method described below relies on the fact that the slip length (and the friction coefficient) are not homogeneous over the whole geometry. We have tried to use a ring as the top geometry, instead of the plate. We write R_1 and R_2 its inner and outer radiis. Using the TPP measurements, we can choose R_1 and R_2 so that the slip length for $R_1 < r < R_2$ remains rather constant. A schematic illustration is shown in Fig. 7.29. This idea did not work well, mainly because we cannot deburr the liquid in $r = R_1$ and thus we cannot control the inner edges of the liquid. We have tried two solutions to solve this problem. Firstly, we have tried to change the wettability of the surface at the centre of the set-up to control the spreading of the liquid in the middle (solution 1 in green in Fig. 7.29). Secondly, we have tried to inject air inside the inner cavity to prevent the liquid spreading (solution 2 in green in the same figure). Both solutions did not work, and we did not manage to obtain reproducible results. With the ring geometry, much less liquid is sheared, thus the measurements are more noisy, and we have much more interface with air, which significantly increase the experimental errors.

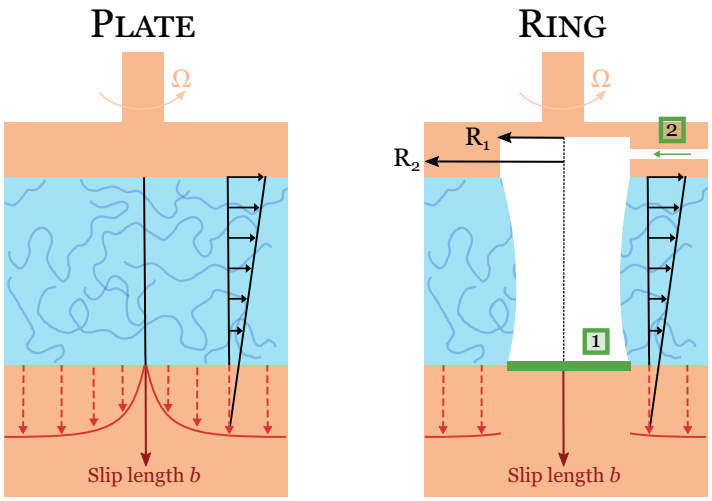

Figure 7.29: Schematic illustration of the plate-plate geometry described in the previous section (left) and the ring-plate geometry described here. In green, we illustrate the two solutions we have tried to improve the reproducibility of the measurements using the ring-plate geometry.

These results are encouraging. The analysis we have derived seems to measure quantitatively the same slip lengths and friction coefficients as the TPP technique. The great advantage of this method is that it is relatively simple and quick to do, it does not require labelled chains, and it gives access to a broad range of shear-rates. The drawback is that it necessitates a very good parallelism between the two plates, which is not that easy to achieve, and we only have access to the apparent shear-rate when the TPP technique gives the true-shear rate. The next step would be to finely tune this method by doing systematic measurements on PS/DEP solutions at various concentrations and molar masses to verify that all the expected scaling laws are verified. An interesting development of this technique would be to do oscillatory shear on our solutions, to have access to the frequency dependent friction coefficient $\lambda(\omega)$, as we have done for the LJ liquid in Chapter 4. If this works, we could push it further towards Large-Amplitude Oscillatory Shear

(LAOS) to obtain even more information on the frequency response of slippage.

7.4 Conclusion

The purpose of this well-filled chapter was to discuss the bulk and interfacial rheology of our PS/DEP semi-dilute solutions. We have started by describing the bulk rheology, which in itself opens the discussion on the glass transition of binary components and a possible link with the rheological scaling laws. Then, we have run through slippage of these solutions on silicon wafers. We have first presented experiments using the TPP technique, and its limitations regarding the temperature dependency of slip. For this reason, we have chosen to spend time to derive a method to probe the friction coefficient directly from measurements obtained with a rheometer. We have obtained promising results, which pave the way for many more experiments. In particular, it has raised the issue of the dependency of the friction coefficient with the shear-rate, which is rarely tackled in slip measurements. We saw that this shear-rate dependency might be formalised by an interfacial "shear-thinning" with a typical relaxation time much larger than the corresponding bulk one.

Conclusions of Chapter 7

In this chapter, we have seen that:

- the scaling law $\eta \propto \phi^{\alpha}$ deviates from the predicted law ($\alpha = 15/4$). This deviation is correlated to the temperature of the liquid, and is larger when the liquid is cooler. This might be due either to the proximity of a θ-temperature, the not-so-good quality of the DEP solvent, or some reminiscent glassy effects.
- the TPP technique is a powerful method to measure the slip length b while accessing the **true** shear-rate. Yet, it relies on the fluorescence of the sample, which is strongly affected by changing the temperature, which makes this technique non-suitable for an analysis of the role of temperature in slip.
- we can measure slip using a rheometer. The classical Mooney's analysis does not always work. We have derived a new analysis, based on the comparison between the measured torque when the liquid slips and the calculated no-slip torque. This method seems robust, and gives us access to the shear-rate dependency of the friction coefficient λ.
- surprisingly, λ strongly depends on the shear-rate, leading to a non-trivial $b(\dot{\gamma})$ profile. This might be attributed to an effective interfacial shear-thinning.
- the friction coefficient of our solution follows an activated process. We could extract a typical interfacial relaxation time, that is also activated, and much smaller than the bulk relaxation time.

Chapter 8

Adsorption kinetics of PDMS melts

Contents

This chapter stands apart from the others. One of the main goal of this thesis was to study the effect of temperature on slip. In particular, for polymers, the slip length depends on the amount of adsorbed chains, and the kinetics of adsorption in fastened when the liquid is heated. Therefore, we needed a proper description of the effect of temperature on the adsorption kinetics of polymers. To this end, we have chosen to study a polymer that strongly adsorbs on silicon wafers, namely PDMS. We have used PDMS melts of a molar mass around 208 kg/mol. It turned out that the adsorption kinetics of our PDMS is very slow, so that the measurements have been carried out over a whole year. Even though the kinetics followed the usual trend of other polymer melts, we noticed some peculiar behaviours, and in particular the exceptionally slow adsorption of PDMS compared to other polymers. With the help of Erik Thoms and Simone Napolitano from Université Libre de Bruxelles, we could rationalise these results, but the story is not completely over and further experiments are in process.

In Section 8.1, we make a general introduction on adsorption, adsorption kinetics and its link with molecular relaxation processes. In Section 8.2, we show our results on the adsorption kinetics of PDMS melts as a function of temperature. In Section 8.3, we present dielectric relaxation spectra of PDMS, and we try to link them to our adsorption kinetics.

8.1 Introduction

Decorating a surface with polymers is useful in many domains: it can promote adhesion, it plays a central role in coatings, it stabilizes particles suspensions... It is also

important to understand adsorption since many biological objects, such as proteins, adsorb on surfaces, which can be used for medical detection devices for example.

Usually, we distinguish two ways of attaching polymer chains on a solid surface: either the chains are grafted or they are adsorbed [200]. We call **attached chains** chains that are attached to the wall, either by grafting or by adsorption.

8.1.1 Adsorption and grafting

Grafted chains. We talk about grafting when the chains are chemically bound to the surface through one of their extremities. Thus, the anchoring of the chain is strong (much larger than k_BT), and the conformation of the grafted layer depends on the length of the grafted chains and on the grafting density. A schematic illustration is shown in Fig. 8.1. If we write D the average distance between two consecutive grafting points, the grafting density ν is given by:

$$\nu = \frac{1}{D^2} \tag{8.1}$$

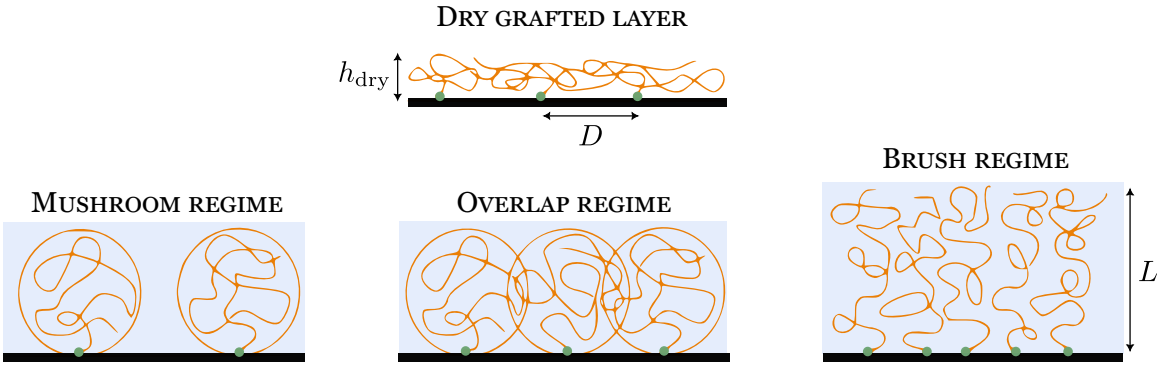

Figure 8.1: Top: dry grafted layer. The average distance between two grafting points is D. Green circles refer to chemical grafting points. Bottom: various grafting regimes for a grafted layer in a liquid. From left to right, the grafting density is increased. Left: mushroom regime. Middle: overlap regime. Right: brush regime. In the brush regime, the chains are stretched and the thickness of the brush is called L. Figure adapted from M. Hénot's PhD thesis [72].

When the grafting layer has been obtained from a solution, and then dried and exposed to air, it flattens, and we call h_{dry} its resulting thickness. This thickness can be measured with ellipsometry (see Section 5.4.2) and X-Rays reflectivity (see Section 5.4.3) and is related to the grafted density ν. Volume conservation yields $h_{dry}D^2 = Nv_0$ with v_0 the volume of a monomer. Thus, the grafting density ν can be expressed as:

$$\nu = \frac{h_{dry}}{v_0 N} = \frac{h_{dry}\rho_{graft}\mathcal{N}_A}{M_0 N} \tag{8.2}$$

with M_0 the molar mass of a monomer, N the number of monomers per chain, ρ_{graft} the density of the grafted polymer and $\mathcal{N}_A$ the Avogadro's number. Thus, the measurement of h_{dry} gives access to the grafting density.

We can also define a dimensionless grafting density Σ by:

$$\Sigma = \frac{a^2}{D^2} = a^2\nu \tag{8.3}$$

Adsorbed chains. When put near a solid surface, polymer chains can also spontaneously adsorb onto the wall. The interaction at play is weaker than a chemical bond, it can be a H-bonding or a Van der Waals attractive interaction. This interaction can happen from any monomer of the chain, and not only its extremities. The conformation of the adsorbed layer, when put in a good solvent, is self-similar, as described by Guiselin [201]. We talk about a Guiselin *pseudo-brush*. Similarly to grafted chains, adsorbed chains put in air flatten, and we call h_{dry} the thickness of this dry adsorbed layer. Because chains do not attach only by their extremities, the variable used to describe adsorbed chains is not the grafting density ν but rather the total mass of monomers belonging to an adsorbed chain m. A monomer that is itself adsorbed on the wall is called *directly adsorbed*, and a monomer which is not directly adsorbed but which belongs to a chain which is adsorbed is called *indirectly adsorbed*. The mass of directly or indirectly adsorbed monomers inside a layer of thickness dz located at a distance z from the wall is:

$$dm(z) = \rho(z)Sdz \tag{8.4}$$

where S is the surface of the wall and $\rho(z)$ the density of the adsorbed layer at a distance z from the wall. Thus, the total mass of monomers belonging to adsorbed chains is the integral of $dm(z)$, and it is equivalent to a virtually homogeneous slab of thickness h_{dry} (see Fig. 8.2):

$$m = \int_0^{+\infty} \rho(z)Sdz \approx \rho_{\text{ads}}Sh_{\text{dry}} \tag{8.5}$$

with ρ_{ads} the mean density of the adsorbed layer. m is sometimes called Γ in the literature.

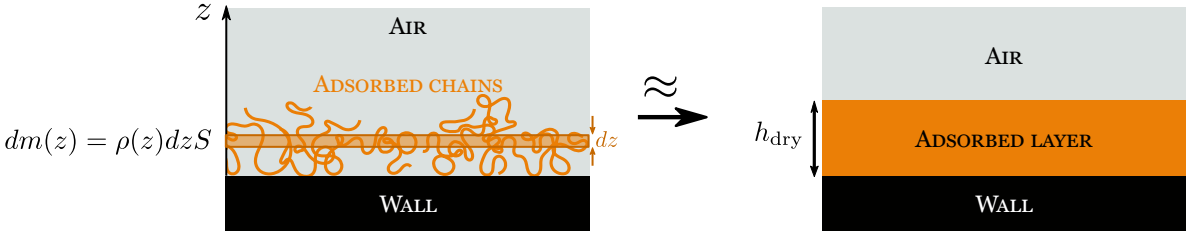

Figure 8.2: Adsorbed layer of polymer on a wall. m is the mass of monomers belonging to adsorbed chains.

The adsorption layer can be formed from either a melt or a solution. The amount of chains increases with the contact time between the liquid and the substrate, and finally reaches a constant amount, corresponding to a final dry thickness $h_{\text{dry},\infty}$. This thickness depends on the chain length N and the volume fraction of the solution ϕ from which the polymer has been adsorbed. Deruelle *et al.* [202] have looked at the dried thickness h_0 of adsorbed OH-terminated PDMS on silicon wafers. They adsorb PDMS of various chain length N and from solutions of various volume fractions ϕ. They put the solution in contact with the solid substrate for a time long enough to reach the saturation of the surface, and then rinse and dry their adsorbed layer. They measure the dry thickness

$h_{\mathrm{dry},\infty}$ of the adsorbed layer as a function of N and ϕ. Their results are shown in Fig. 8.3. They show that[a]:

$$h_{\mathrm{dry},\infty} = aN^{1/2}\phi^{7/8} \tag{8.6}$$

Such a scaling law assumes that the maximum adsorption density accessible corresponds to the case where all the chains present in a layer of thickness R_{g} are adsorbed. Inserting additional chains would have an enthalpic cost too high compared to $k_{\mathrm{B}}T$.

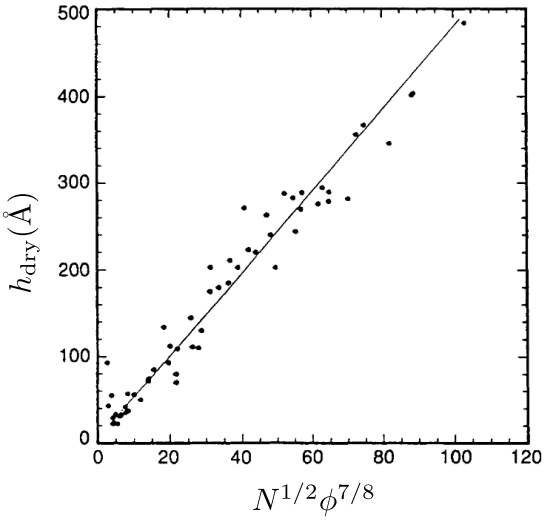

Figure 8.3: Dry thickness h_∞ of adsorbed PDMS layers on silicon wafers as a function of the chain length N and the initial volume fraction ϕ. Adapted from [202].

From this scaling law, one can estimate the dimensionless surface chain density Σ:

$$\Sigma = N^{-1/2}\phi^{7/8} \tag{8.7}$$

Many systems can adsorb on surfaces, but the specificity of polymers is that their adsorption is **quasi-irreversible**. The reason of this irreversibility is not that clear. It is often invoked that polymers being very long molecules, a single chain has many adsorption points. Thus, desorbing a chain would require to desorb all these points at the same time, which is very unlikely. Yet, in an experiment from the 80s reported by de Gennes in [203], Pefferkorn *et al.* [204] have adsorbed radioactively labelled chains on a surface until saturation. Then, they have put this adsorbed surface in a solution of the same chains, but unlabelled (non-radioactive). They have observed a decrease of the interfacial radioactivity with time, suggesting a dynamical exchange between adsorbed and bulk chains. To our knowledge, there is no consensus on the reason why adsorption is irreversible. The important point is that experimentally, we do not observe a significant desorption upon rinsing or plunging the adsorbed layer in a good solvent.

[a] To show this equation, we can say that the volume fraction ϕ is given by the ratio $h_{\mathrm{dry}}/R_{\mathrm{g}}$.

The intermediate case of PDMS. When the interaction between the monomers and the wall is particularly strong, or when the interaction between the end groups of chains and the wall is much stronger than the rest of the monomers, then discriminating between adsorption and grafting is not that easy. This is especially the case for PDMS: all the monomers are able to form H-bonds with exposed OH groups (which are present at the surface of silicon wafers). This interaction is stronger than Van der Waals interactions. In addition, in the case of OH-terminated PDMS, the end groups interact so strongly with the surface that some works even suggest a spontaneous chemical reaction between the end groups and the silica surface [205–207]. In these papers, the authors argue that, indeed, PDMS can chemically attach to the surface through its hydroxyl en groups. They also discuss the possibility that the Si-O-Si of the PDMS chains can break and chemically bond to the surface. This would be catalysed by the presence of water molecules on the surface (which depends on humidity and temperature). These papers are rather recent (2011, 2014 and 2020), and it seems that there is still no consensus on this question, and thus, the distinction between adsorption and grafting is not that clear in the case of PDMS.

8.1.2 Kinetics

Hitherto, we have been focusing on the saturated adsorbed/grafted layer. We now discuss the kinetics of the building up of the attached layer. Probing this kinetics can be done using several techniques, such as Nuclear Magnetic Resonance (NMR) [208], Second Harmonic Generation (SHG) [209], Atomic Force Microscopy (AFM) [210] dielectric spectroscopy [209, 211], ellipsometry [95, 210, 212]... In this section, we discuss the current models used to describe the kinetics of adsorption of the chains. For simplicity, from now on, we will call h the dry thickness h_{dry}.

Grafting kinetics. Since it is not the focus of this chapter, we do not detail the grafting kinetics. Some elements can be found in Ligoure and Leibler [213] and Johner and Joanny [214].

Adsorption kinetics. The adsorption kinetics can be affected by the initial concentration of the solution in contact with the surface. If the concentration is very small (dilute regime), the first chains adsorbing onto the wall are very far away from each other. The kinetics will be controlled by the diffusion of the bulk chains towards the interface [215]. On the contrary, if the concentration of the solution is high, all the chains which will adsorb onto the wall are already at its vicinity, and thus the kinetics is governed by the local rearrangements of these adsorbing near-wall chains. This is the same for melts. In particular, in many adsorption experiments, the polymer is deposited by spin-casting a concentrated solution instead of directly depositing a melt. This allows for a better control on the thickness of the deposited layer. In the following, we will restrain ourselves to adsorption kinetics of polymer melts.

The review of Napolitano [200] nicely summarizes the state of the art about adsorption kinetics of polymer melts. In particular, it sets out the following rules:

1. A chain is adsorbed as soon as at least one of its monomers is adsorbed.

2. Adsorption of a chain is irreversible.

3. h increases if and only if an unadsorbed chain is adsorbed. In particular, if monomers of an already adsorbed chain get adsorbed, it does not affect h.

4. As said before, we neglect any diffusion from the bulk, and we consider that all the chains that will adsorb onto the wall are already at its vicinity.

5. At any time t, the kinetics is governed by the mechanism that allows the more contacts with the substrate. This mechanism can vary with time.

Now that we have enumerated these rules, we can look at the models for the adsorption kinetics. Because of steric constraints, chains adsorbing at shorter times make more contacts with the wall than chains adsorbing at later times. And indeed, in the early stages of adsorption, h increases linearly with time, indicating a zeroth-order reaction dominant mechanism. Consequently, the thickening of the adsorbed layer occurs by incorporating a constant number of polymer chains into the interfacial layer. In this regime, the thickness is proportional to average number of contact between a chain and the surface ($N^{1/2}$ for a melt), and thus, the kinetics is given by:

$$h(t) = vt = qN^{1/2}t \tag{8.8}$$

where v is the growth rate and q the monomer adsorption rate. The latter can stem from various molecular mechanisms, which may exhibit distinct temperature dependencies. For many polymers, the temperature dependence of q is well described by an Arrhenius law:

$$q = q_0 \exp\left(-\frac{E_{\text{ads}}}{RT}\right) \tag{8.9}$$

with E_{ads} a typical activation energy of adsorption per monomer, in J/mol.

At later times, the growth is slowed down because of the presence of already adsorbed chains, and the adsorption kinetics becomes logarithmic [212]:

$$h(t) = h_\infty + \ln\left(1 - A\exp\left(-\frac{t - t_{\text{cross}}}{\tau_{\text{e}}}\right)\right) \tag{8.10}$$

where $A \approx 1$, t_{cross} is the time at which the linear growth regime ends, τ_{e} a characteristic time to reach equilibrium, which in particular depends on h_∞. At even larger times (for $t - t_{\text{cross}} \gg \tau_{\text{e}}$), the thickness tends exponentially towards h_∞, which is independent of temperature. If the deposited melt is a very thin film (typically thinner than the radius of gyration), h_∞ depends on the bulk thickness [216].

This model describes very well the experimental adsorption kinetics reported in [212] for thin films of PS melts (see Fig. 8.4). We clearly see the two regimes: the first linear growth, which kinetics is independent of the thickness of the thin film, followed by the logarithmic increase until the saturation thickness, which depends on the thickness of the thin film.

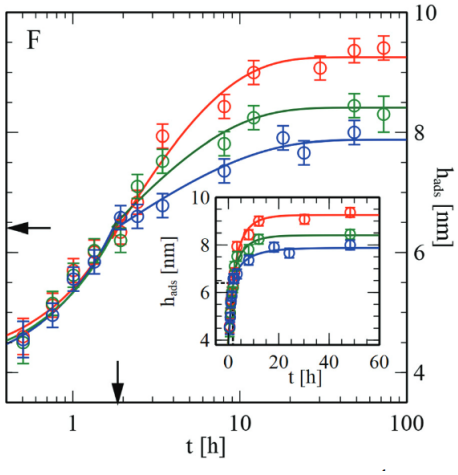

Figure 8.4: Adsorption kinetics of PS melts ($M_n = 1$ Mg/mol) at 433 K for three different thicknesses of the thin film (blue: 130 nm, green: 235 nm and red 325 nm). Arrows enhance t_{cross} and h_{cross}. Taken from [212].

8.1.3 Relaxation processes and temperature effects

We now come back to the fact that the first linear regime is activated (see Eq. 8.9). Following Onsager's regression hypothesis [217], there should be a molecular process whose activation energy matches that of the adsorption kinetics E_{ads}. This implies to discuss the various possible relaxation processes that might be at the origin of the early-time adsorption kinetics. This is the concern of this section.

Similarly to supercooled liquids, relaxation of polymer melts are governed by the segmental relaxation, also called α-relaxation, which follows a super-Arrhenian temperature dependency. However, this process predicts geological relaxation times for materials below T_g, while in practice we can observe their equilibration on a measurable timescale (days or weeks), for example for adsorption kinetics. This suggests the existence of another relaxation process, but none of the usual relaxation processes (β, γ...) could be responsible for such a quick equilibration, and in particular none of them could explain the adsorption kinetics, which displays an Arrhenian temperature dependency with typical activation energies around 100 kJ/mol. It was only recently that Dielectric Spectroscopy (DS) measurements on various polymer melts have noticed the existence of two distinct relaxation peaks [145]: the α peak, and another peak at lower frequencies for $T > T_g$. The latter is associated to the so-called "Slow-Activated Process" (SAP). This peak follows an Arrhenius law for T above and below T_g, and the corresponding activation energy matches the ones of adsorption kinetics. Therefore, the SAP is a very good candidate to explain the mechanisms of adsorption kinetics of polymer melts at short times.

The link between adsorption kinetics (and more generally equilibration measurements) and relaxation processes in various polymer melts has been described very recently (in 2022) by Song *et al.* [145]. In this work, they compare the temperature dependency of the α and SAP peaks with the one of adsorption. Their main result is reproduced in Fig. 8.5, where they plot both temperature dependency of the molecular relaxation times t_{mol} for α relaxation (white symbols) and SAP (red symbols) obtained from DS, and equilibra-

tion times t_{eq} (blues symbols) obtained from various equilibration experiments, including adsorption, physical aging, dewetting *etc.* The main conclusion from this is that, in many cases, equilibration processes follow the same Arrhenian temperature dependency as the SAP.

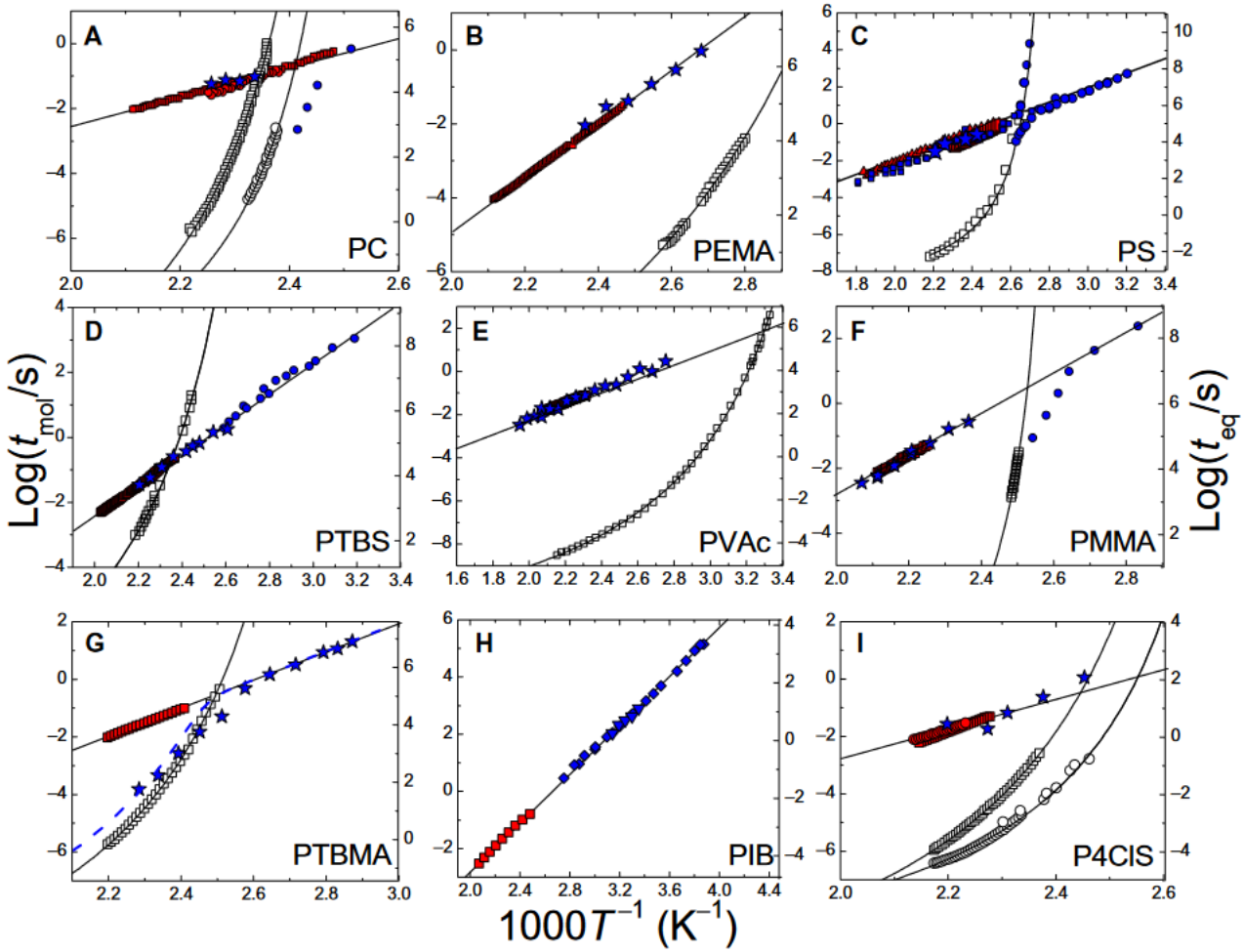

Figure 8.5: Molecular relaxation times t_{mol} and equilibrium times t_{eq} as a function of temperature T for various polymer melts. Molecular relaxation are shown in white (α relaxation) and red (SAP) with squares for bulk samples and circles for thin films. Equilibration data are indicated in blue (stars for adsorption, other symbols for other equilibration experiments). Taken from [145].

These measurements have been made for various polymer melts, but PDMS. As discussed in Section 8.1.1, PDMS is known to interact strongly with silicon wafers, especially the hyroxyl-terminated PDMS. Therefore, we are interested in comparing their adsorption kinetics and relaxation dynamics to see if they display a peculiar behaviour compared to other polymer melts. Logically enough, we will first present our results of adsorption kinetics of PDMS melts onto silicon wafers. This is Section 8.2. In Section 8.3, we show the relaxation spectra of PDMS, obtained by Dielectric Spectroscopy (DS). These measurements, and the following discussion, have been done in close collaboration with Erik Thoms and Simone Napolitano, from Université Libre de Bruxelles. Finally, we discuss

the link between the dielectric relaxation spectra and the adsorption kinetics, and the specificities of PDMS compared to other polymers.

8.2 Adsorption kinetics of PDMS melts on silicon wafers

The adsorbed layer is prepared according to the procedure described in 5.3.2.1. The thickness of the dry adsorbed layer is measured using ellipsometry, as described in 5.4.2. We measure this thickness h as a function of the incubation time t (the contact time between the melt and the surface) at various temperatures. High temperatures are easily obtained by storing the samples in the oven. 278 K (252 K) is obtained by storing the samples in the fridge (the freezer). 293 K correspond to samples stored at room temperature. Since the incubation times span almost a year, the temperature is less controlled for the samples at room temperature, which explain the larger dispersion of these data. Each thickness measurement is done at variable incident angles (every 2 °C between 50 °C C and 70 °C C), and the thickness is measured at (at least) three different positions on the surface. The error bars are given by the standard deviation of these three values, enlarged by the Student coefficient with 95 % of uncertainty, because the number of measurements is rather small.

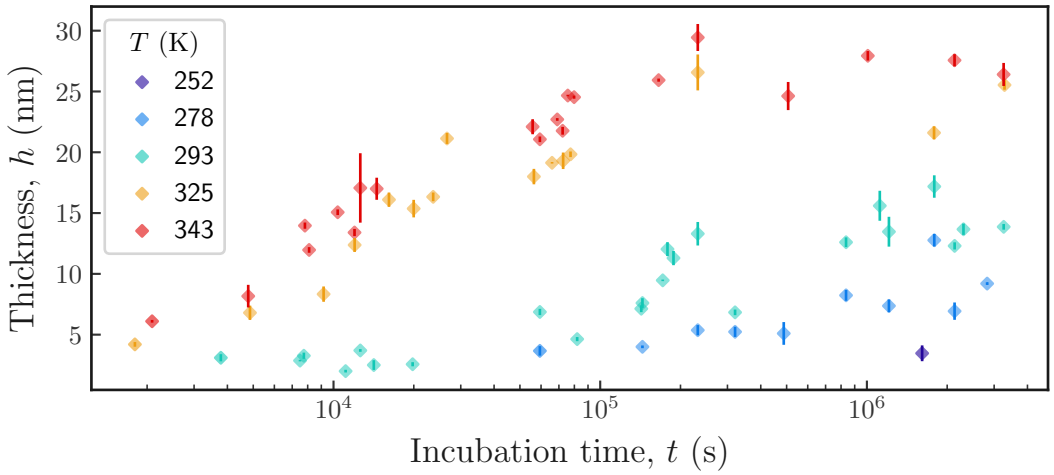

Figure 8.6: Adsorption kinetics of a 208 kg/mol OH-terminated PDMS melt at various temperatures. h correspond to the dry thickness h_{dry}, measured by ellipsometry.

The results are shown in Fig. 8.6. For each temperature used here, we observe an increase of the dry thickness with time. This is quicker for higher temperatures. Over our large time range (from 30 minutes to 1400 hours), the saturation h_∞ is reached only for the two higher temperatures (343 and 325 K). The maximum thickness is very close to the radius of gyration of the chains ($R_g \simeq 23$ nm), which is the theoretical limit assuming that all chains within R_g are adsorbed.

In Fig. 8.7, we zoom on the early kinetics at each temperature. We observe that this early kinetics is linear. The time during which the kinetics is linear increases when the temperature is decreased. We determine "by eye" the range over which the kinetics is

linear, and we fit the early-time kinetics to obtain the growth rate $v = \mathrm{d}h/\mathrm{d}t$.

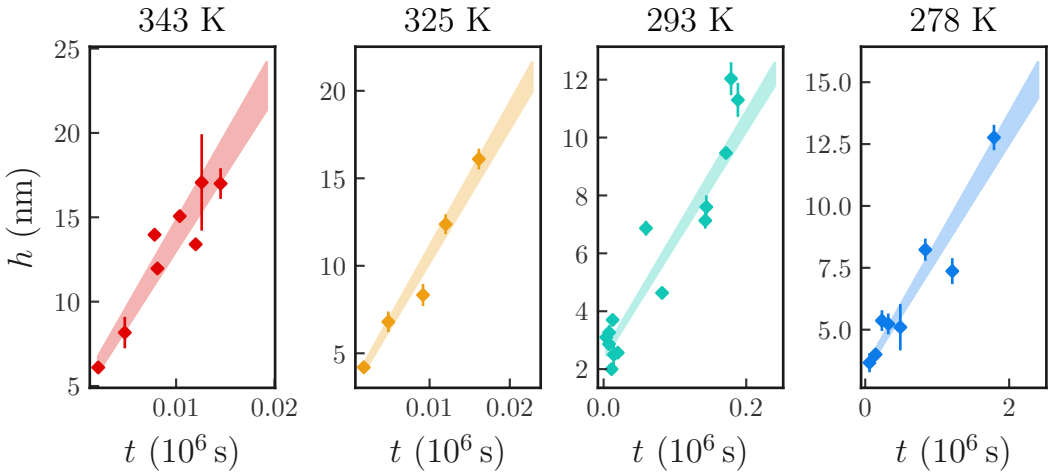

Figure 8.7: Short-times adsorption kinetics of the PDMS melt. The coloured region correspond to a linear regression taking into account the uncertainties.

From the growth rate v, we can calculate the monomer adsorption rate $q = vN^{-1/2}$. We plot q as a function of the inverse temperature in Fig. 8.8. The data seem to be reasonably well described by an Arrhenius law with an activation energy around 67 ± 10 kJ/mol. This is quite similar to what is usually observed for adsorption of polymer melts [200].

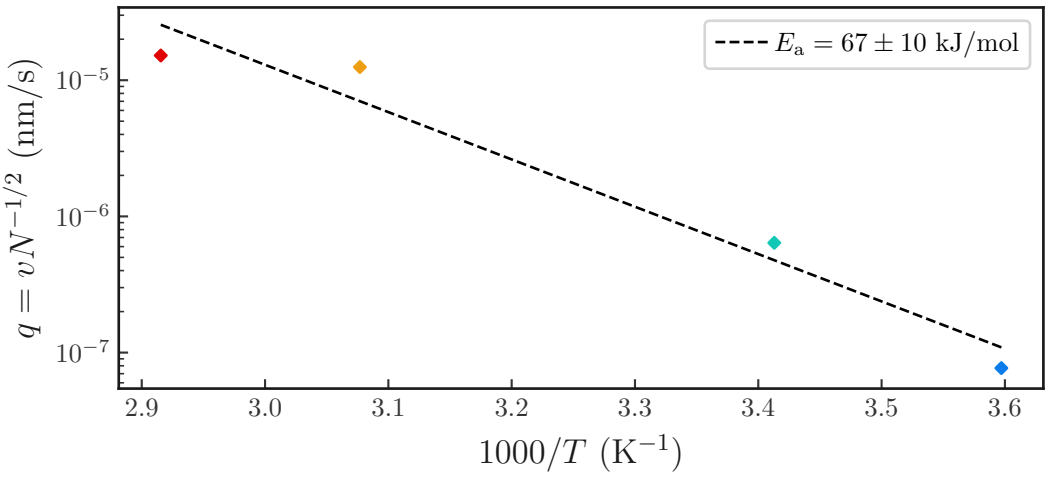

Figure 8.8: Monomer adsorption rate q as a function of temperature.

In the next section, we use dielectric spectroscopy (DS) to probe the relaxation spectra of PDMS as a function of temperature. This allows to extract the temperature dependency of several molecular relaxation frequencies, associated to several relaxation processes. The comparison between their temperature dependency and the temperature dependency of q allows us to infer which molecular process is associated to the adsorption kinetics. The following section is built on the recent results of Song *et al.* [145] and on discussions with Erik Thoms and Simone Napolitano, whose work will be published soon [218].

8.3 Dielectric Spectroscopy of PDMS melts

8.3.1 Experiment

The experimental details of the measurement are described in Section 5.5 and are very similar to the experimental procedure given in [145]. A 125 kg/mol PDMS melt (Polymer Source, Đ = 1.2) is sandwiched between two alumina plates. The thickness of the PDMS layer is 100 nm, determined from both ellipsometric and conductivity measurements. The dielectric response ϵ of the sample is measured as a function of the frequency of excitation f and the temperature T. We are interested in the imaginary part of ϵ, defined as $\epsilon^*(f,T) = \epsilon'(f,T) - \mathrm{j}\epsilon''(f,T)$. The 3D dielectric response $\epsilon''(f,T)$ is shown in Fig. 8.9.

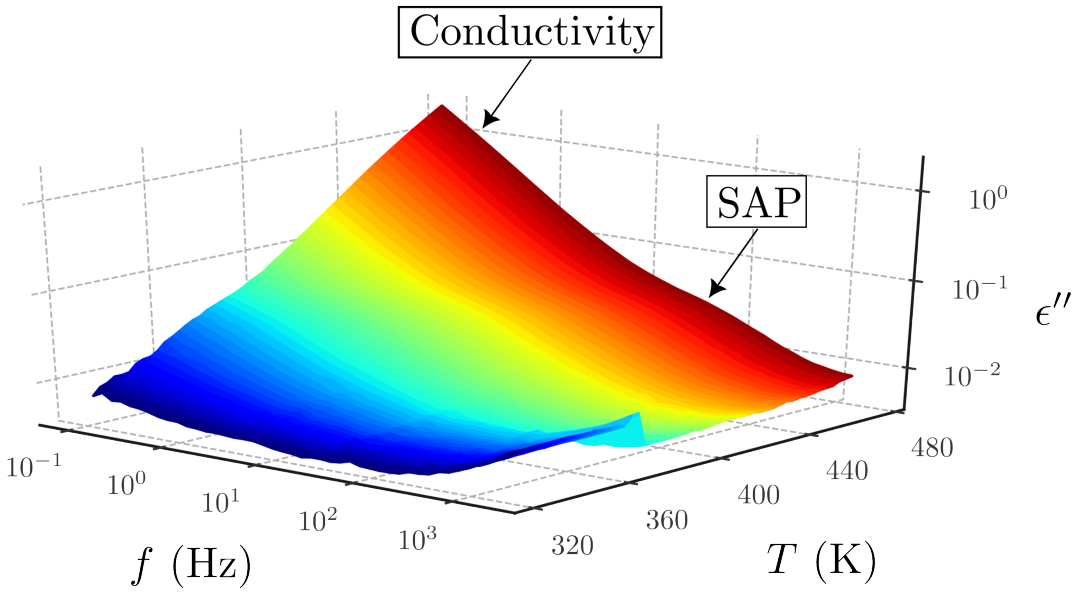

Figure 8.9: 3D plot of the dielectric loss ϵ'' as a function of frequency f and temperature T for a 100 nm thick film of PDMS. Colours correspond to temperatures.

We observe a pronounced peak at high T and low f due to the conductivity of the sample. A second and less-pronounced peak is visible at large T and intermediate frequencies. This peak is ascribed to the SAP. The α peak is not visible, and is expected at larger frequencies. The increase at low T and high f is an electronic artefact due to the non-negligible resistance of the metallic contacts [145, 219]. We therefore ignore this increase in the discussion.

At a given temperature, the dielectric spectrum can be fitted by the sum of the contributions of the purely electronic conductivity, the segmental process (described by the empirical Havriliak-Negami function [220], HN) and the SAP process (described by the Cole-Cole function [221], SAP).:

$$\epsilon(\omega) = \epsilon'(\omega) - \mathrm{j}\epsilon''(\omega) = \epsilon_\infty + \frac{\Delta\epsilon_{\mathrm{HN}}}{(1+(\mathrm{j}\omega\tau_{\mathrm{HN}})^{a_{\mathrm{HN}}})^{b_{\mathrm{HN}}}} + \frac{\Delta\epsilon_{\mathrm{SAP}}}{1+(\mathrm{j}\omega\tau_{\mathrm{SAP}})^{a_{\mathrm{SAP}}}} + \frac{\mathrm{j}\sigma}{\epsilon_0\omega^n} \tag{8.11}$$

with $\omega = 2\pi f$, ϵ_∞ an effective dielectric constant of the sample, σ the conductivity, $n \leq 1$, ϵ_0 the vacuum permittivity. The rest are various parameters corresponding to the SAP

and segmental peaks.

A 2D cut of the 3D relaxation spectrum is shown in Fig. 8.10 (left), for a temperature $T = 428$ K. The solid line in the inset correspond a fit of the data using Eq. 8.11. It yields $n = 0.79$, $\sigma = 1.95\,10^{-12}$ S/m, $\tau_{\mathrm{SAP}} = 0.039$ s, $\Delta\epsilon_{\mathrm{SAP}} = 0.0416$, $a_{\mathrm{SAP}} = 0.81$, $\tau_{\mathrm{HN}} = 0.000247$ s, $\Delta\epsilon_{\mathrm{HN}} = 0.005$, $a_{\mathrm{HN}} = 0.5$, $b_{\mathrm{HN}} = 1.0$ and $\epsilon_\infty = 2.409$. In the right figure, we plot the SAP frequency f_{SAP} as a function of the inverse temperature. We see that f_{SAP} follows an Arrhenius trend, with an activation energy of 90.4 ± 0.6 kJ/mol. This is in the range of the activation energies found for adsorption kinetics of polymer melts [200].

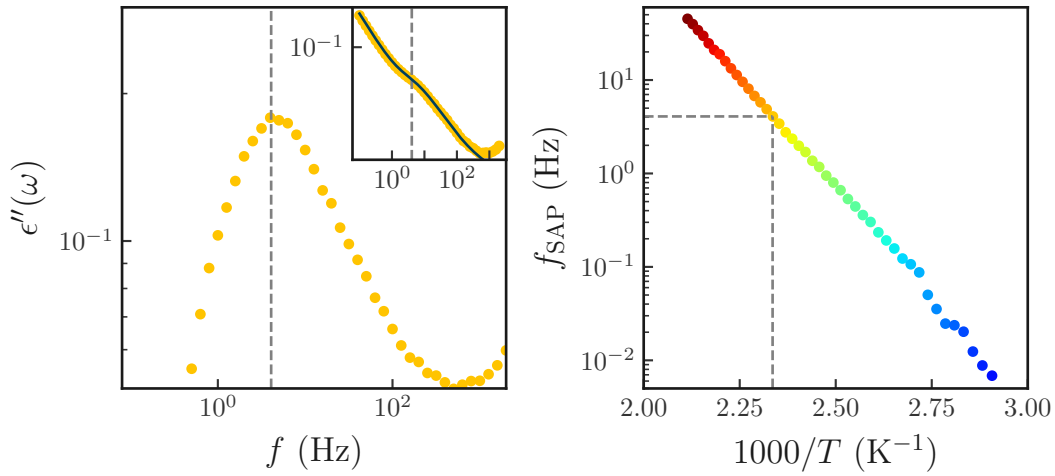

Figure 8.10: Left: dielectric loss ϵ'' as a function of the excitation frequency at $T = 428$ K. The contribution of conductivity is removed for clarity. Data with the contribution of conductivity are shown in the inset. The solid line correspond to Eq. 8.11. Right: SAP frequency as a function of $1000/T$. Gray dotted lines correspond to the SAP frequency at $T = 428$ K. The colour scale is the same as in Fig. 8.9.

8.3.2 Comparison with adsorption kinetics

In Fig. 8.11, we plot both the SAP frequency f_{SAP} and the monomer adsorption rate $q_{\mathrm{adsorption}} = \nu N^{-1/2}$ as a function of the inverse temperature. Both follow an Arrehnius law. The activation energy of the SAP process is 90.4 ± 0.6 kJ/mol. For adsorption, we had found an activation energy 67 ± 10 kJ/mol (see Fig. 8.8), but with a poor precision due to the small number of data points. Therefore, in Fig. 8.11, we only plot Arrhenius lines corresponding to $E_{\mathrm{a}} = 90.4$ kJ/mol. It seems to describe reasonably well our adsorption data.

Similarly to many other polymer melts [145], both the SAP and the adsorption rate are described by an Arrhenius law with the same activation energy, around 10^2 kJ/mol. This supports the fact that the SAP is also at the origin of adsorption of PDMS melts. In Fig. 8.11, the two vertical axis (f_{SAP} and $q_{\mathrm{adsorption}}$) are plotted with identical scales. For many polymers, the vertical shift between the SAP and the adsorption data is always the same, and is $Y\rho N^{1/2}$ with ρ the bulk density of the polymer melt, N the number of monomers per chain and Y a constant that is such that $Y = 4.0\,.10^{-6}$ for all the polymers tested. This will be extensively explained and discussed in a future publication by Thoms

et al. [218]. Here, for PDMS, we find a shift factor of about 10^2, yielding to a significantly larger value of Y: $Y = 10^{-4.7}$ compared to other polymers.

This shows that, despite the fact that, as all other polymers, the activation energies measured by SAP and adsorption kinetics are the same, the prefactor time is different with PDMS. This might be due to the strong interaction between PDMS and the wafer, compared to other polymers. In particular, we have used hydroxyl-terminated PDMS, which interact very strongly with the surface. This could explain the high values of adsorption rates compared to other polymers. To check this hypothesis, we are currently running adsorption kinetics of PDMS with various end-groups to see if they affect the adsorption rate.

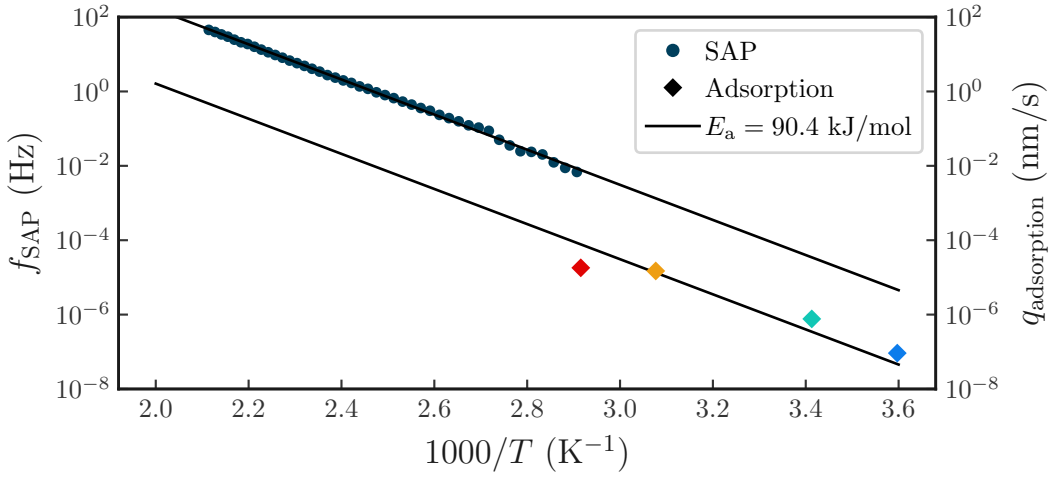

Figure 8.11: SAP relaxation frequency f_{SAP} (from DS measurements) and monomer adsorption rate $q_{adsorption} = \nu N^{-1/2}$ (from adsorption measurements) as a function of the inverse temperature. The bottom solid line is the same as the top one, but shifter by a factor 10^{-2} to match the adsorption data.

8.4 Conclusion

This chapter stands apart from the rest of the experimental work presented in this thesis. Here, we have discussed the adsorption kinetics of PDMS melts on silicon wafers. Similarly to other polymers, adsorption of PDMS melts is an activated process with an activation energy of about 10^2 kJ/mol. It should be associated with one or several molecular mechanisms. The Arrhenian temperature dependency of adsorption kinetics rules out the segmental relaxation process. By comparing adsorption kinetics and dielectric relaxation spectra, it has recently been shown that the mechanism at the origin of the early adsorption kinetics is a slower process (compared to the segmental relaxation), which follows an Arrhenius law. It has been called the Slow Arrhenius Process (SAP). This has been investigated in many polymer melts but PDMS. Here, we have shown that it is also valid for PDMS melts. However, the adsorption rate for PDMS stands out from the rest of polymer melts. This is likely due to the particularly strong interaction between PDMS and the surface, and especially through its hydroxyl end-groups. This hypothesis is currently under investigation.

Conclusions of Chapter 8

In this chapter, we have seen that:

- PDMS adsorbs a lot on silicon wafers.
- its adsorption kinetics is activated, with an activation energy around 10^2 kJ/mol. This is similar to other polymer melts.
- similarly to other polymer melts, the early adsorption kinetics is not governed by the segmental relaxation time but rather by a molecular relaxation time called SAP, which matches its temperature dependency.
- yet, the adsorption rates of PDMS are much larger than expected from measurements on other polymers. This might be due to the particularly strong interaction between the hydroxyl end-groups and the surface.

Conclusion of Part II

In this second and last part of the thesis, we have used various experimental techniques to probe the behaviour of semi-dilute entangled polymer solutions in the vicinity of a solid wall. We have started by describing the materials and methods in Chapter 5. Then, in Chapter 6, we have presented neutrons reflectivity experiments at the interface between a smooth sapphire surface and a dPS/DEP semi-dilute solution. In particular, we have highlighted the fact that it is possible to have both a depletion of polymers near the surface and adsorption of some chains on the wall. Using a home-made reflectivity cell, we were able to see that the flow has no effect on the near-surface concentration profile up to moderate Weissenberg numbers. The results of this chapter have helped us to discuss the experiments presented in Chapter 7. In this chapter, we have first presented the temperature dependence of the bulk rheology of our PS/DEP solutions. We haev shown that the expected scaling law for the viscosity as a function of the concentration does not work in our system, and we have discussed the reasons for this discrepancy using the temperature dependence of the viscosity. In a second part, we have briefly presented the Tracking of Photobleached Pattern technique and the way we can measure slip with it. Finally, we have dedicated the last section to present a new methodology to measure slip and friction using a rheometer. This last part is promising, and some experiments are still ongoing to improve the method. In the last chapter (Chapter 8), we have shown some results about the effect of temperature on the adsorption kinetics of PDMS melts. These results are compared to dielectric measurements in order to link the adsorption kinetics to some microscopic relaxation processes. Interestingly, PDMS seems to display an original behaviour compared to other polymer melts, and this is probably due to the strong affinity between its end groups and the substrate.

General Conclusion

The first part of this work tackles this question using a model liquid in which atoms interact through a model Lennard-Jones (LJ) potential. Using Molecular Dynamics, we have described the temperature dependency of the liquid/solid friction both at high temperatures and in the supercooled regime for a bi-disperse LJ fluid. We have shown that, for the melted liquid, both the viscosity and the friction coefficient follow activated laws, in harmony with what has been observed for PDMS melts in the literature. For the supercooled liquid, we have noticed two possible behaviours: for weak liquid/solid interactions, we observe a phase separation near the wall, and thus a crystallisation of the first liquid layers. This leads to a solid/solid like friction, which is much lower than the liquid/solid friction because of the incommensurability between the crystalline layers and the wall. On the contrary, when the liquid/solid interaction is strong, phase separation is prevented, and the friction coefficient, as the viscosity, becomes super-Arrhenian. These results have been published recently in [108]. In a second chapter, we have looked at a simple monodisperse LJ fluid. The purpose of using a pure LJ in this second chapter was to reduce the number of relaxation times in the system, as well as using a system able to crystallise. We have first shown that both the viscosity and the friction coefficient become non-Newtonian at high shear-rates. We have related this to density inhomogeneities due to the strong flow, and in particular, the Cox-Merz rule is violated. We have also measured the stress at the wall as we cross the melting temperature of the liquid. We have noticed that the temperature dependency of the wall stress is opposite between the fluid and the crystallised LJ. In addition, in the latter case, the stress at the wall significantly depends on the shear velocity, which is *a priori* unexpected for a solid/solid friction. This second chapter contains results of simulations that have been launched very recently. We present them in this thesis since they open interesting questions, and in particular, the shear-rate dependency of the friction is also observed experimentally in the seecond part of the thesis. Yet, these are preliminary results, and we are currently performing more simulations and bibliographical research in order to improve this content.

The second part of this work is in the continuation of the numerical simulations, but this time, we look at the friction of polymers on smooth surfaces using experimental techniques. Except for the last chapter, we always use semi-dilute entangled polystyrene inside diethylphtalate (PS/DEP) solutions. We have combined neutron reflectivity and an in-depth analysis of rheological data to probe the near-surface behaviour of polymer chains during the flow.

The neutron reflectivity technique has allowed us to obtain the near-surface concentration profile inside our PS/DEP semi-dilute solutions. Usually, surfaces are classified as "attractive" or "repulsive" for a given polymer solution, meaning that there is either an over-concentration of polymers at the surface, in addition to adsorption of some chains on the wall, or a depletion of polymers near the wall, leading to a solvent-rich interfacial layer. Interestingly, we show that these two situations are not mutually exclusive, as we have observed a simultaneous depletion and adsorption at the wall. In addition, we have shown that moderate flows do not impact this interfacial layer.

The second chapter is divided into three sections. In the first one, we focus on the bulk viscosity of our PS/DEP solutions. We show that the viscosity does not follow the expected volume fraction dependency, and that this deviation is larger as the temperature is decreased. We suggest that this discrepancy is related to an effect of the proximity to the glass transition temperature, which would impact the bulk dynamics on a temperature range much larger than expected. In order to settle this question, we would need to do more experiments with various good solvents and on a broad range of temperatures. This is not that easy, since many solvents of PS are volatile and toxic. In the second part of this chapter, we describe the Tracking of Photobleached Pattern (TPP) technique, and we apply it to the measurement of slip lengths of PS/DEP solutions. This technique is powerful to directly measure slip lengths as a function of the true applied shear-rate. This is the reason why we spent a lot of times trying to add a fine temperature control on this set-up. Even though we managed to finely control the temperature of the liquid over a wide range ($10-90$ °C), we evidence that the fluorescence of the molecular probes we used is quenched as the temperature increases. Such an undesirable behaviour strongly limits the accurate determination of the slip length as a function of temperature with TPP. Thus, in a third section, we have developed a new analysis of rheological data obtained with a rheometer to extract the friction coefficient of a liquid polymer, allowing to overcome the previous experimental limitations. This work is still in progress, but the first results seem promising. We are able to measure slip lengths comparable to what we had measured using the TPP technique. In particular, we observe a shear-rate dependency of the friction coefficient, which might be linked to either a broad slip transition, or some shear-thinning behaviour of the interfacial liquid. The temperature dependency of the friction coefficient gave us access to the near-surface relaxation time, which is lower than the bulk relaxation time. A possible development of this method would be to probe the oscillatory response of the liquid in order to experimentally measure the frequency-dependent friction coefficient.

Finally, in the last chapter, we have studied the adsorption kinetics of PDMS melts. Looking at the early kinetics, we were able to measure an activated adsorption rate, which activation energy matches that of other adsorbing polymers. Using dielectric spectroscopy, we have related this to a molecular relaxation process called the Slow Activated Process (SAP), with the same activation energy. Yet, PDMS stands apart from the rest of polymer melts studied in the literature because of particularly high values of adsorption rates compared to what was expected. We attribute this specificity to the strong interaction between the hydroxyl end groups of our PDMS and the surface. More experiments are in process, and in particular, we are currently recording the adsorption kinetics of PDMS with various end-groups to probe the effect of the extremities on the early kinetics.

As is often the case in science, this thesis has raised more questions than it has answered. The first question we asked ourselves at the beginning of this work was **what is the effect of temperature on slip and friction?** What this work has shown, or − at least − suggested, is that far from the glass transition temperature, both the viscosity and the friction coefficient are **activated**, and thus, so is the slip length. The activation barrier depends on the liquid-liquid interaction for the viscosity, and on the liquid-solid interaction (thus, the wettability) for the friction coefficient. This is correlated to a modification of the relaxation dynamics of the interfacial liquid due to the presence of the wall. Near the glass transition, numerical simulations suggest that the liquid/solid friction becomes super-Arrhenian, similarly to the viscosity. Experimentally, this regime is

more difficult to study, and this is still ongoing work.

Another question I find interesting is **whether viscosity and friction can be decoupled, or whether they are intrinsically linked**. The formalism used to describe slip makes the hypothesis that these are decorrelated effects: we can conceive viscosity independently of liquid/solid friction (this is rather intuitive, since viscosity can be defined in a flow with no walls), and we can define a friction coefficient without introducing the viscosity of the liquid. The latter point is much less intuitive, but − as far as I understand − this is implicitly postulated in the way the problem is described, where the quantity that couples these two *a priori* independent variables is the slip length b, which is the result of the competition between these two independent effects. This thesis does not provide an answer to that question, but investigating the effect of temperature on both viscosity and friction is, I think, a good start to tackle this problem. If they are truly independent variables, temperature effects on both will be uncorrelated. Yet, this is very difficult to achieve experimentally, since the near-surface liquid composition is different from the bulk one, and thus, we have only access to an averaged friction due to this whole interfacial liquid. Nonetheless, coupling different techniques such as neutron reflectivity and interfacial rheology could be a good approach to overcome this issue.

Finally, I would take the opportunity of the last paragraph of this thesis to give a personal feeling. I would like to quote a sentence written by Daniel Pennac in another context, but which I think applies well to the present situation: "*La vérité vient rarement des réponses que tu reçois [...], la vérité naît de l'enchaînement logique des questions que tu poses.*" [b]. I feel like being a researcher is being both a professor and its own student: you explain yourself what you understand, and you question yourself about it, and this permanent dialogue drives you towards more and more questions, and thus towards a deeper and deeper understanding of what you thought you knew.

[b] La petite marchande de prose, D. Pennac, Gallimard (1990). A translation in english could be: "*Truth rarely comes from the answers you receive [...], truth comes from the logical sequence of questions you ask.*"

Appendices

Quantifying parallelism of the plate-plate geometry

In Section 7.3.2 of Chapter 7, we try to extract the slip length of a PS/DEP solution with the rheometer using a plate-plate geometry. The top geometry is a rough plate bough from Anton Paar, and the bottom geometry is a silicon wafer we have glued. To quantify the error on the torque measurement due to the non-perfect parallelism between the two surfaces, we have measured the torque Γ as a function of time during shear at a constant apparent shear-rate $\dot{\gamma}_a = 0.1\ s^{-1}$. The acquisition time of each point is 2 s. The result is plotted in Fig. 12. The left graph shows the whole curve, with the transient regime followed by the permanent regime. The transient regime lasts around 10^2 s. The right graph is a zoom on the permanent regime. The torque oscillates with a period around 10^2 s, and the value of the torque deviates of about 0.5 % of its values during the oscillation. This gives us error bars on the measurement of the torque.

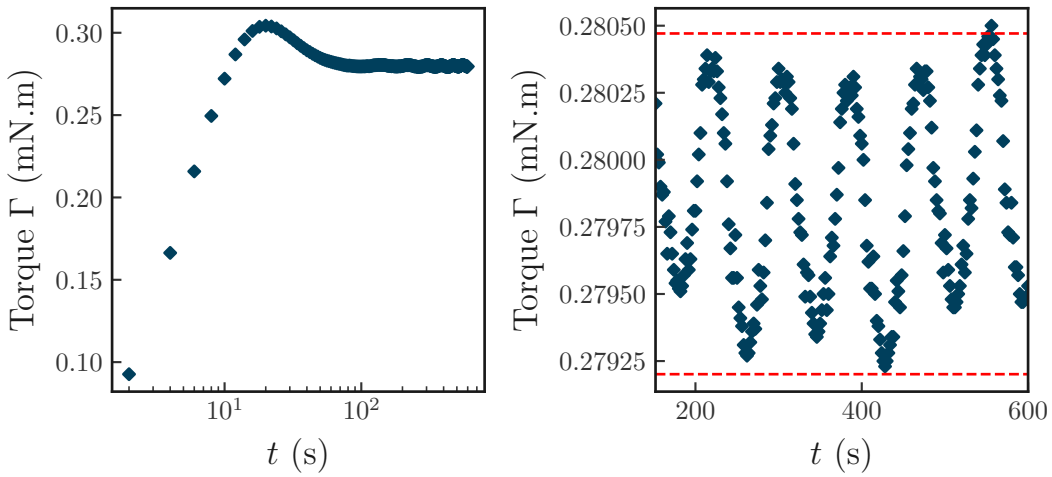

Figure 12: Torque Γ as a function of the shearing time t. The apparent shear-rate $\dot{\gamma}_a$ is fixed at $0.1\ s^{-1}$. The error due to a non-perfect parallelism is less than 0.5 % of the mean value of the torque in the permanent regime.

Effect of the volume fraction on the glass transition temperature

As mentioned in Section 1.3.4, a binary mixture can have one or two glass transition temperatures, and they can depend on the volume fraction of the mixture. Here, we show the glass transition temperatures of PS/DEP semi-dilute solutions at $\phi = 2.3$ % and $\phi = 5$ % together with the glass transition temperature obtained for the DEP solvent (see Fig. 13). These results have been obtained using DSC (see Section 5.3).

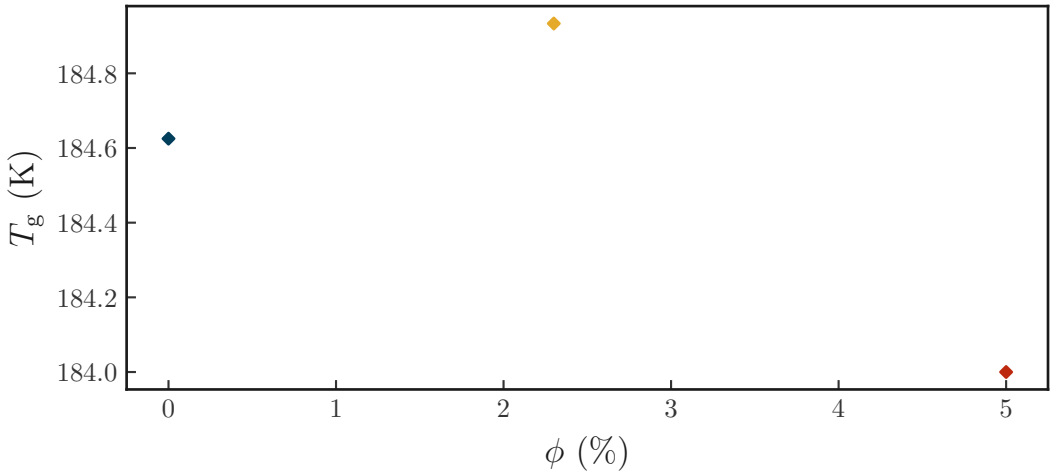

Figure 13: Glass transition temperature measured by DEP for pure DEP and two semi-dilute PS/DEP solutions at two different volume fractions ϕ.

We observe that the glass transition temperature of the two solutions is nearly the same as the glass transition temperature of the solvent, which is around 185 K, in agreement with the literature [222].

Synthèse en français

Cette thèse vise à mieux comprendre la façon dont les fluides peuvent s'écouler au voisinage d'une paroi solide. En mécanique des fluides, une hypothèse très commune est de supposer qu'il n'y a pas de différence entre la vitesse de la paroi et la vitesse du fluide à la paroi. On appelle cela la condition limite de **non-glissement**. Pourtant, plusieurs observations expérimentales ont mis en évidence des situations où le liquide a une vitesse non nulle v_g relativement à la paroi : on parle de condition limite de **glissement**. On peut définir une **longueur de glissement** b définie par la distance, dans le solide, à laquelle le profil de vitesse s'extrapole à 0 (voir Fig. 8.14).

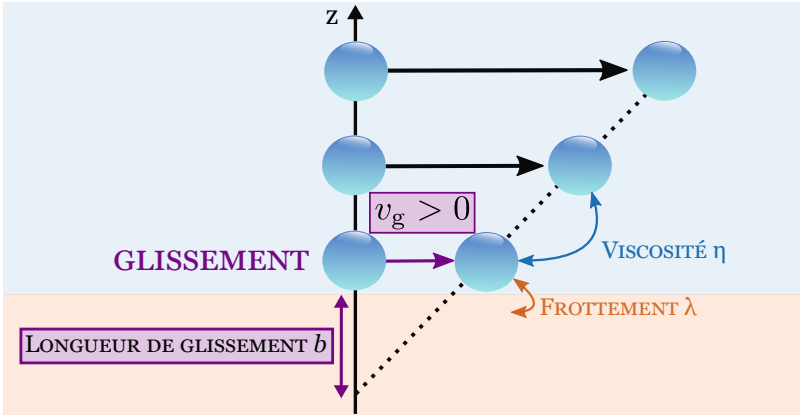

Figure 8.14: Schéma de la condition limite de glissement.

Schématiquement, lorsque le fluide est mis en écoulement, chaque couche de fluide entraîne les couches voisines d'autant plus fortement que la viscosité η du fluide est importante. En particulier, au voisinage de la paroi, le fluide est entraîné par l'écoulement en volume, et a tendance à glisser d'autant plus que la viscosité est élevée. Cependant, si le fluide en contact avec la paroi acquiert une vitesse de glissement non nulle, il exerce une contrainte sur la surface elle-même, qui, étant immobile, résiste à l'entraînement induit. Cela crée donc un **frottement** du fluide sur la paroi. Dès 1822, Navier avait envisagé cette situation de **glissement** et avait proposé que, dans ce cas, la contrainte σ exercée par le fluide sur la paroi fût proportionnelle à la vitesse de glissement v_g, de sorte que $\sigma = \lambda v_g$, où λ est un **coefficient de frottement**, caractéristique de l'interaction fluide/surface.

Il est alors aisé de montrer, en supposant la continuité de la contrainte entre le volume et l'interface et en linéarisant le profil de vitesse au voisinage de la paroi, que l'on peut exprimer la longueur de glissement b comme étant : $b = \eta/\lambda$. Cette expression est utile, car expérimentalement, nous avons généralement accès à η et b, et ainsi, le paramètre λ est déduit du ratio η/b.

Cette thèse vise à comprendre quels sont les mécanismes à l'origine du glissement et du frottement à l'interface liquide/solide. Un bon moyen de comprendre quels sont les

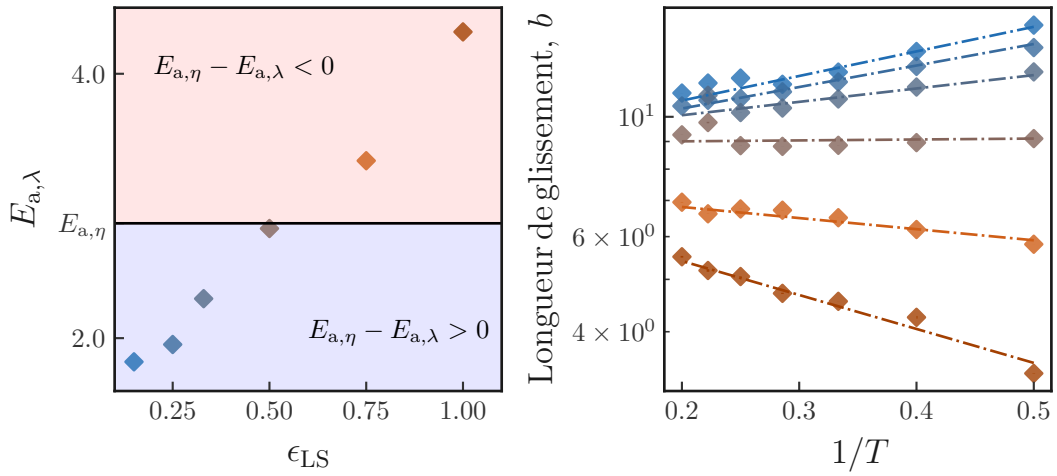

Figure 8.15: Gauche : énergie d'activation du coefficient de frottement en fonction du paramètre d'interaction liquide/solide ϵ_{LS}. Droite : longueur de glissement en fonction de la température pour différentes valeurs du paramètre ϵ_{LS}. Le code couleur est le même sur les deux graphes.

mécanismes en jeu est de changer la température du liquide : en augmentant la température, l'agitation moléculaire augmente. La dépendance de la viscosité avec la température est déjà bien décrite par différents modèles moléculaires. En revanche, l'effet de la température sur le glissement et le frottement n'a été que très peu étudié. Dans la littérature, on peut observer des longueurs de glissement croissantes, décroissantes, constantes, voire non monotones avec la température. Il manque donc ici une description moléculaire qui permette de comprendre dans les détails le rôle de la température sur le coefficient de frottement λ.

Pour répondre à cette problématique, nous avons travaillé en deux temps. Tout d'abord, nous avons utilisé des simulations numériques de dynamique moléculaire. Nous avons simulé un système très simple, un fluide bi-disperse de Lennard-Jones (appelé fluide de Kob-Andersen), capable d'atteindre un régime surfondu lorsqu'il est refroidi en dessous de sa température de fusion. Nous avons confiné ce fluide entre deux parois cristallines et nous l'avons ainsi soumis numériquement à diverses expériences de rhéologie. Nous avons distingué le régime "chaud", pour lequel la température du fluide est supérieure à la température de fusion, et le régime "froid", en dessous de la température de fusion, dans lequel le fluide est surfondu. Nous avons observé que dans le régime chaud, la viscosité η et le coefficient de frottement λ sont tous les deux bien décrits par une loi d'Arrhenius $x = x_0 \exp\left(\frac{E_a}{RT}\right)$ où E_a est une énergie d'activation caractéristique du processus moléculaire mis en jeu. Pour le système étudié ici, nous avons $E_{a,\eta} \simeq 2,9$ pour la viscosité. De façon intéressante, l'énergie d'activation associée au coefficient de frottement dépend fortement de l'énergie d'interaction liquide/solide ϵ_{LS}. Plus précisément, nous avons observé que $E_{a,\lambda}$ est une fonction croissante de ϵ_{LS}, et que $E_{a,\lambda=}E_{a,\eta}$ pour $\epsilon_{LS} \simeq 0.50$. Cela implique un changement de sens de variation de la fonction $b(T)$, qui est donnée par $b(T) = \frac{\eta_0}{\lambda_0} \exp\left(\frac{E_{a,\eta} - E_{a,\lambda}(\epsilon_{LS})}{RT}\right)$, entre $\epsilon_{LS} < 0.50$ et $\epsilon_{LS} > 0.50$ (voir Fig. 8.15) et permet de rationaliser les diverses tendances de $b(T)$ observées expérimentalement dans la littérature.

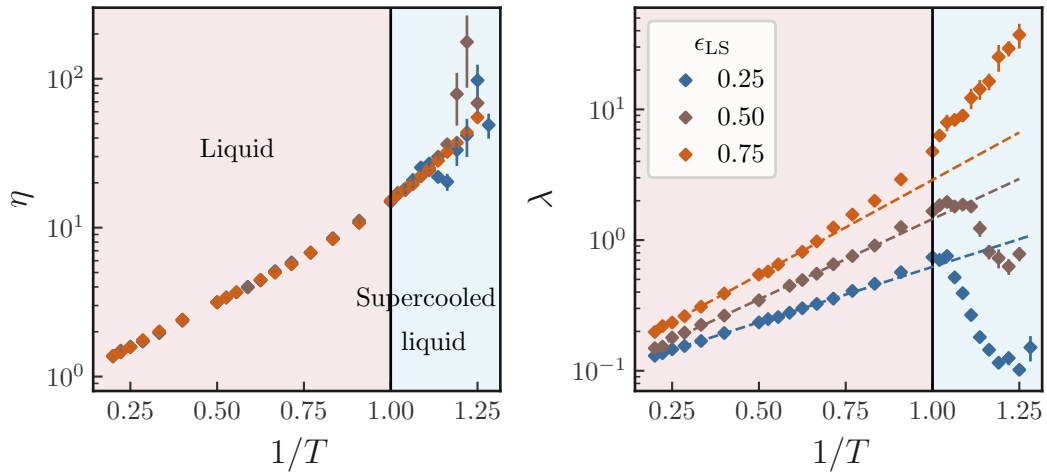

Figure 8.16: Viscosité (à gauche) et coefficient de frottement (à droite) en fonction de la température pour différentes valeurs du paramètre d'interaction liquide/solide ϵ_{LS}.

Lorsque le liquide est surfondu (régime "froid"), sa viscosité devient super arrhénienne, et est bien décrite par une loi de type Vogel-Fulcher-Tammann (VFT). Pour le coefficient de frottement, deux comportements sont visibles (voir Fig. 8.16). Aux faibles valeurs de ϵ_{LS}, on observe une démixtion du fluide au voisinage de la paroi : une région de fluide monodisperse est formée à la paroi, et celui-ci cristallise en cristal hexagonal. La structure cristalline de la paroi étant carrée, le frottement diminue brutalement par incommensurabilité des deux structures mises en jeu. Au contraire, aux fortes valeurs de ϵ_{LS}, la démixtion est empêchée, et le fluide reste surfondu même au voisinage de la paroi. Dans ce cas-ci, le coefficient de frottement devient super arrhénien, et il peut également être décrit par une loi de type VFT, avec des paramètres différents de ceux de la viscosité.

Ce premier travail nous fournit plusieurs pistes de réflexion. Il semblerait que, dans la majorité des cas, le coefficient de frottement suive des dépendances en températures de la même forme que la viscosité, mais avec des paramètres qui lui sont propres, et qui dépendent - entre autres - de l'interaction fluide/surface. Cela avait déjà été observé dans la littérature dans le cas du régime arrhénien pour des fondus de PDMS. La suite de notre travail a eu pour objectif de développer des méthodes expérimentales dans le but de sonder ces comportements dans le cas de fluides réels. Nous avons choisi de travailler avec des polymères liquides, car leur viscosité élevée en fait un système pouvant présenter de fortes longueurs de glissement b, qui sont aisément mesurables. Nous avons choisi de travailler avec des solutions semi-diluées de polystyrène (PS) de grande masse molaire dans la diéthylphtalate (DEP), qui est un bon solvant du PS.

Nous avons dans un premier temps étudié la dépendance en température de la viscosité des solutions. Pour une solution semi-diluée enchevêtrée en bon solvant, les prédictions théoriques stipulent que la viscosité η de la solution varie avec la fraction volumique en polymère ϕ selon la loi :

$$\eta \propto \phi^{15/4} \tag{8.12}$$

Cette prédiction théorique est bien vérifiée dans plusieurs bons solvants (toluène, benzène...). Cependant, nous avons observé que l'exposant que obtenu dans le cas du solvant

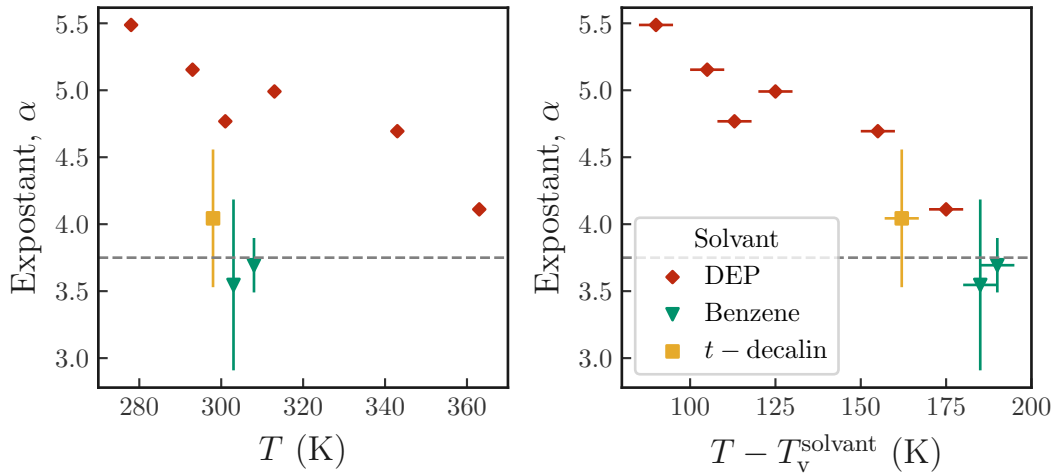

Figure 8.17: Exposant α en fonction de la température de la solution T. $T_v^{solvant}$ est la température de transition vitreuse du solvant, qui est à peu près égale à la température de transition vitreuse de la solution pour nos gammes de concentrations.

DEP est nettement supérieur à 15/4. En effet, nous mesurons un exposant de presque 5.0 à température ambiante. Cela avait déjà été observé dans la littérature pour ce solvant. De plus, nous observons que cet exposant dépend de la température : plus la température est basse, plus l'exposant augmente, et donc dévie de la loi attendue (voir Fig. 8.17). Plusieurs hypothèses pourraient expliquer cette déviation. D'une part, nous pourrions imaginer que la DEP n'est pas un si bon solvant du PS. Cependant, des mesures de diffraction de neutrons aux petits angles (SANS) à différentes températures ont permis de vérifier que la longueur de corrélation ξ suivait bien la loi d'échelle attendue avec la fraction volumique pour des solutions semi-diluées enchevêtrées en bon solvant. Cela suggère fortement que la DEP est un bon solvant du PS. Une autre possibilité serait un effet de transition vitreuse, manifeste sur une gamme étonnamment étendue de température. Il est en général considéré que les effets vitreux peuvent jouer jusqu'à 100 °C au-delà de la transition vitreuse. La température de transition vitreuse des solutions étudiées est autour de −80 °C, donc il n'est pas exclu que des effets vitreux puissent être présents à température ambiante. Pour comprendre plus en détail l'origine de cette déviation, des mesures systématiques de l'exposant en fonction de la température dans différents bons solvants du PS seraient nécessaires.

Nous avons ensuite étudié la dépendance en température du coefficient de frottement λ de ces solutions sur des pastilles nues de silicium. Pour ce faire, nous avons employé deux techniques différentes. La première technique est le "suivi de motif photoblanchi" : une petite quantité de marqueurs fluorescents est introduite dans la solution de polymère. Celle-ci est confinée entre une pastille nue de silicium, immobile, et un prisme de quartz, pouvant se déplacer parallèlement à la pastille. Un laser est ensuite focalisé le long d'une ligne dans l'échantillon, et vient éteindre la fluorescence des marqueurs de long de celle-ci, dessinant une ligne noire à travers la solution. Le fluide est ensuite cisaillé, et nous suivons le déplacement de cette ligne au cours du cisaillement. Cela permet une visualisation directe de la longueur de glissement b et du taux de cisaillement subit par le fluide $\dot{\gamma}$. Malheureusement, cette technique n'est pas adaptée à une étude en température, car

la fluorescence des marqueurs est rapidement éteinte lorsque le fluide est chauffé. Nous avons donc développé une autre méthode de mesure du coefficient de frottement.

Pour cela, nous avons utilisé la grande précision de mesure du rhéomètre. Nous confinons la solution entre une pastille nue de silicium, immobile, et une géométrie circulaire (de rayon R) et rugueuse du rhéomètre. L'épaisseur de liquide est notée h. Le fluide est cisaillé à une vitesse de rotation Ω par la géométrie circulaire, et nous mesurons le couple exercé sur celle-ci par le fluide en écoulement. Nous comparons ensuite le couple mesuré au couple calculé sous différentes hypothèses. En supposant des conditions limites de non-glissement aux deux parois, nous obtenons un couple calculé nettement supérieur au couple mesuré. Cependant, en faisant l'hypothèse qu'il y a du glissement sur la pastille de silicium, alors le taux de cisaillement subi par le fluide est :

$$\dot{\gamma} = \frac{R\Omega}{h+b} \tag{8.13}$$

Le caractère non-newtonien du fluide nécessite une hypothèse supplémentaire. Nous supposons alors que $b = \eta(\dot{\gamma})/\bar{\lambda}$ où $\eta(\dot{\gamma})$ est la viscosité de la solution, qui présente une rhéofluidification, et qui est mesurée dans une expérience indépendante, et $\bar{\lambda}$ est un coefficient de frottement moyen à la vitesse de rotation Ω appliquée. De cette façon, nous pouvons trouver, pour chaque valeur de Ω, une valeur de $\bar{\lambda}$ telle que le couple calculé soit égal au couple mesuré (voir Fig.8.18). Nous obtenons une courbe $\lambda(\bar{\Omega})$ que nous pouvons également tracer comme $\bar{\lambda}(\dot{\gamma}_{\text{app}})$. Nous retrouvons des valeurs similaires à celles observées avec la méthode de suivi de motif photoblanchi. Nous observons que $\bar{\lambda}(\dot{\gamma}_{\text{app}})$ a une forme identique à $\eta(\dot{\gamma})$. Il apparaît encore une fois l'idée que le coefficient de frottement λ peut être interprété comme une viscosité d'interface. Nous modélisons ces deux fonctions par une loi de Carreau-Yasuda :

$$x = x_0(1 + (\tau_x\dot{\gamma})^a)^{(n-1)/a} \tag{8.14}$$

et nous extrayons la valeur de plateau x_0, le temps caractéristique τ_x et les exposants a et n pour $\eta(\dot{\gamma})$ et pour $\bar{\lambda}(\dot{\gamma}_{\text{app}})$.

Pour une solution de PS de masse molaire 20.6 Mg/mol dans la DEP avec une fraction volumique de 5 %, nous mesurons $\tau_\eta > \tau_\lambda$, et ainsi la rhéofluidification en volume (η) apparaît à des taux de cisaillement plus faibles que la rhéofluidification en surface ($\bar{\lambda}$). Par conséquent, la courbe $b(\dot{\gamma}_{\text{app}})$ est décroissante. Cependant, pour une solution de masse molaire plus faible (10 Mg/mol) et de fraction volumique plus faible aussi ($\phi = 4$ %), nous mesurons $\tau_\eta < \tau_\lambda$, et ainsi la courbe $b(\dot{\gamma}_{\text{app}})$ est cette fois-ci croissante.

Nous avons enfin regardé l'effet de la température sur ces solutions. Nous avons mesuré les valeurs de plateau (η_0 et λ_0) et les temps caractéristiques (τ_η et τ_λ) en fonction de la température. Nous observons que tous ces paramètres suivent des lois d'Arrhenius, avec une énergie d'activation autour de 21 kJ/mol pour η_0 et τ_η et autour de 26 kJ/mol pour λ_0 et τ_λ (voir Fig.8.19).

Il a été observé que les solutions de polymères peuvent présenter des variations de concentration au voisinage d'une paroi solide. En particulier, de Gennes distingue généralement deux cas :

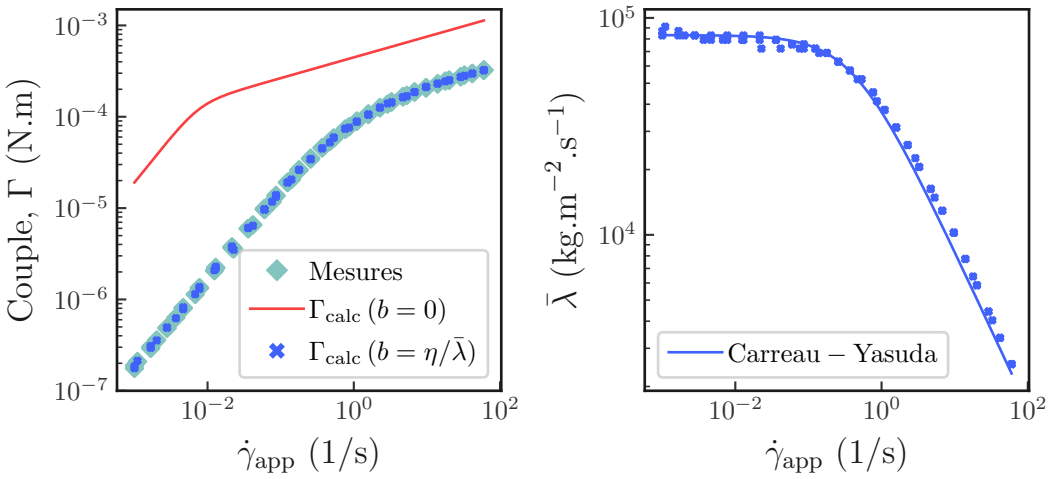

Figure 8.18: Gauche : couple mesuré (losanges verts), couple calculé dans l'hypothèse de non-glissement (ligne rouge) et couple calculé dans l'hypothèse d'un glissement $b = \eta(\dot{\gamma})/\bar{\lambda}$. Dans ce dernier cas, le paramètre $\bar{\lambda}$ est ajusté afin de retrouver le couple mesuré. Droite : paramètre ajusté $\bar{\lambda}$ en fonction du taux de cisaillement apparent $\dot{\gamma}_{app}$.

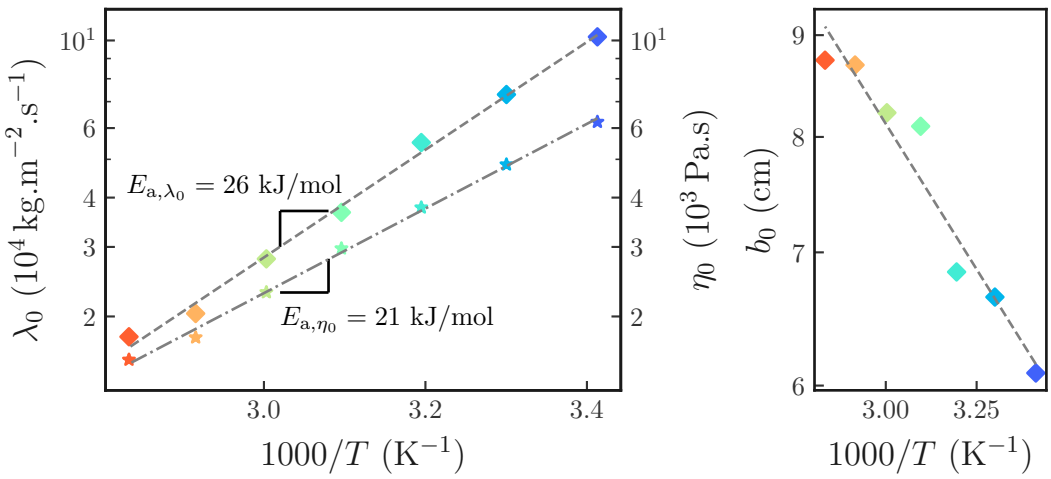

Figure 8.19: Gauche : coefficient de frottement newtonien λ_0 et viscosité newtonienne η_0 en fonction de la température. Droite : longueur de glissement newtonien $b_0 = \eta_0/\lambda_0$ en fonction de la température. Les droites représentent des régressions de type Arrhenius. Les données ont été obtenues avec une solution de PS/DEP 20 Mg/mol 5 %.

- le cas d'une surface **répulsive**, dans lequel l'interaction solvant/surface est plus favorable que l'interaction polymère/surface. Dans ce cas, la concentration en polymère au voisinage de la surface est inférieure à la concentration en volume.

- le cas d'une surface **attractive**, dans lequel l'interaction polymère/surface est plus favorable que l'interaction solvant/surface. Dans ce cas, la concentration en polymère au voisinage de la surface est supérieure à la concentration en volume, et des chaînes de polymères sont adsorbées sur la paroi.

Nous comprenons aisément que, selon le cas, le comportement de glissement et de frottement de la solution de polymère ne sera pas le même. Dans le cas d'une surface répulsive, la viscosité au voisinage de l'interface est plus faible que la viscosité en volume. Dans le cas d'une surface attractive, non seulement la viscosité à l'interface est plus élevée qu'en volume, mais la présence de chaînes adsorbées peut entraîner une **transition de glissement** : à faible taux de cisaillement, le glissement est faible, car les chaînes de volumes s'enchevêtrent avec les chaînes adsorbées. À fort taux de cisaillement, celles-ci sont désenchevêtrées par l'écoulement et le glissement augmente.

Afin de pouvoir expliquer les courbes $\lambda(\dot{\gamma}_{\text{app}})$ obtenues, nous avons regardé les profils de concentration de nos solutions au voisinage de la surface. Pour cela, nous avons utilisé de la réflectivité des neutrons à l'interface entre des solutions semi-diluées enchevêtrées de dPS (polystyrène deutéré) dans la DEP hydrogénée et un saphir lisse. Nous avons montré que nous étions dans le cas d'une surface répulsive, c'est-à-dire que près de la surface, la concentration en PS est plus faible qu'en volume, formant une **zone de déplétion** (voir Fig. 8.20). Si l'on regarde les interactions chimiques entre les composants, l'existence d'une zone de déplétion a du sens. En effet, la surface du saphir possède des groupes oxydés de type hydroxyle. Or, contrairement au PS, la DEP peut faire des liaisons H, et ainsi interagir plus favorablement avec la surface.

La taille caractéristique de la zone de déplétion d varie avec la fraction volumique en polymère ϕ de la même façon que la taille de blob ξ, ce qui valide l'hypothèse de de Gennes selon laquelle $d \propto \xi$. Cependant, nous avons mis en évidence la présence de chaînes de dPS adsorbées sur la surface, malgré la présence d'une couche de déplétion (voir Fig. 8.21). La quantité de chaînes adsorbées est faible, mais non nulle. Cela permet de nuancer la distinction surface attractive/surface répulsive : il semblerait qu'il soit possible d'avoir une surface répulsive (et donc une couche de déplétion) tout en ayant des chaînes adsorbées à la surface. En effet, dans la couche de déplétion, la concentration en polymère est faible, mais non nulle, et l'interaction polymère/paroi est certes plus faible que l'interaction solvant/paroi, mais pas inexistante pour autant. Des simulations de DFT ont permis de montrer l'existence d'une interaction attractive de type Van der Waals entre le PS et la surface de saphir, qui serait à l'origine de l'adsorption de ces chaînes sur la surface.

Enfin, nous avons regardé si l'écoulement de la solution avait un effet sur la taille caractéristique de la zone de déplétion. Pour cela, nous avons généré un écoulement de Poiseuille dans notre cellule, que nous caractérisons par le nombre de Weissenberg $\text{Wi} = \frac{6Q\tau_\eta}{\ell h^2}$ où Q est le débit volumique, τ_η le temps de relaxation caractéristique de la

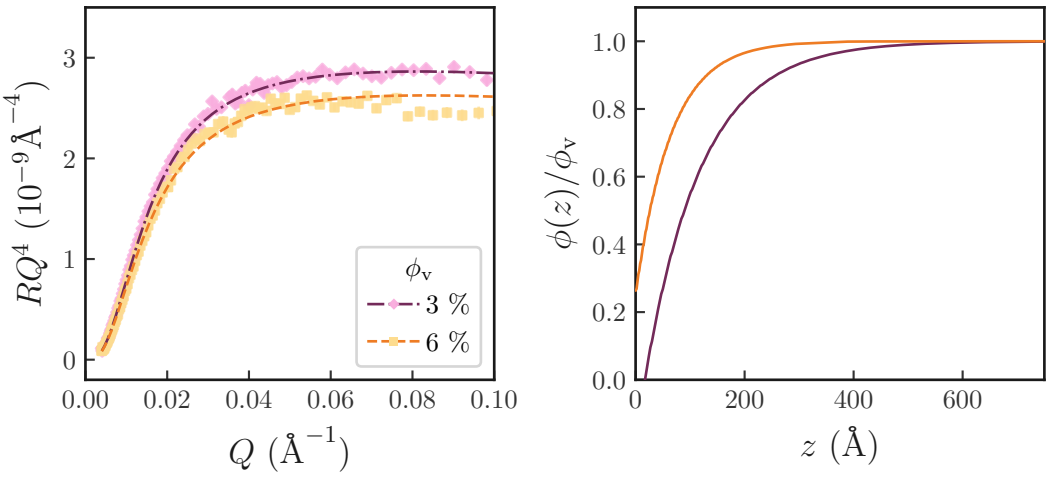

Figure 8.20: Gauche : profils de réflectivité neutrons pour des solutions de dPS/DEP à deux fractions volumiques ϕ_v différentes. Droite : profils de concentration au voisinage de la surface de saphir en fonction de la distance à la surface, obtenus par régression des profils de réflectivité.

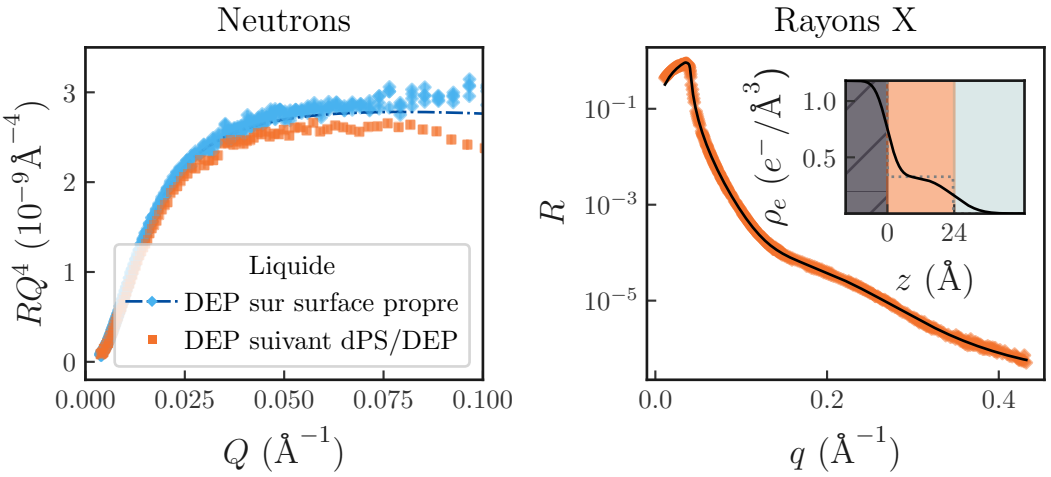

Figure 8.21: Gauche : courbes de réflectivité neutrons à l'interface saphir/DEP sur une surface de saphir propre (losanges bleus) et une surface de saphir précédemment mise en contact avec une solution de dPS/DEP (carrés orange). Droite : profil de réflectivité en rayons X à l'interface saphir/air pour une surface de saphir précédemment mise en contact avec une solution de PS/DEP. Insert : profil de densité électronique au voisinage de la surface de saphir, obtenu par régression du profil de réflectivité X.

viscosité, ℓ la largeur de la cellule et h l'épaisseur de liquide. Nous observons que, jusqu'à $\mathrm{Wi} = 10^{-1}$, la zone de déplétion n'est pas affectée par l'écoulement. Des mesures supplémentaires à plus grandes valeurs de Wi seraient nécessaires pour observer un éventuel effet de l'écoulement, notamment pour $\mathrm{Wi} > 1$, pour lequel des effets non linéaires sont susceptibles d'apparaître.

Pour finir, un dernier volet de ce travail a été dédié à la cinétique d'adsorption de chaînes de PDMS sur une pastille de silicium à partir d'un fondu. En particulier, nous avons quantifié la vitesse d'adsorption des chaînes en fonction de la température. Le PDMS utilisé est un PDMS de masse molaire 208 kg/mol, terminé par des groupements hydroxyles. Nous mesurons l'épaisseur adsorbée en fonction du temps de contact entre le fondu et la surface $h(t)$ à différentes températures d'incubation T. La cinétique présente deux régimes : un premier régime linéaire, duquel nous extrayons la vitesse d'adsorption v définie par $h = vt$. Ce régime est suivi d'un régime plus lent, logarithmique, que nous ne regardons pas ici.

Nous traçons le paramètre $q_{\mathrm{adsorption}} = vN^{-1/2}$ en fonction de la température. Nous observons que celui ici suit une loi d'Arrhenius avec une énergie d'activation autour de 67 kJ/mol. Il a été montré que la cinétique d'adsorption de polymères en fondus peut être associée à un processus de relaxation moléculaire appelé "Slow Arrhenian Process" (SAP), qui suit également une loi d'Arrhenius. Ce processus est notamment visible en spectroscopie diélectrique, avec laquelle on peut observer le spectre diélectrique $\epsilon(f)$ du fondu à différentes températures. La partie imaginaire ϵ'' possède un pic à la fréquence f_{SAP}, qui lui aussi suit une loi d'Arrhenius. Pour de nombreux polymères fondus, il a été montré que l'énergie d'activation associée à la loi d'Arrhenius $f_{\mathrm{SAP}}(T)$ est similaire à l'énergie d'activation de la vitesse d'adsorption $q_{\mathrm{adsorption}}(T)$. Nous observons que cela est également vrai pour le PDMS étudié ici (voir Fig. 8.22). Cependant, pour les polymères fondus étudiés jusqu'à présent dans la littérature, le ratio f_{SAP}/q est une constante qui ne dépend que de la densité du fondu ρ et de $N^{1/2}$. Dans le cas du PDMS hydroxyle-terminé, le ratio f_{SAP}/q est plusieurs ordres de grandeur plus grand qu'attendu.

Cette déviation pourrait être due à la nature du groupe terminal OH. En effet, certains travaux issus de la littérature suggèrent que les PDMS hydroxyle-terminés ne s'adsorbent pas, mais se greffent spontanément à la surface des pastilles de silicium, via une réaction de condensation avec les OH présents en surface, catalysée par la présence d'eau. Cela pourrait expliquer la différence de comportement de ces PDMS par rapport aux autres polymères fondus. Pour confirmer cette hypothèse, il serait nécessaire de quantifier la dépendance en température de la cinétique d'adsorption de PDMS méthyle-terminés pour voir si la déviation est toujours observée dans ce cas-ci.

Pour conclure, ce travail de thèse a mis en évidence la ressemblance de dépendance en température entre le coefficient de frottement λ et la viscosité η. λ peut alors être pensé comme une viscosité interfaciale, caractéristique de la dynamique du fluide au voisinage de la paroi. Expérimentalement, nous avons pu sonder sa dépendance en température dans des régimes pour lesquels η et λ étaient arrhéniens. Une différence dans l'énergie d'activation de ces deux paramètres implique un changement de monotonie de la longueur de glissement avec la température $b(T)$. Nous avons également observé cela en dynamique

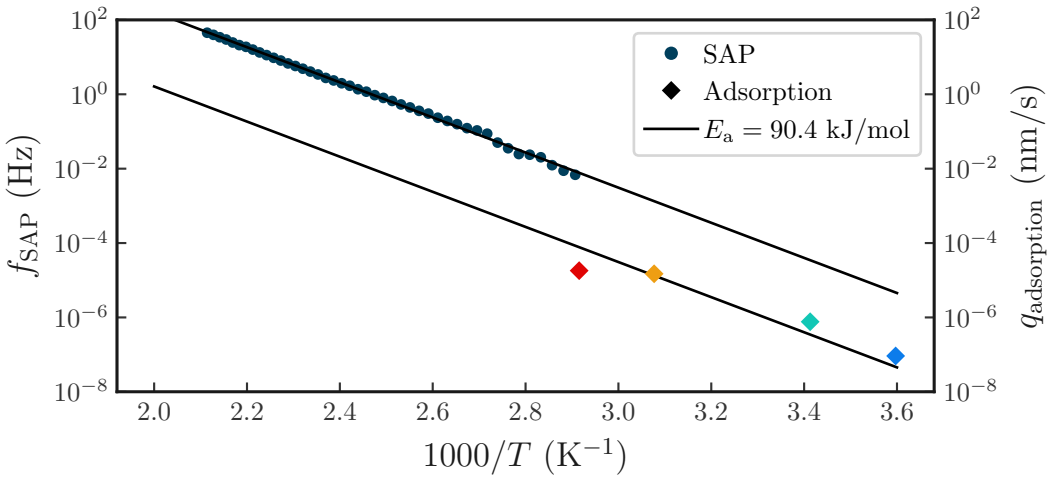

Figure 8.22: Fréquences SAP obtenues par spectroscopie diélectrique du PDMS (ronds bleus) et vitesses d'adsorption $q_{\text{adsorption}}$ déduites des cinétiques d'adsorption en température pour du PDMS sur pastille de silicium. Les lignes pleines correspondent à une loi d'Arrhenius d'énergie d'activation 90.4 kJ/mol.

moléculaire. Les simulations numériques nous ont donné accès à un régime surfondu. Dans ce régime-là, la viscosité et le coefficient de frottement deviennent tous les deux super-Arrhéniens. Nous n'avons pour l'instant pas observé ce comportement expérimentalement. Cela appelle à mesurer $\lambda(T)$ pour des fluides présentant un état surfondu et pour lesquels la viscosité est suffisamment importante pour avoir un glissement accessible expérimentalement.

Bibliography

[1] Henri Navier. Mémoire sur les lois du mouvement des fluides. 1822. 10

[2] Marceau Hénot, Marion Grzelka, Jian Zhang, Sandrine Mariot, Iurii Antoniuk, Eric Drockenmuller, Liliane Léger, and Frédéric Restagno. Temperature-Controlled Slip of Polymer Melts on Ideal Substrates. *Physical Review Letters*, 121(17):177802, October 2018. 11, 18, 24, 38, 56, 136

[3] Marion Grzelka. *Mécanismes de frottement aux interfaces polymères liquides / solide : propriétés de glissement et structure interfaciale*. PhD thesis, Paris-Saclay University, 2019. 11, 29, 31, 79, 103, 114, 118, 119, 120, 122, 127, 137

[4] Tatiana Schmatko, Hubert Hervet, and Liliane Leger. Friction and Slip at Simple Fluid-Solid Interfaces: The Roles of the Molecular Shape and the Solid-Liquid Interaction. *Physical Review Letters*, 94(24):244501, June 2005. 11

[5] David M. Huang, Christian Sendner, Dominik Horinek, Roland R. Netz, and Lydéric Bocquet. Water Slippage versus Contact Angle: A Quasiuniversal Relationship. *Physical Review Letters*, 101(22):226101, November 2008. 11, 13

[6] L. Bocquet and E. Charlaix. Nanofluidics, from bulk to interfaces. *Chem. Soc. Rev.*, 39(3):1073–1095, 2010. 11, 13, 14

[7] Marion Grzelka, Iurii Antoniuk, Eric Drockenmuller, Alexis Chennevière, Liliane Léger, and Frédéric Restagno. Viscoelasticity-Induced Onset of Slip at the Wall for Polymer Fluids. *ACS Macro Letters*, 9(7):924–928, July 2020. 11, 16, 128

[8] Eric Lauga, Michael Brenner, and Howard Stone. Microfluidics: The No-Slip Boundary Condition. In Cameron Tropea, Alexander L. Yarin, and John F. Foss, editors, *Springer Handbook of Experimental Fluid Mechanics*, pages 1219–1240. Springer Berlin Heidelberg, Berlin, Heidelberg, 2007. 12, 18

[9] Erhard Schnell. Slippage of Water over Nonwettable Surfaces. *Journal of Applied Physics*, 27(10):1149–1152, October 1956. 12

[10] N.V Churaev, V.D Sobolev, and A.N Somov. Slippage of liquids over lyophobic solid surfaces. *Journal of Colloid and Interface Science*, 97(2):574–581, February 1984. 12, 19

[11] A. Siria, P. Poncharal, A.-L. Biance, R. Fulcrand, X. Blase, S. T. Purcell, and L. Bocquet. Giant osmotic energy conversion measured in a single transmembrane boron nitride nanotube. *Nature*, 494:455–458, 2013. 12

[12] A. Siria, M.-L. Bocquet, and L. Bocquet. New avenues for the large-scale harvesting of blue energy. *Nat. Rev. Chem.*, 1(0091), 2017. 12

[13] Jung A. Lee, Dokeun Lee, Sungmin Park, Hyomin Lee, and Sung Jae Kim. Non-negligible water-permeance through nanoporous ion exchange medium. *Sci Rep.*, 8(12842), 2018. 12

[14] Jean-Pierre Hansen and Ian R. McDonald. *Theory of simple liquids*. Elsevier / Academic Press, Amsterdam ; Boston, 3rd ed edition, 2007. OCLC: ocm62290613. 12, 47

[15] Lydéric Bocquet and Jean-Louis Barrat. On the Green-Kubo relationship for the liquid-solid friction coefficient. *The Journal of Chemical Physics*, 139(4):044704, July 2013. 12, 15

[16] L. Joly, C. Ybert, and L. Bocquet. Probing the Nanohydrodynamics at Liquid-Solid Interfaces Using Thermal Motion. *Physical Review Letters*, 96(4):046101, February 2006. 13, 20

[17] Jean-Louis Barrat and Lydéric Bocquet. Influence of wetting properties on the hydrodynamic boundary condition at a fluid-solid interface. *Faraday Disc.*, 112:119–128, 1999. 15, 60

[18] Elizabeth D. Smith, Mark O. Robbins, and Marek Cieplak. Friction on adsorbed monolayers. *Physical Review B*, 54(11):8252–8260, September 1996. 15

[19] Lydéric Bocqueg and Jean-Louis Barrat. Flow boundary conditions from nano- to micro-scales. *Soft Matter*, 3(6):685, 2007. 15, 36

[20] K. Falk, F. Sedlmeier, L. Joly, R. R. Netz, and L. Bocquet. Ultralow liquid/solid friction in carbon nanotubes: comprehensive theory for alcohols, alkanes, omcts and water. *Langmuir*, 28(40):14261–14272, 2012. 15, 51

[21] Alexander M. Smith, James E. Hallett, and Susan Perkin. Solidification and superlubricity with molecular alkane films. *Proceedings of the National Academy of Sciences*, 116(51):25418–25423, December 2019. 15

[22] Martin Dienwiebel, Gertjan S. Verhoeven, Namboodiri Pradeep, Joost W. M. Frenken, Jennifer A. Heimberg, and Henny W. Zandbergen. Superlubricity of Graphite. *Physical Review Letters*, 92(12):126101, March 2004. 15

[23] John A. Thomas and Alan J. H. McGaughey. Water Flow in Carbon Nanotubes: Transition to Subcontinuum Transport. *Physical Review Letters*, 102(18):184502, May 2009. 15

[24] Kerstin Falk, Felix Sedlmeier, Laurent Joly, Roland R. Netz, and Lydéric Bocquet. Molecular Origin of Fast Water Transport in Carbon Nanotube Membranes: Superlubricity versus Curvature Dependent Friction. *Nano Lett.*, 10(10):4067–4073, October 2010. 15, 60

[25] Joshua D. McGraw, Mischa Klos, Antoine Bridet, Hendrik Hähl, Michael Paulus, Juan Manuel Castillo, Martin Horsch, and Karin Jacobs. Influence of bidisperse self-assembled monolayer structure on the slip boundary condition of thin polymer films. *The Journal of Chemical Physics*, 146(20):203326, May 2017. 15

[26] Tamaki Nakano. *π-Stacked Polymers and Molecules*. Springer Tokyo, 1st edition, 2013. 15

[27] Nikita Kavokine, Marie-Laure Bocquet, and Lydéric Bocquet. Fluctuation-induced quantum friction in nanoscale water flows. *Nature*, 602(7895):84–90, February 2022. 16

[28] F. Brochard and P.-G. de Gennes. Shear-dependent slippage at a polymer/solid interface. *Langmuir*, 8:3033–3037, 1992. 17, 138

[29] K. B. Migler, H. Hervet, and L. Leger. Slip transition of a polymer melt under shear stress. *Physical Review Letters*, 70(3):287–290, January 1993. 17, 37, 118, 119

[30] K B Migler, G Massey, I Hervet, and L Leger. The slip transition at the polymer-solid interface. *Journal of Physics: Condensed Matter*, 6(23A):A301–A304, June 1994. 17, 37

[31] E Durliat, H Hervet, and L Leger. Influence of grafting density on wall slip of a polymer melt on a polymer brush. *Europhysics Letters (EPL)*, 38(5):383–388, May 1997. 17, 118, 119, 138

[32] Mark Ilton, Thomas Salez, Paul D Fowler, Marco Rivetti, Mohammed Aly, Michael Benzaquen, Joshua D McGraw, Elie Raphaël, Kari Dalnoki-Veress, and Oliver Bäumchen. Adsorption-induced slip inhibition for polymer melts on ideal substrates. *Nature Communications*, page 8, 2018. 17, 20

[33] Peter A. Thompson and Sandra M. Troian. A general boundary condition for liquid flow at solid surfaces. *Nature*, 389(6649):360–362, September 1997. 17

[34] F. P. Bowden and D. Tabor. *The Friction and Lubrication of Solids*. Oxford University Press, 2001. 17

[35] J. A. Greenwood and J. P. Williamson. Contact of nominally flat surfaces. *Proceedings of the royal society of London. Series A. Mathematical and physical sciences*, 295(1442):300–319, 1966. 17

[36] Lionel Bureau. *Elasticité et rhéologie d'une interface macroscopique: du piégeage au frottement solide*. PhD thesis, 2002. 18

[37] L. Bureau, T. Baumberger, and C. Caroli. Rheological aging and rejuvenation in solid friction contacts. *The European Physical Journal E*, 8(3):331–337, June 2002. 18

[38] Y. Brechet and Y. Estrin. The effect of strain rate sensitivity on dynamic friction of metals. *Scripta Metallurgica et Materialia*, 30(11):1449–1454, June 1994. 18

[39] L. Bocquet, E. Charlaix, S. Ciliberto, and J. Crassous. Moisture-induced ageing in granular media and the kinetics of capillary condensation. *Nature*, 396(6713):735–737, December 1998. 18

[40] J Crassous, L Bocquet, S Ciliberto, and C Laroche. Humidity effect on static aging of dry friction. *Europhysics Letters (EPL)*, 47(5):562–567, September 1999. 18

[41] B.N.J. Persson. *Sliding Friction: Physical Principles and Applications*. Springer Berlin, Heidelberg, 2000. 18

[42] Chiara Neto, Drew R Evans, Elmar Bonaccurso, Hans-Jürgen Butt, and Vincent S J Craig. Boundary slip in Newtonian liquids: a review of experimental studies. *Reports on Progress in Physics*, 68(12):2859–2897, December 2005. 18

[43] R. K. Schofield and G. W. Scott Blair. The Influence of the Proximity of a Solid Wall on the Consistency of Viscous and Plastic Materials. *The Journal of Physical Chemistry*, 34(2):248–262, February 1930. 19

[44] Melvin Mooney. Explicit Formulas for Slip and Fluidity. *Journal of Rheology*, 2(2):210–222, April 1931. 19, 125

[45] Ann Yoshimura and Robert K. Prud'homme. Wall Slip Corrections for Couette and Parallel Disk Viscometers. *Journal of Rheology*, 32(1):53–67, January 1988. 19, 125

[46] Javier Sanchez-Reyes and Lynden A. Archer. Interfacial Slip Violations in Polymer Solutions: Role of Microscale Surface Roughness. *Langmuir*, 19(8):3304–3312, April 2003. 19, 114, 115, 117, 118, 125, 127, 128, 129, 139

[47] Cécile Cottin-Bizonne, Audrey Steinberger, Benjamin Cross, Olivier Raccurt, and Elisabeth Charlaix. Nanohydrodynamics: The Intrinsic Flow Boundary Condition on Smooth Surfaces. *Langmuir*, 24(4):1165–1172, February 2008. 19

[48] P. Joseph, C. Cottin-Bizonne, J.-M. Benoît, C. Ybert, C. Journet, P. Tabeling, and L. Bocquet. Slippage of Water Past Superhydrophobic Carbon Nanotube Forests in Microchannels. *Physical Review Letters*, 97(15):156104, October 2006. 19

[49] Liliane Léger, H. Hervet, and G. Massey. Slip at the wall. *Rheology Series, Elsevier*, 5:337–355, 1996. 19

[50] Ph Nghe, E. Terriac, M. Schneider, Z. Z. Li, M. Cloitre, B. Abecassis, and P. Tabeling. Microfluidics and complex fluids. *Lab on a Chip*, 11(5):788, 2011. 19

[51] Gabriel Guyard, Alexandre Vilquin, Nicolas Sanson, Stéphane Jouenne, Frédéric Restagno, and Joshua D McGraw. Near-surface rheology and hydrodynamic boundary condition of semi-dilute polymer solutions. *Soft Matter*, 17(14):3765–3774, 2021. 19, 36, 111, 112

[52] Svetlana A. Sukhishvili, Yan Chen, Joachim D. Müller, Enrico Gratton, Kenneth S. Schweizer, and Steve Granick. Diffusion of a polymer 'pancake'. *Nature*, 406(6792):146–146, July 2000. 20

[53] Svetlana A. Sukhishvili, Yan Chen, Joachim D. Müller, Enrico Gratton, Kenneth S. Schweizer, and Steve Granick. Surface Diffusion of Poly(ethylene glycol). *Macromolecules*, 35(5):1776–1784, February 2002. 20

[54] B. Pottier, C. Frétigny, and L. Talini. Boundary Condition in Liquid Thin Films Revealed through the Thermal Fluctuations of Their Free Surfaces. *Physical Review Letters*, 114(22):227801, June 2015. 20

[55] Edward Andrade. The Viscosity of Liquids. *Nature*, 125:309–310, 1930. 20

[56] Henry Eyring. Viscosity, Plasticity, and Diffusion as Examples of Absolute Reaction Rates. *The Journal of Chemical Physics*, 4(4):283–291, April 1936. 20, 21

[57] A. J. Batschinski. Untersuchungen aber die innere reibnng der flüssigkeiten. *Z. Physik Chem.*, 84(644), 1913. 20, 22

[58] D. B. Macleod. On the viscosity of liquid mixtures showing maxima. *Trans. Faraday Soc.*, 19:17–34, 1923. 20, 22

[59] H. Vogel. The law of the relation between the viscosity of liquids and the temperature. *Phys. Z*, 22:645–646, 1921. 20, 56, 59, 60

[60] G. S. Fulcher. Analysis of recent measurements of the viscosity of glasses. *Journal of the American Ceramic Society*, 8:339–355, 1925. 21, 56, 59, 60

[61] G. Tammann and W. Hesse. The dependence of viscosity upon the temperature of supercooled liquids. *Z. Anorg. Allg. Chem*, 156:245–257, 1926. 21, 56, 59, 60

[62] Arthur K. Doolittle. Studies in Newtonian Flow. II. The Dependence of the Viscosity of Liquids on Free-Space. *Journal of Applied Physics*, 22(12):1471–1475, December 1951. 21, 22

[63] D. Tabor. *Gases, Liquids and Solids*. Cambridge University Press, 1969. 21, 56, 136

[64] H. Eyring and M. Polanyi. Über einfache gasreaktionen. *Z. Phys. Chem. Abt. B*, 12:279–311, 1931. 21

[65] Rizk Farid, Gelin Simon, Biance Anne-Laure, and Joly Laurent. Microscopic origins of the viscosity of a lennard-jones liquid. *Physical Review Letters*, 129(7), 2022. 22, 56

[66] G. Adam and J.H. Gibbs. On the temperature dependence of cooperative relaxation properties in glass-forming liquids. *J. Chem. Phys.*, page 43:139, 1965. 22

[67] J.-S. Wang and R. S. Porter. On the viscosity-temperature behavior of polymer melts. *Rheologica Acta*, 34(5):496–503, 1995. 22, 23

[68] Malcolm L. Williams, Robert F. Landel, and John D. Ferry. The Temperature Dependence of Relaxation Mechanisms in Amorphous Polymers and Other Glass-forming Liquids. *Journal of the American Chemical Society*, 77(14):3701–3707, July 1955. 23

[69] J. Servantie and M. Müller. Temperature Dependence of the Slip Length in Polymer Melts at Attractive Surfaces. *Phys. Rev. Lett.*, 101(2):026101, July 2008. 24, 25, 59

[70] Oliver Bäumchen, Matthias Lessel, Renate Fetzer, Ralf Seemann, and Karin Jacobs. Sliding fluids: Dewetting experiments reveal the solid/liquid boundary condition. *Journal of Physics: Conference Series*, 216:012002, March 2010. 24, 25

[71] Micha Klos and Karin Jacobs. Exploring the Boundary Condition of Polymeric Liquids. Disseration, 2016. 24, 25

[72] Marceau Hénot. *Glissement de polymères liquides*. PhD thesis, Paris-Saclay University, 2018. 25, 37, 103, 118, 119, 120, 138, 139, 148

[73] Inc CiteDrive. The nobel prize in chemistry 1953, 2022. 26

[74] P.-G. De Gennes. Reptation of a Polymer Chain in the Presence of Fixed Obstacles. *The Journal of Chemical Physics*, 55(2):572–579, 1971. 26, 31

[75] P.-G. de Gennes. *Scaling Concepts in Polymer Physics*. Cornell University Press, 1979. 26, 114

[76] Masao Doi and S.F. Edwards. *The Theory of Polymer Dynamics*. Oxford Science Publications, 1988. 26, 31

[77] Michael Rubinstein and Ralph H. Colby. *Polymer Physics*. Oxford University Press, 2003. 26, 27, 30, 115

[78] Paul J. Flory. *Principle of Polymer Chemistry*. Cornell University Press, 1953. 27, 28

[79] J. P. Cotton, D. Decker, H. Benoit, B. Farnoux, J. Higgins, G. Jannink, R. Ober, C. Picot, and J. des Cloizeaux. Conformation of Polymer Chain in the Bulk. *Macromolecules*, 7(6), 1974. 27

[80] V.N. Novikov and E.A. Rössler. Correlation between glass transition temperature and molecular mass in non-polymeric and polymer glass formers. *Polymer*, 54(26):6987–6991, December 2013. 32, 33

[81] Timothy P. Lodge and Thomas C. B. McLeish. Self-Concentrations and Effective Glass Transition Temperatures in Polymer Blends. *Macromolecules*, 33(14):5278–5284, July 2000. 32

[82] T. R. Lutz, Yiyong He, and M. D. Ediger. Segmental Dynamics of Dilute Polystyrene Chains in Miscible Blends and Solutions. *Macromolecules*, 38(23):9826–9835, November 2005. 32, 33, 34

[83] P.-G. de Gennes. Polymer solutions near an interface. adsorption and depletion layers. *Macromolecules*, 14(6):1637–1644, 1981. 35, 94, 105, 106

[84] Guy Chauveteau. Rodlike Polymer Solution Flow through Fine Pores: Influence of Pore Size on Rheological Behavior. *Journal of Rheology*, 26(2):111–142, April 1982. 35

[85] D. Ausserré, J. Edwards, J. Lecourtier, H. Hervet, and F. Rondelez. Hydrodynamic thickening of depletion layers in colloidal solutions. *Europhysics Letters*, 14(1):33–38, 1991. 35, 95, 109

[86] L. Lee, O. Guiselin, A. Lapp, B. Farnoux, and J. Penfold. Direct measurements of polymer depletion layers by neutron reflectivity. *Physical Review Letters*, 67(20):2838–2841, 1991. 36, 94, 106

[87] D. Ausserre, H. Hervet, and F. Rondelez. Concentration dependence of the interfacial depletion layer thickness for polymer solutions in contact with nonadsorbing walls. *Macromolecules*, 19(1):85–88, January 1986. 36, 95

[88] A Dobrynin and M Rubinstein. Theory of polyelectrolytes in solutions and at surfaces. *Progress in Polymer Science*, 30(11):1049–1118, November 2005. 36

[89] C. Barraud, B. Cross, C. Picard, F. Restano, L. Léger, and E. Charlaix. Large slippage and depletion layer at the polyelectrolyte/solid interface. *Physical Review Letters*, 67(20):2838–2841, 1991. 36, 107, 111, 112

[90] Olga I. Vinogradova. Drainage of a Thin Liquid Film Confined between Hydrophobic Surfaces. *Langmuir*, 11(6):2213–2220, June 1995. 36

[91] L. Léger, E. Raphaël, and H. Hervet. *Polymers in Confined Environments*, chapter "Surface-Anchored Polymer Chains: Their Role in Adhesion and Friction". Springer, Berlin, Heidelberg, 1999. 37, 111, 112

[92] Patrick P. Drda and Shi-Qing Wang. Stick-Slip Transition at Polymer Melt/Solid Interfaces. *Physical Review Letters*, 75(14):2698–2701, October 1995. 37

[93] Shi-Qing Wang and Patrick A. Drda. StickSlip Transition in Capillary Flow of Polyethylene. 2. Molecular Weight Dependence and Low-Temperature Anomaly. *Macromolecules*, 29(11):4115–4119, January 1996. 37

[94] N. Plucktaveesak, S. Q. Wang, and A. Halasa. Interfacial Flow Behavior of Highly Entangled Polybutadiene Solutions. *Macromolecules*, 32(9):3045–3050, May 1999. 37

[95] Marceau Hénot, Eric Drockenmuller, Liliane Léger, and Frédéric Restagno. Sensing adsorption kinetics through slip velocity measurements of polymer melts. *The European Physical Journal E*, 41(7):83, July 2018. 37, 138, 151

[96] P.-G. de Gennes. Écoulements viscomécriques de polymères enchevêtrés. *C. R. Acad. Sc. Paris.*, Série B, 1979. 38

[97] Marion Grzelka, Iurii Antoniuk, Eric Drockenmuller, Alexis Chennevière, Liliane Léger, and Frédéric Restagno. Slip and friction mechanisms at polymer semi-dilute solutions / solid interfaces. *Macromolecules*, 54(10), 2021. 38, 39, 114, 115, 127

[98] A. P. Thompson, H. M. Aktulga, R. Berger, D. S. Bolintineany, W. M. Brown, P. S. Crozier, P. J.in't Veld, A. Kohlmeyer, S. G. Moore, T. D. Nguyen, and *et al.* Lammps – a flexible simulation tool for particle-based materials modeling at the atomic, meso, and continuum scales. *Comput. Phys. Commun.*, 271(108171), 2022. 43

[99] W. Kob and H. C. Andersen. Testing mode-coupling theory for a supercooled binary lennard-jones mixture. *Phys. Rev. E*, 51(4626), 1995. 43, 48, 55

[100] P. Español and I. Zúñiga. Force autocorrelation function in brownian motion theory. *J. Chem. Phys.*, 98:574–580, 1993. 48, 57, 58

[101] P. Gallo, F. Sciortino, P. Tartaglia, and S.-H. Chen. Slow Dynamics of Water Molecules in Supercooled States. *Physical Review Letters*, 76(15):2730–2733, April 1996. 48

[102] W Gotze and L Sjogren. Relaxation processes in supercooled liquids. *Reports on Progress in Physics*, 55(3):241–376, March 1992. 48

[103] Tsuyoshi Yamaguchi. Stress-structure coupling and nonlinear rheology of Lennard-Jones liquid. *The Journal of Chemical Physics*, 148(23):234507, June 2018. 48, 67, 68

[104] Cecilia Herrero, Takeshi Omori, Yasutaka Yamaguchi, and Laurent Joly. Shear force measurement of the hydrodynamic wall position in molecular dynamics. *The Journal of Chemical Physics*, 151(4):041103, July 2019. 49

[105] Cecilia Herrero, Gabriele Tocci, Samy Merabia, and Laurent Joly. Fast increase of nanofluidic slip in supercooled water: the key role of dynamics. *Nanoscale*, 12(39):20396–20403, 2020. 49, 59

[106] Ulf R. Pedersen, Thomas B. Schrøder, and Jeppe C. Dyre. Phase Diagram of Kob-Andersen-Type Binary Lennard-Jones Mixtures. *Phys. Rev. Lett.*, 120(16):165501, April 2018. 52, 55

[107] Rupal Agrawal and David A. Kofke. Thermodynamic and structural properties of model systems at solid-fluid coexistence: II. Melting and sublimation of the Lennard-Jones system. *Molecular Physics*, 85(1):43–59, May 1995. 53, 54

[108] Suzanne Lafon, Alexis Chennevière, Frédéric Restagno, Samy Merabia, and Laurent Joly. Giant slip length at a supercooled liquid-solid interface. *Physical Review E*, 107(2):025101, February 2023. 55, 73, 163

[109] Peter F. Pelz and Tobias Corneli. The activation energy for wall slip. http://arxiv.org/abs/2111.09693, 2021. 56

[110] Terence D. Blake. Slip between a liquid and a solid: D.M. Tolstoi's (1952) theory reconsidered. *Colloids and Surfaces*, 47:135–145, January 1990. 56

[111] K. Jacobs, R. Seemann, G. Schatz, and S. Herminghaus. Growth of holes in liquid films with partial slippage. *Langmuir*, 14(18), 1998. 56

[112] Seth Lichter, Ashlie Martini, Randall Q. Snurr, and Qian Wang. Liquid slip in nanoscale channels as a rate process. *Physical Review Letters*, 98(22):226001, 2007. 56

[113] Wang Feng-Chao and Zhao Ya-Pu. Slip boundary conditions based on molecular kinetic theory: The critical shear stress and the energy dissipation at the liquid–solid interface. *Soft Matter*, 7(18):8628, 2011. 56

[114] Gerald J. Wang and G. Hadjiconstantinou. Universal molecular-kinetic scaling relation for slip of a simple fluid at a solid boundary. *Physical Review Fluids*, 4(6):064201, 2019. 56

[115] Z. Guo, T. S. Zhao, and S. Yong. Temperature dependence of the velocity boundary condition for nanoscale fluid flows. *Physical Review E*, 72(3):036301, 2005. 56, 58

[116] Lydéric Bocquet and Jean-Louis Barrat. Hydrodynamic boundary conditions, correlation functions, and Kubo relations for confined fluids. *Physical Review E*, 49(4):3079–3092, April 1994. 57

[117] Laurent Joly, Gabriele Tocci, Samy Merabia, and Angelos Michaelides. Strong Coupling between Nanofluidic Transport and Interfacial Chemistry: How Defect Reactivity Controls Liquid–Solid Friction through Hydrogen Bonding. *The Journal of Physical Chemistry Letters*, 7(7):1381–1386, April 2016. 57

[118] Haruki Oga, Yasutaka Yamaguchi, Takeshi Omori, Samy Merabia, and Laurent Joly. Green-Kubo measurement of liquid-solid friction in finite-size systems. *The Journal of Chemical Physics*, 151(5):054502, August 2019. 57

[119] Martin Dienwiebel, Gertjan S Verhoeven, Namboodiri Pradeep, Joost WM Frenken, Jennifer A Heimberg, and Henny W Zandbergen. Superlubricity of graphite. *Physical review letters*, 92(12):126101, 2004. 60

[120] Qing Zhang, Yue Qi, Louis G. Hector, Tahir Cagin, and William A. Goddard. Atomic simulations of kinetic friction and its velocity dependence at al/al and α (al_2o^3/α (al_2o^3 interfaces. *Physical Review B*, 72(4):045406, 2005. 61

[121] A. Franchini, V. Bortolani, G. Santoro, and K. Xheka. Effects of the commensurability and disorder on friction for the system xe/cu. *Journal of Physics: Condensed Matter*, 23(48):484004, 2011. 61

[122] Marek Cieplak, Elizabeth D. Smith, and Mark O. Robbins. Molecular origins of friction: the force on adsorbed layers. *Science*, 265(5176):1209–1212, 1994. 61

[123] W. P. Cox and E. H. Merz. Correlation of dynamic and steady flow viscosities. *Journal of Polymer Science*, 28(118):619–622, 1958. 67, 82

[124] Scott Bair, Tsuyoshi Yamaguchi, Ludwig Brouwer, Hubert Schwarze, Philippe Vergne, and Gerhard Poll. Oscillatory and steady shear viscosity: The Cox–Merz rule, superposition, and application to EHL friction. *Tribology International*, 79:126–131, November 2014. 67

[125] Akira Furukawa. Onset of shear thinning in glassy liquids: Shear-induced small reduction of effective density. *Physical Review E*, 95(1):012613, January 2017. 67

[126] S. Capaccioli, D. Prevosto, A. Best, A. Hanewald, and T. Pakula. Applications of the rheo-dielectric technique. *Journal of Non-Crystalline Solids*, 353(47-51):4267–4272, December 2007. 67

[127] Kazushi Horio, Takashi Uneyama, Yumi Matsumiya, Yuichi Masubuchi, and Hiroshi Watanabe. Rheo-Dielectric Responses of Entangled *cis* -Polyisoprene under Uniform Steady Shear and LAOS. *Macromolecules*, 47(1):246–255, January 2014. 67

[128] J. Mark. *Polymer Data Handbook*. Oxford University Press, 1999. 78, 89

[129] L.J. Fetters, D. J. Lohse, D. Richter, T. A. Witten, and A. Zirkel. Connection between polymer molecular weight, density, chain dimensions, and melt viscoelastic properties. *Macromolecules*, 27(17):4639–4647, 1994. 78

[130] L. Aras and M. J. Richardson. The glass transition behaviour and thermodynamic properties of amorphous polystyrene. *Polymer*, 30, 1989. 78

[131] J. Maul, B. G. Frushour, J. R. Kontoff, H. Eichenauer, K.-H. Ott, and C. Schade. *Polystyrene and Styrene Copolymers*. Ullmann's Encyclopedia of Industrial Chemistry, 2007. 78

[132] M. Carrega and V. Verney. *Matières plastiques*. Dunod, Paris, 2012. 79

[133] A. M. Api. Toxicological profile of diethyl phthalate: a vehicle for fragrance and cosmetic ingredients. *Food and Chemical Texocology*, 39(2), 2000. 79

[134] Hsin-Hui Shen, Tsung-Wu Lin, Robert K. Thomas, Diana J. F. Taylor, and Jeffrey Penfold. Surfactin Structures at Interfaces and in Solution: The Effect of pH and Cations. *The Journal of Physical Chemistry B*, 115(15):4427–4435, April 2011. 80, 107

[135] Nicolas Merle, Tarnuma Tabassum, Susannah L. Scott, Alessandro Motta, Kai Szeto, Mostafa Taoufik, Régis Michaël Gauvin, and Laurent Delevoye. High-Field NMR, Reactivity, and DFT Modeling Reveal the -Al $_2$ O $_3$ Surface Hydroxyl Network**. *Angewandte Chemie*, 134(37), September 2022. 80, 107

[136] Thomas G. Mezger. *The Rheology Handbook*. Vincentz Network, Hanover, Germany, 3 edition, 2020. 80

[137] J. R. Vig. Uv/ozone cleaning of surfaces. *Journal of Vacuum Science and Technology A: Vacuum, Surfaces, and Films*, 3(3), 1985. 83

[138] W. Kern and D. Puotinen. Cleaning solutions based on hydrogen peroxide for use in silicon semiconductor technology. *RCA Rev.*, 31:187–206, 1970. 83

[139] Harland G. Tompkins and Eugene A. Irene, editors. *Handbook of ellipsometry*. William Andrew Pub. ; Springer, Norwich, NY : Heidelberg, Germany, 2005. 87

[140] R. M. A. Azzam and N. M. Bashara. *Ellipsometry and Polarized Light*, chapter 4. North-Holland Physics Publishing, 1986. 88

[141] N. Sultanova, S. Kasarova, and I. Nikolov. Dispersion properties of optical polymers. *Acta Physica Polonica*, 116:585–587, 2009. 89

[142] I. H. Malitson. Interspecimen comparison of the refractive index of fused silica. *J. Opt. Soc. Am.*, 55(10):1205–1209, 1965. 89

[143] M. A. Green and M. J. Keevers. Optical properties of intrinsic silicon at 300 k. *Progress in Photovoltaics : Research and Applications*, 3(3):189–192, 1995. 89

[144] H. Robertson, I.J. Gresham, S. W. Prescott, G.B. Webber, E. J. Wanless, and A. Nelson. *refellips*: A python package for the analysis of variable angle spectroscopic ellipsometry data. *SoftwareX*, 20:101225, 2022. 89

[145] Zijian Song, Cristian Rodríguez-Tinoco, Allen Mathew, and Simone Napolitano. Fast equilibration mechanisms in disordered materials mediated by slow liquid dynamics. *Science Advances*, 8(15):eabm7154, April 2022. 90, 153, 154, 156, 157, 158

[146] Suzanne Lafon, Tiago Outerelo-Corvo, Marion Grzelka, Arnaud Hélary, Philipp Gutfreund, Liliane Léger, Alexis Chennevière, and Frédéric Restagno. Simultaneous depletion and adsorption in polymer solutions near a solid wall. https://arxiv.org/abs/2305.05960, 2023. 93, 112

[147] Sho Asakura and Fumio Oosawa. Interaction between particles suspended in solutions of macromolecules. *Journal of Polymer Science*, 33(126):183–192, December 1958. 94

[148] F.K.R. Li-In-On, B. Vincent, and F.A. Waite. Stability of sterically stabilized dispersions at high polymer concentrations. *Colloidal Dispersions and Micellar Behaviour*, 9(165), 1975. 94

[149] C. Cowell, R. Li-In-On, and B. Vincent. Reversible flocculation of sterically-stabilised dispersions. *J. Chem. Soc. Faraday Trans.*, 74(337), 1978. 94

[150] Jean-François Joanny, Ludwik Leibler, and Pierre-Gilles de Gennes. Effects of polymer solutions on colloid stability. *J. Polym. Sci.*, 17(1073), 1979. 94, 106

[151] C. Allain, D. Ausserré, and F. Rondelez. Direct optical observation of interfacial depletion layers in polymer solutions. *Physical Review Letters*, 49(23):1694–1697, 1982. 94

[152] Johan Marra and Michael L Hair. Double-layer forces in nonadsorbing ionic micellar solutions and polyelectrolyte solutions. *Journal of Colloid and Interface Science*, 128(2):511–522, March 1989. 94

[153] G. Chauveteau, M. Tirrell, and A. Omari. Concentration dependence of the effective viscosity of polymer solutions in small pores with repulsive or attractive walls. *Journal of Colloid and Interface Science*, 100(1):41–54, July 1984. 94

[154] M. Gvaramia, P. Maroni, and D. Kosior. Depletion of polyelectrolytes near like-charged substrates probed by optical reflectivity. *The Journal of Physical Chemistry C*, 126(29):12313–12317, 2022. 94

[155] Jean Louis Barrat. A possible mechanism for swelling of polymer brushes under shear. *Macromolecules*, 25(2):832–834, January 1992. 95

[156] J. L. Harden and M. E. Cates. Deformation of grafted polymer layers in strong shear flows. *Physical Review E*, 53(4):3782–3787, April 1996. 95

[157] Jacob Klein, Dvora Perahia, and Sharon Warburg. Forces between polymer-bearing surfaces undergoing shear. *Nature*, 352(6331):143–145, July 1991. 95

[158] A. Korolkovas, C. Rodriguez-Emmenegger, A. de los Santos Pereira, A. Chennevière, F. Restagno, M. Wolff, F. A. Adlmann, A. J. C. Dennison, and P. Gutfreund. Polymer brush collapse under shear flow. *Macromolecules*, 50:1215–1224, 2017. 95, 104, 110

[159] Juan José De Pablo, Hans Christian Öttinger, and Yitzhak Rabin. Hydrodynamic changes of the depletion layer of dilute polymer solutions near a wall. *AlChE Journal*, 38(2):273–283, 1992. 95, 110

[160] Hongbo Ma and Michael D. Graham. Theory of shear-induced migration in dilute polymer solutions near solid boundaries. *Physics of Fluids*, 17(8):083103, August 2005. 95

[161] Seong Jun Park, Anisha Shakya, and John T. King. Depletion layer dynamics of polyelectrolyte solutions under Poiseuille flow. *Proceedings of the National Academy of Sciences*, 116(33):16256–16261, August 2019. 95

[162] O. Hahn and F. Strassmann. Über den nachweis und das verhalten der bei der bestrahlung des urans mittels neutronen entstehenden erdalkalimetalle. *Naturwissenschaften*, 27(1):11–15, 1939. 96

[163] C. Fermon, F. Ott, and A. Menelle. *Neutron Reflectometry*, pages 183–234. Springer Berlin Heidelberg, Berlin, Heidelberg, 2009. 100

[164] L. G. Parratt. Surface studies of solids by total reflection of x-rays. *Physical Review*, 95(2), 1954. 101

[165] Andrew RJ Nelson and Stuart W Prescott. refnx: neutron and x-ray reflectometry analysis in python. *Journal of applied crystallography*, 52(1):193–200, 2019. 102

[166] Mathieu Doucet, Richard K Archibald, and William T Heller. Machine learning for neutron reflectometry data analysis of two-layer thin films *. *Machine Learning: Science and Technology*, 2(3):035001, September 2021. 102

[167] Daniil Mironov, James H Durant, Rebecca Mackenzie, and Joshaniel F K Cooper. Towards automated analysis for neutron reflectivity. *Machine Learning: Science and Technology*, 2(3):035006, September 2021. 102

[168] T. Saerbeck, R. Cubitt, A. Wildes, G. Manzin, K. H. Andersen, and P. Gutfreund. Recent upgrades of the neutron reflectometer d17 at ill. *J. Appl. Cryst.*, 51:249–256, 2018. 102

[169] A. Silberberg. Adsorption of flexible macromolecules. iv. effect of solvent–solute interactions, solute concentration, and molecular weight. *J. Chem. Phys.*, 48(2835), 1968. 106

[170] Yergou B. Tatek and Mesfin Tsige. Structural properties of atactic polystyrene adsorbed onto solid surfaces. *The Journal of Chemical Physics*, 135:174708, 2011. 107

[171] Alexa Courty, Michel Mons, Iliana Dimicoli, François Piuzzi, Marie-Pierre Gaigeot, Valérie Brenner, Patrick De Pujo, and Philippe Millié. Quantum Effects in the Threshold Photoionization and Energetics of the BenzeneH $_2$ O and BenzeneD $_2$ O Complexes: Experiment and Simulation. *The Journal of Physical Chemistry A*, 102(33):6590–6600, August 1998. 107

[172] E. A. Meyer, R. K. Castellano, and F. Diederich. Interactions with aromatic rings in chemical and biological recognition. *Angew. Chem. Int. Ed.*, 42(11):1210–1250, 2003. 107

[173] P.-G. de Gennes. Dynamics of Entangled Polymer Solutions. II. Inclusion of Hydrodynamic Interactions. *Macromolecules*, 9(4):594–598, July 1976. 114

[174] M. Adam and M. Delsanti. Viscosity and longest relaxation time of semi-dilute polymer solutions. I. Good solvent. *Journal de Physique*, 44(10):1185–1193, 1983. 114, 115, 117, 118

[175] W. M. Kulicke and R. Kniewske. The shear viscosity dependence on concentration, molecular weight, and shear rate of polystyrene solutions. *Rheologica Acta*, 23(1):75–83, January 1984. 114, 115, 117, 118

[176] E. Raspaud, D. Lairez, and M. Adam. On the Number of Blobs per Entanglement in Semidilute and Good Solvent Solution: Melt Influence. *Macromolecules*, 28(4):927–933, July 1995. 114, 115, 117, 118

[177] P. K. Bhattacharjee, J. P. Oberhauser, G. H. McKinley, L. G. Leal, and T. Sridhar. Extensional Rheometry of Entangled Solutions. *Macromolecules*, 35(27):10131–10148, December 2002. 114, 115

[178] Vijay Mhetar and L. A. Archer. Slip in Entangled Polymer Solutions. *Macromolecules*, 31(19):6639–6649, September 1998. 114, 115, 139

[179] Kunihiro Osaki, Mitsutoshi Fukuda, and Michio Kurata. Relaxation spectra of concentrated polystyrene solutions. *Journal of Polymer Science: Polymer Physics Edition*, 13(4):775–786, April 1975. 114, 115

[180] T. Nose and B. Chu. Static and Dynamical Properties of Polystyrene in trans-Decalin. *Macromolecules*, 1979. 115

[181] Daniel A. Savin, Anne M. Larson, and Timothy P. Lodge. Effect of composition on the width of the calorimetric glass transition in polymer-solvent and solvent-solvent mixtures. *Journal of Polymer Science Part B: Polymer Physics*, 42(7):1155–1163, April 2004. 116

[182] D. Frot. *Etude expérimentale de la dynamique de polymères au voisinage d'une surface solide par recouvrement de fluorescence après photolyse en onde évanescente.* PhD thesis, Université Paris VI, 1991. 118, 119

[183] J. Vasquez. *Etude expérimentale des mécanismes moléculaires de la friction aux interfaces polymère fondu - solide.* PhD thesis, Université Paris VI, 2003. 118, 119

[184] Krzysztof Nawara and Jacek Waluk. Goodbye to Quinine in Sulfuric Acid Solutions as a Fluorescence Quantum Yield Standard. *Analytical Chemistry*, 91(8):5389–5394, April 2019. 119

[185] Céline Cohen. *Mécanismes moléculaires de la friction aux interfaces polymères souples*. PhD thesis, Université Paris-Sud, 2011. 119

[186] G. Massey. *Etude expérimentale du glissement de polymères fondus sous cisaillement à une interface solide*. PhD thesis, Université Paris VI, 1995. 119

[187] Marceau Hénot, Alexis Chennevière, Eric Drockenmuller, Liliane Léger, and Frédéric Restagno. Comparison of the Slip of a PDMS Melt on Weakly Adsorbing Surfaces Measured by a New Photobleaching-Based Technique. *Macromolecules*, 50(14):5592–5598, July 2017. 120, 122, 123

[188] S. G. Hatzikiriakos and J. M. Dealy. Wall slip of molten high density polyethylene. I. Sliding plate rheometer studies. *Journal of Rheology*, 35(4):497–523, May 1991. 125

[189] O. Wein and V. V. Tovchigrechko. Rotational viscometry under presence of apparent wall slip. *Journal of Rheology*, 36(5):821–844, July 1992. 125

[190] V. Bertola, F. Bertrand, H. Tabuteau, D. Bonn, and P. Coussot. Wall slip and yielding in pasty materials. *Journal of Rheology*, 47(5):1211–1226, September 2003. 125

[191] Steven P. Meeker, Roger T. Bonnecaze, and Michel Cloitre. Slip and flow in pastes of soft particles: Direct observation and rheology. *Journal of Rheology*, 48(6):1295–1320, November 2004. 125

[192] C. W. Macosko. *Rheology principles measurements and applications*, chapter 5. Wiley-VCH, New-York, 1994. 126

[193] Chang-Hwan Choi and Chang-Jin Kim. Large slip of aqueous liquid flow over a nanoengineered superhydrophobic surface. *Physical Review Letters*, 96(6):066001, February 2006. 129

[194] Lydéric Bocquet, Patrick Tabeling, and Sébastien Manneville. Comment on "large slip of aqueous liquid flow over a nanoengineered superhydrophobic surface". *Physical Review Letters*, 97:109601, 2006. 129

[195] Chang-Hwan Choi and Chang-Jin Kim. Choi and kim reply:. *Physical Review Letters*, 97:109602, 2006. 129

[196] Pierre Jean Carreau. *Image de couverture pour Rheological equations from molecular network theories Rheological equations from molecular network theories*. PhD thesis, University of Wisconsin–Madison, 1968. 130

[197] Pierre J. Carreau. Rheological Equations from Molecular Network Theories. *Transactions of the Society of Rheology*, 16(1):99–127, March 1972. 130

[198] K. Yasuda, R. C. Armstrong, and R. E. Cohen. Shear flow properties of concentrated solutions of linear and star branched polystyrenes. *Rheologica Acta*, 20(2):163–178, March 1981. 130

[199] Céline Cohen, Frédéric Restagno, Christophe Poulard, and Liliane Léger. Incidence of the molecular organization on friction at soft polymer interfaces. *Soft Matter*, 7(18):8535, 2011. 140, 142

[200] Simone Napolitano. Irreversible adsorption of polymer melts and nanoconfinement effects. *Soft Matter*, 16(23):5348–5365, 2020. 148, 151, 156, 158

[201] O. Guiselin. Irreversible adsorption of a concentrated polymer solution. *Europhysics Letters*, 17(3):225, jan 1992. 149

[202] Martial Deruelle, Matthew Tirrell, Yves Marciano, Hubert Hervet, and Liliane Léger. Adhesion energy between polymer networks and solid surfaces modified by polymer attachment. *Faraday Discuss.*, 98:55–65, 1994. 149, 150

[203] P.-G. de Gennes. Polymers at an interface; a simplified view. *Advances in Colloid and Interface Science*, 27(3-4):189–209, 1987. 150

[204] E. Pefferkorn, A. Carroy, and R. Varoqui. Dynamic behavior of flexible polymers at a solid/liquid interface. *Journal of Polymer Science: Polymer Physics Edition*, 23(10):1997–2008, October 1985. 150

[205] Joseph W. Krumpfer and Thomas J. McCarthy. Rediscovering Silicones: "Unreactive" Silicones React with Inorganic Surfaces. *Langmuir*, 27(18):11514–11519, September 2011. 151

[206] Gabriel Graffius, Frank Bernardoni, and Alexander Y. Fadeev. Covalent Functionalization of Silica Surface Using "Inert" Poly(dimethylsiloxanes). *Langmuir*, 30(49):14797–14807, December 2014. 151

[207] Hannu Teisala, Philipp Baumli, Stefan A. L. Weber, Doris Vollmer, and Hans-Jürgen Butt. Grafting Silicone at Room Temperature—a Transparent, Scratch-resistant Nonstick Molecular Coating. *Langmuir*, 36(16):4416–4431, April 2020. 151

[208] J.-P. Cohen-Addad and N. Morel. NMR Investigations into Polydimethylsiloxane Adsorption on Silica Aggregates. *Journal de Physique III*, 6(2):267–277, 1996. 151

[209] Cinzia Rotella, Simone Napolitano, Stefaan Vandendriessche, Ventsislav K. Valev, Thierry Verbiest, Maria Larkowska, Stanislaw Kucharski, and Michael Wübbenhorst. Adsorption Kinetics of Ultrathin Polymer Films in the Melt Probed by Dielectric Spectroscopy and Second-Harmonic Generation. *Langmuir*, 27(22):13533–13538, November 2011. 151

[210] Caroline Housmans, Michele Sferrazza, and Simone Napolitano. Kinetics of Irreversible Chain Adsorption. *Macromolecules*, 47(10):3390–3393, May 2014. 151

[211] Anna Panagopoulou and Simone Napolitano. Irreversible Adsorption Governs the Equilibration of Thin Polymer Films. *Physical Review Letters*, 119(9):097801, August 2017. 151

[212] David Nieto Simavilla, Weide Huang, Philippe Vandestrick, Jean-Paul Ryckaert, Michele Sferrazza, and Simone Napolitano. Mechanisms of Polymer Adsorption onto Solid Substrates. *ACS Macro Letters*, 6(9):975–979, September 2017. 151, 152, 153

[213] Christian Ligoure and Ludwik Leibler. Thermodynamics and kinetics of grafting end-functionalized polymers to an interface. *Journal de Physique*, 51(12):1313–1328, 1990. 151

[214] A. Johner and J. F. Joanny. Dynamics of polymeric brushes: End exchange and bridging kinetics. *The Journal of Chemical Physics*, 98(2):1647–1658, January 1993. 151

[215] A. N. Semenov and J.-F. Joanny. Kinetics of Adsorption of Linear Homopolymers onto Flat Surfaces: Rouse Dynamics. *J. Phys. II France*, 5:859–876, 1995. 151

[216] David Nieto Simavilla, Weide Huang, Caroline Housmans, Michele Sferrazza, and Simone Napolitano. Taming the Strength of Interfacial Interactions via Nanoconfinement. *ACS Central Science*, 4(6):755–759, June 2018. 152

[217] Lars Onsager. Reciprocal Relations in Irreversible Processes. I. *Physical Review*, 37(4):405–426, February 1931. 153

[218] Erik Thoms and Simone Napolitano. To be published, 2023. 156, 159

[219] Gernot Blum, Friedrich Kremer, Thomas Juworek, and Gerkard Wegner. Molecular dynamics of poly(-octadecyl-co-methyl-L-glutamate) in ultrathin films and in the bulk. *Advanced Materials*, 7(12):1017–1020, December 1995. 157

[220] S. Havriliak and S. Negami. A complex plane representation of dielectric and mechanical relaxation processes in some polymers. *Polymer*, 8:161–210, January 1967. 157

[221] Friedrich Kremer and Andreas Schönhals, editors. *Broadband Dielectric Spectroscopy*. Springer Berlin Heidelberg, Berlin, Heidelberg, 2003. 157

[222] L. J. Garfield and S. E. Petrie. Viscosity and glass-transition behavior of polymer—diluent systems. *The Journal of Physical Chemistry*, 68(7):1750–1754, 1998. 171